Universidad Carlos III de Madrid
Department of Continuum Mechanics and Structural Analysis

A continuum mechanics framework for hyperelastic materials: connecting experiments and modelling

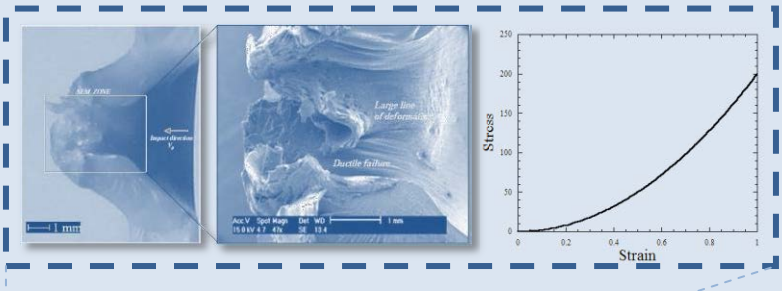

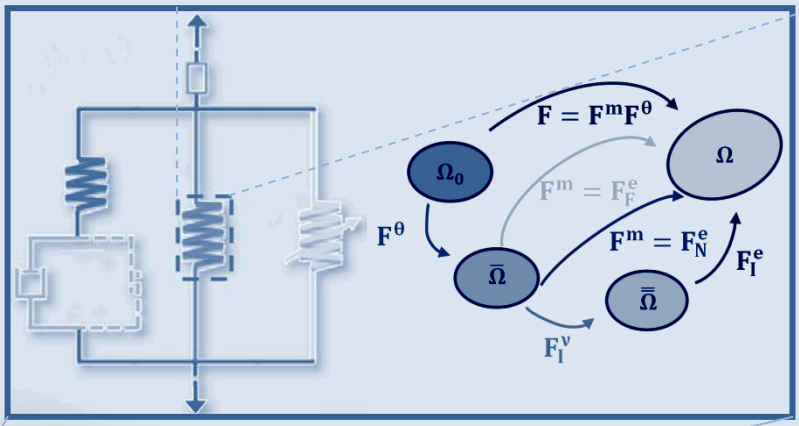

DOCTORAL THESIS

Daniel García González

Supervisor: Ángel Arias Hernández

Leganés, 2016

Universidad
Carlos III de Madrid
www.uc3m.es

TESIS DOCTORAL

A continuum mechanics framework for hyperelastic materials: Connecting experiments and modelling

Autor:

Daniel García González

Director:

Ángel Arias Hernández

DEPARTAMENTO DE MECÁNICA DE MEDIOS CONTINUOS Y TEORÍA DE ESTRUCTURAS

Leganés, noviembre de 2016

Universidad
Carlos III de Madrid
www.uc3m.es

TESIS DOCTORAL

A CONTINUUM MECHANICS FRAMEWORK FOR HYPERELASTIC MATERIALS: CONNECTING EXPERIMENTS AND MODELLING

Autor: *Daniel García González*

Director: **Ángel Arias Hernández**

Firma del Tribunal Calificador:

Firma

Presidente: Prof. Dr. D. José Fernández Sáez

Vocal: Prof. Dr. D. Miguel Ángel Martínez Barca

Secretario: Prof. Dr. D. Sidney Chocron Benloulo

Calificación:

Leganés, 30 de Noviembre de 2016

Agradecimientos

En primer lugar, agradecer a mis padres sus consejos y apoyo incondicional durante estos años. Agradecer también el apoyo recibido por el resto de mi familia, especialmente a mi hermano Arturo y a mi tía Soledad.

Agradecer a mi tutor Ángel Arias la confianza que ha depositado en mí y las grandes oportunidades que me ha ofrecido estos años. Desde la realización del trabajo fin de grado hasta la finalización de esta tesis doctoral has sido un apoyo fundamental para mí. Por todo ello, Gracias.

A Ramón Zaera, por la enorme dedicación que ha tenido en este trabajo y lo mucho que ha aportado al mismo. De veras ha sido un placer haber tenido la posibilidad de colaborar y aprender con él.

Quiero agradecer a Antoine Jerusalém, profesor del Departament of Engineering Science de University of Oxford y supervisor durante mi estancia doctoral, su gran apoyo y contribución a este proyecto. Ha sido un placer colaborar juntos durante este proyecto y las muchas ideas y conocimiento que he obtenido de él.

A Alexis Rusinek, por su colaboración y ayuda en la comprensión del comportamiento de materiales bajo condiciones de carga extrema.

Gracias a todo el Departamento de Mecánica de Medios Continuos y Teoría de Estructuras por hacer que este trabajo haya visto la luz. A José Fernández y Ramón Zaera por acogerme en el grupo de investigación Dinámica y Fractura de Elementos Estructurales. A los técnicos de laboratorio Sergio y David por su inestimable ayuda en toda la componente experimental de esta tesis. También agradecer el apoyo y amistad recibidos por mis compañeros Damián, Mahy, Javi, Sara, Ángel, Mata, Vila, Pablo, Lorena y Óscar. Me gustaría agradecer de forma especial la ayuda y discusiones sobre el trabajo de esta tesis a Damián, Mahy y Sara.

A mis compañeros durante la estancia en University of Oxford, especialmente a Daniel por su ayuda y amistad.

A Penelope Miller por el gran esfuerzo realizado. Su ayuda ha supuesto una enorme mejora en la versión final de este documento.

Por último, agradecer el cariño y apoyo recibido a aquellos amigos que han estado a mi lado durante estos años, especialmente los que estuvieron en los momentos más duros. Nunca estaré lo suficientemente agradecido.

Abstract

The research carried out in this Doctoral Thesis provides new ideas and methodologies on the development of hyperelastic-based constitutive models and may motivate future contributions within this line of investigation. To achieve the main objective of providing a general continuum mechanics framework, the methodology has been divided into the following specific activities:

(i) With the aim of supporting the modelling assumptions of the framework, an experimental and numerical analysis of the mechanical behaviour of hyperelastic materials has been conducted. This study provides new insights into the mechanisms that govern the deformation process.

(ii) A new constitutive model for semi-crystalline thermoplastic polymers has been developed. The formulation of this model is based on physical evidence from the analysis of the mechanical behaviour of thermoplastic polymers, thereby connecting experiments with modelling. In this sense, the model accounts for strain rate and temperature dependencies, and pressure sensitivity within a thermodynamically consistent framework formulated in finite deformations. The model parameters have been identified for polyether-ether-ketone (PEEK) and the model has been validated for a wide range of loading conditions.

(iii) The constitutive framework of the model proposed for semi-crystalline polymers has been generalized for transversely isotropic hyperelastic-based models. This general framework allows for the formulation of constitutive models taking into account: viscoelasticity, viscoplasticity, hyperelasticity, thermal expansion and anisotropy induced by fibre orientation. The general continuum framework has been particularized, providing constitutive models for two materials: short carbon fibre reinforced PEEK composites; and white matter of brain.

(iv) Finally, the constitutive and numerical tools developed in this thesis have been implemented in finite element commercial codes and applied to study a real problem, the analysis of the mechanical behaviour of thermoplastic cranial implants subjected to impact loading. For this purpose, a finite element head model comprising scalp, skull, cerebral falx, cerebrospinal fluid and brain tissue, with a cranial implant replacing part of the skull, has been developed from magnetic resonance imaging data.

Resumen

La investigación llevada a cabo en esta Tesis Doctoral proporciona nuevas ideas y metodologías para el desarrollo de modelos constitutivos con base hiperelástica, con fundamentación física y basados en evidencias experimentales. Estos modelos han sido aplicados al estudio del comportamiento termomecánico de polímeros termoplásticos y tejidos blandos en un amplio intervalo de condiciones de trabajo. La simulación de este tipo de sólidos debe considerar grandes desplazamientos, rotaciones y deformaciones, efectos inerciales, cambios de condiciones de contorno durante el proceso de deformación, generación de calor por deformación plástica, y requieren de leyes de comportamiento de material complejas. Con objeto de proporcionar un marco general del continuo para la formulación de modelos constitutivos, se han desarrollado las siguientes actividades:

(i) Se ha realizado un análisis experimental y numérico del comportamiento mecánico de materiales hiperelásticos. Este estudio proporciona nuevas observaciones sobre los mecanismos que gobiernan el proceso de deformación de este tipo de sólidos.

(ii) Se ha desarrollado un nuevo modelo constitutivo para predecir el comportamiento de polímeros semicristalinos. La formulación de este modelo se basa en evidencias físicas observadas durante el análisis del comportamiento mecánico de polímeros termoplásticos, conectando de esta manera técnicas experimentales con la modelización constitutiva. El modelo ha sido formulado en hipótesis de grandes deformaciones dentro de un marco termodinámicamente consistente que considera: la dependencia del comportamiento mecánico con la presión y la deformación plástica volumétrica; el endurecimiento del material asociado a la sensibilidad con la velocidad de deformación; la generación de calor en el proceso de deformación inducida por disipación plástica y la evolución de la temperatura debida al flujo térmico; el ablandamiento térmico y la expansión térmica del material. Los parámetros del modelo han sido identificados para el polímero poliéter-éter-cetona (PEEK) y la capacidad predictiva del modelo ha sido verificada para un amplio intervalo de condiciones de carga.

(iii) El marco constitutivo del modelo propuesto para polímeros semicristalinos ha sido generalizado para la formulación de modelos transversalmente isótropos con base hiperelástica. Este marco general considera: viscoelasticidad; viscoplasticidad; hiperelasticidad; expansión térmica y anisotropía debida a la orientación de las fibras. El marco general del continuo ha sido particularizado dando lugar a modelos constitutivos

para dos materiales específicos: materiales compuestos de matriz termoplástica PEEK reforzados con fibra corta de carbono; y la materia blanca del cerebro.

(iv) Finalmente, los modelos constitutivos y las herramientas numéricas desarrolladas en esta tesis doctoral han sido implementados en un código comercial de elementos finitos y se han aplicado al estudio de un problema real: el análisis del comportamiento mecánico de implantes craneales fabricados con polímeros termoplásticos que están expuestos a cargas de impacto. Para este propósito, se ha desarrollado un modelo de cabeza humana en elementos finitos a partir de resonancias magnéticas que incluye tejido dérmico, cráneo, líquido cefalorraquídeo y el tejido cerebral, incluyendo un implante craneal termoplástico que sustituye parte del cráneo.

Índice

Chapter 1.
Introduction

1.1 Motivation

This Doctoral Research focuses on materials whose behaviour can be suitably described with hyperelastic-based constitutive models (these materials are hereafter referred to as *hyperelastic materials*). Hyperelastic materials present complex phenomena such as large deformations and non-linear mechanical behaviour. In recent years there has been an increasing interest in the study of hyperelastic materials due to their application in a large range of industrial sectors, and especially in biomedical applications. This has motivated the consideration of specific types of hyperelastic materials in this thesis: **(i)** thermoplastic matrix and their composites; and **(ii)** soft tissues. The complicated behavior of these materials makes it challenging to predict their mechanical response and performance. Therefore, reliable models able to describe the mechanical behavior, including the variables which govern their response, are of both theoretical and practical interest.

A hyperelastic material (also called a Green-elastic material) postulates a Helmholtz free energy function defined per unit reference volume, from which the constitutive equation is derived. In addition, the definition of the Helmholtz free energy function should preferably be based on the physical fundamentals behind the deformation mechanisms that govern the mechanical behaviour of the material. In addition, the hyperelasticity theory often needs to be combined with the viscoelasticy theory in order to describe viscous mechanisms of deformation such as rate-dependency or heat generation due to inelastic dissipation. To this end, there is a need to connect observations from experimental evidence with the assumptions that define the continuum mechanics framework for the formulation of constitutive models. Many hyperelastic materials, especially thermoplastic polymers and soft tissues, present nonlinear behaviour that reflects its time, pressure, strain rate and temperature dependencies and the coupling of viscoelastic and viscoplastic behaviours [Krairi and Doghri, 2014; Chatelin et al., 2011]:

(i) In the case of thermoplastic polymers, the consideration of thermal and strain rate effects on the material behaviour is particularly relevant [Rae et al., 2007; Serban et al., 2013; El-Qoubaa et al., 2016]. In addition, the coupling between thermal and mechanical behaviour of thermoplastic polymers leads to thermal softening induced by adiabatic heating, increasing at high strain rates [Mohagheghian et al., 2015]. Furthermore, when thermoplastic polymers are reinforced with short fibres, the directional dependence of short fibres leads to an anisotropic mechanical behaviour which is determined by a manufacturing process dependent preferred but distributed fibre orientation [Fu et al., 2009].

(ii) Moreover, soft tissues are known to exhibit hyperelastic material behaviour [Fung, 1981] and, when they are embedded with fibres, anisotropic behaviour [Fung, 1981; Cowin and Humphrey, 2001; Guo et al., 2007].

With the aim of establishing a general constitutive framework and methodology for the formulation of constitutive models under certain modelling assumptions, **this Doctoral Thesis proposes a thermodynamically consistent continuum framework for hyperelastic materials physically motivated on experimental evidence**. The constitutive formulation is based on a Helmholtz free energy function additively decoupled into a hyperelastic-viscoelastic/viscoplastic component associated with the response of the matrix material, which is assumed isotropic; and a component associated with anisotropic deformations that represent the resistance to stretch due to fibres, as suggested by Holzapfel et al. (2000). In this thesis, the constitutive framework is used as the basis for the development of constitutive models for materials of different natures: from thermoplastic materials and their composites to transversely isotropic soft tissues.

With the aim of providing numerical tools that predict the mechanical behaviour of specific structural elements, **in this Doctoral Thesis these constitutive models have been implemented in finite element commercial codes and applied to study real problems.** Particularly, the analysis of thermoplastic cranial implants subjected to impact loading has been carried out for a real patient. This study has allowed a complete analysis that cannot be addressed by the exclusive use of experimental techniques.

1.2 Objectives and methodology

The principal objective of the investigation carried out in this Doctoral Thesis is the development of a new continuum mechanics framework for the formulation of hyperelastic-based constitutive models. This continuum framework aims to be valid for several materials with different natures: thermoplastic polymers, short fibre reinforced polymers and soft tissues. To achieve this main purpose, specific objectives have been established based on the following methodology:

- Analysis of the mechanical behaviour of hyperelastic materials covering a large range of loading conditions. This study focuses on the effect of strain rate, temperature, stress state and thermomechanical coupling on the material behaviour. This part of the work has been carried out through analysis of studies reported in the available literature combined with experimental and preliminary numerical results developed in this thesis. This analysis allowed us to understand

the physical fundamentals behind the deformation and failure mechanisms that govern the mechanical behaviour of this type of materials.

- Formulation of a new constitutive model for semi-crystalline thermoplastic polymers within a thermodynamically consistent framework. This model has been physically based on the experimental and numerical results obtained in the previous analysis of the mechanical behaviour of hyperelastic materials.

- Generalization of the constitutive framework of the model proposed for semi-crystalline polymers with the aim of formulating a general continuum framework for hyperelastic materials. To this end, the predictive capacities of the constitutive model proposed for semi-crystalline polymers, and the methodology used in its development, have been taken as the starting point for the development of the general continuum framework to support the achievement of the main objective of the Doctoral Thesis. In this regard, the general continuum framework proposed establishes the basis for the constitutive modelling of different materials: thermoplastic polymers, short fibre reinforced polymers and soft tissues.

- Development of a finite element head model (FEHM) comprising scalp, skull, cerebral falx, cerebrospinal fluid and brain tissue, with a cranial implant replacing part of the skull has been developed from magnetic resonance imaging data. The combination of the FEHM with the constitutive models particularized for biomedical polymers has permitted the analysis of the mechanical behaviour of cranial implants.

Note that, although this Doctoral Thesis focuses on biomedical applications, the constitutive framework, numerical tools and methodology developed could be potentially useful in other industrial sectors where hyperelastic materials are employed, such as the aeronautical or automotive sectors.

1.3 Original contributions

The principal achievement of this Doctoral Thesis is the ***development of a continuum mechanics framework and associated methodology for the formulation of hyperelastic-based constitutive models***.

In addition to this principal achievement, the following four original contributions have also been achieved:

(i) *Analysis of mechanical behaviour: identification of the physical evidence behind the deformation mechanisms of materials that can be potentially defined by hyperelastic-based models.*

- The experimental and numerical study of the mechanical behaviour of unfilled PEEK under impact loading.
- The experimental and numerical study of the mechanical behaviour of SCFR PEEK under impact loading.
- The study of the influence of temperature on the mechanical behaviour of PEEK composites.

(ii) *Development of constitutive models and validation.*

- A new constitutive model for semi-crystalline thermoplastic polymers has been developed from the physical evidence of the previous experimental study. This model takes into account strain rate and temperature sensitivities, pressure dependency and temperature evolution induced by inelastic dissipation within a thermodynamically consistent framework formulated in finite deformations.
- The parameters of the constitutive model for semi-crystalline polymers have been identified for PEEK. This model has been applied to the analysis of the influence of temperature and strain rate on the mechanical behaviour of PEEK.

(iii) *Particularization of the general continuum framework.*

- Formulation of a constitutive model for SFR thermoplastic composites and identification of its parameters for SCFR PEEK.
- Formulation of a constitutive model for transversely isotropic soft tissues and identification of its parameters for white matter.

(iv) *Application of the constitutive models.*

- Development of a FEHM comprising scalp, skull, cerebral falx, cerebrospinal fluid and brain tissue, with a cranial implant replacing part of the skull, from magnetic resonance imaging data.
- Application of the constitutive models and the FEHM to the study of the mechanical behaviour of cranial implants under impact loading.

1.4 Thesis structure

This Doctoral Thesis has been divided into nine chapters with a clear identification and description of objectives and tasks. This structure is intended to facilitate the reader's understanding of this work. The chapters of this thesis are listed and briefly explained below:

Chapter 1. This chapter introduces the main objective of the research and the methodology followed. In addition, the principal contributions of this Doctoral Thesis are highlighted.

Chapter 2. This chapter presents the fundamentals of continuum mechanics in order to introduce the basis for the development of continuum constitutive models. Chapter 2 summarizes the continuum modelling fundamentals in four basic sections: large strain kinematics; stress tensors; balance laws and field equations; and derivation of constitutive equations.

Chapter 3. This chapter outlines the fundamentals of hyperelasticity and several free energy functions in constitutive models for two modelling assumptions: isotropic hyperelasticity and anisotropic hyperelasticity.

Chapter 4. This chapter introduces the fundamentals of finite viscoelasticity and some examples of established constitutive models of this type to facilitate the understanding of complex models developed in latter sections.

Chapter 5. This chapter presents experimental results of hyperelastic materials and mechanical analyses of their material behaviour obtained from the preliminary modelling of their mechanical response. Specifically, the study is focused on the mechanical behaviour of PEEK composites under dynamic loading and is structured in three sections: the first section analyzes the impact behaviour of unfilled PEEK; the second section analyzes the impact behaviour of SFR PEEK composites; and the third section analyzes

specifically the temperature-dependence of both PEEK-based materials under impact conditions.

Chapter 6. A new constitutive model is proposed for semi-crystalline thermoplastic polymers based on the experimental and numerical results obtained in the previous chapter. This model is formulated for finite deformations within a thermomechanically consistent framework and takes into account strain rate and temperature sensitivities, pressure dependency and temperature evolution induced by inelastic dissipation. The model parameters are calibrated for PEEK and the constitutive model is validated for a wide range of strain rates, temperatures and stress states. Finally, the model is used for the study of thermomechanical coupling in two dynamic applications: impact tests in a drop weight tower; and dynamic necking of slender bars.

Chapter 7. The constitutive model developed in Chapter 6 is generalized to provide a general mechanical continuum framework for hyperelastic materials. This general model allows for the development of constitutive models for transversally isotropic hyperelastic materials of different natures by the particularization of the Helmholtz free energies associated with each constitutive branch. Finally, the continuum framework is particularized for two distinct materials: SCFR PEEK composites; and white matter of the brain.

Chapter 8. In this chapter the constitutive model developed for semi-crystalline polymers and calibrated to PEEK is used for the analysis of the impact behaviour of PEEK cranial implants. To this end, a finite element head model comprising scalp, skull, cerebral falx, cerebrospinal fluid and brain tissue, with a cranial implant replacing part of the skull, has been developed from magnetic resonance imaging data. The models and methodology proposed in this section are designed to help clinicians to optimize biomedical devices and evaluate medical conditions induced by mechanical factors, such as in the study of impact loading on the head.

Chapter 9. This concluding chapter summarizes the main scientific achievements of this Doctoral Thesis and proposes future work that will be built on the research started in this Doctoral Thesis. Essentially, an experimental investigation has been carried out in order to study the mechanical behaviour of a specific hyperelastic material and its composites. The results obtained from these experimental results and preliminary modelling have supported the development of a new constitutive model for semi-crystalline polymers. Taking the methodology followed during the development of this constitutive model, a general continuum framework has been proposed for transversally isotropic hyperelastic materials. Finally, the models developed in this thesis have been used in a specific biomedical application: the study on the impact behaviour of PEEK cranial implants.

In addition, some appendices are included in order to introduce some explanations about the derivation of the constitutive equations, the numerical implementation of the constitutive models and the constitutive modelling of the different components of the FEHM.

Appendix A. Provides a detailed explanation of the complete formulation of the Helmholtz free energy function and its derivation to obtain the constitutive equations of the model proposed in *Chapter 6*.

Appendix B. Presents the numerical implementation of the explicit algorithm used in the material subroutines for the plastic flow and temperature evolution.

Appendix C. This section presents the constitutive modelling of each human tissue involved in the finite element head model, as well as the determination of the mechanical properties of the exact macroporous HA material. To this end, characterization tests on specimens manufactured from a real prosthesis were conducted and then, in order to assess the relevant mechanical properties of the implant, its homogenized behaviour after bone growth was estimated.

Appendix D. Presents an extended model to describe the mechanical behaviour of Ultra High Molecular Weight Polietilene (UHMWPE).

Chapter 2.
Continuum mechanics modelling

In this chapter, the basic fundamentals of hyperelastic constitutive modelling are introduced. These fundamentals establish the basis for the understanding and development of the constitutive framework proposed in this thesis.

2.1 Introduction

All materials, independent of whether they are solids, liquids or gases, present a discontinuous structure with discrete particles and spaces. However, several physical phenomena can be analyzed applying the assumption that materials exist as a continuous mass. This assumption underlies continuum mechanics, the study of kinematics and mechanical behaviour of materials modelled as a continuous mass. Continuum mechanics deals with the modelling of materials by the use of tensors treated as mathematical objects which allow for the derivation of differential equations describing the materials behaviour by applying the fundamental physical laws. This chapter presents the fundamental principles of continuum mechanics support the technical analysis in later chapters:

- The study of motion and deformation: finite deformation kinematics.
- The study of the stress in a continuum: stress tensors.
- The mathematical description of the fundamental laws of physics governing the motion of a continuum: balance laws and field equations.
- The equations which describe the material dependent relationships between quantities: constitutive equations.

This chapter is adapted from Holzapfel (2000) and Bergström (2015). For a more detailed explanation of the derivation of each principle see elsewhere [Ogden, 1997; Holzapfel, 2000; Bergström, 2015].

2.2 Finite deformation kinematics

Kinematics of deformation rules the mathematical treatment of the displacements of different parts of a body of interest. It is therefore a key foundation for understanding the evolution of stresses and strains when the object is subjected to external forces. To this aim, let us consider a body that at an initial time $t = 0$, has an undeformed or reference configuration (shape and location) Ω_o. At some time $t > 0$, the body has another deformed or current configuration Ω, see Fig. 2.1.

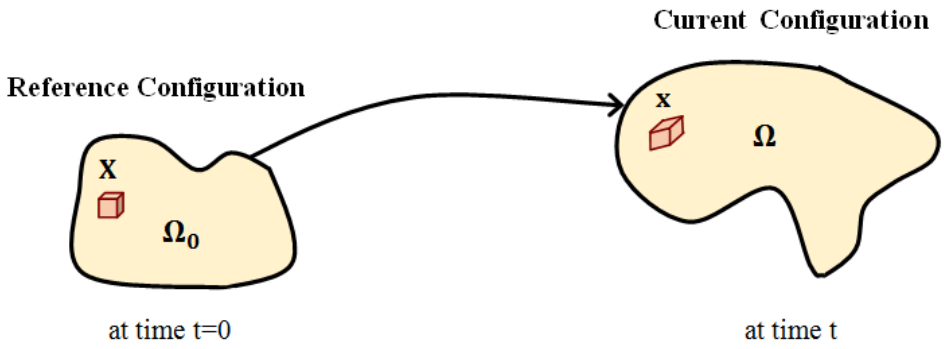

Figure 2.1: Scheme of a body that evolves from a reference configuration to a current configuration as a function of time.

2.2.1 Deformation gradient

Understanding the body as a collection of small volume elements, each of these infinitesimal elements can be referred to a material point. In order to describe the movement of material points during a deformation event, the concept of deformation gradient, **F**, is introduced in the field of kinematics. The deformation gradient is a second-order tensor which characterizes the behaviour of motion in the neighbourhood of a point. Taking **X** as an arbitrary material point in Ω_o, it is possible to reach the current configuration Ω, through the mapping $\mathbf{x} = \boldsymbol{\chi}(\mathbf{X},t)$, from which the deformation gradient, velocity (**v**) and velocity gradient (**l**) can be derived as

$$\mathbf{F} = \nabla_X \boldsymbol{\chi} \tag{2.1}$$

$$\mathbf{v} = \dot{\boldsymbol{\chi}} \tag{2.2}$$

$$\mathbf{l} = \nabla_x \mathbf{v} = \dot{\mathbf{F}}\mathbf{F}^{-1} \tag{2.3}$$

where ∇_X denotes the material gradient and ∇_x denotes the spatial gradient. Eq. (2.1) can be rearranged to obtain

$$\mathbf{F}(\mathbf{X})d\mathbf{X} = d\mathbf{x} \tag{2.4}$$

The arbitrary line element d**X**, under deformation, transforms to become the line element d**x**. **F** is a non-singular tensor as there is no possibility of a non-zero line element in Ω_o ($\mathbf{dX} \neq 0$) and, therefore, d**x** must be non-zero and $\mathbf{F}d\mathbf{X} \neq 0$. Considering also that the current and reference infinitesimal volume elements dv and dV formed by the infinitesimal line elements d**x** and d**X** are related by $dv = J(\mathbf{X}, t)dV$, then

$$J(\mathbf{X}, t) = \det \mathbf{F}(\mathbf{X}, t) > 0 \tag{2.5}$$

J being the Jacobian determinant which gives the ratio of the current volume to the reference volume.

2.2.2 Strain tensors

Since the deformation gradient is a quantitative measure of changes in material elements during motion, it can be used as the base for the description of strain. Strain is a measure of deformation independent of rotation and can be described in many ways depending on the assumptions made. The strain tensors predominantly used throughout this work are the right and left Cauchy-Green deformation tensors, **C** and **B** respectively, and the Green-Lagrange strain tensor **E**, defined as

$$\mathbf{C} = \mathbf{F}^{\mathbf{T}}\mathbf{F} \tag{2.6}$$

$$\mathbf{B} = \mathbf{F}\mathbf{F}^{\mathbf{T}} \tag{2.7}$$

$$\mathbf{E} = \frac{1}{2}\left(\mathbf{F}^{\mathbf{T}}\mathbf{F} - \mathbf{I}\right) = \frac{1}{2}(\mathbf{C} - \mathbf{I}) \tag{2.8}$$

where **I** is the identity tensor.

The deformation state of the body can alternatively be measured by scalar components. In this regard, the stretch λ is the ratio of the deformed length of a material line element to its reference length. This stretch must be greater than zero length in any deformed configuration $\lambda > 0$.

The deformation gradient **F** can be broken down into a pure stretch component and a pure rotation component. At each point $\mathbf{X} \in \Omega_o$ and each time t, there is a unique polar decomposition of the deformation gradient as

$$\mathbf{F} = \mathbf{R}\mathbf{U} = \mathbf{V}\mathbf{R} \tag{2.9}$$

where **U** and **V** define unique, positive, definite, symmetric tensors called the right (or material) stretch tensor and the left (or spatial) stretch tensor respectively. **R** is the orthogonal rotation tensor ($\mathbf{R}^T\mathbf{R} = \mathbf{I}$).

2.3 Stress tensors

The motion and deformation of a continuum body within the kinematic framework discussed in the previous section, result in interactions between the material points in the interior of the material modelled. As a principal consequence, stresses that appear along the body are responsible for the deformation of the material and, are therefore crucial elements in continuum mechanics. The stress is expressed as a mathematical tensor that can be formulated in different ways depending on the configuration chosen for its definition. This section identifies some relevant forms of alternative stress measures used throughout this work including Cauchy, Piola- Kirchhoff and Mandel stress tensors.

In order to define the concept of mechanical stress, let us consider a general body exposed to an external force per unit surface area called as *traction vector*, see Fig. 2.2. Here, the vector **t** is called the Cauchy (or true) traction vector, and represents this force on the deformed body at a time t. In the case of carrying out the study in the reference configuration, this force is represented by **p** and called the first Piola-Kirchhoff (or nominal) traction vector.

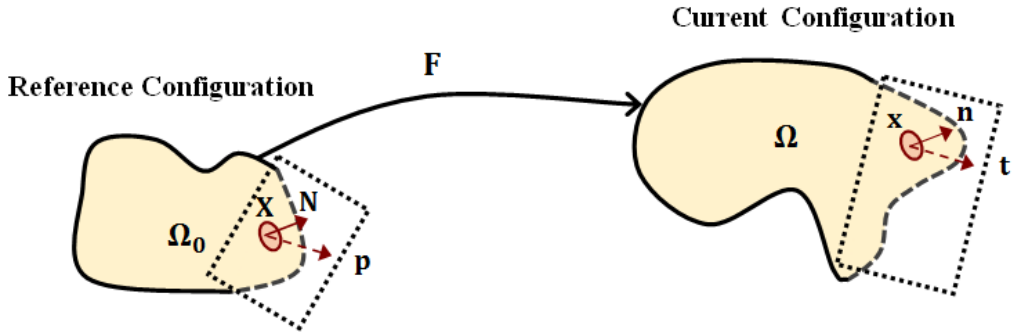

Figure 2.2: Traction vectors expressed in reference and current configurations.

2.3.1 Cauchy and First Piola-kirchhoff stress tensors

The material point **X** is intersected by an imaginary plane which dissects a body. **N** is the unit normal vector to the cutting surface S in the reference configuration. Working in this

configuration, **p** is associated with infinitesimal area dS at point **X**. The equivalent system in the deformed configuration is represented by the traction vector **t** and the unit normal **n** associated with infinitesimal area ds. Taking the previous concepts as the starting point, the Cauchy's stress theorem states that there exist unique second-order tensor fields **σ** and **P** so that

$$\mathbf{t}(\mathbf{x}, t, \mathbf{n}) = \boldsymbol{\sigma}(\mathbf{x}, t)\mathbf{n} \tag{2.10}$$

$$\mathbf{p}(\mathbf{X}, t, \mathbf{N}) = \mathbf{P}(\mathbf{X}, t)\mathbf{N} \tag{2.11}$$

where **σ** denotes the Cauchy (or true) stress tensor and **P** is the first Piola-Kirchhoff (or nominal) stress tensor.

The first Piola-Kirchhoff stress tensor (**P**) represents the stress state expressed in the reference configuration. This stress tensor is generally not symmetric, what supposes a lack of physical meaning. This is the cause why **P** is uncommonly used in the modelling of materials. However, it is useful in the description of the momentum balance laws in the material description and it is commonly used in finite element codes that usually operate in the reference configuration to avoid rigid body rotations.

The Cauchy stress tensor is a symmetric tensor that is also called the true stress because represents a true measure of the force per unit area in the current/deformed configuration.

Note that the first Piola-Kirchhoff stress tensor and Cauchy stress tensor represent the same stress state but are expressed in the reference configuration (**P**) and in the deformed configuration (**σ**). It means that one can be determined from the other using Nanson's formula, which relates a material surface in the reference configuration with a material surface in the current configuration as

$$ds = J\mathbf{F}^{-\mathbf{T}}dS \tag{2.12}$$

Thus, applying Nanson's formula, stress tensors expressed in different configurations can be related. This relationship for Cauchy and first Piola-Kirchhoff stress tensors reads as

$$\mathbf{P}(\mathbf{X}, t) = J\boldsymbol{\sigma}(\mathbf{x}, t)\mathbf{F}^{-\mathbf{T}} \tag{2.13}$$

2.3.2 Second Piola-Kirchhoff stress tensor

The second Piola-Kirchhoff stress tensor is a symmetric tensor that can be expressed in all intermediate configurations and then, although it admits no physical interpretation, is convenient and useful to work with in the formulation of the constitutive equations. This stress tensos is parameterized by material coordinates and can be related to the Cauchy and first Piola-Kirchhoff stress tensors as

$$\mathbf{S} = J\mathbf{F}^{-1}\boldsymbol{\sigma}\mathbf{F}^{-T} = \mathbf{F}^{-1}\mathbf{P} \tag{2.14}$$

2.3.3 Mandel stress tensor

Moreover, when intermediate configurations are introduced in kinematics, it is often useful to use the Mandel stress tensor **M** which is generally not symmetric and is defined with respect to an intermediate configuration (often used to describe inelastic materials). This admits no physical interpretation but is convenient and useful to operate with due to it is invariant to rotations:

$$\mathbf{M} = \mathbf{CS} \tag{2.15}$$

2.4 Balance laws and field equations

During the development of constitutive equations for a material, there are physical principles that must be satisfied for all times and loading conditions. These physical principles are: conservation of mass, conservation of linear momentum, conservation of angular momentum and the first and second laws of thermodynamics. At the end, the structure of principles can be summarized as the master balance (inequality) principle from which the constitutive relationships can be stated.

2.4.1 Conservation of mass

The mass of a body is given by the sum of its parts. In addition, it can be stated that, from a non-relativistic physics perspective, mass cannot be produced or destroyed. Therefore, if there are neither mass sources nor mass sinks, the mass of a body is a conserved quantity. Defining $\rho_o(\mathbf{X}, t)$ and $\rho(\mathbf{x}, t)$ as the mass density of the body in the reference and current configurations respectively, if no material enters or leaves the body, the time derivative of the total mass must be zero

$$\frac{D}{Dt}\int_{\Omega_o}\rho_o(\mathbf{X},t)dV=\frac{D}{Dt}\int_{\Omega}\rho(\mathbf{x},t)dv=0 \tag{2.16}$$

From the previous equation, since the domain Ω_o is not dependent on time, the time derivative operator can be moved inside the integral sign

$$\int_{\Omega_o}\frac{D}{Dt}[\rho_o(\mathbf{X},t)]dV=0 \tag{2.17}$$

Hence

$$\dot{\rho}_o(\mathbf{X},t)=0 \tag{2.18}$$

defines the field equation for mass concentration in Ω_o.

Using the definition of the Jacobian determinant, $dv=J(\mathbf{X},t)\,dV$, and changing the integration variable from $\mathbf{x}=\boldsymbol{\chi}(\mathbf{X},t)$ to $\mathbf{X}$, the reference mass density can be related to the current mass density by

$$\int_{\Omega_o}[\rho_o(\mathbf{X},t)-\rho(\boldsymbol{\chi}(\mathbf{X},t),t)J(\mathbf{X},t)]dV=0 \tag{2.19}$$

leading to the continuity mass equation

$$\rho_o(\mathbf{X})=J\rho(\mathbf{x}) \tag{2.20}$$

2.4.2 Conservation of linear momentum

Newton's law of motion can be expressed from the theory of dynamics of rigid bodies as: *"The force on a body is equal to the time-derivative of its linear momentum"*.

The total linear momentum **L** can be defined by

$$\mathbf{L}(t)=\int_{\Omega_o}\rho_o(\mathbf{X})\mathbf{V}(\mathbf{X},t)dV=\int_{\Omega}\rho(\mathbf{x},t)\mathbf{v}(\mathbf{x},t)dv \tag{2.21}$$

where **V** and **v** are the velocity fields in the reference and current configurations.

The balance of linear momentum for deformable bodies that undergo large deformations can be understood as: *the sum of surface and volumetric forces acting on a body are equal to the time derivative of the linear momentum of the body*. Then, in the current configuration

$$\int_{\partial\Omega} \mathbf{t}\,ds + \int_{\Omega} \mathbf{b_f}\,dv = \frac{D}{Dt}\int_{\Omega} \mathbf{v}\rho\,dv \tag{2.22}$$

where $\mathbf{t}$ is the distribution of Cauchy surface tractions on the configuration boundary and $\mathbf{b_f}$ is the vector field of body forces per unit current volume.

Applying the Cauchy stress theorem, Eq. (2.10), the divergence theorem on the first term in Eq. (2.22) and the mass conservation principle, the balance of linear momentum reads

$$\int_{\Omega} [\operatorname{div}\boldsymbol{\sigma} + \mathbf{b_f} - \rho\dot{\mathbf{v}}]\,dv = 0 \tag{2.23}$$

This balance equation has to be valid for any arbitrary sub-domain of Ω, hence the field equation of the balance of linear momentum can be given by

$$\operatorname{div}\boldsymbol{\sigma} + \mathbf{b_f} = \rho\dot{\mathbf{v}} \tag{2.24}$$

Finally, this equation can be also expressed in reference configuration as

$$\operatorname{Div}\mathbf{P} + \mathbf{B_f} = \rho_o\dot{\mathbf{V}} \tag{2.25}$$

2.4.3 Conservation of angular momentum

The total angular momentum $\mathbf{J}$ for an arbitrary point is

$$\mathbf{J}(t) = \int_{\Omega} [\mathbf{x} \times \rho(\mathbf{x},t)\mathbf{v}(\mathbf{x},t)]\,dv = \int_{\Omega_o} [\mathbf{X} \times \rho_o(\mathbf{X},t)\mathbf{V}(\mathbf{X},t)]\,dV \tag{2.26}$$

Taking as starting point the linear momentum equation, the balance angular momentum principle can be obtained from the cross-product of both the force and the linear momentum with the position vector. Thus, the balance angular momentum principle states that the moment applied on a body is equal to its time-derivative of the angular momentum. If a deformable body undergoes large deformations, this principle can be

understood as: *the sum of moments from surface and volumetric forces acting on a body are equal to the time derivative of angular momentum of the body*.

This can be written in the current configuration as the following balance law

$$\int_{\partial\Omega} \mathbf{x} \times \mathbf{t} \mathrm{ds} + \int_{\Omega} \mathbf{x} \times \mathbf{b_f} \mathrm{dv} = \frac{\mathrm{D}}{\mathrm{Dt}} \int_{\Omega} \mathbf{x} \times \mathbf{v} \rho \mathrm{dv} \tag{2.27}$$

This equation can be rewritten using the Cauchy stress theorem, Eq. (2.10) and the divergence theorem on the first term in Eq. (2.22) as

$$\int_{\partial\Omega} \mathbf{x} \times \mathbf{t} \mathrm{ds} = \int_{\partial\Omega} \mathbf{x} \times \boldsymbol{\sigma} \mathbf{n} \mathrm{ds} = \int_{\Omega} \mathbf{x} \times \mathrm{div}(\boldsymbol{\sigma}) + \mathcal{E} : \boldsymbol{\sigma}^{\mathbf{T}} \mathrm{dv} \tag{2.28}$$

where $\mathcal{E}$ is a third-order permutation tensor expressed as $\mathcal{E} : (\mathbf{u} \times \mathbf{v}) = \mathbf{v} \times \mathbf{u}$. The terms in Eq. (2.27) can be rewritten and rearranged to get its equivalent from as

$$\int_{\Omega} \mathbf{x} \times (\rho \dot{\mathbf{v}} - \mathbf{b_f} - \mathrm{div}\, \boldsymbol{\sigma}) \mathrm{dv} = \int_{\Omega} \mathcal{E} : \boldsymbol{\sigma}^{\mathbf{T}} \mathrm{dv} \tag{2.29}$$

Using the equation of motion, Eq. (2.24), the following conclusion can be stated

$$\mathcal{E} : \boldsymbol{\sigma}^{\mathbf{T}} = 0 \tag{2.30}$$

And, therefore, the equivalent condition of symmetry is obtained

$$\boldsymbol{\sigma} = \boldsymbol{\sigma}^{\mathbf{T}} \tag{2.31}$$

2.4.4 First law of thermodynamics

The first law of thermodynamics in presented below considering both mechanical and thermal energies. The system studied is assumed to be a closed system that can perform work and exchange heat with its surroundings, but material transfer is not allowed through its boundary. This law states that: *"the rate of energy increase in the system is equal to the sum of the rate of heat supplied to the system and the rate of work done by external forces on the system"*. This can be expressed as a balance law in the current configuration as

$$\frac{\mathrm{D}}{\mathrm{Dt}}\int_{\Omega}\left(\mathrm{e}+\frac{\rho}{2}\mathbf{vv}\right)\mathrm{dv}=\int_{\partial\Omega}-\mathbf{qn}\mathrm{ds}+\int_{\Omega}\mathrm{rdv}+\int_{\partial\Omega}\mathbf{tv}\mathrm{ds}+\int_{\Omega}\mathbf{b_f v}\mathrm{dv} \tag{2.32}$$

e being the specific internal energy per unit volume, **q** the heat flux per unit area and r the heat source per unit volume in Ω.

The first term of Eq. (2.32) expressed the time-derivative of the internal and kinetic energies, and can be simplified by transforming the integration to the reference configuration

$$\frac{\mathrm{D}}{\mathrm{Dt}}\int_{\Omega}\left(\mathrm{e}+\frac{\rho}{2}\mathbf{v^2}\right)\mathrm{dv}=\int_{\Omega_0}\frac{\mathrm{D}}{\mathrm{Dt}}\left(\mathrm{eJ}+\frac{\rho}{2}\mathbf{v^2}\mathrm{J}\right)\mathrm{dV}=\int_{\Omega_0}\left(\dot{\mathrm{e}}\mathrm{J}+\mathrm{e}\dot{\mathrm{J}}+\frac{1}{2}\frac{\mathrm{D}}{\mathrm{Dt}}(\rho+\mathrm{J})\mathbf{v^2}\mathrm{J}+\dot{\mathbf{v}}\mathbf{v}\mathrm{J}\rho\right)\mathrm{dV} \tag{2.33}$$

By combining Eq. (2.32) and Eq. (2.33), the conservation of mass and the divergence theorem, the field equation for energy conservation in the current configuration can be obtained from the balance linear momentum as

$$\boldsymbol{\sigma}:\mathbf{d}-\mathrm{div}\,\mathbf{q}+\mathrm{r}=\dot{\mathrm{e}}+\mathrm{e}\,\mathrm{div}\,\mathbf{v} \tag{2.34}$$

This field equation can also be expressed in the reference configuration as

$$\mathbf{P}:\dot{\mathbf{F}}-\mathrm{Div}\,\mathbf{Q}+\mathrm{R}=\dot{\mathrm{e}}_0 \tag{2.35}$$

2.4.5 Second law of thermodynamics

The second law of thermodynamics states that: *"the entropy of a thermally activated isolated macroscopic system never decreases"*. Entropy represents the amount of energy that the system cannot convert to work and is also associated with the disorder of the system. In this regard, the second law of thermodynamics can be expressed in the current configuration as the following balance law

$$\frac{\mathrm{D}}{\mathrm{Dt}}\int_{\Omega}\eta\mathrm{dv}=\int_{\partial\Omega}-\frac{\mathbf{qn}}{\theta}\mathrm{ds}+\int_{\Omega}\frac{\mathrm{r}}{\theta}\mathrm{dv}+\Gamma \tag{2.36}$$

where η is the specific internal entropy per unit volume, θ is the current temperature and $\Gamma > 0$ is the entropy generation rate due to irreversible mechanisms.

This balance equation can be also expressed indistinctly in the reference configuration as

$$\frac{\mathrm{D}}{\mathrm{Dt}}\int_{\Omega_0}\eta_0 \mathrm{dV} = \int_{\partial\Omega_0} -\frac{\mathbf{QN}}{\theta}\mathrm{dS} + \int_{\Omega_0}\frac{\mathrm{R}}{\theta}\mathrm{dV} + \Gamma \tag{2.37}$$

By using the divergence theorem, the field equation in the current configuration, often referred as the Clausius-Duhen equation, becomes

$$\dot{\eta} + \eta\,\mathrm{div}\,\mathbf{v} \geq -\,\mathrm{div}\left(\frac{\mathbf{q}}{\theta}\right) + \frac{\mathrm{r}}{\theta} \tag{2.38}$$

and in the reference configuration

$$\dot{\eta}_0 \geq -\,\mathrm{Div}\left(\frac{\mathbf{Q}}{\theta}\right) + \frac{\mathrm{R}}{\theta} \tag{2.39}$$

2.5 Constitutive equations

A constitutive equation, $\boldsymbol{\sigma} = \hat{\sigma}(\mathbf{F})$, is a relationship between the strain of a material and some thermo-mechanical variables with the stress response which describes the mechanical behaviour of the material to be modelled.

2.5.1 Helmholtz free energy function

When dealing with the development of constitutive equations and their formulation, the first and second thermodynamic principles can be combined in order to express the Clausius-Duhen inequality in terms of energy potentials and stress tensors. This form of the inequality allows us to define the constitutive relationships between the Helmholtz free energy function Ψ and stress tensors that satisfy the thermodynamic consistency of the model. In order to obtain these expressions, the term R is obtained from Eq. (2.35) and substituted into Eq. (2.39), thus

$$-\,\mathrm{Div}\left(\frac{\mathbf{Q}}{\theta}\right) + \frac{\dot{e}_0}{\theta} - \frac{\mathbf{P}:\dot{\mathbf{F}}}{\theta} + \frac{\mathrm{Div}(\mathbf{Q})}{\theta} \geq \dot{\eta}_0 \tag{2.40}$$

And, by expanding the divergence operator, the previous equation can be rewritten as

$$\frac{\mathbf{Q}\,\nabla_X\,\theta}{\theta^2}+\frac{\dot{e}_0}{\theta}-\frac{\mathbf{P}:\dot{\mathbf{F}}}{\theta}\geq\dot{\eta}_0 \tag{2.41}$$

The terms e_0 and η_0 can be related by the Helmholtz free energy. This concept represents a thermodynamic potential that measures the useful work obtainable from a closed thermodynamic system at a constant temperature and its expression per unit volume is defined as

$$\Psi=e_0-\theta\eta_0 \tag{2.42}$$

and expressed in rate form

$$\dot{\Psi}=\dot{e}_0-\dot{\theta}\eta_0-\theta\dot{\eta}_0 \tag{2.43}$$

Inserting the expression of $\dot{e}_0$ from Eq. (2.39) into (2.37)

$$\dot{\Psi}+\dot{\theta}\eta_0-\mathbf{P}:\dot{\mathbf{F}}+\frac{\mathbf{Q}\,\nabla_X\,\theta}{\theta}\geq 0 \tag{2.44}$$

Assuming that the Helmholtz free energy depends on the "state of deformation" by **F** and on the temperature as $\Psi=\Psi(\mathbf{F},\theta)$, then

$$\left(\frac{\partial\Psi}{\partial\mathbf{F}}-\mathbf{P}\right):\dot{\mathbf{F}}+\left(\frac{\partial\Psi}{\partial\theta}+\eta_0\right)\dot{\theta}+\frac{\mathbf{Q}\,\nabla_X\,\theta}{\theta}\geq 0 \tag{2.45}$$

Notice that since the Helmholtz free energy has to satisfy objectivity, it has to have the following functional forms

$$\Psi(\mathbf{F},\theta)=\Psi(\mathbf{U},\theta)=\Psi(\mathbf{C},\theta) \tag{2.46}$$

2.5.2 Stress tensors derivation from Helmholtz free energy

Due to the inequality in Eq. (2.44) must be satisfied for all $\dot{\mathbf{F}}$ and $\dot{\theta}$, the first Piola-Kirchhoff and the entropy per unit volume have to de equal to

$$\mathbf{P} = \frac{\partial \Psi(\mathbf{F}, \theta)}{\partial \mathbf{F}} \tag{2.47}$$

$$\eta_0 = -\frac{\partial \Psi(\mathbf{F}, \theta)}{\partial \theta} \tag{2.48}$$

The expression which relates the stress with Ψ can be also obtained for other alternative stress tensors such as for the second Piola-Kirchhoff and Cauchy stress tensors

$$\mathbf{S} = 2\frac{\partial \Psi(\mathbf{C}, \theta)}{\partial \mathbf{C}} \tag{2.49}$$

$$\boldsymbol{\sigma} = \frac{2}{\mathrm{J}}\mathbf{F}\frac{\partial \Psi(\mathbf{C}, \theta)}{\partial \mathbf{C}}\mathbf{F}^{\mathbf{T}} \tag{2.50}$$

Chapter 3.
Hyperelasticity

In this chapter, the fundamentals of hyperelasticity and several constitutive models are outlined.

3.1 Introduction

Hyperelasticity is a type of non-linear elasticity which is suitable for large deformation predictions and is commonly used for modelling a range of materials including polymers and soft tissues. The definition of these constitutive models is based on an energy potential from which the expression for the stress is derived according to *Chapter 2*. An important and interesting consideration here is that these energy potentials can be physically motivated on the micromechanisms that drive the deformation behaviour of materials. This section outlines the fundamentals of hyperelasticity and some constitutive models for two modelling assumptions: isotropic hyperelasticity and anisotropic hyperelasticity. This content is adapted from Bergström (2015) and Hashiguchi and Yamakawa (2012).

3.2 Isotropic hyperelasticity

In this section, some widely employed isotropic energy functions and their stress derivation are presented. The material property called *isotropy* is based on the idea that the physical response of a material is the same in all directions. These Helmholtz free energies can either be taken from a phenomenological expression or from a physically motivated representation of the deformation of the material microstructure.

3.2.1 Neo-Hookean model

The classical Neo-Hookean model is a hyperelastic formulation based on two material parameters: a shear modulus μ controlling the deviatoric response; and a bulk modulus κ controlling the volumetric response. This theory can be presented for both compressible and incompressible deformations. The Helmholtz free energy is assumed to be dependent only on the deformation state, and is therefore identical to the energy per unit reference volume, e_0, as no temperature dependence is considered. Thus, the Helmholtz free energy per unit reference volume for a Neo-Hookean model reads as

$$\Psi(\mathbf{C}) = \frac{\mu}{2}(I_1^* - 3) + \frac{\kappa}{2}(J - 1)^2 \tag{3.1}$$

where $I_1^* = \mathrm{tr}(\mathbf{C}^*)$ is the deviatoric first strain invariant. $\mathbf{C}^* = J^{-2/3}\mathbf{C}$ being the distortional right Cauchy-Green deformation tensor.

By using Eq. (3.1), the expression for the Cauchy stress tensor can be derived from the energy potential as

$$\boldsymbol{\sigma} = \frac{\mu}{J}\mathrm{dev}(\mathbf{B}^*) + \kappa(J-1)\mathbf{I} \tag{3.2}$$

where $\mathbf{B}^* = J^{-2/3}\mathbf{B}$ is the distortional left Cauchy-Green deformation tensor. Note that the previous formulation presented in Eqs. (3.1) and (3.2) is based on the decomposition of the stress into deviatoric and volumetric parts. In this regard, the deviatoric response is formulated in terms of distorsional deformation tensors which are related to the distortional part of the deformation gradient $\mathbf{F}^* = J^{-1/3}\mathbf{F}$. The Neo-Hookean model can be also formulated using alternatives formulations based on the total deformation gradient as in the following

$$\Psi(\mathbf{C}) = \frac{1}{2}\lambda \ln(J) - \mu \ln(J) + \frac{1}{2}\mu[\mathrm{tr}(\mathbf{C}) - 3] \tag{3.3}$$

where λ and μ are the classical Lamé constants of the linearized theory. Using Eq. (2.50), the Cauchy stress tensor can be defined by

$$\boldsymbol{\sigma} = \frac{\lambda \ln(J)}{J}\mathbf{I} + \frac{\mu}{J}(\mathbf{B} - 1) \tag{3.4}$$

3.2.2 Mooney-Rivlin model

The Mooney-Rivlin model [Mooney, 1940; Rivlin, 1948] can be understood as an extension of the Neo-Hookean model in which the deviatoric response is defined depending on both first and second strain invariants instead of on the first only. Thus, its Helmholtz free energy per unit reference volume is defined as

$$\Psi(\mathbf{C}) = C_{10}(I_1^* - 3) + C_{01}(I_2^* - 3) + \frac{\kappa}{2}(J-1)^2 \tag{3.5}$$

where C_{10} and C_{01} are material parameters and $I_2^* = \frac{1}{2}\left[I_1^{*2} - (\mathbf{C}^*:\mathbf{C}^*)\right]$ is the deviatoric second strain invariant. The equivalent shear modulus of the material can be related with the Mooney-Rivlin material parameters as $\mu = \frac{C_{10}+C_{01}}{2}$.

The Cauchy stress tensor can be defined by using Eq. (2.50)

$$\boldsymbol{\sigma} = \frac{1}{J}\left[2(C_{10} + I_1^* C_{01})\,\mathbf{B}^* - 2C_{01}\mathbf{B}^*\mathbf{B}^* - \frac{2}{3}(C_{10}I_1^* + 2C_{01}I_2^*)\mathbf{I}\right] + \kappa(J-1)\mathbf{I} \tag{3.6}$$

3.2.3 Gent model

The Gent model [Gent, 1996] can be considered as a phenomenological extension of the Neo-Hookean model that aims to better characterize the mechanical response of hyperelastic materials at large deformations. The Helmholtz free energy is postulated such that it has a singularity when the first strain invariant reaches a limiting value associated with the limited chain extensibility. This energy function is defined as

$$\Psi(\mathbf{C}) = -\frac{\mu}{2} j_m \ln\left(1 - \frac{I_1^* - 3}{j_m}\right) + \frac{\kappa}{2}(J-1)^2 \tag{3.7}$$

where μ is the shear modulus of the matrix, j_m is a dimensionless parameter controlling the limited chain extensibility, and κ is the bulk modulus.

The constitutive equation for the Cauchy stress tensor can be derived by using Eq. (2.50) as

$$\boldsymbol{\sigma} = \frac{\mu}{J}\frac{1}{1-\frac{I_1^*-3}{j_m}}\mathrm{dev}(\mathbf{B}^*) + \kappa(J-1)\mathbf{I} \tag{3.8}$$

3.2.4 Eight-Chain model

The eight-chain model is a hyperelastic model physically motivated by the deformation mechanisms of elastomers and proposed by Arruda and Boyce (1993). The physical motivation of this model relies on the assumption that the chain molecules on average are located along the diagonals of a unit cell, Fig. 3.1. Experimental observations for elastomers have demonstrated that the internal energy $e_o(J)$ does not depend on the applied distortional stretch. In this regard, the Helmholtz free energy adopts the form

$$\Psi\left(\bar{\lambda}^*, J, \theta\right) = e_o(J) - \theta\eta_0\left(\bar{\lambda}^*\right) \tag{3.9}$$

where $e_o(J)$ represents the volumetric response and $\eta_0\left(\bar{\lambda}^*\right)$ the deviatoric response, with $\bar{\lambda}^* = \sqrt{\frac{I_1^*}{3}}$ being the effective distortional stretch. The expressions for the internal energy and the specific internal entropy for the eight-chain model are

$$e_o(J) = \kappa J\left(\frac{J}{2} - 1\right) \tag{3.10}$$

$$\eta_0\left(\bar{\lambda}^*\right) = Nk_B \ln[\Omega(r)] + c \tag{3.11}$$

where κ is the bulk modulus, N is the number of chains per reference unit volume, k_B is the Boltzmann's constant and $\Omega(r)$ is the probability distribution of the end-to-end distance of the molecular chain depending on end-to-end distance of the molecular chains r. $\Omega(r)$ can be expressed in the previous equation by using the Langevin function (see Bergström (2015) for more details).

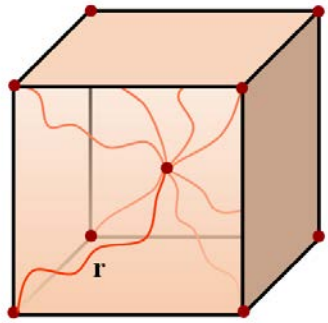

Figure 3.1: Location of the eight chain molecules in the unit cell.

According to Eq. (3.11), the change in entropy with chain length can be written as

$$\frac{\partial\eta_0}{\partial r} = -\frac{Nk_B}{l}\mathfrak{L}^{-1}\left(\frac{r}{nl}\right) \tag{3.12}$$

n being the number of *rigid links* of macromolecules in the polymer microstructure and l the length of each.

The derivation of the Cauchy stress tensor from the Helmholtz free energy can be directly obtained by expressing Eq. (2.50) in terms of invariants as

$$\boldsymbol{\sigma} = \frac{2}{J}\left[\frac{\partial \Psi}{\partial I_1^*} + \frac{\partial \Psi}{\partial I_2^*} I_1^*\right]\mathbf{B}^* - \frac{2}{J}\frac{\partial \Psi}{\partial I_2^*}(\mathbf{B}^*)^2 + \left[\frac{\partial \Psi}{\partial J} - \frac{2I_1^*}{3J}\frac{\partial \Psi}{\partial I_1^*} - \frac{4I_2^*}{3J}\frac{\partial \Psi}{\partial I_2^*}\right]\mathbf{I} \tag{3.13}$$

and, particularizing this expression for the Helmholtz free energy proposed

$$\boldsymbol{\sigma} = \frac{2}{J}\frac{\partial \Psi}{\partial I_1^*}\mathrm{dev}(\mathbf{B}^*) + \frac{\partial \Psi}{\partial J}\mathbf{I} \tag{3.14}$$

Both derivative terms in Eq. (3.14) can be developed obtaining

$$\frac{\partial \Psi}{\partial J} = \frac{\partial e_o}{\partial J} = \kappa(J-1) \tag{3.15}$$

$$\frac{\partial \Psi}{\partial I_1^*} = \frac{\partial \eta_0}{\partial I_1^*} = \frac{\partial \eta_0}{\partial r}\frac{\partial r}{\partial \bar{\lambda}^*}\frac{\partial \bar{\lambda}^*}{\partial I_1^*} = \frac{Nk_B\theta}{6}\frac{\lambda^{lock}}{\bar{\lambda}^*}\mathfrak{L}^{-1}\left(\frac{\bar{\lambda}^*}{\lambda^{lock}}\right) \tag{3.16}$$

where $\lambda^{lock} = nl$ is the maximum (fully extended) stretch that a molecule can be exposed to.

Therefore, the final expression for the Cauchy stress tensor can be obtained by substituting the terms in Eqs. (3.15) and (3.16) into Eq. (3.14) as

$$\boldsymbol{\sigma} = \frac{Nk_B\theta}{3J}\frac{\lambda^{lock}}{\bar{\lambda}^*}\mathfrak{L}^{-1}\left(\frac{\bar{\lambda}^*}{\lambda^{lock}}\right)\mathrm{dev}(\mathbf{B}^*) + \kappa(J-1)\mathbf{I} \tag{3.17}$$

3.3 Anisotropic Hyperelasticity

Materials are often heterogeneous in the sense that they present different compositions throughout the body of the material. This heterogeneity is commonly a consequence of the composition of these materials based on a matrix material (often called as ground substance) and fibres embedded in the matrix. Due to this structure, these composites have strong directional properties which result in an anisotropic mechanical response. In this section, the fibres are assumed to be continuously arranged in the matrix material following a preferred direction. According to these assumptions, the stiffness of the

composite in the fibre direction is typically much greater than in the transverse directions to the fibres. It is assumed that the material behaves in an isotropic manner along orthogonal directions to the preferred fibre direction and, therefore, the material mechanical response can be treated as *transversely isotropic*. When dealing with transverse isotropy under small elastic deformations it is often sufficient to use anisotropic elasticity. Constitutive models for these assumptions are well established and can be found elsewhere [Tsai and Hahn, 1980; Jones, 1999]. However, the aim of this section is to provide transversely isotropic constitutive models capable of supporting finite strains. In this regard, there are two commonly used approaches: strain based [Fung, 1993] and invariant based [Spencer, 1984] hyperelasticity.

3.3.1 Generalized Fung model

The Fung model [Fung, 1993] is an anisotropic hyperelastic model commonly used for the modelling of engineered and native soft tissues. Its Helmholtz free energy per unit reference volume is defined as

$$\Psi\left(c, b_{ijkl}, \kappa\right) = \frac{c}{2}\left[\exp(Q) - 1\right] + \frac{\kappa}{2}(J-1)^2 \tag{3.18}$$

where c, b_{ijkl} and κ are material parameters. Q is a scalar variable which depends on the dimensionless symmetric fourth order tensor $\mathbf{b}$ (with components b_{ijkl}) and on the distortional Green-Lagrange strain $\mathbf{E}^* = (\mathbf{C}^* - \mathbf{I})/2$

$$Q = \mathbf{E}^* : \mathbf{b} : \mathbf{E}^* \tag{3.19}$$

The Cauchy stress tensor can be derived from Eq. (3.18) as

$$\boldsymbol{\sigma} = \frac{1}{J}\mathbf{F}\frac{\partial \Psi}{\partial \mathbf{E}^*}\mathbf{F}^{\mathbf{T}} + \frac{\partial \Psi}{\partial J}\mathbf{I} \tag{3.20}$$

3.3.2 Invariant based model

A common alternative approach for the formulation of transversely anisotropic constitutive models is based on the introduction of two additional invariants, I_4 and I_5. These invariants are representative variables of the material deformation projected along the fibre direction and, therefore, can be used to take into account the stress contribution due to the longitudinal stretch of the fibres. The fourth and fifth strain invariants are defined by

$$I_4 = \mathbf{a_o C a_o} = \lambda_F^2 \tag{3.21}$$

$$I_5 = \mathbf{a_o C^2 a_o} \tag{3.22}$$

where a_o is the fibre direction and λ_F is the stretch in the provided fibre direction.

The total Helmholtz free energy per unit reference volume can be then formulated as the sum of the stress contribution due to the total deformation of the material (Ψ_1) and the fibres deformation along the preferred fibre direction (Ψ_2)

$$\Psi = \Psi_1(I_1^*, I_2^*, J) + \Psi_2(I_4, I_5) \tag{3.23}$$

By using Eq. (2.50) and the derivative of the invariants with respect to **C**

$$\frac{\partial I_1}{\partial \mathbf{C}} = \mathbf{I};\ \ \frac{\partial I_2}{\partial \mathbf{C}} = I_1\mathbf{I} - \mathbf{C};\ \ \frac{\partial I_3}{\partial \mathbf{C}} = I_3\mathbf{C^{-1}};\ \ \frac{\partial I_4}{\partial \mathbf{C}} = \mathbf{a_o}\otimes\mathbf{a_o};\ \ \frac{\partial I_5}{\partial \mathbf{C}} = \mathbf{a_o}\otimes\mathbf{C a_o} + \mathbf{a_o C}\otimes\mathbf{a_o} \tag{3.24}$$

the Cauchy stress tensor is given by [Holzapfel, 2000]

$$\boldsymbol{\sigma} = \frac{2}{J}\left[\frac{\partial \Psi}{\partial I_1^*} + \frac{\partial \Psi}{\partial I_2^*} I_1^*\right]\mathbf{B}^* - \frac{2}{J}\frac{\partial \Psi}{\partial I_2^*}(\mathbf{B}^*)^2 + \left[\frac{\partial \Psi}{\partial J} - \frac{2I_1^*}{3J}\frac{\partial \Psi}{\partial I_1^*} - \frac{4I_2^*}{3J}\frac{\partial \Psi}{\partial I_2^*}\right]\mathbf{I} + \frac{2}{J} I_4 \frac{\partial \Psi}{\partial I_4}\mathbf{a}\otimes\mathbf{a} + \frac{2}{J} I_5 \frac{\partial \Psi}{\partial I_5}(\mathbf{a}\otimes\mathbf{b a} + \mathbf{a b}\otimes\mathbf{a}) \tag{3.25}$$

$\mathbf{a} = |\mathbf{F a_o}|$ being the fibre direction expressed in the current configuration.

3.3.3 Holzapfel-Gasser-Ogden model

The Holzapfel-Gasser-Ogden model [Holzapfel et al., 2000] was originally developed to predict the anisotropic hyperelastic behaviour of arterial tissue. This model follows a constitutive formulation based on a Helmholtz free energy function additively decoupled into a hyperelastic component associated with the matrix response (modelled by a Neo-Hookean model); and an anisotropic component associated with up to three different families of fibres. Regarding the three families of fibres, their initial directions are given by the three vectors $\mathbf{a_1}$, $\mathbf{a_2}$ and $\mathbf{a_3}$.

The total Helmholtz free energy per unit reference volume is defined as

$$\Psi = \frac{\mu}{2}(I_1^* - 3) + \frac{k_1}{2k_2}\sum_{i=1}^{3}\left[e^{k_2\langle E_i\rangle^2} - 1\right] + \frac{\kappa}{2}(J-1)^2 \tag{3.26}$$

where the energy term E_i is defined by

$$E_i = d(I_1^* - 3) + (1 - 3d)(I_{4i}^* - 1) \tag{3.27}$$

d being the dispersion and $I_{4i}^* = (\mathbf{F}^* \mathbf{a_i})(\mathbf{F}^* \mathbf{a_i})$. The term $\langle E_i \rangle$ is the ramp function defined as

$$\langle E_i \rangle = \frac{(E_i + |E_i|)}{2} \tag{3.28}$$

Chapter 4.
Finite viscoelasticity

In this chapter, constitutive models that combine hyperelasticity with viscoelasticity are introduced. The methodology followed in the development of the constitutive models presented has motivated the methodology used in the formulation of the general constitutive framework.

4.1 Introduction

In the previous chapter, some purely elastic models are presented for the modelling of hyperelastic materials. However, many polymers and soft tissues, do not behave in a purely elastic manner but also exhibit viscous characteristics. In this regard, more complex and sophisticated models are proposed in order to predict the non-linear, rate- and temperature-dependent response of materials. A common methodology for the development of these types of models is the definition of rheological models composed of different elements (springs, dashpots, friction elements...) which describe the basis for the kinematics and formulation of the constitutive models. The implementation of these models requires additional software components (user material subroutines) and typically implies higher computational expense and more experiments for proper calibration. This chapter attempts to present examples of this these models and introduce the fundamentals and methodology of their formulation in order to facilitate the understanding of more complex models developed in latter sections. This content is adapted from [Bergström, 2015].

4.2 Bersgström-Boyce model

The Bergström-Boyce (BB) model is a hyperelastic-viscoelastic constitutive model which takes into account the non-linear and time-dependent behaviour of elastomer-like materials within a finite deformation formulation. It can be considered as a generalization of linear viscoelasticity which overcomes issues related to large deformations and strain dependence of the dynamic properties. In this sense, the BB model has been demonstrated to be able to accurately predict the mechanical behaviour of engineering rubbers and soft biomaterials.

Experimental observations of the stress response in elastomer materials have shown that this stress behaviour can be divided into an equilibrium response and a time-dependent deviation from equilibrium. According to these observations, the BB model is based on the rheological model shown in Fig. 4.1 leading to a true response of the material decomposed into two parallel networks A and B. While network A introduces a

hyperelastic back-stress, the network *B* introduces a viscous contribution that consists of a non-linear hyperelastic spring in series with a non-linear viscoelastic dashpot. In other words, the total stress is decomposed into elastic and history dependent components.

According to the rheological scheme, Fig. 4.1, the deformation gradient is equal for both constitutive branches in parallel so that $\mathbf{F} = \mathbf{F_A} = \mathbf{F_B}$. While the contribution of network *A* is assumed as purely elastic, the time-dependent network *B* is multiplicatively decomposed into an elastic, $\mathbf{F_B^e}$, and a viscoelastic, $\mathbf{F_B^v}$, components

$$\mathbf{F_B} = \mathbf{F_B^e F_B^v} \tag{4.1}$$

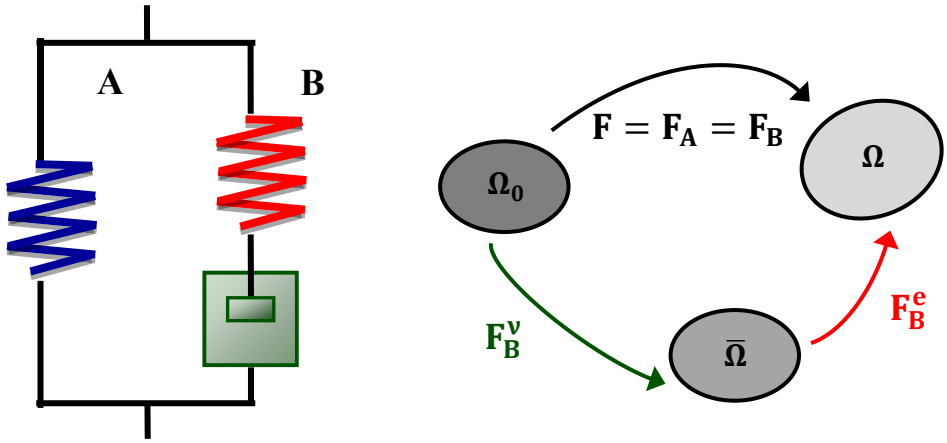

Figure 4.1: (a) Rheological scheme of the BB model; and (b) kinematics of the BB model.

The non-linear hyperelastic spring of network *A* is defined by the eight-chain model, so the expression for the Cauchy stress tensor associated with this constitutive branch follows Eq. (3.17), where the term $Nk_B\theta$ is replaced by the equivalent shear modulus of the network μ. Regarding the network *B*, the stress response is also defined by the eight-chain model in terms of the elastic deformation gradient of this part, but introducing the variable s which is a dimensionless parameter specifying how much stiffer the shear modulus of network *B* is with respect to network *A*. Thus

$$\boldsymbol{\sigma_B} = \frac{s\mu}{J_B \bar{\lambda}_B^{e*}} \mathfrak{L}^{-1}\left(\frac{\bar{\lambda}_B^{e*}/\lambda^{lock}}{1/\lambda^{lock}}\right) \mathrm{dev}(\mathbf{B_B^{e*}}) + \kappa(J_B^e - 1)\mathbf{I} \tag{4.2}$$

where $\bar{\lambda}_B^{e*}$ is the chain stretch in the elastic part of network *B*.

Therefore, the total Cauchy stress is given by the sum of both parts as

$$\boldsymbol{\sigma} = \boldsymbol{\sigma}_{\mathbf{A}} + \boldsymbol{\sigma}_{\mathbf{B}} \tag{4.3}$$

Note that since the stress formulation for the network *B* contribution is based on the elastic component of the deformation gradient, it is necessary to take into account the viscoelastic flow which rules the evolution of $\mathbf{F}_{\mathbf{B}}^{\boldsymbol{\nu}}$. The velocity gradient on network *B* is defined by

$$\mathbf{L}_{\mathbf{B}} = \mathbf{L}_{\mathbf{B}}^{\mathbf{e}} + \mathbf{F}_{\mathbf{B}}^{\mathbf{e}}\mathbf{L}_{\mathbf{B}}^{\boldsymbol{\nu}}\mathbf{F}_{\mathbf{B}}^{-\mathbf{e}} = \mathbf{L}_{\mathbf{B}}^{\mathbf{e}} + \bar{\mathbf{L}}_{\mathbf{B}}^{\boldsymbol{\nu}} \tag{4.4}$$

where

$$\mathbf{L}_{\mathbf{B}}^{\boldsymbol{\nu}} = \dot{\mathbf{F}}_{\mathbf{B}}^{\boldsymbol{\nu}}\mathbf{F}_{\mathbf{B}}^{-\boldsymbol{\nu}} = \mathbf{D}_{\mathbf{B}}^{\boldsymbol{\nu}} + \mathbf{W}_{\mathbf{B}}^{\boldsymbol{\nu}} \tag{4.5}$$

$$\bar{\mathbf{L}}_{\mathbf{B}}^{\boldsymbol{\nu}} = \bar{\mathbf{D}}_{\mathbf{B}}^{\boldsymbol{\nu}} + \bar{\mathbf{W}}_{\mathbf{B}}^{\boldsymbol{\nu}} \tag{4.6}$$

Assuming the intermediate configuration invariant to the body rotation, the skew part of the viscous velocity gradient is null, $\bar{\mathbf{W}}_{\mathbf{B}}^{\boldsymbol{\nu}} = 0$, so that $\bar{\mathbf{L}}_{\mathbf{B}}^{\boldsymbol{\nu}} = \bar{\mathbf{D}}_{\mathbf{B}}^{\boldsymbol{\nu}}$. The rate of viscous deformation is constitutively prescribed by defining the symmetric part of the viscous velocity gradient

$$\bar{\mathbf{D}}_{\mathbf{B}}^{\boldsymbol{\nu}} = \dot{\gamma}_B \mathbf{N}_{\mathbf{B}}^{\boldsymbol{\nu}} \tag{4.7}$$

where $\mathbf{N}_{\mathbf{B}}^{\boldsymbol{\nu}}$ provides the direction of the viscoelastic flow and is defined as

$$\mathbf{N}_{\mathbf{B}}^{\boldsymbol{\nu}} = \frac{\mathrm{dev}(\boldsymbol{\sigma}_{\mathbf{B}})}{\boldsymbol{\tau}} \tag{4.8}$$

The effective scalar stress τ drives the viscous flow and can be expressed as

$$\tau = \sqrt{\mathrm{tr}[\mathrm{dev}(\boldsymbol{\sigma}_{\mathbf{B}})\,\mathrm{dev}(\boldsymbol{\sigma}_{\mathbf{B}})]} \tag{4.9}$$

The effective flow rate $\dot{\gamma}_B$, can be defined in many different ways. The simplest one is by defining the dashpot as linear

$$\dot{\gamma}_B = \dot{\gamma}_o \left[\frac{\tau}{\tau_B}\right] \tag{4.10}$$

where $\dot{\gamma}_o$ is a constant introduced to ensure dimensional consistency and τ_B is a material constant.

A more sophisticated definition of $\dot{\gamma}_B$ uses a micromechanism-inspired model based on the assumption that the reptation of the *elastically inactive* macromolecules is the mechanism responsible for the time-dependent response. Thus,

$$\dot{\gamma}_B = \dot{\gamma}_o \left(\bar{\lambda}_B^v - 1 + \xi\right)^C \left[R\left(\frac{\tau}{f_v \tau_{base}} - \tau_{cut}\right)\right]^m \tag{4.11}$$

where ξ, C, τ_{base}, τ_{cut} and m are material parameters, R is the ramp function, f_v is the network interaction factor and $\bar{\lambda}_B^v$ is the viscoelastic chain stretch.

4.3 Arruda-Boyce model

The Arruda-Boyce (AB) model is a reference model for glassy polymers. This model takes into account rate and temperature dependencies of the mechanical behaviour of glassy polymers within a large deformation formulation. These materials typically present mechanical behaviour based on an initial linear elastic response followed by yielding and then strain hardening at large strains. The kinematics of the AB model are based on the rheological model shown in Fig. 4.2, resulting in a total deformation gradient decomposed into elastic and plastic components, $\mathbf{F} = \mathbf{F^e F^p}$. According to the rheological model, the material response can be interpreted as two network acting in series: an elastic contribution (e) and a plastic contribution (p).

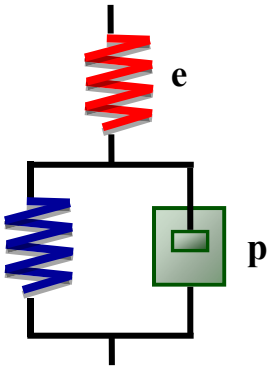

Figure 4.2: Rheological scheme of the AB model.

The expression for the total Cauchy stress can be defined by the following linear elastic relationship

$$\boldsymbol{\sigma} = \frac{1}{J^e}\left(2\mu^e \mathbf{E^e} + \lambda^e \operatorname{tr}[\mathbf{E^e}]\mathbf{I}\right) \tag{4.12}$$

where $\mathbf{E^e} = \operatorname{tr}(\mathbf{V^e})$ is the logarithmic true strain and μ^e and λ^e are Lamé's constants. The total stress is equal to the sum of the plastic convected back stress $\boldsymbol{\sigma}^{\mathbf{p}}$ and the stress associated with the spring in parallel $\boldsymbol{\sigma}^*$

$$\boldsymbol{\sigma} = \boldsymbol{\sigma}^* + \frac{1}{J^e}\mathbf{F^e}\boldsymbol{\sigma}^{\mathbf{p}}\mathbf{F^{eT}} \tag{4.13}$$

where the deviatoric back stress is given by the incompressible form of the eight-chain model

$$\boldsymbol{\sigma}^{\mathbf{p}} = \frac{\mu^p}{\bar{\lambda}^p}\mathfrak{L}^{-1}\left(\frac{\bar{\lambda}^p/\bar{\lambda}^p_{lock}}{1/\bar{\lambda}^p_{lock}}\right)\operatorname{dev}(\mathbf{B^p}) \tag{4.14}$$

μ^p and $\bar{\lambda}^p_{lock}$ being physically motivated material constants, $\bar{\lambda}^p = (\operatorname{tr}[\mathbf{B^p}]/3)^{1/2}$ and $\mathbf{B^p} = \mathbf{F^p}\mathbf{F^{pT}}$.

The plastic multiplier can be defined for isothermal deformation histories as

$$\dot{\gamma}_p = \dot{\gamma}_o \exp\left[\frac{\tau}{\tau_p}\right] \tag{4.15}$$

where $\dot{\gamma}_o$ and τ_p are material parameters and τ is the effective scalar of the driving stress $\boldsymbol{\sigma}^*$. This expression can be modified to explicitly include temperature effects as

$$\dot{\gamma}_p = \dot{\gamma}_o \exp\left[\frac{\tau}{k_B\theta/A}\right] \tag{4.16}$$

with θ being the absolute temperature, A a material parameter and k_B is Boltzamann's constant.

4.4 Three network model

The Three Network (TN) model was originally developed for the prediction of the mechanical behaviour of thermoplastic materials. This model considers the total deformation gradient decoupled into thermal and mechanical contributions as $\mathbf{F} = \mathbf{F^M F^\theta}$. The thermal part corresponds to thermal expansion and is defined to be isotropic as

$$\dot{\mathbf{F}}^{\boldsymbol{\theta}} = f_\theta \mathbf{F}^{\boldsymbol{\theta}} \dot{\theta} \tag{4.17}$$

The kinematics of the mechanical part of the deformation gradient, consists of three networks acting in parallel, Fig. 4.3, so that $\mathbf{F^M} = \mathbf{F_A^M} = \mathbf{F_B^M} = \mathbf{F_C^M}$.

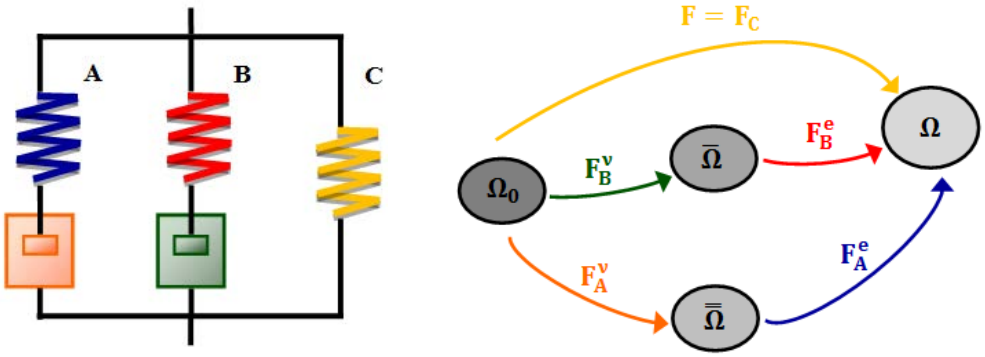

(a) (b)

Figure 4.3: (a) Rheological scheme of the TN model; and (b) kinematics of the TN model.

The deformation gradient associated with network *A* is multiplicatively decomposed into elastic and viscous components

$$\mathbf{F}_\mathbf{A}^\mathbf{M} = \mathbf{F}_\mathbf{A}^\mathbf{e}\mathbf{F}_\mathbf{A}^\mathbf{v} \tag{4.18}$$

The Cauchy stress contribution of this constitutive branch is defined by a temperature-dependent eight-chain model depending on the elastic deformation gradient, expressed as

$$\boldsymbol{\sigma}_\mathbf{A} = \frac{\mu_A}{J_A^e \bar{\lambda}_A^{e*}}\left[1+\frac{\theta-\theta_O}{\hat{\theta}}\right]\mathfrak{T}^{-1}\left(\frac{\bar{\lambda}_A^{e*}/\lambda^{lock}}{1/\lambda^{lock}}\right)\mathrm{dev}(\mathbf{B}_\mathbf{A}^{e*}) + \kappa(J_A^e - 1)\mathbf{I} \tag{4.19}$$

where μ_A, λ^{lock}, $\hat{\theta}$ and κ are material parameters and $\bar{\lambda}_A^{e*}$ is the effective chain stretch based on the eight-chain topology assumption.

The definition of the viscous flow rule is necessary in order to indentify the elastic component of $\mathbf{F}_\mathbf{A}^\mathbf{M}$. As in the BB model, Eqs. (4.4), (4.5) and (4.6) can be applied to network *A*. By considering the intermediate configuration invariant to rigid body rotations then, $\bar{\bar{\mathbf{W}}}_\mathbf{A}^\mathbf{v} = 0$, so that $\bar{\bar{\mathbf{L}}}_\mathbf{A}^\mathbf{v} = \bar{\bar{\mathbf{D}}}_\mathbf{A}^\mathbf{v}$. The rate of viscous deformation is constitutively prescribed by defining the symmetric part of the viscous velocity gradient

$$\bar{\bar{\mathbf{D}}}_\mathbf{A}^\mathbf{v} = \dot{\gamma}_A \mathbf{N}_\mathbf{A}^\mathbf{v} \tag{4.20}$$

with $\mathbf{N_A^v}$ specifying the direction of the viscous flow and $\dot{\gamma}_A$ specifying the effective flow rate. For the viscoelastic multiplier $\dot{\gamma}_A$, a temperature-dependent expression is used as

$$\dot{\gamma}_A = \dot{\gamma}_o \left(\frac{\tau_A}{\hat{\tau}_A + aR(p_A)}\right)^{m_A} \left(\frac{\theta}{\theta_o}\right)^{n} \tag{4.21}$$

where $\dot{\gamma}_o$, $\hat{\tau}_A$, a, m_A, n and θ_o are specified material parameters, R(x) is the ramp function and $p_A = -(\boldsymbol{\sigma_{A11}} + \boldsymbol{\sigma_{A22}} + \boldsymbol{\sigma_{A33}})/3$ is the hydrostatic pressure.

The Cauchy stress contribution of the network *B* is given by the same formulation as for network *A*

$$\boldsymbol{\sigma_B} = \frac{\mu_B}{J_B^e \bar{\lambda}_B^{e*}} \left[1 + \frac{\theta - \theta_O}{\hat{\theta}}\right] \mathfrak{L}^{-1}\left(\frac{\bar{\lambda}_B^{e*}/\lambda^{lock}}{1/\lambda^{lock}}\right) \mathrm{dev}(\mathbf{B}_B^{e*}) + \kappa(J_B^e - 1)\mathbf{I} \tag{4.22}$$

where the effective shear modulus μ_B evolves along the deformation process with the plastic strain from an initial value of μ_{Bi} according to

$$\dot{\mu}_B = -\beta[\mu_B - \mu_{Bf}]\dot{\gamma}_A \tag{4.23}$$

The definition of the viscous flow rule for the network *B* is defined in the same way as for network *A*, by considering the intermediate configuration invariant to rigid body rotations and then, $\bar{\mathbf{W}}_\mathbf{B}^\mathbf{v} = 0$, so that $\bar{\mathbf{L}}_\mathbf{B}^\mathbf{v} = \bar{\mathbf{D}}_\mathbf{B}^\mathbf{v}$. Here the flow rule follows the same formulation as $\bar{\mathbf{D}}_\mathbf{B}^\mathbf{v} = \dot{\gamma}_B \mathbf{N}_\mathbf{B}^\mathbf{v}$ and the effective deviatoric flow rate is given by an equivalent expression that Eq. (4.21) for this network

$$\dot{\gamma}_B = \dot{\gamma}_o \left(\frac{\tau_B}{\hat{\tau}_B + aR(p_B)}\right)^{m_B} \left(\frac{\theta}{\theta_o}\right)^{n} \tag{4.24}$$

To complete the model, the Cauchy stress associated with network *C* is also defined by a temperature-dependent eight-chain model as

$$\boldsymbol{\sigma_C} = \frac{\mu_C}{J\bar{\lambda}^*} \left[1 + \frac{\theta - \theta_O}{\hat{\theta}}\right] \mathfrak{L}^{-1}\left(\frac{\bar{\lambda}^*/\lambda^{lock}}{1/\lambda^{lock}}\right) \mathrm{dev}(\mathbf{B}^*) + \kappa(J - 1)\mathbf{I} \tag{4.25}$$

where μ_C, λ^{lock}, $\hat{\theta}$ and κ are material parameters and $\bar{\lambda}^*$ is the effective chain stretch. Finally, according to the rheological model shown in Fig. 4.3, the total stress response is given by

$$\boldsymbol{\sigma} = \boldsymbol{\sigma_A} + \boldsymbol{\sigma_B} + \boldsymbol{\sigma_C} \tag{4.26}$$

Chapter 5.

Mechanical behaviour of hyperelastic materials under dynamic loading: Experimental and preliminary modelling of PEEK and SCFR PEEK composites

This chapter presents an analysis of previous studies reported in the literature and experimental and numerical studies carried out in this work. The main aim of this chapter is to understand the physical fundamentals behind the mechanical behaviour of hyperelastic materials that underlie the assumptions on which constitutive models are formulated. To this end, the thermo-mechanical and impact behaviour of PEEK and its composites have been studied. The content of this chapter is presented in three sections: first, a study that focuses on unfilled PEEK; second, a study that focuses on SCFR PEEK; and third, a study that focuses on the influence of temperature on the dynamic mechanical behaviour of both materials.

5.1 Mechanical characterization and impact behaviour of PEEK

5.1.1 Introduction

The developments of new technologies and biocompatible materials have made it possible to replace more parts of the human body. Titanium alloy was generally used in biomedical applications [Niiomi, 2008], but in recent years, following confirmation of biocompatibility [Rivard et al., 2002; Korak et al., 2010], the polymer polyether-ether-ketone (PEEK) has been increasingly employed as matrix material for composites in trauma, orthopaedic, dentals, spinal and cranial implants [Kurtz et al., 2007; Halabi et al., 2011; Lovald et al., 2012]. Implant applications of PEEK materials usually involve impact loading during medical installation and the useful life of prostheses, such as hip stems, bone anchors and cranial implants, Fig.5.1. In this regard, cranial implants have experienced a significant evolution in the last decade in different aspects such as materials, method of fixation, and manufacturing process [Halabi et al., 2011]. An important aspect to take into account is the load-bearing capacity of these structural prostheses. Indeed, the implant must resist at different loading including those generated by a fall, an accidental impact or a bike accident. Mechanical impact process is a complex problem that includes dynamic behaviour, fracture, damage, contact and friction [Arias et al., 2008]. Therefore, impact loads can affect the structural response of materials used in prosthetic devices. In particular, the dynamic behaviour of PEEK composites is highly influenced by the matrix properties due to its semi-crystalline nature [Talbot et al., 1987]. About this matter, interesting thermo-mechanical phenomena have been reported for PEEK matrix [Sobieraj et al., 2012; El-Qouba et al., 2014], including changes in crystallinity, deformation-induced heating, macroscopic decolouration, high strain rate and large deformations associated with impact. The elastic properties of PEEK are relatively unaffected by rate effects at body temperature, which is below the glass transition [Kurtz et al., 2007]. However, the yielding and plastic flow behaviours are

affected by strain rate at physiological temperatures [El-Qoubaa et al., 2014]. Additionally, adiabatic heating, associated with dynamic behaviour of the impact process can induce rapid crystallization of PEEK at temperatures above glass transition [El-Qoubaa et al., 2014]. In this regard, the impact behaviour of PEEK has not been deeply studied in terms of kinetic energy absorption and failure under impact loading [Millet et al., 2006; Rae et al., 2007], and perforation tests have not been reported in the scientific literature. In this section, perforation tests using rigid spheres have been conducted on plates of PEEK 450G and compared with Ti6Al4V titanium alloy, an alloy frequently used in medical applications. The perforation experiment covered impact kinetic energies from 21 J to 131 J. A numerical approach, including the influence of strain rate and temperature, is presented and validated with experimental data. This numerical model can be useful to understand the mechanisms behind the deformation process of this type of materials.

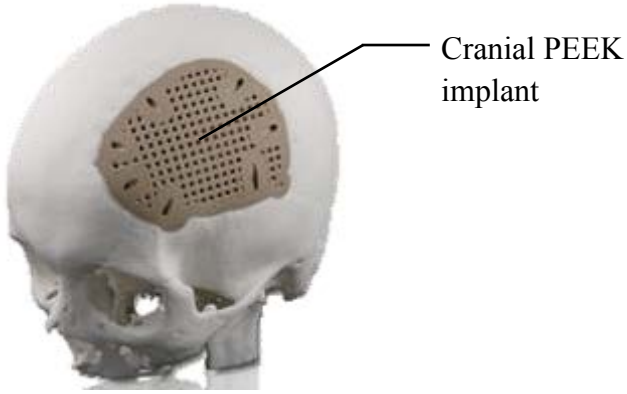

Figure 5.1: Cranial implant using PEEK material [Lovald and Kurtz, 2007].

5.1.2 Mechanical characterization

A commercial plate of unfilled PEEK 450G, general purpose grade, with a density $\rho = 1300 kg \cdot m^{-3}$ was purchased measuring 130x130x30 mm^3. Mechanical and thermal properties are reported in Table 5.1 [Lati, 2016] in agreement with data published by other authors [Rae et al., 2007]. Due to its high strength and biocompatibility, unfilled PEEK has been used in both cervical and lumbar spinal cages and cranial implants with considerable clinical success [Sobieraj et al., 2009; Halabi et al., 2011; Lovald et al., 2012].

Table 5.1: Material Properties of PEEK [Lati, 2016].

Mechanical properties		Thermal properties	
Elastic Modulus (GPa)	3.6	Thermal Conductivity (W/mK)	0.29
Poisson's ratio	0.38	Specific Heat (J/kgK)	2180
Density (kg/m^3)	1300	Glass transition temperature (K)	416
Yield stress (MPa)	107	Melt transition temperature (K)	616

5.1.2.1 Crystallinity

PEEK is a two-phase semi-crystalline polymer, consisting of an amorphous phase and a crystalline phase. The crystalline content of injection-moulded PEEK in implants typically ranges from 30% to 35%, [Kurtz and Devine, 2007]. From differential scanning calorimetry (DSC) a degree crystallinity of $30 \pm 2\%$ was calculated for PEEK 450G by integrating the melt endotherm and relating it to the literature value of 100% crystalline PEEK [Jonas et al., 1991]. These data are in agreement with data reported by El-Qoubaa and Ramzi (2014) for PEEK 450G and with the calculated degree of crystallinity χ_c, by Eq. (5.1):

$$\chi_c = \frac{\rho_c(\rho-\rho_a)}{\rho(\rho_c-\rho_a)} \tag{5.1}$$

where ρ is the sample density, $\rho_a = 1260\ \mathrm{kg\,m^3}$, is the extrapolated density of the pure amorphous phase and $\rho_c = 1400\ \mathrm{kg\,m^3}$, is the extrapolated density of pure crystalline phase [Jonas et al., 1991]. Mechanical properties of PEEK materials are influenced by the degree of crystallinity. Several authors have shown that increasing the degree of crystallinity can increase elastic modulus and yield strength while decreasing fracture toughness [Jonas et al., 1991; Rae et al., 2007]. Different behaviours have been reported generating some controversy about the relationship between crystallinity and high strain rate. Hamdan and Swallowe (1996) reported an increase in crystallinity of samples deformed by large strains under adiabatic conditions. However, Rae et al. (2007) reported a decrease in crystallinity of all samples deformed by large strains.

5.1.2.2 Strain rate and temperature sensitivity

The PEEK 450G has been tested by Rae et al. (2007) for different initial temperatures and strain rates. In this study, positive strain rate sensitivity was observed with the mechanical properties increasing with the strain rate. However, for a certain strain rate, $\dot{\varepsilon}_{\mathrm{transition}} \approx 0.1\ \mathrm{s^{-1}}$, a thermal softening is observed and therefore, the process of plastic deformation has to be considered as adiabatic, Fig. 5.2a. Concerning the temperature effect, a loss of

ductility was observed when the initial temperature was lower than the room temperature $\theta_o = 300\,\mathrm{K}$. Nonetheless, the ductility was retained with a strain level larger than $\varepsilon_{\text{low temperature}} > 0.2$. In addition, using experimental results published by Rae et al. (2007), it was observed that the material behaviour was still ductile for a temperature higher than $\theta_o > 413\,K$, Fig. 5.2b, knowing that the glass temperature is equal to $\theta_g = 416\,\mathrm{K}$. It was also demonstrated that PEEK behaviour was more brittle under tensile loading at low temperature compared with compression loading [Rae et al., 2007], with a failure strain level lower than $\varepsilon_{failure}^{tension} < 0.1$ at 223K. Overall, the temperature sensitivity and the strain rate sensitivity are similar under tension and compression. The two major parameters under dynamic loading have been defined. The values for the strain rate and temperature sensitivity are respectively equal to $\mathrm{m} = \frac{\partial \log(\sigma)}{\partial \log(\dot{\varepsilon})} \approx 0.46$ and $v = \frac{\partial \sigma}{\partial \theta} \approx -0.63\,MPa\,K^{-1}$. In dynamic loading, for a strain rate close to $\dot{\varepsilon} \approx 3000\,\mathrm{s}^{-1}$, the temperature sensitivity is equal to $v = \frac{\partial \sigma}{\partial \theta} \approx -0.71\,MPa\,K^{-1}$.

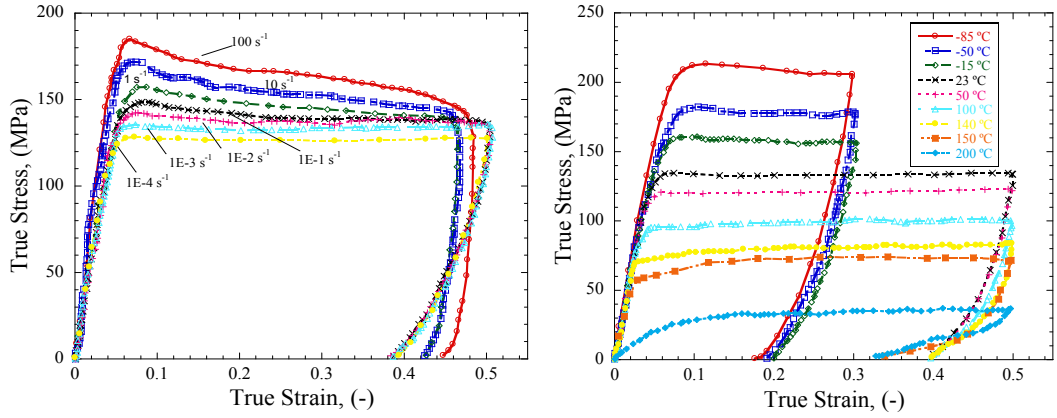

(a) (b)

Figure 5.2: Mechanical behaviour of PEEK under compression for, a) different initial strain rates at room temperature and b) different temperatures at 0.001 1/s [Rae et al., 2007].

5.1.3 Experimental impact test

5.1.3.1 Skull fracture energy

Skull fracture is a frequently observed type of severe head injury. Historically, different impact test set-ups and techniques have been used for investigating skull fractures. The most frequently used are drop tower and impactor pneumatic launcher [Verschueren et al., 2007]. Head protection measures and proposed skull fracture criteria typically include the absorbed energy until skull fracture [Karger et al., 1989; Yoganadan et al., 1995; Verschueren et al., 2007; Asgharpur et al., 2013; Caccese et al., 2013; Monea et al., 2014]. The reference of skull fracture energy ranges from 14.0 to 68.5 J [Yoganadan et al., 1995]. More recent studies reported values of 21.1 J $\leq E_{skull}^{fracture} \geq$ 40.5 J at high impact velocities [Monea et al., 2014]. For comparison, the impact velocity presented by a human head assuming a person with a height of h=*1.8 m*, is equal to $V_0 = \sqrt{2gh} \approx 6\, m/s$. If we assumed an average mass of $\bar{m}_{head} \approx 4.5\, kg$ for a human head, the maximum impact energy corresponding to an accidental fall is equal to $W_{head} \approx$ 80 J. In this study, the kinetic energy range has been 21.0 J $\leq E_K \geq$ 131.0 J within the range of skull fracture energy and upper. For this proposal, perforation tests using rigid spheres have been conducted on plates of PEEK 450G and compared with Ti6Al4V titanium alloy.

5.1.3.2 Setup

The set-up used was a gas gun capable of shooting a rigid spherical projectile with a mass of $m_p = 1.3$ g and a diameter of $\phi_p = 7.25$ mm. This experimental device uses helium up to pressures of 200 bar to impel the projectile. The initial impact velocity V_0 was in a range of 180 m/s $\leq V_0 \geq$ 450 m/s. In order to measure the impact and the residual velocity, a high speed video camera, Photron Ultima APX-RS, was used. Since the exposure time was very short, 10 µs, a 1200W HMI lamp was used to ensure adequate lighting. The camera was configured to obtain 36000 fps. Two materials, PEEK 450G and Ti6Al4V titanium alloy, were studied. The thickness of each plate was selected to obtain comparable areal density [Arias et al., 2003], a parameter frequently used to optimize impact protection, Table 5.2. The thickness of the Ti6Al4V was set at t=1 mm to provide a representative comparison. Due to the boundary conditions used to avoid sliding and to ensure correct clamping of the specimen, the size of the active part of the plate was reduced to 100x100 mm^2, Fig. 5.3.

Table 5.2: Biomaterials considered for impact tests.

Material	Dimensions (mm^3)	Mass (gr)	Areal density (kg/m^2)
PEEK 450G	130x130x3	65.5	3.9
Ti6Al4V	130x130x1	78.5	4.6

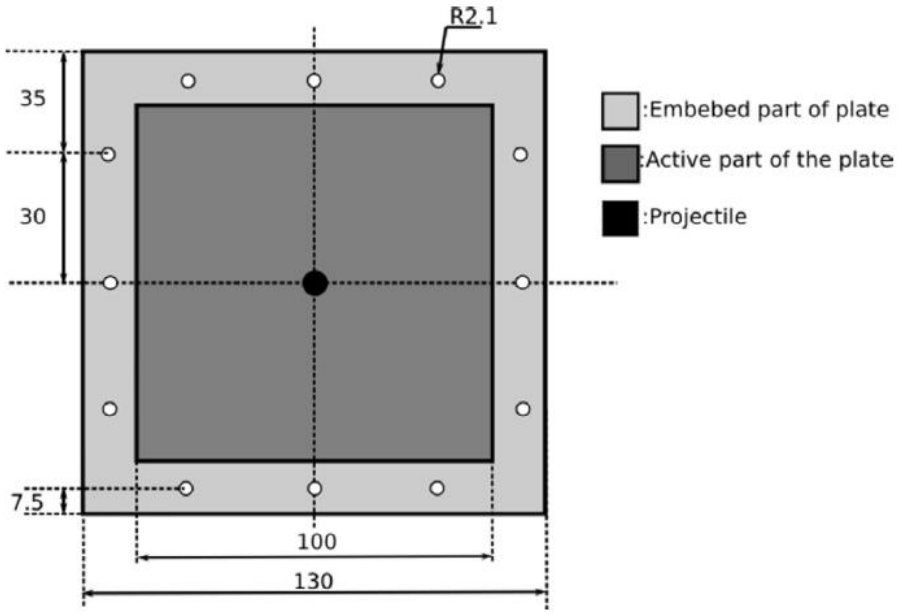

Figure 5.3: Geometry of plate specimen and boundary conditions.

5.1.4 Preliminary modelling

5.1.4.1 Viscoelasticity

The stress-strain curves obtained at different strain rate show the viscoelastic effect observed in unfilled PEEK [Rae et al., 2007], see Fig. 5.4. This behaviour is also reported by El-Qoubaa and Othman (2014). For low strain rates, the difference between elastic modulus is weak and the value obtained is constant at 3600 MPa. For high strain rates, an increase is observed until a value of 3900 MPa for $\dot{\varepsilon} \approx 10^2\ s^{-1}$ is observed according the Eq. (5.2), [Epee et al., 2011]

$$E = E_0 + \eta \dot{\varepsilon}^k \tag{5.2}$$

where E_o is the quasi-static elastic modulus, η is the consistency parameter, and k is the viscoelastic coefficient, Table 5.3. A direct identification of the material parameters which define the viscoelastic behaviour law was done, taking E_o=3600 MPa as the static Young modulus for null strain rate.

Table 5.3: Material parameters of the viscoelastic behaviour law of PEEK 450G.

E_o (MPa)	η (MPa)	k
3600	1.25	0.9

5.1.4.2 Viscoplasticity

Different models have been developed with the aim of reproducing the stress-strain constitutive relationship of semi-crystalline polymers based on phenomenological and physical approaches [Duan et al., 2001; Eppe et al., 2011]. In this section, the phenomenological Johnson Cook model (1985) was used as material model, according to the strain rate and temperature sensitivity viscoplastic behaviour of PEEK reported by Rae et al. (2007), Fig. 5.2. Significant inelastic deformation, denoted as viscoplastic, may be observed even at very small deformation levels, Fig. 5.2. For semi-crystalline polymers, it is reported that the viscoplastic deformation of crystalline phase is analogous to the viscoplastic deformation of crystallographic materials [Ghoberl, 2008]. The JC model is frequently used in ductile metal alloys [Arias et al., 2008] and it was previously used for analyze the dynamic behaviour of polymeric materials [Duan et al., 2001, Louche et al., 2009]. JC model is generally pre-implemented in FE codes, including ABAQUS/Explicit. This hardening law is defined by Eq. (5.2). The first term defines strain hardening $\bar{\varepsilon}^p$, the second strain rate sensitivity $\dot{\bar{\varepsilon}}^p$and the third one is related to thermal softening Θ, Eqs. (5.3) and (5.4)

$$\bar{\sigma}(\bar{\varepsilon}^p, \dot{\bar{\varepsilon}}^p, \theta) = [A + B(\bar{\varepsilon}^p)^n]\left[1 + C \ln\left(\frac{\dot{\bar{\varepsilon}}^p}{\dot{\bar{\varepsilon}}_o^p}\right)\right][1 - \Theta^m] \tag{5.3}$$

$$\Theta = \frac{\theta - \theta_o}{\theta - \theta_m} \tag{5.4}$$

where *A* and *B* are material constants, *n* is the strain hardening exponent, *C* the strain rate sensitivity parameter, *m* is the temperature sensitivity, $\theta_o$is the initial temperature and θ_m is the melting temperature. In addition, this constitutive relation coupled to the heat equation, Eq. (5.5), allows us to obtain the temperature increase Δθ, in adiabatic conditions

$$\Delta\theta(\bar{\varepsilon}^p, \dot{\bar{\varepsilon}}^p, \theta_o) = \frac{\beta}{\rho C_p}\int_{\varepsilon}^{\bar{\varepsilon}^p} \bar{\sigma}(\bar{\varepsilon}^p, \dot{\bar{\varepsilon}}^p, \theta)\, d\,\bar{\varepsilon}^p \tag{5.5}$$

where θ is the current temperature, β is the Quinney-Taylor heat fraction coefficient, ρ is the density of material and C_p is the specific heat at constant pressure. The model parameters were identified according to the experimental results of compressive tests at various strain rates and temperatures [Hamdan and Swallowe, 2007], Fig. 5.2, with the methodology reported for ductile metals [Arias et al., 2008; Gambirasio and Rizzi, 2014] and polymer [Louche et al., 2009]. First, the hardening parameters A, B and n of the JC model were identified on the basis of tests at room temperature. Parameter C was obtained by Eq. (5.6) at different strain rates and plastic strain equal to cero ($\bar{\sigma} = \bar{\sigma}_y$) at room temperature, 296 K. The temperature sensitivity parameter m was identified by Eq. (5.7) during compressive tests over a wide range of imposed temperatures, Fig. 5.2, from initial temperature to transition temperature.

$$C = \frac{\bar{\sigma}_y - A}{A \ln\left(\frac{\dot{\bar{\varepsilon}}^p}{\dot{\bar{\varepsilon}}_o^p}\right)} \tag{5.6}$$

$$m = \frac{1 - \frac{\bar{\sigma}}{A + B(\bar{\varepsilon}^p)^n}}{\ln\left(\frac{\theta - \theta_o}{\theta - \theta_m}\right)} \tag{5.7}$$

Different authors have measured the Quinney-Taylor coefficient in polymers [Rittel, 1998; Bjerke et al., 2002; Nasraoui et al., 2012]. In this work, it is assumed constant and equal to ratio $\beta = 0.9$. This data is reported for the inelastic work fraction generating the heat of semi-crystalline polymers [Pouriayevali et al., 2013]. The identified values of JC model parameters are indicated in Table 5.4. Fig. 5.4 shows the comparison between experimental data [Rae et al., 2007] and JC model for different strain rates at room temperature. Adequate predictions are obtained with the identified constants. The strain rate and the temperature sensitivity of the 450 G PEEK material are reported in Fig. 5.5 [Rae et al., 2007; El-Qoubba and Othman, 2014]. As ductile metals, PEEK 450G shows non-linear strain rate sensitivity and the stress increase is more important at high strain rates than low strain rates [El-Qoubba and Othman, 2014]. Although this non linear strain rate of the material cannot be completely defined using the JC model due to the analytical formulation, Eq. (5.3), a good agreement is obtained for the identified constants from quasi-static to dynamic loading. In the range of strain rates from $10^{-4}s^{-1}$ to $10\ s^{-4}$, the differences between experimental data and JC model are less than 10%. For high strain

rates, from 10 s^{-1} to 10^4 s^{-4}, the differences between experimental data and JC model are less 7%.

Table 5.4: Constants used to define the thermoviscoplastic behaviour of PEEK 450G at high strain rates in adiabatic conditions.

Elasticity		**Thermoviscoplastic Behaviour**					
E_0 (GPa)	ν (-)	A (MPa)	B (MPa)	n (-)	$\dot{\varepsilon}_0^{\,p}$ (s^{-1})	C (-)	m (-)
3.6	0.4	132	10	1.2	0.001	0.034	0.7
Other physical constants							
ρ (kg/m^3)		β (-)		C_p (J/kg K)		θ_m (K)	
1304		0.9		2180		614	

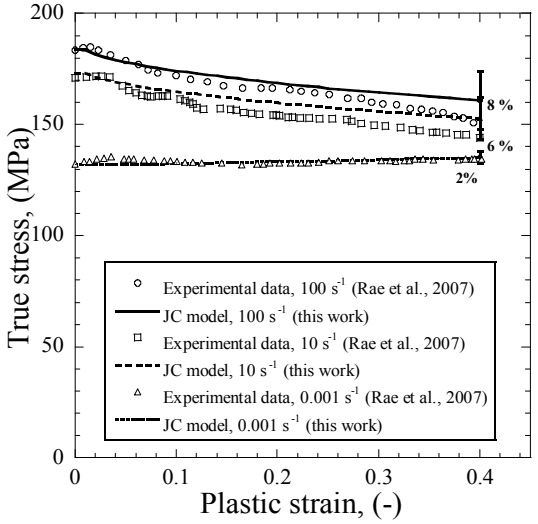

Figure 5.4: Comparison of stress-strain of PEEK 450G given by the experimental data [Rae et al., 2007] and JC model predictions at room temperature and different strain rates.

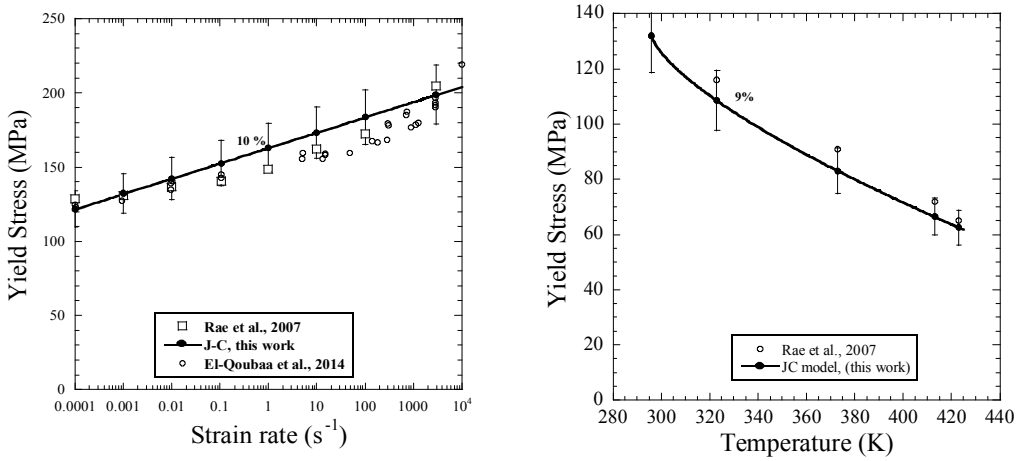

(a) (b)

Figure 5.5: Strain rate (a) and the temperature sensitivity (b) of PEEK 450G, experimental data [Rae et al., 2007; El-Qoouba and Othman, 2015] and JC model predictions.

5.1.4.3 Fracture model

To completely define the problem of impact perforation on PEEK plates, it is necessary to introduce a fracture model. Some results have been reported in the literature concerning failure strain of unfilled PEEK [Rae et al, 2007; Sobieraj et al., 2009] and other semi-crystalline polymers as UHMWPE [Mourad et al., 2003]. In these works, ductility of semi-crystalline polymers, associated to void coalescence due tensile states, have been reported as dependent on the initial stress triaxilitiy σ^* ($\sigma^* = \sigma_m/\bar{\sigma}$, where σ_m is the mean stress and $\bar{\sigma}$ is the equivalent stress) and strain rate $\dot{\bar{\varepsilon}}^p$. For PEEK 450G, Sobieraj et al. (2012) reported an average value of failure strain of 1.1 for unnotched specimen and stress triaxilitiy of 0.33. However, for high triaxility values, these authors found that there was a dramatic change in the fracture micromechanism of PEEK, and the deformation and fracture micromechanics changed drastically, from one of plastic deformation and void coalescence to one dominated by crazing and brittle fast fracture with a average value of failure strain of 0.05 for notched specimens. Mourad et al. (2003) reported that the ductility of semi-crystalline polymer UHMWPE is strongly dependent of strain rate of such a way that fracture strain reduces with strain rate. For PEEK 450G, Rae et al. (2007) found that strain failure dependent of strain rate and temperature, with a clear upward trend in strain to failure when the temperature was increased. The fracture model used in

this work has been proposed by Johnson and Cook (1985) to include strain hardening, strain rate and temperature dependencies. This model includes stress triaxiality. JC fracture model is frequently used in ductile metal alloys [Arias et al., 2008] and it was previously used for analyze the fracture behaviour of semi-crystalline polymer [Mourad et al., 2003]. Failure is assumed when a parameter D exceeds unity. The D parameter is summed over all increments of deformation. The evolution of D is the following:

$$D(\bar{\varepsilon}^p, \dot{\bar{\varepsilon}}^p, \theta) = \sum \frac{\Delta\bar{\varepsilon}^p}{\bar{\varepsilon}_f^p(\dot{\bar{\varepsilon}}^p, \theta, \sigma^*)} \tag{5.8}$$

where $\Delta\bar{\varepsilon}^p$ is an increment of accumulated equivalent plastic strain that occurs during an integration cycle, and $\bar{\varepsilon}_f^p$ is the critical failure strain level. This kind of fracture model is erosive in ABAQUS inducing an instantaneous element deletion when an imposed plastic strain level is reached. Thus, using this kind of criterion the mesh in the damaged part must be very fine to not affect the numerical results in terms of energy. The plastic failure strain $\bar{\varepsilon}_f^p$ is assumed to be dependent on a non-dimensional plastic strain rate $\dot{\bar{\varepsilon}}^p/\dot{\bar{\varepsilon}}_o^p$, a dimensionless pressure–deviatoric stress ratio σ^* and a non-dimensional temperature Θ as defined previously. The dependencies are assumed separable and take the following expression

$$\bar{\varepsilon}_f^p = [D_1 + D_2 \exp(D_3 \sigma^*)] \left[1 + D_4 \ln\left(\frac{\dot{\bar{\varepsilon}}^p}{\dot{\bar{\varepsilon}}_o^p}\right)\right] [1 + D_5 \Theta] \tag{5.9}$$

where D_i are failure constants. The constant D_1 implies a finite strain to fracture even at very high values of stress triaxiality [Mourat et al., 2003]. This value is assumed to be $D_1=0.05$, according an average failure strain of 0.05 for high triaxiality reported for PEEK 450G [Sobieraj et al., 2012]. The constant D_2 and D_3 are identified from experimental data [Sobieraj et al., 2012] of tensile tests of unnotched specimens of PEEK 450G at strain rate equal to 0.001 s^{-1} and room temperature. The value is close to $\bar{\varepsilon}_f^p \approx 1.1$ in these conditions. The constant D_4 and D_5 are identified from experimental data [Rae et al., 2007] of uniaxial tests of unnotched specimens of PEEK 450G at different strain rate and temperatures. According these experimental data D_4 defines the dependence on the strain rate as negative sensibility whereas D_5 defines the temperature as large positive sensibility, Fig. 5.6. The constants identified of fracture model of PEEK 450G are given in Table 5.5.

Table 5.5: Constants used to define fracture model of PEEK 450G.

Fracture criterion constants				
D_1	D_2	D_3	D_4	D_5
0.05	1.2	-0.254	-0.009	1.0

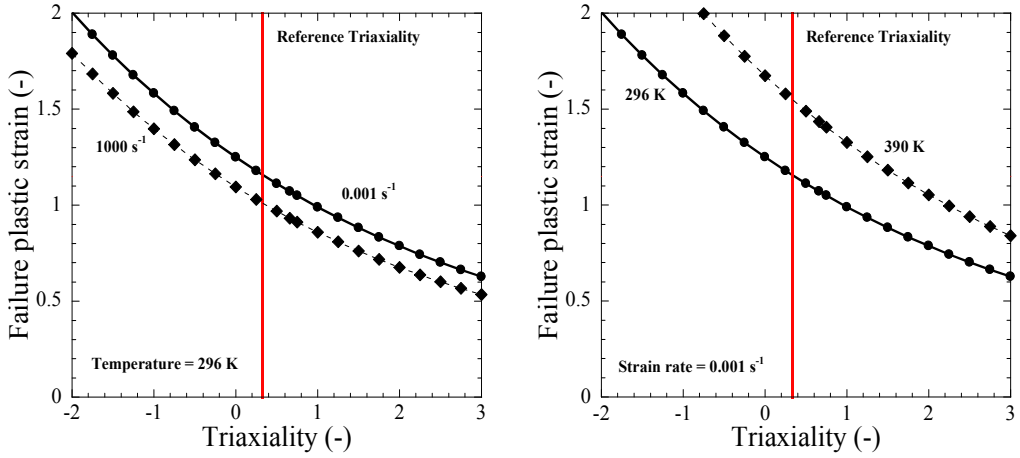

Figure 5.6: Strain Failure strain level (JC fracture model) depending on solicitation state at different strain rates (a) and at different temperatures (b).

5.1.5 Numerical simulations

A Lagrangian 3D finite element model for the simulation of the perforation process was developed in ABAQUS/Explicit (2014). The geometry of plates is equal to the active area of the experimental tests specimens (100x100 mm^2) with a value of thickness of 1 mm for Ti6Al4V and 3 mm for PEEK (Table 5.2). The fully 3D configuration allows the model to describe the radial cracking and the petalling failure mode that characterize the perforation of plates by spherical projectiles [Rusinek et al., 2009]. The target mesh developed is shown in Fig. 5.7, where twelve elements were placed across the thickness of the target. This is in agreement with the recommendations reported [ABAQUS/Explicit 2012], where it is suggested that at least four elements should be used through the thickness when modelling any structures carrying bending loads. The mesh presents radial symmetry to avoid appearance of spurious generation of cracks. The mesh is split into three different zones. The zone directly affected by the impact has been meshed with 32400 tri-linear elements with reduced integration (C3D8R in ABAQUS notation). In order to reduce the computational time, beyond the zone directly affected by the impact is

defined a transition zone using 48000 elements. After the transition zone, the mesh is defined using C3D8R elements until getting the perimeter of the target. This optimum configuration has been obtained from a convergence study using different mesh densities. Since the experimental observations revealed absence of erosion on the projectile-surface after the impact (the projectile was not deformed plastically in any test), the projectile has been defined as rigid body. It enables to reduce the computational time required for the simulations. A constant friction coefficient value μ = 0.2 has been used to define the contact projectile/plate [Borruto, 2010]. The potential dependence of the friction coefficient on the temperature and the sliding velocity is not taken into account. The constant value used for the friction coefficient is based on the assumption of a constant pressure along the projectile-plate contact zone. The authors confirmed this hypothesis by FE analysis of different projectile-target configurations [Rusinek et al., 2009]. The impact velocities covered with the numerical simulations are those covered during the normal impact experiments.

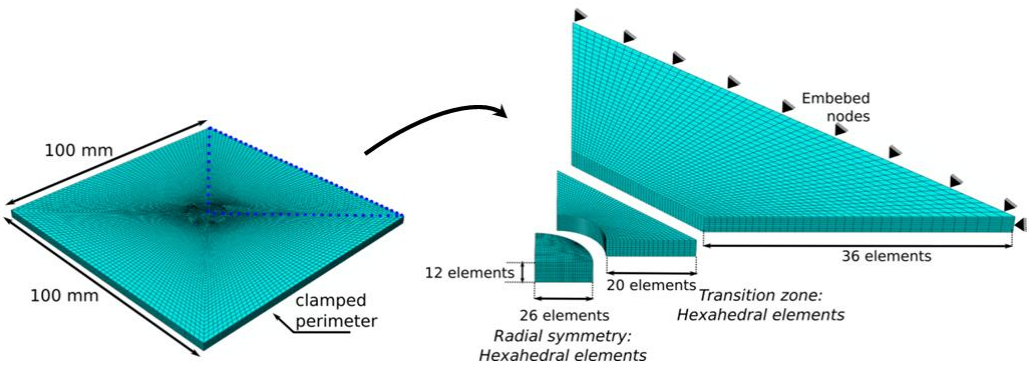

Figure 5.7: Strain Numerical configuration used in the simulations.

5.1.6 Discussion

5.1.6.1 Energy absorption and residual velocity

Firstly, the experimental results of impact velocities are analysed. Fig. 5.8a shows the residual velocity versus impact velocity (V_r-V_o) curves obtained for both materials tested, PEEK 450G and Ti6Al4V. The ballistic limit V_{bl} is the maximum value of the initial impact velocity V_o which induces a residual velocity V_r equal to zero. The ballistic limit of PEEK 450G, $V_{bl}^{PEEK} \approx 265\, m/s$ was found greater than that corresponding to the

Ti6Al4V plates, $V_{bl}^{Ti6Al4V} \approx 232\, m/s$. The results shown in Fig. 5.8 have fitted via the expression proposed by Recht and Ipson (1963)

$$V_r = \left(V_o^k - V_{bl}^k\right)^{1/k} \tag{5.10}$$

where k is a fitting parameter. The values of k determined are k=1.9 for PEEK 450G and k=2 for Ti6Al4V. The residual velocity of PEEK 450G plates within of the range of impact velocities tested is lower than Ti6Al4V. It was noted that the flow stress of Ti6Al4V is ten times higher than the flow stress of PEEK 450G in quasi-static conditions, [Khan et al., 2004; Rae et al., 2007] and seven times in dynamic conditions, 10^3 s^{-1}-10^4 s^{-1}, [Rae et al., 2007; Qoubaa and Othman, 2014]. This suggests that the energy absorption mechanics shown by both materials investigated are largely different to each other. Thanks to the measurements described previously, it is possible to estimate the energy absorption W, Eq. (5.11), of PEEK 450G material under dynamic impact and the minimum energy to perforation, $W_{perforation}$, Eq. (5.12)

$$\mathrm{W} = \frac{1}{2}\mathrm{m_p}(\mathrm{V_o^2} - \mathrm{V_r^2}) \tag{5.11}$$

$$\mathrm{W_{perforation}} = \frac{1}{2}\mathrm{m_p}\mathrm{V_{bl}^2} \tag{5.12}$$

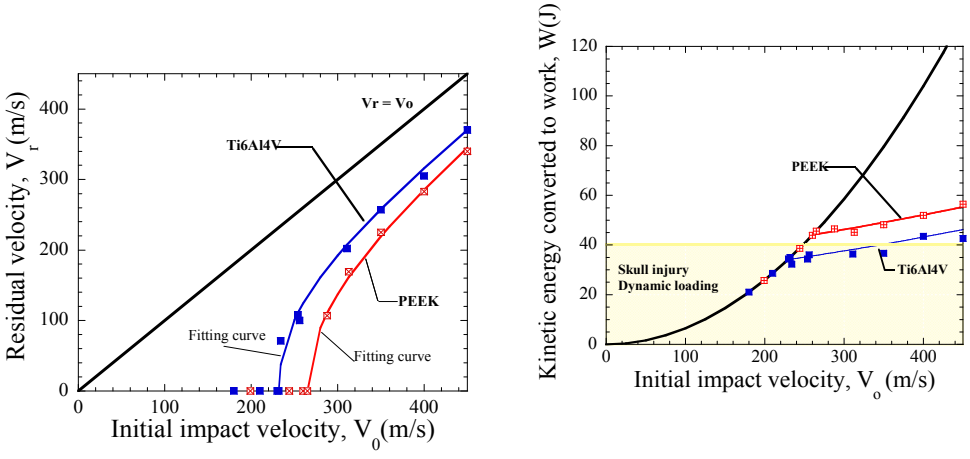

Figure 5.8: a) Residual velocity V_r versus impact velocity V_o, comparison between PEEK 450G and Ti6Al4V ; b) Energy absorbed the plate W versus impact velocity V_o, comparison between PEEK 450G and Ti6Al4V.

Fig. 5.8b shows the kinetic energy of the projectile converted into energy absorption W of plate. For both materials W increases with initial velocity. This tendency is in agreement with experimental results published in the literature for spherical noses of projectile [Arias et al., 2008]. Comparing the values obtained, it is observed that PEEK material can absorb enough energy to avoid skull injury not depending on the impact velocity used, Fig. 5.8b. The reference used for comparison is the maximum skull fracture energy reported by Monea et al. (2014), $E_{skull}^{fracture} = 40.5\,J$. The values of perforation energy are respectively $W_{perforation}^{PEEK} = 45.6\,J$ and $W_{perforation}^{Ti6Al4V} = 35\,J$. Moreover, in all range of impact velocities, PEEK material is more efficient for energy absorption in comparison with titanium alloy with a medium ratio of R=1.26. One of the reasons for the good capability to absorb energy is the adiabatic deformation of PEEK at high strain rates with large strain values (ε>1.0) in compressive states characteristics of impact process, as reported Rae et al. (2007) for Taylor impact tests.

5.1.6.2 Failure mode

5.1.6.2.1 Ductile behaviour of PEEK

Figs. 5.9 and 5.10 illustrate the final stage of the impact process for different initial velocities and both materials tested. The failure mode of PEEK plates is clearly different from that observed in titanium alloy. The shear failure of Ti6Al4V plates is characterized by small energy consumption. Namely, the energy required for perforation is that required for the onset of the shear band, plug ejection and cracks propagation, Fig. 5.10. The length of cracks is larger at velocities below the ballistic limit, and the crack propagation path is transverse to the rolling direction [Nasiri-Aborbekoh et al., 2012], Fig. 5.10. Once the instability is formed, very low energy consumption is needed to perforate the plate. However, at all impact energies, ductile process of PEEK plates was noted and no evidence of brittle failure was observed, Fig. 5.9 and Fig. 5.11. Moreover, multi-hit capability [Bless and Junick, 1998] for impact absorption energy of PEEK material has been demonstrated due to localized ductile damage, Fig. 5.11b. Based on the ballistic tests, it is observed a ductile failure mode without plug ejection as frequently observed for metal materials using a spherical or hemispherical projectile [Arias et al., 2008; Rusinek et al., 2009].

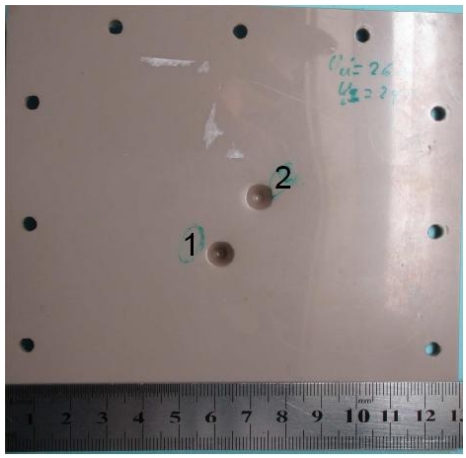

$V_0(1)=260$ m/s; $V_0(2)=244$ m/s; $V_r=0$; front

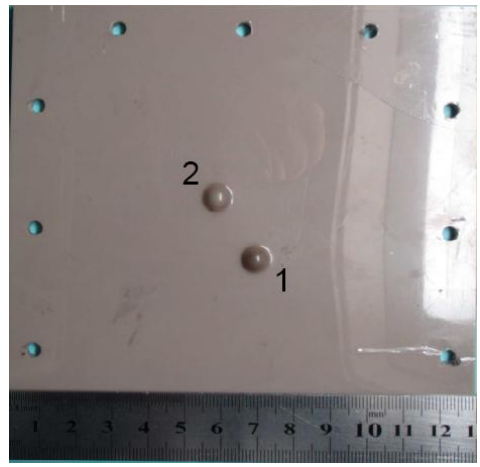

$V_0(1)=260$ m/s; $V_0(2)=244$ m/s; $V_r=0$; back

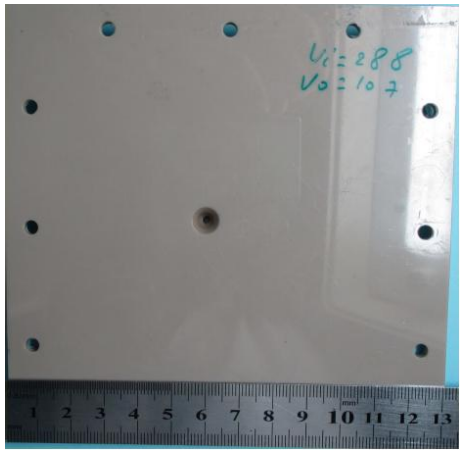

$V_0=288$ m/s: $V_r=107$: front

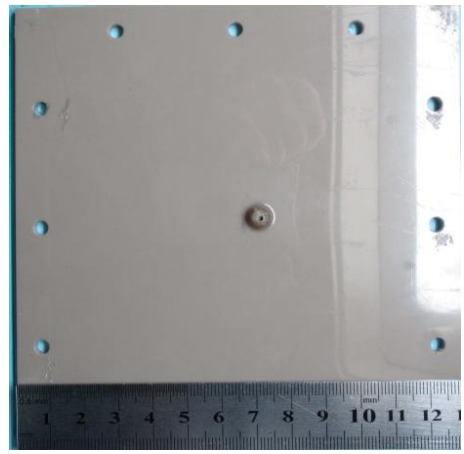

$V_0=288$ m/s: $V_r=107$: back

Figure 5.9: Final stage of the perforation process of PEEK for different impact velocities (front and back of plates).

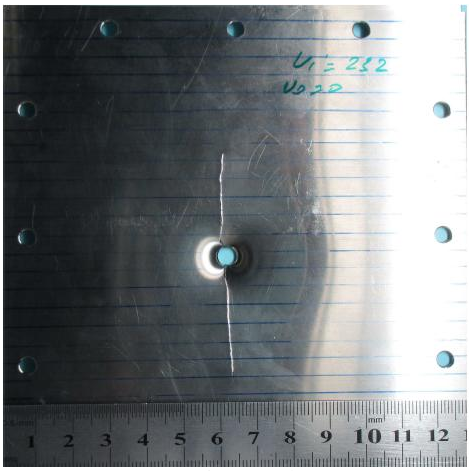

V_0=232 m/s; V_r=0; front

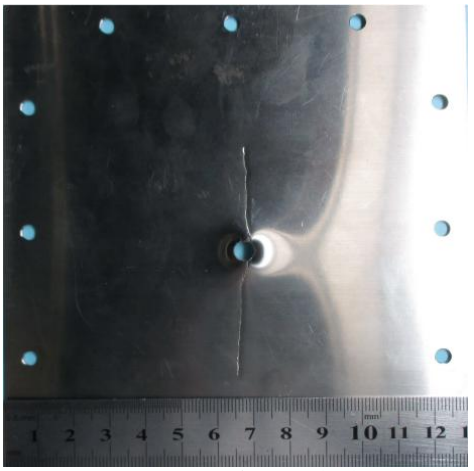

V_0=232 m/s; V_r=0; back

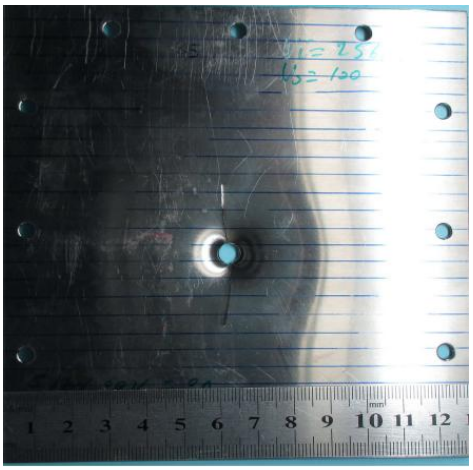

V_0=256 m/s; V_r=100; front

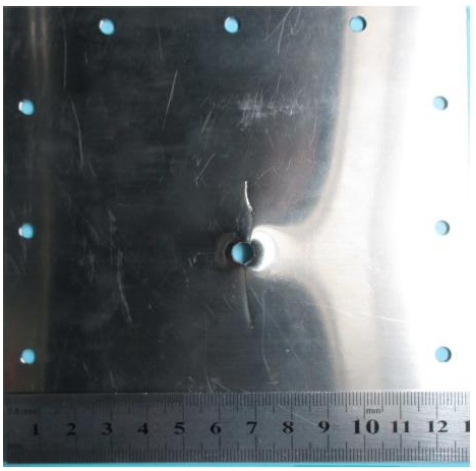

V_0=256 m/s; V_r=100; back

Figure 5.10: Final stage of the perforation process of Ti6Al4V for different impact velocities (front and back of plates).

(a) (b)

Figure 5.11: Final stage of the impact process of PEEK at impact velocity below ballistic limit: a) V_0=200 m/s; b) Two different impact at V_0=260m/s and V_0=244m/s.

Comparing PEEK with metals, it is observed a hole enlargement when the projectile is passing through the plate followed by an enclosing hole stage, Fig. 5.12. It is also observed a local deflection without real bending of the whole plate comparing to metal. The plastic deformation is confined close to the impact zone. Moreover, using SEM photo, it is possible to note a ductile failure mode and large plastic deformation lines, Fig. 5.13. The same failure mode has been observed no matter the initial impact velocity V_0 used. This observation agrees with the results provided by Rae et al. (2007) using Taylor's test at high impact velocity.

Figure 5.12: Final stage of PEEK at impact velocity above ballistic limit: V_0=288 m/s (V_r=107 m/s).

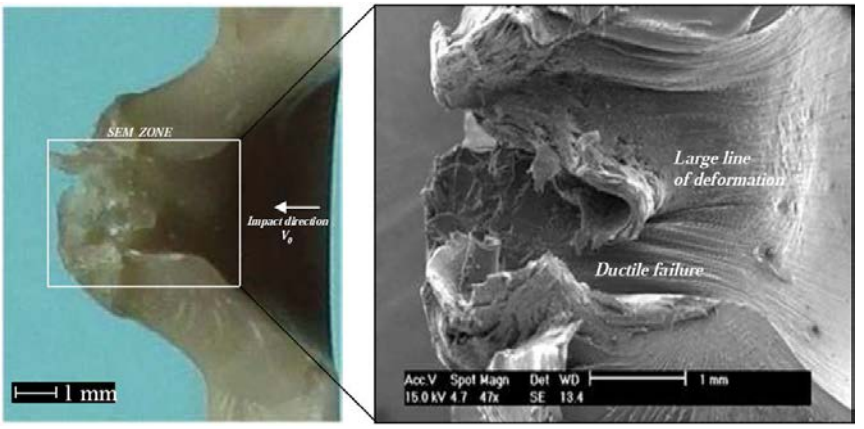

Figure 5.13: Cross section of final stage of PEEK at impact velocity V_0=288 m/s (V_r=107 m/s).

5.1.6.2.2 Darkening at large strain

At all velocities, darkening is noticed in the highly deformed regions associated to local damage in plates. Fig. 5.14 clearly shows the concave rod end and the discolouration associated with the large-strain regions. A number of authors have focused on identifying whether the colour change of PEEK was a result of the strain rate or large strain. Fig. 5.14 shows the cross-sections of virgin and three large-strain samples impacted at different velocities below ballistic limit and photographed under identical conditions. The more impact energy, the larger the strain and darker the damage area. From the associated colour changes it is therefore clear that the colour change is associated with large-strain compression, not strain rate. PEEK in tension undergoes stress whitening in common with many other polymers.

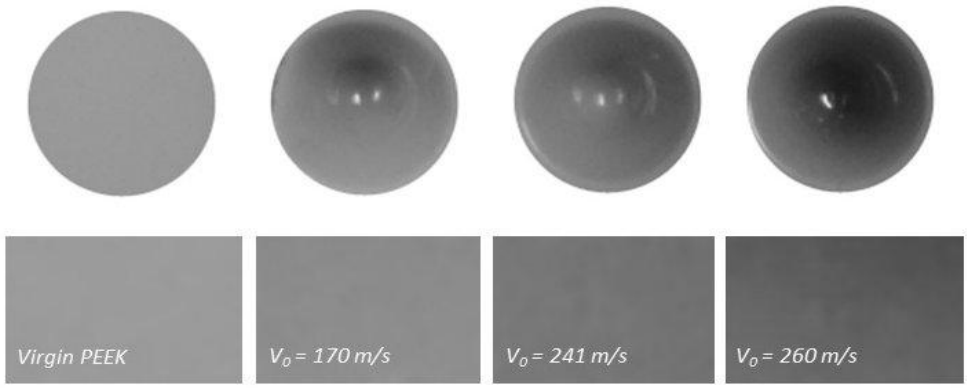

Figure 5.14: Polished sections of four PEEK samples photographed under identical conditions to show the colour change associated with large-strain deformation. The grayscale value, in the range from 0 to 255 where 255 is black, 93 is for virgin PEEK, 114 for V_0=170m/s, 141 for V_0=241m/s and 156 for V_0=260 m/s.

5.1.6.3 Crystallinity at high strain rate and large strain

The percentage of crystallinity is responsible of the material fragility. To change the microstructure from amorphous to crystalline, the material needs additional energy coming mainly derived from temperature increase $\Delta\theta$. For this reason, it is interesting to analyze the behaviour of PEEK polymer at high velocity impact V_0 to check if a brittle transition is observed since for high velocity, the initial temperature θ_o shows a strong increase. Differential scanning calorimetry (DSC) experiments were carried out in a Perkin Elmer Diamond calorimeter with nitrogen as purge gas. PEEK samples of highly deformed regions corresponding to different impact energies of tests have been analysed. Samples with a mass of ≈10 mg were sealed in a 50 ml aluminium pan, and an empty pan was used as reference. They were heated from 293 K to 433 K at a heating rate of 10 K/min and then cooled at the same rate. Enthalpies of melting were determined with a average value of $\Delta H_f \approx 39\, Jg^{-1}$. The crystallinity of all samples deformed to large strains was found similar and equal to 30%. There is a point of contention in this regard about the relationship between high strain rate, large strain and crystallinity. While some authors, Hamdan and Swallowe (1996) reported an increase in crystallinity in dynamic conditions under high strain rates, $\dot{\varepsilon} \approx 10^3 s^{-1}$, others authors [Rae et al., 2007] reported decrease of crystallinity in dynamic conditions for samples deformed to large strains $\varepsilon > 0.1$. An explanation of this behaviour is not obvious. In the research reported here, no changes in degree of crystallinity in relation with virgin PEEK were measured. Below

glass transition temperature, crystallinity evolution can be considered as a competition between the stabilizing effect of strain rate on crystal structure [Swallone et al., 1997] and the probably destruction associated with large strain. In this regards, it has been reported that high compressive deformation can degrade the crystalline structure of polymer at temperatures $\theta < \theta_g$ [Sobieraj et al, 2005].

5.1.6.4 Numerical simulation

A good correlation was found between experimental and numerical results (less than 10%), which demonstrate that the models used in this study faithfully reproduce the impact behaviour of tested materials, PEEK 450G and Ti6Al4V, see Fig. 5.15. From numerical simulations, it has been computed the maximum temperature increase of PEEK on the contact zone specimen-ball. Therefore, an estimation of the temperature during the process of plastic deformation has been performed for a velocity corresponding near to the ballistic limit V_0=*265 m/s*, Fig. 5.16. An increase of the temperature is observed during perforation process. However, for high impact velocity the temperature seems to be lower. The reason is certainly due to bending effect which induces an increase of plastic work. For high impact velocity the failure appears quickly without bending effect and in this case the plastic work is lower. Generally, the tendency of the temperature is an increase with an average value corresponding to complete failure equal to $\Delta\theta \approx 100$ K. The maximum local temperature has been compared with the glass transition temperature and the melting temperature. It is observed that locally the temperature is lower than the glass transition temperature, Fig. 5.16. This numerical prediction is in agreement with experimental data, where it is observed that the material is still ductile for a temperature $\theta < \theta_g = 416$ K [Rae et al., 2007]. Indeed at high impact velocity, no brittle behaviour has been observed and PEEK material is capable to absorb more energy as velocity increases, Fig. 5.8b. Thus it is observed using these numerical simulations that the behaviour of the material must be well defined since it depends strongly on the temperature sensitivity and strain rate and amplified by large deformation. During this kind of application the strain level observed is higher to 1.

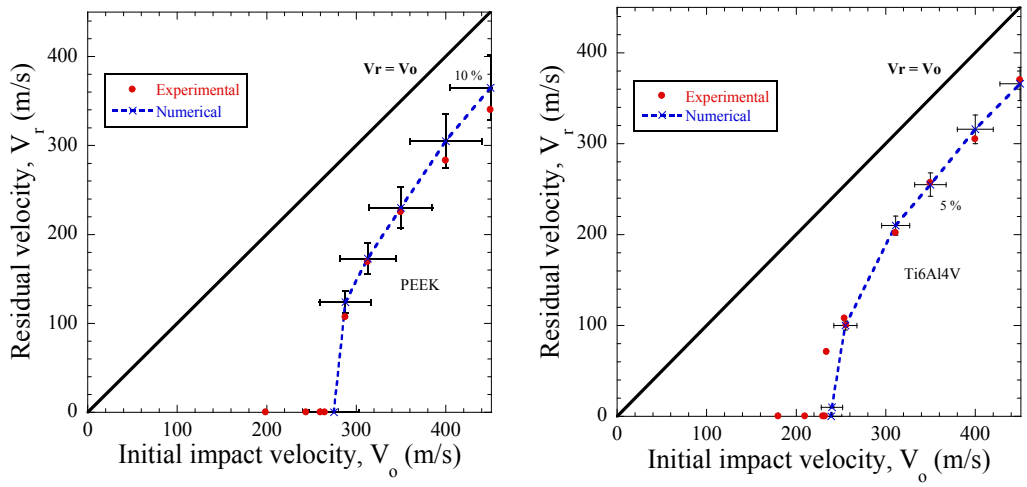

Figure 5.15: Experimental and numerical data of residual velocity versus impact velocity: a) PEEK 450G, b) Ti6Al4V.

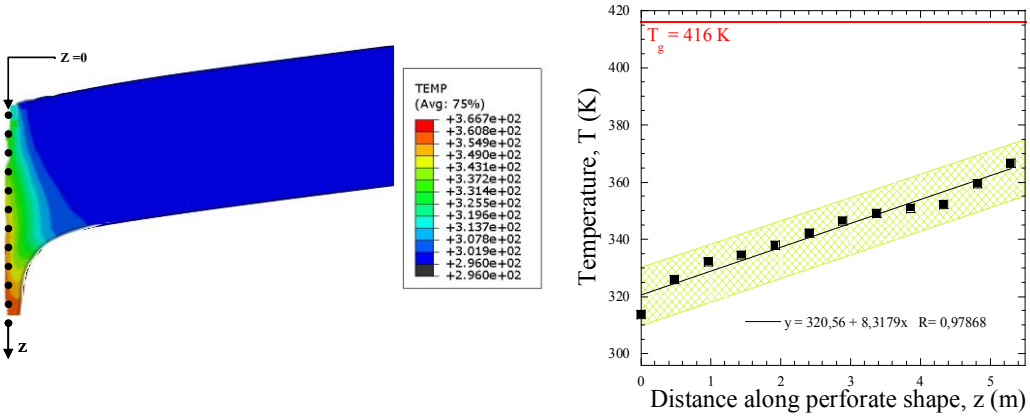

Figure 5.16: Numerical predictions of maximum temperature increase in PEEK for impact velocity, V_0=265m/s.

5.1.7 Conclusions

The impact behaviour of unfilled PEEK was examined through a combination of experiments and finite element simulations. In the full range of impact kinetic energies considered, from 21 J to 131 J, PEEK material is more efficient for energy absorption in comparison with titanium alloy. During experiments, the material was observed to behave in a ductile manner without evidence of brittle failure and darkening is noticed in highly deformed regions. Finite element simulations of experiments were performed using a plasticity model typically used for ductile metals. The simulation was in good agreement with the experimental data, confirming the predominantly ductile response of PEEK under high strain rate. From numerical simulations, it has been computed the maximum temperature increase in the perforation process. The numerical predictions of maximum local temperature are lower than the glass transition temperature of PEEK, in agreement with the ductile behaviour observed in impact tests. In conclusion, PEEK appears to be an attractive candidate as matrix material for impact applications, implants or to design passive security equipment such as helmets.

5.2 Mechanical characterization and impact behaviour of short carbon fibre reinforced PEEK composites

5.2.1 Introduction

There is an increasing interest and use of new biocompatible polymers in the biomedical industry. Biocompatible purely polymeric materials are showing better properties than metal to use them for prosthetics which are in direct skeletal contact. This is because they require a lower elastic modulus to be structurally compatible [Scholz et al., 2011]. However, purely polymeric materials can present low strength and high ductility. In order to accomplish both low elastic modulus as well as high strength in an efficient manner, polymers are reinforced with fibres [Scholz et al., 2011; Lovald et al., 2012]. The use of short fibre reinforcement reduces the fibre length reinforcing efficiency compared with long fibres, but offers economic and design advantages in biomedical applications with complex geometries, for example injection moulding of composite parts with complex shapes.

Short carbon fibre-reinforced PEEK (SCFR PEEK) composites have proven to be a versatile material for use in medical implants due to their suitability for modern imaging technologies, excellent mechanical properties and biocompatibility [Wang, 1979; Rivard et al., 2002; Green, 2012]. In addition, SCFR PEEK is a strong and durable composite in the extremely aggressive environment of the human body [Horak et al., 2010; Lovald et al., 2012]. This family of composites is of particular interest to those manufacturers who develop applications that interact with bone, such as spinal fusion cages and hip prostheses. These prosthetic implants are usually made from metallic alloys with stiffness 10-20 times higher than the adjacent cortical bone leading to problems of mechanical incompatibility [Green, 2012]. In contrast, the stiffness and strength of PEEK composites can be modified through short carbon fibre filling [Lovald et al., 2012] to match closely the values of bone and achieve optimum mechanical properties for prostheses devices (Fig. 5.17).

Although incorporating short carbon fibres in a PEEK thermoplastic matrix produces an improvement of its biomechanical properties, it can also cause a marked reduction in ductility and associated embrittlement of the material [Ramsteiner et al., 1979; Sarasua et al., 1995]. This deterioration in impact behaviour can limit the application of prosthetic devices. Bones and potential prosthetic devices provide structural support for the body and they must be able to absorb enough energy above its ultimate strength without showing fracture [Lovald et al., 2012]. Therefore, it is essential to study the effect of reduced ductility in order to determine the levels of energy absorption of prostheses, such

as cranial implants and hip systems [Kurz et al., 2012], in dynamic conditions. Investigation of mechanical impact behaviour of medical implants needs to include levels of dynamic loading commonly generated in a fall or accident.

Experimental observations of some authors have shown no significant influence on mechanical properties of short fibre reinforced thermoplastic composite under low strain rates demonstrating elasto-plastic behaviour [Kammount, 2011]. For high strain rates experimental stress-strain curves showed an elasto-viscoplastic behaviour although this dependence is neglectable for temperatures near to glass transition [Mouhmid, 2006; Kammount, 2011]. Moreover, especially in dynamic conditions, the mechanical response of such composite material is highly sensitive to the short fibre orientation. In this regard, injection moulding is the widely used process for the production of SCFR PEEK composites with complex shapes. The orientation of the fibres induces heterogeneity throughout the material, making the prediction of its behaviour and ruptures a challenging task. The impact behaviour of SCFR PEEK composites has not been deeply studied in terms of kinetic energy absorption and failure under impact loading, and perforation tests have not been reported in the scientific literature. In this section, a study in terms of energy absorbed has been experimentally developed in order to analyze the mechanical impact behaviour of SCFR PEEK composites and unfilled PEEK biomaterials which are frequently used for medical applications. The perforation experiment covered an impact kinetic energy range from 21 J to 131 J, equivalent to the range observed in a fall of a person. C-Scan and scanning electron microscope (SEM) inspection tests have been conducted to reach a better understanding of damage extension and failure mechanisms. Additionally, in order to predict the response of material a preliminary approach for modelling the behaviour of SCFR PEEK composites has been developed. The model includes homogenization of elastic material and anisotropic damage. A validation of the predictions against experimental data is conducted for SCFR PEEK composite.

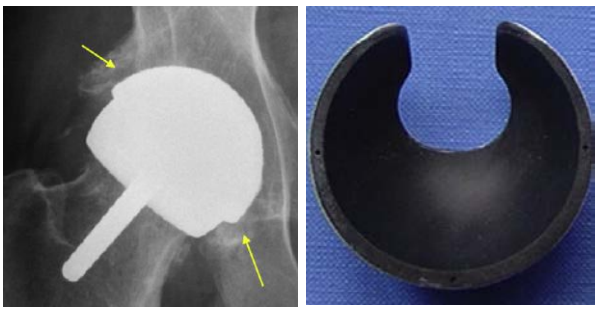

Figure 5.17: Fixation of acetabular prosthesis of CF30 short fibre PEEK [Kurz et al., 2012].

5.2.2 Mechanical characterization

Commercial plates of PEEK composites reinforced with PAN short carbon fibres 30 % in weight, named CF30 PEEK, and unfilled PEEK plates of general purpose grade were purchased measuring 130x130x3 mm^3. Both materials are produced with injection moulding technology. Carbon fibre is currently the most widely used fibrous reinforcing agent for PEEK based composites [Molazemhosseini et al., 2013] due to the strong interfacial interaction between short carbon fibres and PEEK matrix. The interfacial strength between short carbon fibres and PEEK polymer is higher than other known combinations of fibres and thermoplastic matrices [Ramsteiner et al., 1979; Green et al., 2012; Chukov et al., 2015], and on average, at least an order of magnitude stronger than that between carbon fibres and ultra-high-molecular-weight polyethylene (UHMWPE) polymers [Kammoun et al., 2011; Chukov et al., 2015]. This supports the use of PEEK in preference to UHMWPE in combination with carbon fibres for applications such as bearing medical surfaces. For CF30 PEEK, the diameter and length of PAN carbon fibre were 7 μm and 200 μm respectively. The percentage of 30% carbon fibre in weight (23.5% in volume) of CF30 PEEK provides optimum rigidity and load bearing capability. Due to its biocompatibility and high strength, CF30 PEEK has been successfully used in humeral plates, cranial implants and composite acetabular inserts in hip replacement procedures [Wang, 1999, Lovald, 2012; Steinberg et al., 2013]. The mechanical properties of PEEK and CF30 PEEK composite are shown in Table 5.8 [Larpeek, 2015]. Addition of short fibre into PEEK matrix increases the low elastic modulus from 3.6 GPa for neat PEEK to 24 GPa for SCFR PEEK and it doubles the failure strength value. Failure strength is here referred to ultimate tensile strength or yield stress, according to which was reached first in tensile testing [Ramsteiner, 1979].

Table 5.8: Mechanical Properties of PEEK and CF30 PEEK Composite [LarPEEK, 2015].

Material property	SCFR PEEK Composite (CF30)	Unfilled PEEK
Elastic Modulus (GPa)	24	3.6
Poisson's ratio	0.385	0.38
Density (kg/m^3)	1400	1300
Yield stress (MPa)	-	107
Tensile strength (MPa)	214	95
Elongation at break (%)	2.0	40.0
Charpy impact strength (kJ/m^2)	6.50	7.0
Glass transition temperature (K)	416	416
Melt transition temperature (K)	610	616

One inherent problem in processing short fibre reinforced thermoplastics (SFRTPs) by flow moulding techniques is that the fibres will tend to become aligned during the flow process, inducing anisotropic material properties. To investigate the effect of orientation on the mechanical behaviour, tensile and compressive tests of injection moulded specimens were conducted using a servo-hydraulic testing machine INSTROM 8516 under displacement control at 1 $mm \cdot min^{-1}$. Tensile and compressive samples were machined on the ASTM D-638 recommendations, Fig. 5.18a, and ASTM D-695, Fig. 5.18b. An INSTROM 2620 extensometer and HBM strain gages were used to increase the accuracy of the strain data. Young's modulus and failure strain and their respective strains were determined as the mean value of at least eight specimens and results are shown in Table 5.9. Fig. 5.19 shows stress-strain curves of CF30 PEEK composite, in agreement with data of the works published by Sarasua et al. (1995) and Lee et al. (1996). Fig. 5.20 shows the stress-strain curves of tensile and compression tests for CF30 PEEK composite in both IFD longitudinal and transverse directions. These experimental results show that tensile strength, compressive strength and failure of CF30 PEEK composite is dependent on material direction. Longitudinal values are higher for both tensile strength and compressive strength. Short fibres are mainly aligned in the injection flow direction (IFD), providing higher longitudinally than in the transverse direction. In addition, the results showed an enhanced behaviour under compressive loading than tensile loading (Table 5.9). Specimens machined in the flow direction showed tensile and compressive strength approximately 40% lower than specimens machined transverse to the flow direction. It was observed no significant influence of strain rate on stress-strain curves in the range from 10^{-4} s^{-1} to 10^{-1} s^{-1}, in agreement with the work of Kammount et al. (2011).

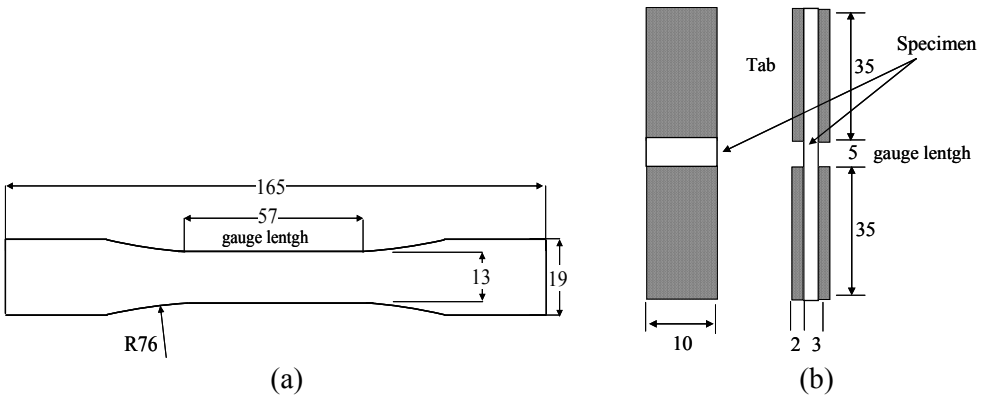

Figure 5.18: Geometry of specimen for tensile test ASTM D-638 and compression test ASTM D-695 (dimensions in mm).

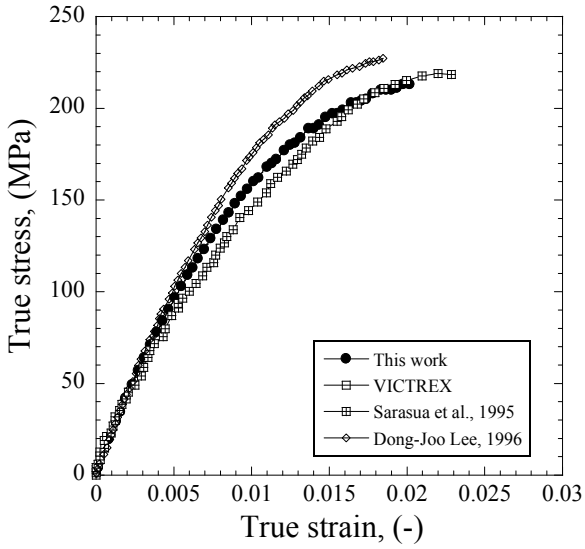

Figure 5.19: Comparison of stress-strain of CF 30 PEEK composite given by experimental data of this work and experimental data of works of Sarasua et al. (1995) and Lee et al. (1996).

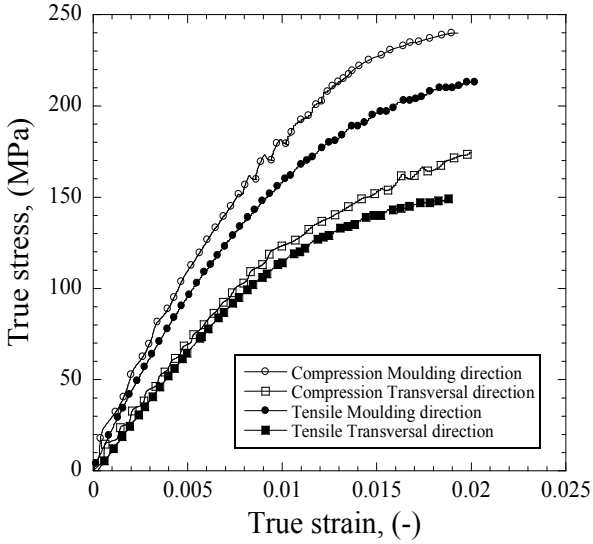

Figure 5.20: Mechanical behaviour of CF 30 PEEK composite under compression and tension for specimen machined in the IFD longitudinal direction and transverse direction.

Table 5.9: Mechanical properties of SCFR PEEK in both IFD longitudinal and transversal material directions.

Mechanical properties	SCFR PEEK composite (CF30), this work		SCFR PEEK composite (CF30) [Lee, 1996]
	Transversal	Longitudinal	Longitudinal
Tensile strength (MPa)	148	214	220.8
Compressive strength (MPa)	174	239	246.2
Tensile elastic modulus (GPa)	12.6	24	23.2
Compressive elastic modulus(GPa)	15	44	43.5
Poisson's ratio (-)	0.38	0.38	0.38
Elongation at break (%)	1.9	2.0	1.8

5.2.2.1 Crystallinity

Mechanical properties of PEEK materials are influenced by the degree of crystallinity. Several authors have shown that increasing the degree of crystallinity can increase elastic modulus and yield strength while decreasing fracture toughness [Rae et al., 2007; El-Qoouba, 2015]. From differential scanning calorimetry (DSC) a degree of crystallinity of 30±2% was calculated for PEEK and 32±2% for CF30 PEEK integrating the melt endotherm [Jonas et al., 1991; Sarausa et al., 1995]. The results of DSC testing did not show significant differences in the ability of matrix to crystallize between unreinforced PEEK and CF30 PEEK. This finding is in agreement with data reported by Sarasua and Remiro (1995).

5.2.2.2 Strain rate and temperature sensitivity

The effect of strain rate and temperature on mechanical behaviour of short fibre thermoplastic composites has been reported in the literature [Karger and Friedrich, 1986; Wang et al., 2002; Zhen et al., 2002; Sobieraj et al., 2012]. Wang et al. (2002) showed that short fibre thermoplastic composite is a strain rate and temperature dependent material. Both the elastic modulus and tensile strength of the composite increased with strain rate and decreased with temperature. However, for temperatures near to glass transition the stress-strain curves of composites are not sensitive to strain rates with less than 2% change in elastic modulus and less than 10% change in tensile strength. The value of impact fracture toughness of short fibre reinforced PEEK is similar to unfilled PEEK at room temperature and quasi-static conditions [Karger and Friedcrich, 1986; Sobieraj et al., 2012]. Toughness of short fibre reinforced PEEK and unfilled PEEK

decreases with strain rate but this effect is inverted if high temperatures near glass transition are reached due to adiabatic effects associated with the impact process.

5.2.3 Experimental impact tests

5.2.3.1 Hip and skull fracture energies

Hip fractures, the leading morbidity resulting from falls, constitute a major and growing socioeconomic problem in health care [Borruto, 2010; Colón-Emeric, 2015]. Since PEEK composites studied in this work are employed for hip replacements [Wang et al., 1998; Kurtz et al., 2012], the impact energy generated in a fall has been used as the reference level. Estimating the available energy W_{hip} just before impact by kinetic energy E_k, it is possible to approximate the impact energy involved in a fall affecting the hip. The average value for vertical hip impact velocity has been determined as 2.75 m/s [Kroonenberg et al., 1996]. For a person of 66 kg, taking the effective mass corresponding to the hip zone as one sixth of the total body weight (overestimated), the maximum impact energy affecting the hip corresponding to an accidental fall is equal to $W_{hip}^{fracture} = 42\,J$. Head protection measures and proposed skull fracture criteria typically include the energy absorbed up to the point of skull fracture [Asgharpur, 2013; Monea, 2014]. This reference skull fracture energy ranges from 21.1 J to 40.5 J. Therefore, in this study, the kinetic energy range has been $21.0\ J \leq E_K \leq 131.0\ J$ including the range of hip and skull fracture impact energy and incorporating a higher upper limit. For this proposal, perforation tests using rigid spheres were conducted on plates of CF30 PEEK and unfilled PEEK.

5.2.3.2 Experimental setup

The set-up used was the gas gun employed in *Section 5.1*, which is capable of shooting a rigid spherical projectile with a mass of $m_p = 1.3\ g$ and a diameter of $\phi_p = 6.82\ mm$. The initial impact velocity V_0 was in a range of $170\ m/s \leq V_0 \leq 450\ m/s$. Plates of CF30 PEEK and unfilled PEEK were tested. Plates of Ti6Al7Nb and Ti6Al4V titanium alloys were also studied to allow comparison between the PEEK composites and alloys used in biomedical applications. The thickness of each plate was selected to obtain comparable areal density [Arias et al., 2003], a parameter frequently used to optimize impact protection (Table 5.10). The thickness of both titanium alloys was set at $t=1\ mm$ providing a representative comparison. Due to the boundary conditions used to avoid sliding and to ensure correct clamping of the specimen, the size of the active part of all the plates were reduced to 100x100 mm^2, Fig. 5.3.

Table 5.10: Biomaterials considered for impact testing.

Material	Dimensions (mm^3)	Mass (g)	Areal density (kg/m^2)
CF30 PEEK Composite	130x130x3	70.2	4.1
Unfilled PEEK	130x130x3	65.5	3.9
Ti6Al4V	130x130x1	78.5	4.6
Ti6Al7Nb	130x130x1	79.4	4.7

5.2.4 Preliminary modelling

Accurate description of the SCFR-PEEK mechanical impact behaviour needs to take into account the preferential alignment of fibres in the injection moulding direction, IFD [Sarasua et al., 1995; Kammoun et al., 2015]. The results of experimental testing in this study (Fig. 5.20), consistent with other studies [Ramsteiner and Theysohn, 1979; Sarasua et al., 1995], have demonstrated that fibre alignment affects the mechanical properties of SCFR-PEEK. Model parameters were identified based on the experimental results of compressive tests and assuming brittle linear elastic behaviour in compression [Dano et al., 2002; Zhu et al., 2003; Dano et al., 2006].

5.2.4.1 Linear elastic behaviour

The mechanical response of the material to stress state is the result of both the matrix and the fibres contributions to that response. The constitutive modelling of thermoplastics reinforced with short carbon fibres has been widely investigated and constitutive models relying on two main approaches have been developed. The first approach is based on the consideration of an assembly of the damageable elastoplastic matrix material and one-dimensional linear elastic fibre media. These models treat separately the matrix response and the fibres response following any variation of the composite materials mixture rule [Tsukamoto, 2010; Notta-Cuvier et al., 2014; Notta-Cuvier et al., 2015]. The second approach is based on the homogenization of the elastic composite behaviour by defining a homogenized stiffness tensor from the matrix and the reinforcement fibres [Kammoun et al., 2011; Müller et al., 2015]. Amongst those using models based on homogenization, some authors assume linear elastic behaviour [Müller et al., 2015], while others include rate-dependency in the elastic behaviour [Kammoun et al., 2011]. The preliminary model described in this section follows a simple homogenization scheme based on the Voigt mixing rule algorithm. In order to get a more clear understanding of the formulation proposed in this model, all the tensor components are written in bold style and scalar

components in normal style. This model assumes uniform strain in the two phases and defines the homogenized stiffness tensor as:

$$\mathbf{C_{comp}}=[(1-\phi_m)\cdot\mathbf{C_f}+\phi_m\ \mathbf{C_m}] \tag{5.13}$$

where ϕ_m is the matrix material in concentration and $\boldsymbol{C_f}$ and $\boldsymbol{C_m}$ are the fibre stiffness tensor and the matrix stiffness tensor respectively. Thus, the homogenized stress $\boldsymbol{\sigma_{comp}}$ can be written as:

$$\boldsymbol{\sigma_{comp}} = \mathbf{C_{comp}}\cdot\ \boldsymbol{\varepsilon_{comp}} \tag{5.14}$$

where $\boldsymbol{\varepsilon_{comp}}$ is the homogenized strain, the macro strain. In this way, the SCFR-PEEK behaviour has been defined as a linear anisotropic elastic material, with a mechanical response that is completely determined by the homogenized stiffness tensor depending on the following elastic parameters: Young's modulus in direction of IFD, $E_{longitudinal} = 44\ GPa$; Young's modulus in transverse direction to the IFD, $E_{transverse} = 24\ GPa$; longitudinal shear modulus $G_{12} = 5.7\ GPa$; and Poisson's coefficient $\nu_{12} = 0.385$. The transverse shear modulus G_{23} and G_{13} have been obtained from the theory of Hill and Hashin [Hashin, 1962; Hill, 1964]. These elastic parameters are all in agreement with the Halpin-Tsai equations [Tucker, 1999] and the experimental data reported by Lee et al. (1996).

5.2.4.2 Damage initiation criterion

Due to good adhesion between short carbon fibres and matrix, the failure of PEEK composite is reported as cohesive [Sarasua, 1995; Lovald et al., 2012; Chukov et al., 2015]. This failure is also dependent on material direction, with both tensile and compressive strength varying with direction. Short fibres are mainly aligned along the injection moulding direction, IFD. This provides higher strength in IFD direction than in the transverse direction under usual loading conditions. As outlined in *Section 5.2.2*, results show an enhanced mechanical behaviour under compressive loading than under tensile loading. With regard to strength, longitudinal values are higher than transverse values both in tension and compression.

Based on these observations, the failure was defined as a Tsai-Hill failure criterion in order to determine damage initiation. Some authors have employed this failure criterion to define the material behaviour of short-fibre reinforced thermoplastics produced by injection moulding [Kammoun et al., 2011; Kulkarni et al., 2012]. Kammoun et al.

(2011), in determining Tsai-Hill criterion, assumed plane stress conditions in laminated composites with aligned, continuous fibres inside individual thin plies. This has been shown to be a valid assumption as injection moulded sheets show quasi in-plane orientation distribution of the fibres. However, these authors have suggested, due to the limitations of this assumption, the selected failure criteria would only reveal approximate trends and they recommend the development of more appropriate 3D failure criterion. Following their recommendations, a Tsai-Hill failure criterion has been programmed in a VUMAT subroutine in order to establish a damage initiation criterion considering the 3D formulation, Eq. (5.15).

$$\frac{\sigma_{11}^2}{X^2}+\frac{\sigma_{22}^2}{Y^2}+\frac{\sigma_{33}^2}{Z^2}-\left(\frac{1}{X^2}+\frac{1}{Y^2}+\frac{1}{Z^2}\right)\sigma_{11}\,\sigma_{22}-\left(\frac{1}{X^2}+\frac{1}{Y^2}+\frac{1}{Z^2}\right)\sigma_{11}\,\sigma_{33}-\left(\frac{1}{X^2}+\frac{1}{Y^2}+\frac{1}{Z^2}\right)\sigma_{22}\,\sigma_{33}+\frac{\tau_{12}^2}{S_{12}^2}+\frac{\tau_{13}^2}{S_{13}^2}+\frac{\tau_{23}^2}{S_{23}^2}=1 \quad (5.15)$$

where the normal strengths in the IFD in traction and compression were defined as X_t=*214 MPa* and X_c=*239 MPa*; the normal strengths in the transverse direction to the IFD (*Y* and Z) in traction and compression were defined as $Y_t=Z_t$=*214 MPa* and $Y_c= Z_c$=*239 MPa*; and the shear strengths were defined as S_{ij}=*109.9 MPa*. These data is in agreement with the experimental observations of the anisotropic behaviour presented by the elastic composite material considered in this study.

5.2.4.3 Damage evolution

In order to define the material behaviour once the damage has been initiated, a damage evolution model has been defined to describe the degradation rate of the material strength after the initiation criterion is satisfied. The stress-strain curve exhibits a linear elastic stage until the load increases to the critical value at *Point 1*, see Fig. 5.21. This point is reached when the damage initiation criteria, in our case Tsai-Hill criterion, is satisfied. Following the scheme shown in Fig. 5.21, degeneration of the load carrying capacity after damage initiation occurs from Point 1 to Point 2. The value of the damage parameter D goes from 0 (indicating there is no damage, at Point 1) to 1 (indicating a complete failure of the material, reached in Point 2). This parameter is used in combination with the stiffness coefficients to calculate the stiffness coefficient in damage evolution, defined as:

$$\mathbf{K} = (1 - D)\,\mathbf{K_o} \quad (5.16)$$

where $\boldsymbol{K_o}$ is the stiffness coefficient of intact material.

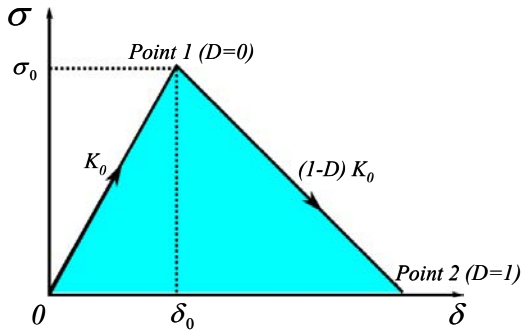

Figure 5.21: Scheme of constitutive model implemented.

In this section, a dependency has been observed between the degradation of the material and the increase in strain once the failure starts. Base on this observation, the damage parameter D has been defined as

$$D(\bar{\varepsilon}) = \sum \Delta\bar{\varepsilon}\,\psi \tag{5.17}$$

where $\Delta\bar{\varepsilon}$ is the strain increment in each time increment and ψ is a material constant controlling the material degradation due to the total strain accumulated once the damage initiation criterion is satisfied. To avoid sudden changes in the stiffness of the finite elements when damage occurs leading to instability problems and lack of convergence during the simulation, the stress components were corrected using a smooth transition, Eq. (5.18).

$$\sigma_{ij}^{*} = \sigma_{ij}\left[1 - \frac{2-e^{s\left(D_i-\frac{1}{2}\right)}}{2-e^{\frac{s}{2}}}\right] \tag{5.18}$$

where σ_{ij}^{*} and σ_{ij} are the stress before and after the correction, D_i is the corresponding damage parameter, and s is the variable which controls the slope of the stress decay when the damage is close to 1. According to recommendations a value $s=30$ was adopted [Rubio-López et al., 2014].

5.2.5 Numerical simulations

A Lagrangian 3D finite element model for the simulation of the perforation process was developed in ABAQUS/Explicit. The geometry of plates is equal to the active area of the experimental tests specimens (100x100 mm^2) with a value of thickness that varies depending on the material defined according to Table 5.10. The target mesh and nodes distribution is shown in Fig. 5.7.

5.2.6 Discussion

5.2.6.1 Energy absorption of SCFR PEEK composite

Firstly, the experimental results of impact velocities are analyzed. Fig. 5.22a shows the residual velocity versus impact velocity (V_r-V_0) curves obtained for both materials tested, SCFR PEEK composite and unfilled PEEK. Fig. 5.22a also shows the experimental results for results for titanium alloys TI6Al4V and Ti6Al7Nb, materials commonly used in biomedical applications. The ballistic limit of PEEK unfilled, $V_{bl}^{PEEK} \approx 265\ m/s$, was found to be greater than that corresponding to the SCFR-PEEK, $V_{bl}^{SCFR-PEEK} \approx 177\ m/s$, and also greater than the ballistic limit of both titanium alloys considered, $V_{bl}^{Ti6Al4V} \approx 232\ m/s$ and $V_{bl}^{Ti6Al7Nb} \approx 237\ m/s$. The results shown in Fig. 8a have fitted via the expression proposed by Recht and Ipson, Eq. (5.22a).

The values of k determined are k=1.8 for SCFR-PEEK composite, k=1.9 for unfilled PEEK, k=2 for Ti6Al4V and k=1.8 for Ti6Al7Nb. The residual velocity of PEEK unfilled plates within the range of impact velocities tested is lower than SCFR-PEEK composite and both titanium alloys. Based on the measurements described previously, it is possible to estimate the energy absorption W of composite under dynamic impact by Eq. (5.11) and the minimum energy to perforation, $W_{perforation}$, Eq. (5.12).

Fig. 5.22b shows the kinetic energy of the projectile converted into energy absorbed W of composite. For all materials tested W increases with initial velocity. Comparing the values obtained, it is observed that PEEK unfilled can absorb enough energy to avoid hip and skull injuries independent of the impact velocity, Fig. 5.22b. The reference used for comparison is the maximum hip fracture energy, $E_{hip}^{fracture} = 42\ J$, reported by Monea et al. (2014). The values of perforation energy are respectively $W_{perforation}^{PEEK} = 45.6\ J$, $W_{perforation}^{SCFR-PEEK} = 20.4\ J$, $W_{perforation}^{Ti6Al4V} = 35\ J$ and $W_{perforation}^{Ti6Al7Nb} = 36.5\ J$. Moreover, over the full range of impact velocities, PEEK material is more efficient in energy absorption compared to both SCFR-PEEK with a medium ratio of *R=1.85* and titanium alloys with a medium ratio of *R=1.26*, Fig. 5.23. In addition, SCFR-PEEK composites do not have the

capacity to absorb all energy without fracture for values higher than 20.4 J. At high strain rate, SCFR-PEEK composites increase its brittleness with associated reduction of toughness [Sobieraj et al., 2012]. The lack of energy dissipation by plastic deformation of the matrix increases the impact energy transferred locally to the composite which can generate fractures and perforation.

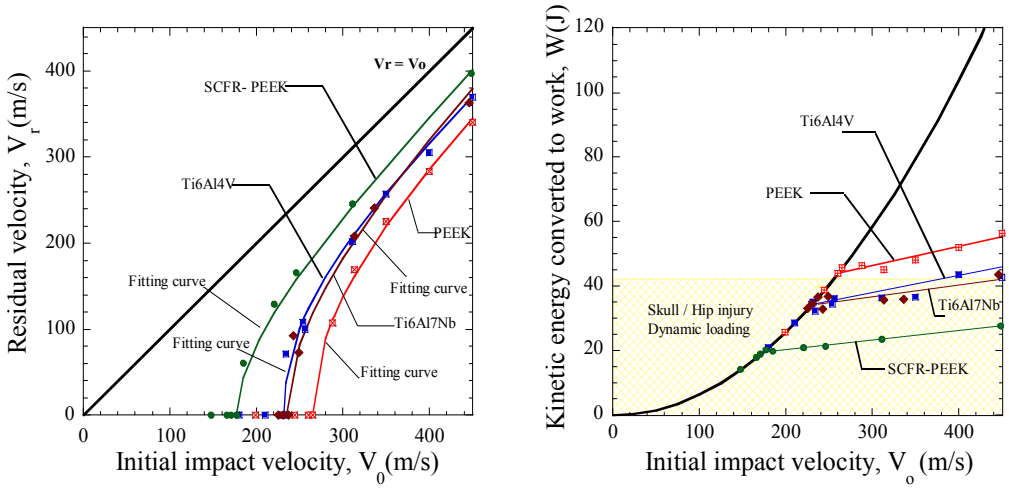

(a) (b)

Figure 5.22: a) Residual velocity V_r versus impact velocity V_0, comparison between PEEK composites and titanium alloys; b) Energy absorbed by the plate W versus impact velocity V_0, comparison between PEEK composites and titanium alloys.

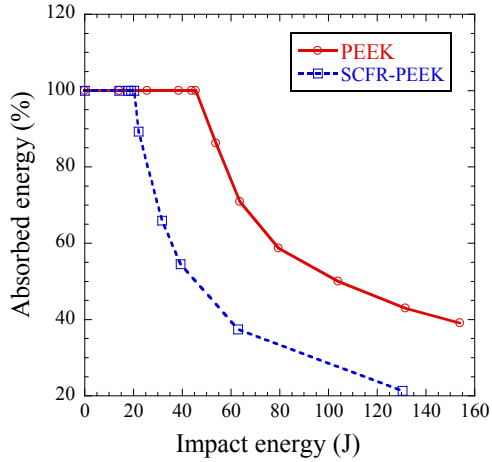

Figure 5.23: Percentage of absorption energy of SCFR PEEK and unfilled PEEK versus impact energy.

5.2.6.2 Failure mode of SCFR PEEK composite

Fracture in short fibre thermoplastic composite takes place progressively by the succession and overlapping of several complex failure mechanisms. In these composites failure occurs as the result of a variety of complex damage mechanisms such as fibre cracking, fibre debonding and pull-out, plastic localization and ductile fracture (void growth and coalescence) in the matrix [Kammoun et al., 2011]. Figs. 5.24 and 5.27 illustrate the final stage of the impact process for different initial impact velocities and both materials tested. The failure mode of SCFR PEEK composite is clearly different from that observed in unfilled PEEK. While PEEK unfilled behaves in a ductile manner, when short fibres are added, the SCFR PEEK shows a marked change to brittle behaviour resulting in a considerable loss in energy absorption capability. For SCFR PEEK composite and on the front and rear, Fig.5.24a and Fig. 5.24b respectively, damage was a combination of localized penetration in local impact zone and four long brittle cracks in radial directions and deep of thickness size of specimen. This observation demonstrates a key failure mechanism based on a cohesive failure mode due to insufficient matrix shear strength in impact conditions. For unfilled PEEK matrix and on the front and rear surfaces, Fig.5.24c and Fig. 5.24d respectively, damage was localized and ductile for two consecutive impacts showing multi-hip capability for impact absorption energy.

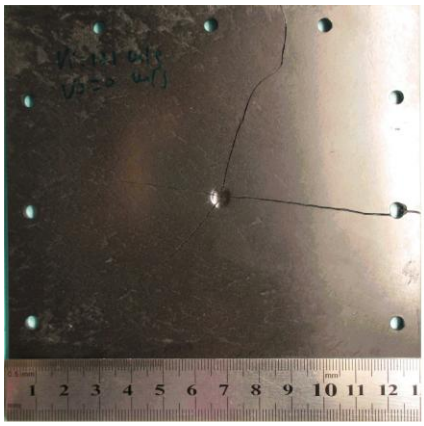

a) *Impact Energy 19.01 J. V_0=171 m/s. V_r =0 m/s. Front surface*

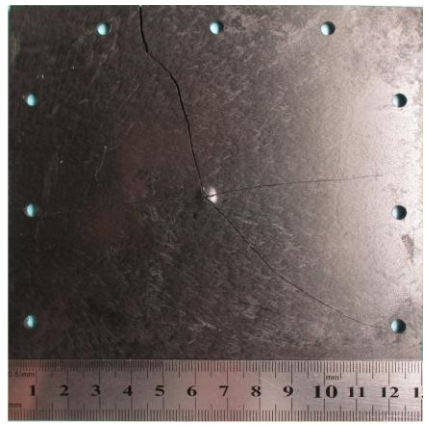

b) *Impact Energy 19.01 J. V_0=171 m/s. V_r =0 m/s. Rear surface*

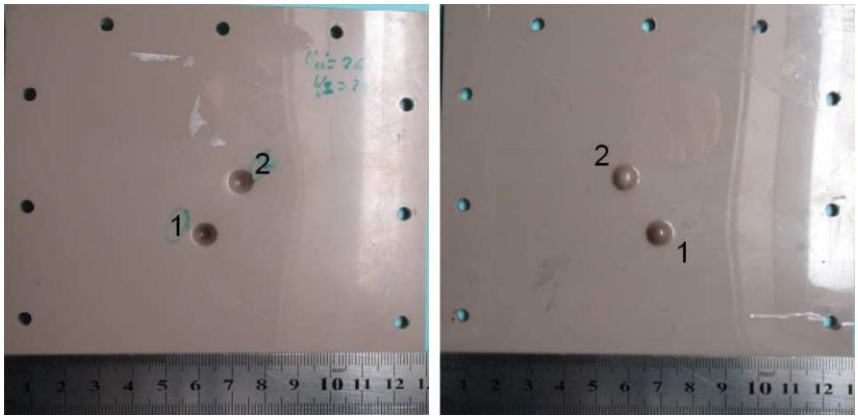

c) *$V_0(1)$=260 m/s; $V_0(2)$=244 m/s; V_r=0 m/s. Front surface*

d) *$V_0(1)$=260 m/s; $V_0(2)$=244 m/s; V_r=0 m/s. Rear surface*

Figure 5.24: Final stage of the perforation process of SCFR PEEK and unfilled PEEK for different impact velocities (front and rear surfaces of plates).

For a better understanding of the impact processes in composite materials [Pernas et al., 2014], two different regimes can be considered: impact velocities below and above ballistic limit V_{bl}. When the impact velocity is not high enough to perforate the composite, below ballistic limit, it is assumed that the plate absorbs all the kinetic energy of the projectile mainly in form of matrix cracking damage, Fig. 5.25a. Low velocity impact involves a long contact time between the impactor and the target, which produces damage in some points far from the contact region (global structure deformation). For this reason, the matrix cracking usually observed due to low-velocity impact, occurs parallel to the fibres of brittle composite. However, if the impact velocity of the projectile is high enough to perforate the plate, the energy absorbed by the composite is only the difference between the initial and the residual kinetic energy of the projectile, Fig. 5.25b-c. In this case, some part of the energy is absorbed by fibre cracking, fibre pull-out and local matrix failure (to create the plug) and some other is used to accelerate the plug (linear momentum transfer) from rest of the projectile residual velocity. Here the damage extension is much greater compared to the previous velocity analyzed. Finally, at very high velocities the damage induced by the projectile is much more localized around the impact point; projectile pushes a plug out of the target approximately equal in diameter to that the projectile; this means that the damaged area is smaller than at lower velocities (above ballistic limit).

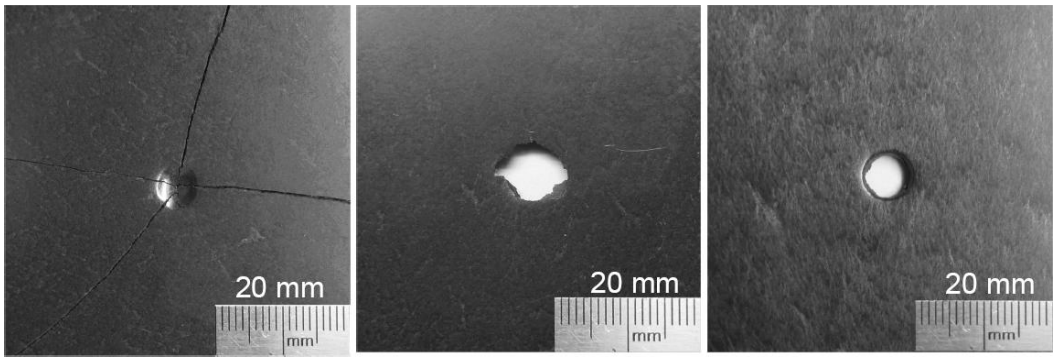

a) *Impact Energy 19.01 J.* V_0*=171 m/s.* V_R*=0 m/s*

b) *Impact Energy 39.34 J.* V_0*=246 m/s.* V_R*=166 m/s.*

c) *Impact Energy 62.86 J.* V_0*=311 m/s.* V_R*=246 m/s.*

Figure 5.25: Final stage of the perforation process of SCFR PEEK composite for different impact velocities below ballistic limit and above ballistic limit.

At impact velocities above the ballistic limit, a spalling process of the material was observed around the hole created by the penetration of the projectile and the plug ejected during the impact is supposed to approximate a truncated cone. On the rear surface (Figs. 5.26 and 5.27) the damage was higher compared to the front surface one. This can be attributed to the global deformation influence (along with the local damage) that causes the damage of the larger area on the rear surface. Moreover, radial cracks are observed in the rear surface. This type of radial fracture is common in materials where the tensile strength is lower than the compressive strength as it has been determined for SCFR composite in *Section 5.2.2*.

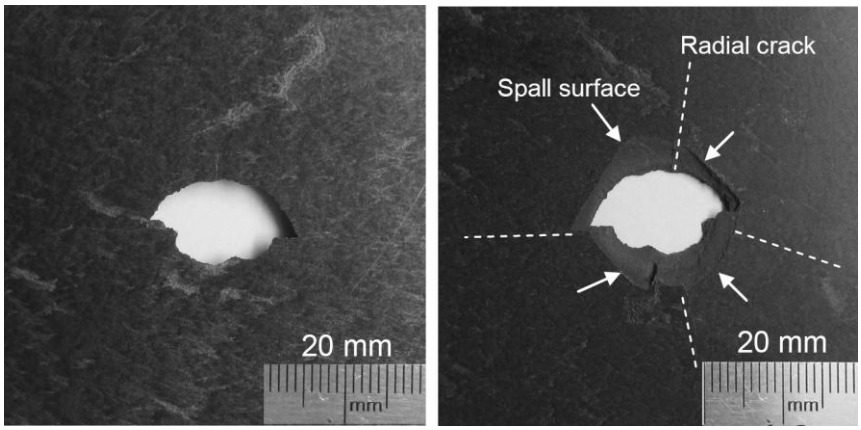

Figure 5.26: Damage in front and rear surface of plates of SCRF PEEK composite impacted at V_0=221 m/s.

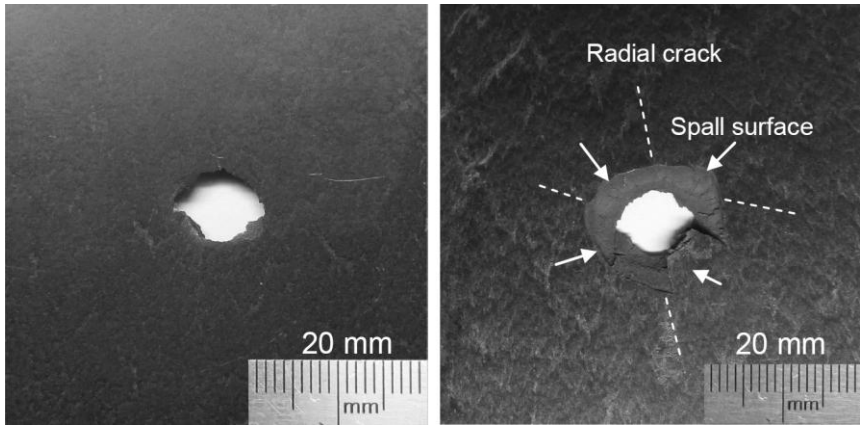

Figure 5.27: Damage in front and rear surface of plates of SCRF PEEK composite impacted at V_0=246 m/s.

As experimental complementary technique, C-Scan was used to measure the damaged area; this non-destructive inspection method allows for performing an accurate quantification of the damage extent based on the elastic wave's attenuation passing through discontinuities. It is corroborated that the extension of damaged area is limited to macroscopic observations: spalling around the hole created by the projectile penetration and radial cracks, Fig. 5.28. The damaged area decreases with impact velocity up to a surface equivalent to the perfect hole of the projectile at high velocities.

Moreover, using SEM photo, Fig. 5.29a-b, it is possible to note a global brittle behaviour characterized by: SCF/PEEK interfaces (I), micro-cracking and matrix deformation (II), fibre pull-out (III) and fibre breakage (IV). Observations of fracture surfaces revealed the existence of a high amount of matrix adhered to fibre surfaces, characteristic of the high interfacial strength between short carbon fibres and PEEK polymer [Sarasua et al., 1995; Chukov et al., 2015]. There are not "clean fibres" and all fibres show some adhering of PEEK polymer [Green, 2012]. Long pull-out lengths are observed in impact at low velocities, Fig. 5.29a, due to a higher contact time between projectile and plate and more energy absorption of composite, Fig. 5.23. Fig. 5.29a-b shows also that debonding is proved to initiate preferentially at fibre tips due to stress concentration in impact zone, followed by of a separation of interface, formation of micro-voids and their propagation along fibre sides up to cracks propagation in the matrix [Bourmaud et al., 2013]. Fibre breakage is minority, Fig. 5.29a in agreement with results of work reported by Notta-Cuvier et al. (2015). Thus, it is confirmed that fibre breakage rarely plays a leading role in the failure of injection moulded SFRC since fibres have an initial length higher than the critical value.

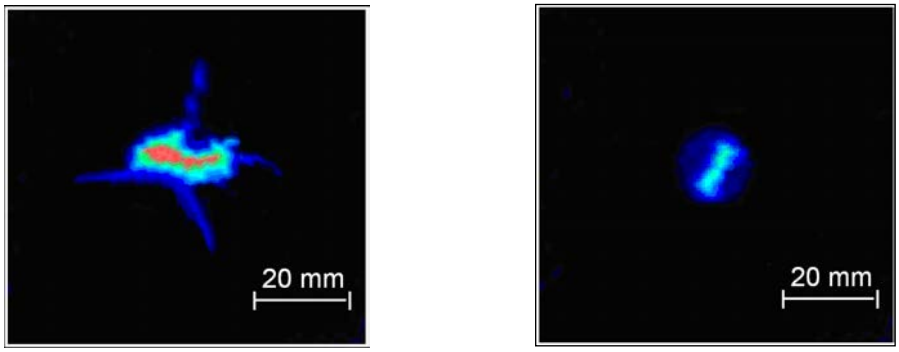

(a) (b)

Figure 5.28: C-Scan image of impacted SCRF PEEK composite plates: a) Impact velocity, V_0=221 m/s; b) Impact velocity, V_0=311 m/s.

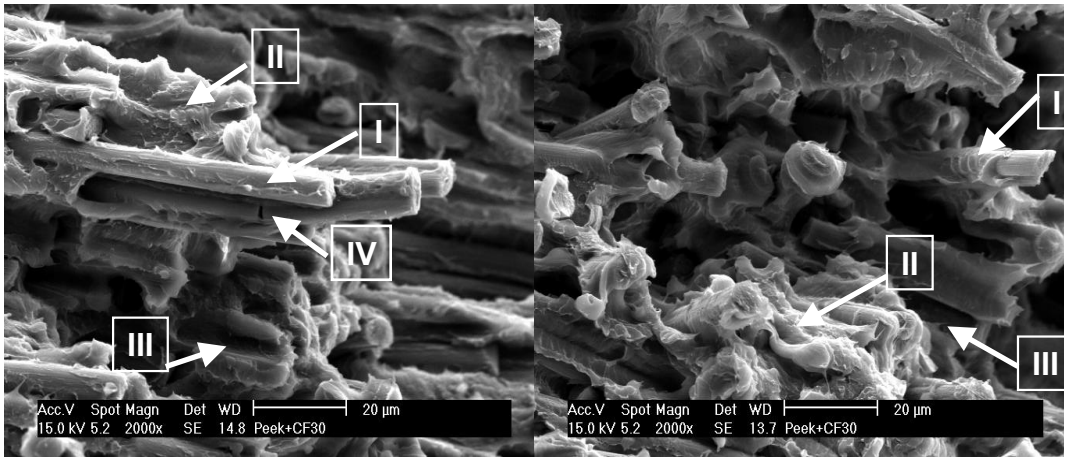

(a) (b)

Figure 5.29: Scanning electron micrograph of the fracture surface of impacted SCRF PEEK composite: a) Impact velocity, V_0=221 m/s; b) Impact velocity, V_0=246 m/s.

5.2.6.3 Numerical results

A good correlation was found between experimental and numerical results, with a maximum error less than 10%, which demonstrates that the models used in this study faithfully reproduce the impact behaviour of SFC PEEK, Fig. 5.30a. From numerical predictions simulations, the values of damage area have been obtained showing a decrease with impact energy. These numerical predictions of the damaged area were

estimated in terms of the damage variable $D(\bar{\varepsilon})$, Eq. (5.17), defined as a state variable in a VUMAT subroutine. The images of impacted laminates obtained by the C-Scan allow measuring the damaged area using an image processor software and hence represent the damaged area versus the impact velocity, Fig. 5.30b.

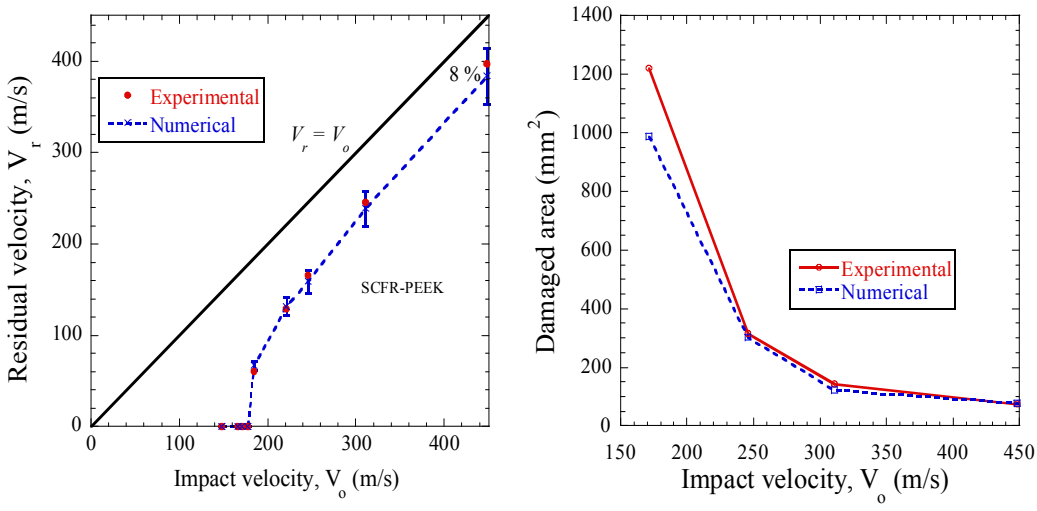

(a) (b)

Figure 5.30: Experimental and numerical data for SCFR PEEK composite subjected to mechanical impact: a) residual velocity b) damage area.

5.2.7 Conclusions

In this section, the mechanical impact behaviour of SCFR PEEK has been investigated using a combination of experiments and finite element simulations. In the full range of impact kinetic energies considered, from 21 J to 131 J, SCFR PEEK composites showed a brittle failure in line with the behaviour studied by other authors in terms of fracture toughness. C-Scan and SEM inspection tests on impacted specimens show that the failure of SCFR PEEK is dependent on material directions, derived of anisotropic material properties due to flow moulding manufacturing. To allow adequate prediction of failure, an approach for modelling the behaviour of SCFR PEEK composites has been proposed which includes homogenization of elastic material and anisotropic damage. The results show good agreement and validation of the predictions against experimental data of energy absorption and damage area for short carbon fibre PEEK composite. In

conclusion, the absorption energy capability of SCFR PEEK decreases drastically in comparison with unfilled PEEK. The brittleness of SCFR PEEK will limit the application of this composite in prosthetic devices employed in areas exposed to impact by accidental fall.

5.3 Remarks on temperature influence on impact behaviour of PEEK composites

5.3.1 Introduction

Thermoplastics and their composites reinforced with short carbon fibres are increasingly employed in many industries due to their attractive mechanical properties, rapid processing by injection moulding and relatively low manufacturing cost. Short fibre reinforced polymers (SFRPs) were developed to fill the mechanical property gap between the continuous-fibre laminates used as primary structures by the aircraft and aerospace industry [Rezai et al., 2009]. The knowledge about the thermal properties of thermoplastics and their composites is essential. Although biomedical applications are rarely exposed to low temperatures, nowadays, these materials are also widely employed in aircraft applications and civilian aircraft materials where usually have to perform their duty in the temperature range from -50ºC to +80ºC.

Many of these applications are subjected to dynamic loadings like impact and, therefore, their structural components must present good energy absorption capability. Strain rate and temperature dependencies play a relevant role in the energy absorption efficiency of thermoplastic materials. The yielding and plastic flow behaviours are affected by strain rate resulting in a continuous hardening and loss in ductility as this variable increases [Rae et al., 2007; El-Qoubaa et al., 2014]. Regarding the temperature-dependent behaviour of thermoplastic polymers, if the temperature is below glass transition, there is a sudden change in the amorphous molecule segments and the polymer molecules lack the ability to undergo considerable motion due to insufficient kinetic energy. In case of exposing the thermoplastic to progressively lower temperatures, the material undergoes another transition, called the ductile-to-brittle transition temperature. During this transition, the polymer loses a substantial level of kinetic energy resulting in restricted motion of the chains. This process results in a sudden, sharp loss in ductility [Gaymans et al., 2000].

This section analyzes the thermomechanical coupling under dynamic deformations and its effect on the mechanical behaviour-transitions of thermoplastic composites. To this end, an investigation on the impact behaviour of PEEK composites is carried out taking into account strain rate and thermal effects, and how these variables influence the energy absorption capability. The results of previous sections focused on the performance of PEEK composites at room temperature cannot be simply transferred to the low temperature regime. Moreover, the impact behaviour of PEEK and SCFR PEEK composites at low temperature has not been reported in the scientific literature. With the

aim of contributing to the understanding of this problem, a set of perforation tests has been conducted varying the testing temperature from -75ºC to +25ºC and the impact kinetic energy from 11 J to 175 J. Experimental observations showed that ductile-to-brittle transition occurs within these conditions. The brittleness of PEEK and SCFR PEEK at low temperature has been demonstrated to be a combination of thermal- and strain rate-activated mechanisms.

5.3.2 Thermomechanical considerations

Commercial plates of PEEK composites reinforced with PAN short carbon fibres 30 % in weight, named CF30 PEEK, and unfilled PEEK plates of general purpose grade were purchased measuring 130x130x3 mm^3. Both materials are produced with injection moulding technology. For more details of the mechanical and manufacturing properties of the PEEK and SCFR PEEK (concretely CF30 PEEK) specimens tested, see *Section 5.2.2*.

5.3.2.1 Macroscopic observations

One inherent problem in processing short fibre reinforced thermoplastics (SFRTPs) by flow moulding techniques is that the fibres tend to become aligned during the flow process, inducing anisotropic material properties. In SCFR PEEK composites, the so called skin-core structure is well documented, see Fig. 5.31 [Evans et al., 1996]. Scanning electron micrographs (SEM) of the fracture surfaces of SCFR PEEK specimens tested in this work, Fig. 5.32, correlate well with the above macroscopic considerations. From the SEM images, a three layered-structure is observed: top and bottom skin layers revealed fibre alignment along the melt flow direction, Fig. 5.32a; whereas in the core layer the fibres are transversely oriented, Fig. 32b.

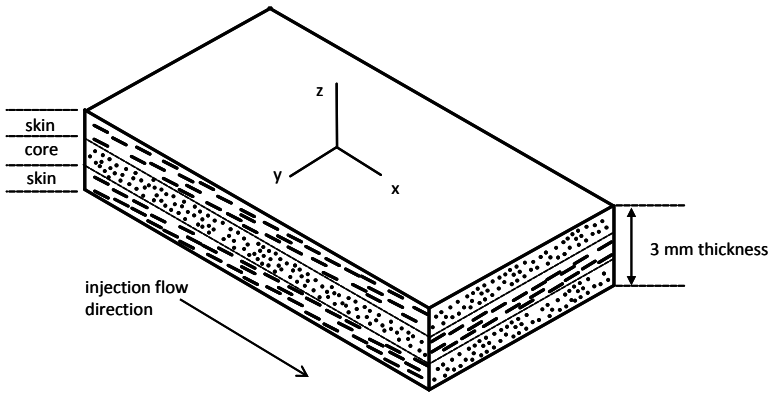

Figure 5.31: Skin/core fibre orientations in the short fibre composite plates of this work in agreement with observations reported by Evans et al. (1996).

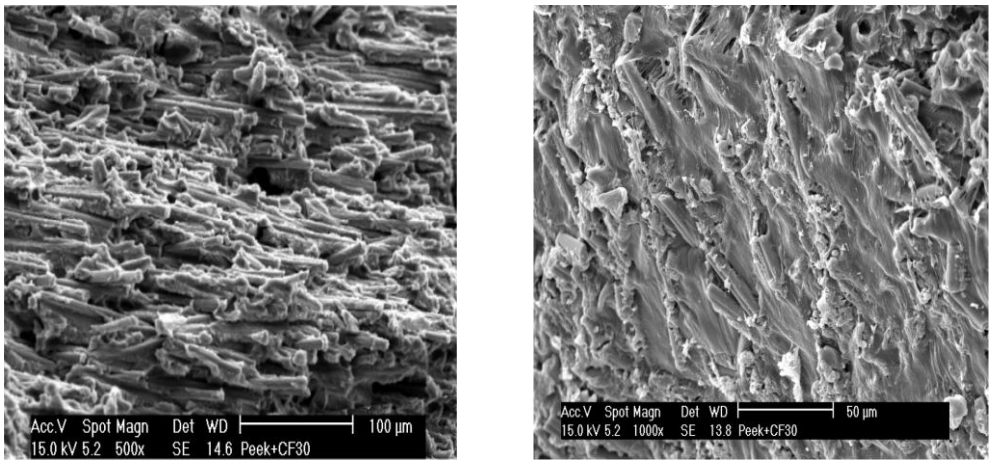

(a) (b)

Figure 5.32: Scanning electron micrograph of SCFR PEEK specimens: a) skin; b) core.

These observations explain the mechanical anisotropy observed in the experimental results shown in *Section 5.2.2*.

5.3.2.2 Temperature sensitivity

Most thermoplastic composites present temperature-dependent mechanical behaviour. This behaviour is mainly due to the dependence of the matrix properties on temperature. For unfilled thermoplastic materials, the glass transition and ductile-to-brittle transition temperatures represent useful cut off points. At temperatures above the glass transition, α temperature, the polymer molecules have sufficient kinetic energy to allow considerable motion. Below the glass transition, the molecules lack the ability to undergo this motion. In semi-crystalline polymers, the glass transition and the melting transition respectively affect the amorphous and crystalline phases. Moreover, when the amorphous phase is progressively exposed to lower temperatures, the material undergoes another transition called the ductile-to-brittle transition, β temperature. This temperature represents passage through a lower order transition. During this transition, the polymer loses a substantial level of kinetic energy which results in restricted motion of the chains. This results in a sudden, sharp loss in ductility. The β transition occurs below the glass transition temperature for many polymers at -100ºC to 100 ºC as a consequence of segments rotation in the polymer chains. Regarding unfilled PEEK, the β transition occurs at -60ºC at quasi-static conditions [Adams, 1993].

5.3.3 Impact behaviour at different temperatures

Low velocity impact tests were conducted in a drop weight tower varying the testing temperature and the impact energy. The drop weight tower is provided with a climatic chamber allowing the variation of the initial testing temperature from -75ºC to 25ºC. A thermocouple is connected to a temperature controller that regulates the opening of an electrovalve. By this way, the volume of liquid nitrogen entering in the chamber is controlled and, thus, the testing temperature can be accurately defined by the operator, see Fig. 5.33. In order to homogenize the testing temperature, PEEK specimens were subjected to this initial temperature during fifteen minutes before the test. This period of time was found to be enough to reach thermal equilibrium material-target/testing-temperature. More details of the drop weight tower used are provided in the work developed by Gómez-del Río et al. (2005). This analysis takes into account impact energy (controlling both impact velocity and striker mass), deformation mode, evolution of the impact force versus striker displacement and testing temperature.

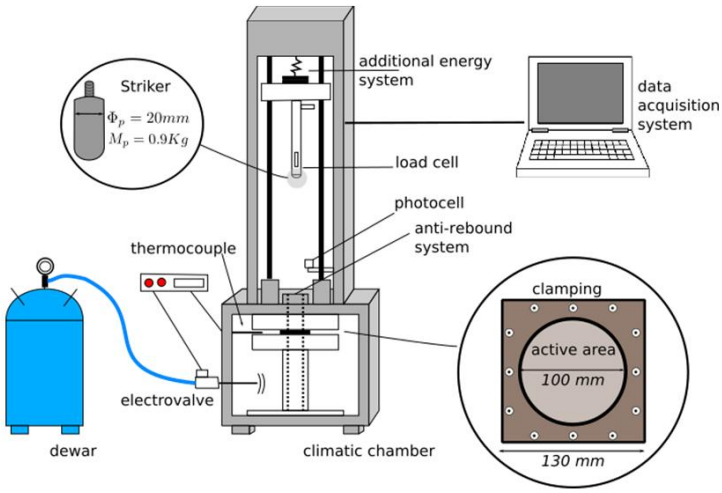

Figure 5.33: Experimental setup for drop weight tower tests at low temperature.

The specimens with dimensions of 130x130x3 mm^3 were clamped in a modular tool by screws all arround a circular active area of 100 mm of diameter. The screws were symmetrically fixed in order to avoid any disturbance during the test. A steel striker with hemispherical shape was used, whose larger diameter is φ_p = 20 mm and whose mass is M_p = 0.90 kg. The striker was attached to the instrumented bar attached to a metal frame, whose mass is M_f = 2.9 kg. Aditional mass was added to the setup in order to increase the

effective mass (M_{total}) from 3.8 kg until 28.8 kg. After the impact, an anti-rebound system held the striker in order to avoid multi-hits on the specimen if no perforation of the plate occurs. A local cell placed on the striker calculates the time dependent displacement $\delta_s(t)$ of the striker during the impact process integrating the impact force F(t) versus time:

$$\delta_s(t) = \int_0^t V_0 \left[\int_0^\tau \frac{F(\theta)M_{total}g}{M_{total}} d\theta\right] d\tau \tag{5.19}$$

where t is the time from the instant at which the striker bar hits the specimen, M_{total} is the striker bar mass and V_0 the striker initial velocity at the beginning of the experiment ($t=0$): During the test, the energy transmitted to the specimen $E(t)$ at any time is approached as

$$E(t) = \int_0^t F d\delta = \int_0^t F(\tau)\left[V_0 \int_0^\tau \frac{F(\theta)M_{total}g}{M_{total}} d\theta\right] d\tau \tag{5.20}$$

5.3.4 Discussion

The ductile/brittle behaviour of thermoplastic composites depends on many factors and most of them can exhibit both responses depending on environmental conditions. The failure mechanisms of a brittle or ductile material are fundamentally different: while brittle fracture occurs fast and is often characterized by instability; ductile failure is more progressive. The conditions that influence the ductile/brittle nature of composites can be grouped into two categories. The first category includes environmental parameters such as temperature (ductility is increased by raising the temperature), strain rate (ductility is increased by decreasing the strain rate) and solvents. The second category includes parameters that are intrinsic to the material: the nature of the polymer matrix, fillers and fibres.

5.3.4.1 Failure mode of unfilled PEEK and SCFR PEEK composite

Figs. 5.34 and 5.35 illustrate the final stage of the impact process on PEEK specimens for different testing temperatures. Figs. 5.36 and 5.37 show the final stage of the impact process on SCFR PEEK specimens for different testing temperatures. The failure mode of SCFR PEEK is different from that observed in unfilled PEEK. While SCFR PEEK shows brittle behaviour for all testing conditions considered, unfilled PEEK shows a transition of its behaviour from ductile to brittle depending on testing temperature.

According to experimental observations in terms of failure mode, Fig. 5.34a, it was observed that, when the specimen is tested at room temperature (≈25ºC), it fails following a hole enlargement mechanism. Moreover, this ductile behaviour is still remained until -25 ºC, Fig. 5.34b. However, when the specimens are tested below -25 ºC, all of them show a brittle behaviour, as it can be observed in Fig. 5.35. Regarding the specimens tested at -25 ºC, there were found cases in which PEEK specimen behaves ductilely and others in which it behaves brittlely. Therefore, the ductile-to-brittle transition under impact conditions was determined at -25 ºC, finding the testing temperature as a key variable in the mechanical behaviour of PEEK. Thus, the ductile-to-brittle transition is defined as the temperature at which brittle and ductile response of the material is equally likely [Motz and Schultz, 1989]. Although the ductile-to-brittle transition temperature for PEEK has been observed to occur at -60ºC in quasi-static conditions [Adams, 1993], other authors have observed that this transition is dependent on both temperature and strain rate. It means that there is a coupling between ductile-to-brittle transition temperature and strain rate: the higher strain rate, the higher ductile-to-brittle transition temperature [Gaymans et al., 2000].

All the specimens tested below the transition temperature, -50ºC in Fig. 5.35a and -75ºC in Fig. 5.35b, have shown a failure based on the propagation of radial cracks from the impact zone. In all these cases, the failure was found brittle without any evidence of local bending in the impact zone. These observations are in agreement with the study reported by Karger-Kocsis and Friedrich (1986), where a trend to brittle fracture with decreasing temperature and/or increasing strain rate was found, while a more ductile failure mode was observed in the opposite direction.

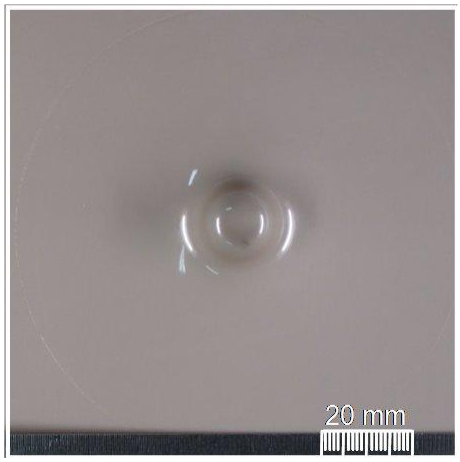

V_0=4.31 m/s
E_0=175J
$\boldsymbol{\theta_0}$=25ºC

V_0=4.31 m/s
E_0=175J
$\boldsymbol{\theta_0}$= -25ºC

Figure 5.34: Final stage of ductile failure after the impact process of unfilled PEEK at testing temperature: a) θ_0=25ºC; b) θ_0= -25ºC.

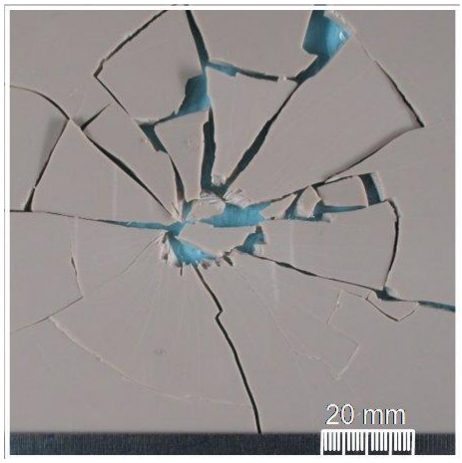

V_0=4.31 m/s
E_0=175J
$\boldsymbol{\theta_0}$=-50ºC

V_0=4.31 m/s
E_0=175J
$\boldsymbol{\theta_0}$= -75ºC

Figure 5.35: Final stage of brittle failure after the impact process of unfilled PEEK at testing temperature: a) θ_0=25ºC; b) θ_0= -25ºC.

For SCFR PEEK composite, Figs. 5.36 and 5.37, the experimental observations allow a thorough study of the damage extension. For impact energies close to the perforation limit, a characteristic mode of failure based on the propagation of some cracks from the impact zone is observed covering the whole plate. When the impact energy is increased, there is a reduction of the damaged area and a failure mode based on an elision shape hole. The failure sequence of cracks generation for SCFR PEEK composites with skin-core structure has been reported in the work of Jen and Chen (2000), see Fig. 5.38. The failure mechanism of SCFR PEEK specimens tested in this work is in agreement with the observation reported by Solomon et al. (2007) for drop weight impact tests on injection moulded SFRT composites. This failure is based on the propagation of a fissure along the IFD and another fissure along the perpendicular direction to the IFD. A brief explanation of these preferential directions in failure process and the effects of fibre orientation is provided in the work of Mortazavian and Fatemi (2015). These authors determined that strain at tensile strength, as a measure of ductility, presents the lowest values in specimens with fibres aligned in longitudinal and transverse directions. In the case of specimens with fibres preferably aligned in the longitudinal direction, the low ductility of the composite can be explained by the low capacity of fibres in straining. In specimens with fibres preferably aligned in the transverse direction, the low ductility can be explained by the limited space for yielded material to transport. Regarding temperature effects, it was observed a higher damage extension as the testing temperature decreases, Figs. 5.36 and 5.37. Although there is evidence of temperature influence on the damage extension, the way all specimens fail does not vary. A failure mode based on an elision shape hole compound by four pieces controls the SCFR-PEEK failure under impact loading, presenting a more localized damage extension for higher impact energies and a higher damage for lower testing temperatures.

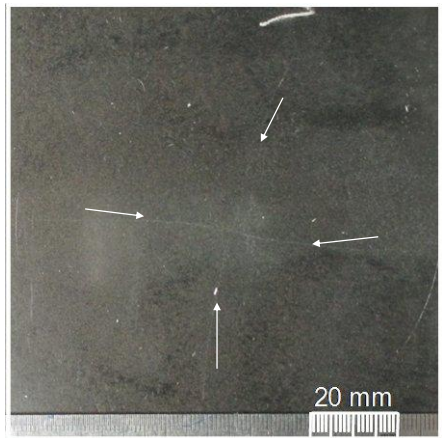

V_0=2.43m/s
E_0=11.5J
$\theta_{0=}$25ºC

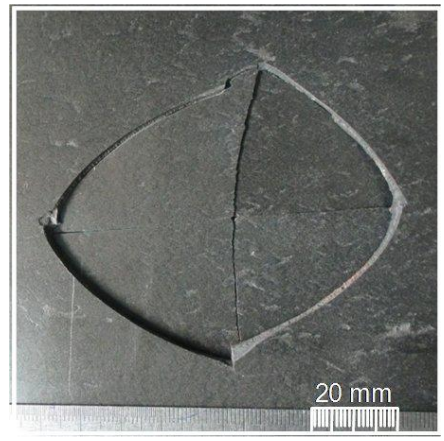

V_0=4.31m/s
E_0=175J
$\theta_{0=}$-25ºC

Figure 5.36: Final stage of brittle failure of the impact process of SCFR PEEK at testing temperature: a) θ_0=25ºC; b) θ_0= -25ºC.

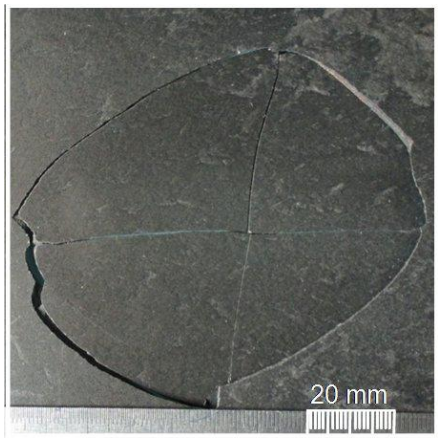

V_0=4.31m/s
E_0=175J
$\theta_{0=}$-50ºC

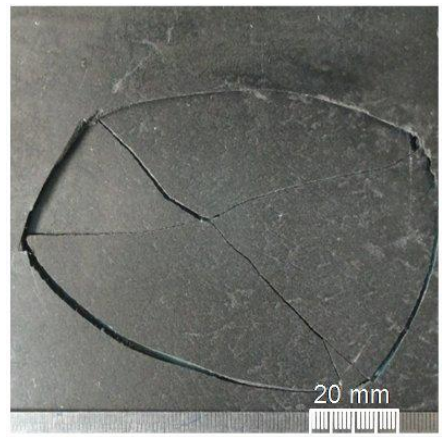

V_0=4.31m/s
E_0=175J
$\theta_{0=}$-75ºC

Figure 5.37: Final stage of brittle failure of the impact process of SCFR PEEK at testing temperature: a) θ_0=-50; b) θ_0= -75ºC.

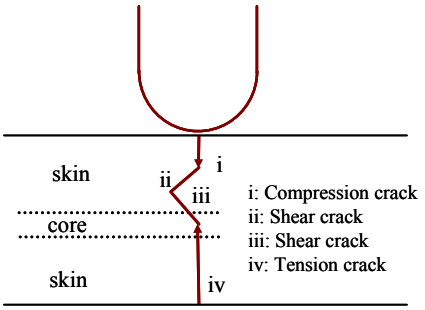

Figure 5.38: Failure sequence of generation of cracks in SCF/PEEK composites subjected to impact load [Jen and Chen, 2000].

SEM images of the fracture surfaces of specimens tested at -75ºC and 25ºC are shown in Fig. 5.39. Observations of fracture surfaces reveal the existence of a high amount of matrix adhered to fibre surfaces, characteristic of the high interfacial strength between short carbon fibres and PEEK polymer. At low temperature, micrograph correlates well with the above macroscopic observations, showing a reduction of matrix plastic deformation and adhesion at -75ºC.

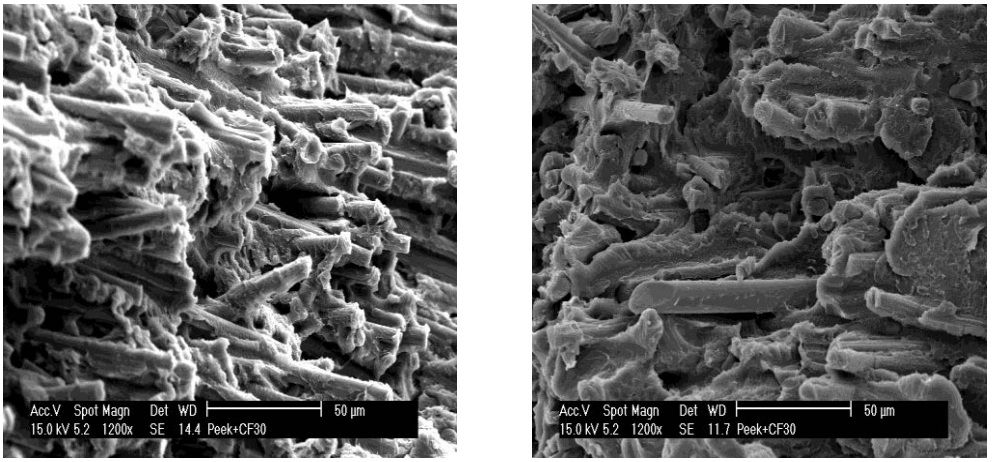

(a) (b)

Figure 5.39: Scanning electron micrograph of the fracture surface of impacted SCRF PEEK composite: a) Room temperature θ_0=23ºC; b) Low temperature θ_0=-75ºC.

5.3.4.2 Low impact velocity response of unfilled PEEK and SCFR-PEEK at room temperature

The analysis of the experimental force-striker displacement curves at room temperature, Fig. 5.40, shows a strong dependence of the material considered on the amount of kinetic energy of the striker converted into plastic work. During perforation, the much greater ductility of unfilled PEEK results on greater strain leading to target failure. Consequently, a different material behaviour is denoted and suggests different failure mechanisms for both materials tested. Despite the higher flow stress level of SCFR PEEK, the slope of the force-striker displacement curve is quite similar for both PEEK materials. The striker displacement at failure is much greater in the case of unfilled PEEK according to what can be expected from tensile tests, Figs. 5.2b and 5.20. According to Fig. 5.40, higher values of force are needed to perforate unfilled PEEK specimens in comparison with SCFR PEEK specimens. The positive strain rate dependence on the mechanical properties of unfilled PEEK has a direct influence on the maximum force reached under dynamic conditions. Regarding SCFR PEEK, early onset fracture initiated on the tension side implies the brittle behaviour of the composite that limits the maximum force that this material can support without perforation. The higher values of maximum force reached and maximum striker displacement at perforation presented by unfilled PEEK make it more competitive than SCFR PEEK in terms of energy absorption capability. Despite the increase in mechanical properties due to the addition of short fibres, the loss in ductility results in a reduction of energy absorption capability. A representative consequence of this energy capability reduction is the decrease of area under the force-striker displacement curve. Therefore, in order to confirm the validity of employing SCFR PEEK in applications that can be subjected to dynamic conditions, a specific consideration in terms of energy absorption capability must be taken into account due to the loss in ductility caused by the addition of short fibres.

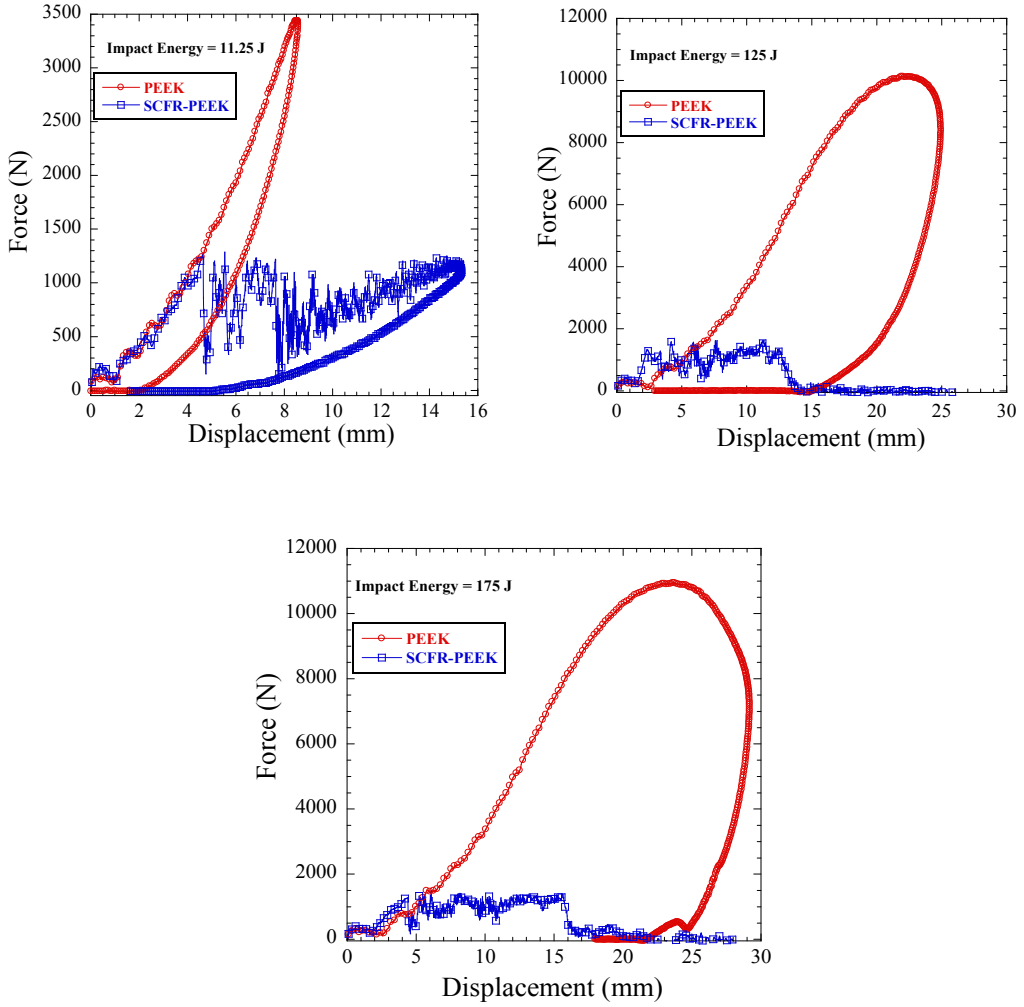

Figure 5.40: Force-displacement curves of unfilled PEEK and SCFR PEEK composite for low velocity impact tests at room temperature, 25ºC.

5.3.4.3 Temperature influence on the impact behaviour of unfilled PEEK

An experimental analysis of the temperature influence on PEEK force-striker displacement curves has been carried out, Fig. 5.41a. These results show a strong dependence of PEEK impact behaviour on testing temperature. While at room conditions a clearly ductile behaviour was found according to observations presented in previous sections, a change in the failure mode is observed when the testing temperature is bellow the ductile-to-brittle transition of this polymer, -25 ºC. As it can be expected from the stress-strain curves, Fig. 5.2b, when temperature is decreased, a material hardening is

appreciated but also a strong reduction in material ductility. This loss in ductility has a direct influence on the energy absorption capability, see Fig. 5.41b. In Fig. 5.41a, the impact behaviour of PEEK specimens for different initial testing temperatures is presented, using an impact kinetic energy equal to 175 J in all tests. No perforation and ductile behaviour are observed in tests at room temperature. The transition behaviour from ductile to brittle starts to be considerable if the temperature decreases until -25ºC. Moreover, an increase in stiffness can be noted due to low temperature effects and also a first loss in ductility which results in a completed perforation of the specimen. These observations are in agreement with the work published by Pettarin et al. (2006), in which a set of thermoplastic polymers is analyzed in terms of temperature-dependent impact fracture data. Regarding the tests conducted at testing temperatures lower that -25ºC, the loss in ductility results in a strong change in the failure mode that becomes brittle. This mode of failure is determined by which of these critical stresses, the fracture stress σ_b or the yield stress σ_y, is firstly exceeded in a sample. While brittle behavior is encouraged below the transition temperature because σ_b is smaller than σ_y; yielding occurs above the transition temperature [Motz and Schultz, 1989]. The embrittlement due to the reach of σ_b before σ_y, directly affects the energy absorption capability making the material less competitive in impact applications where the environmental temperature reaches levels that induce a change in the ductile/brittle behaviour.

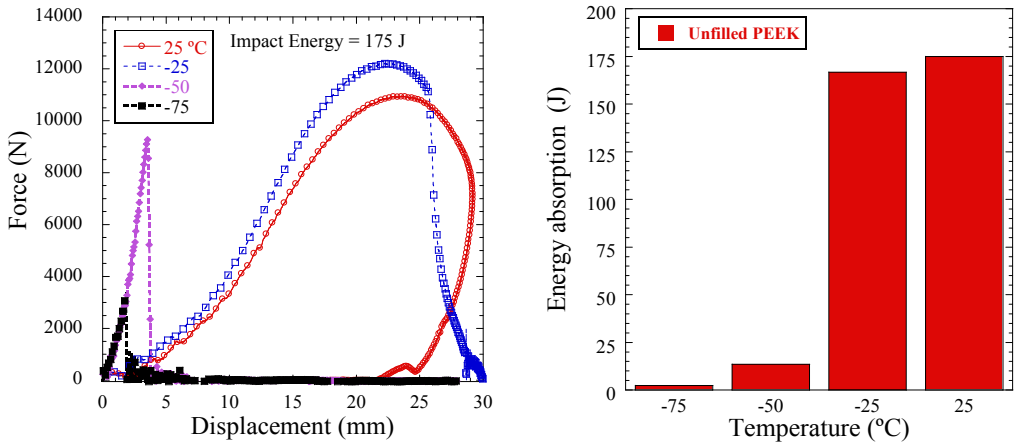

Figure 5.41: a) Force-displacement curves of unfilled PEEK for low velocity impact tests at different initial temperature; b) Energy absorption of unfilled PEEK versus different initial temperature.

For a better understanding of the loss in energy absorption capability, the observations from the study reported by Karger-Kocsis and Fiedrich (1986) have been taken under

consideration. These authors studied the effects of temperature and strain rate on the fracture thoughness of PEEK and its SFR composites. On the one hand, they observed a linear decrease with temperature in terms of elastic tensile modulus. This fact would theorically suposse higher energy absroption capability for lower temepratures. However, they also found a second grade relation between fracture energy and temperature with a maximum peak around 0ºC. For temperatures above the maximum peak of fracture energy, the continuous decrease in the energy needed to reach fracture can be explained by the thermal softening that affects both elastic modulus and yield stress [Rae et al., 2007]. The reduction of fracture energy for temperatures below the maximum peak of fracture energy may be explained by the strong reduction in ductility that limits the deformation until failure. In addition, this reduction in the strain at failure is more pronounced at high strain rates such as the ones applied in impact conditions [Karger-Kocsis and Friedrich, 1986].

5.3.4.4 Temperature influence on the impact behaviour of SCFR-PEEK composite

An analysis of the temperature influence on the SCFR PEEK impact behaviour is also developed in terms of experimental force-striker displacement curves, Fig. 5.42a. Although no change in terms of failure mode due to low temperature effects is observed, a loss in ductility has been found as the temperature is decreased. This results in a loss of energy absorption capability, understood as the area under the force-displacement curve, Fig. 5.42b. The reduction of energy absorption capability is explained by the strong dependence of the mechanical properties of PEEK matrix on temperature.

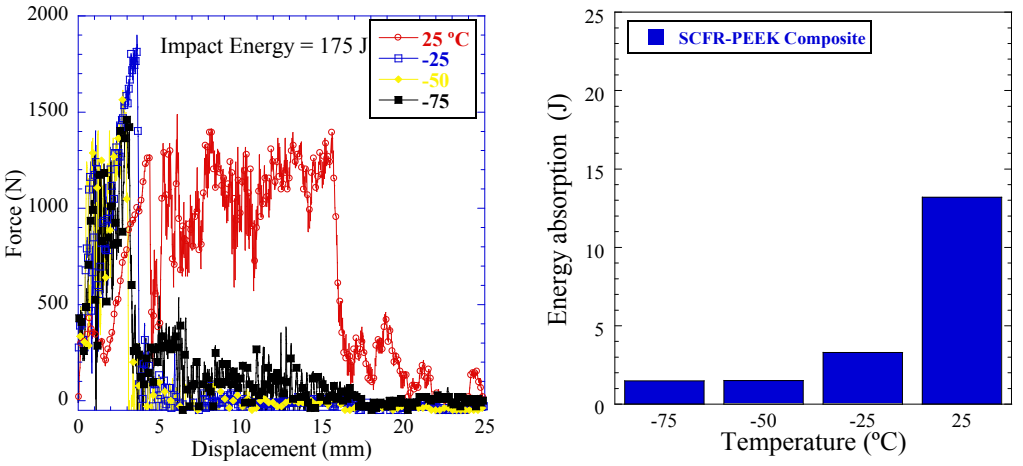

(a) (b)

Figure 5.42: a) Force-displacement curves of SCFR PEEK composite for low velocity impact tests at different initial temperature; b) Energy absorption of SCFR PEEK versus different testing temperature.

5.3.5 Conclusions

In this section, a set of perforation tests have been conducted at low temperatures covering a testing temperature range from -75ºC to +25ºC and an impact kinetic energy range from 11 J to 175 J. In the full range of temperatures considered, SCFR PEEK composites showed a brittle failure in line with the experimental observations studied by other authors in terms of thermal and strain rate-activated mechanisms. SEM inspection tests and macroscopic observations on impacted specimens show that the failure of SCFR PEEK at low temperature is dependent on material directions. This can be explained by the anisotropic material properties due to flow moulding manufacturing. Experimental observations showed a change in PEEK impact behaviour due to the reach of the ductile-to-brittle transition. This change directly affects the energy absorption capability limiting the application of PEEK composites in components subjected to impact loadings at low temperatures. In conclusion, the absorption energy capability of SCFR PEEK is remarkably low in comparison with unfilled PEEK. The brittleness of PEEK composites at low temperatures will limit the application of this composite in structural components.

Chapter 6.

Hyperelastic-thermoviscoplastic constitutive formulation for semi-crystalline polymers

The experimental observations and numerical results from the preliminary constitutive modelling presented in the previous chapter are taken into account to develop a hyperelastic-thermoviscoplastic constitutive model including thermomechanical coupling for semi-crystalline polymers. The constitutive model is based on the original approach developed by Polanco-Loria et al. (2010) and accounts for: material hardening due to strain rate sensitivity, temperature evolution during the deformation process due to heat generation induced by plastic dissipation, thermal softening and thermal expansion of the material. The parameters of the constitutive model have been identified for PEEK from experimental data published by Rae et al. (2007). In order to analyze the predictive capacity of the model under dynamic conditions, the constitutive model has been implemented in a FE code within a large deformation framework to study two different problems: low velocity impact test on PEEK thin plates and dynamic necking on PEEK slender bar. These problems involve large and irreversible deformations, high strain rates and temperature increment due to plastic dissipation. The analysis determines the interplay between strain rate and thermal effects in the material behaviour. The constitutive model presented herein reproduces adequately the mechanical behaviour of PEEK under different thermal and loading conditions, demonstrating the importance of considering the coupling between temperature and strain rate.

The list of symbols used in this chapter is provided in Table 6.1 in order to facilitate the understanding of the formulation presented herein. This nomenclature is also used in *Chapter 7* and *Appendix D*.

Table 6.1: Nomenclature used in the constitutive formulation.

Nomenclature			
$\{\Omega_o, \bar{\Omega}, \bar{\bar{\Omega}}, \Omega\}$	initial, dilated, dilated relaxed and current configurations	$\mathbf{d_N^e}$	symmetric part of the network elastic velocity gradient
$\{e, e_o, \bar{e}\}$	specific internal energy per unit volume in Ω, Ω_o and $\bar{\Omega}$	$\mathbf{d_I^e}$	symmetric part of the intermolecular elastic velocity gradient
$\{\mathbf{q}, \mathbf{Q}, \bar{\mathbf{Q}}\}$	heat flux per unit volume in Ω, Ω_o and $\bar{\Omega}$	$\bar{\mathbf{D}}^{\boldsymbol{\theta}}$	symmetric part of the thermal velocity gradient
$\{r, R, \bar{R}\}$	heat source per unit volume in Ω, Ω_o and $\bar{\Omega}$	$\bar{\bar{\mathbf{D}}}_{\mathbf{I}}^{\mathbf{p}}$	symmetric part of the intermolecular plastic velocity gradient
$\{\eta, \bar{\eta}\}$	specific entropy per unit volume in Ω and $\bar{\Omega}$	$\mathbf{w}$	skew part of the velocity gradient
$\bar{C}$	heat capacity per unit volume	$\bar{\mathbf{W}}^{\boldsymbol{\theta}}$	skew part of the thermal velocity gradient
$\{\theta, \theta_{ref}, \theta_{melt}\}$	current, reference and melting temperature	$\bar{\bar{\mathbf{W}}}_{\mathbf{I}}^{\mathbf{p}}$	skew part of the intermolecular plastic velocity gradient
f_θ	temperature-dependent function	$\boldsymbol{\sigma}$	Cauchy stress tensor
$\bar{\Psi}$	Helmholtz free energy per unit volume	$\boldsymbol{\sigma}_{\mathbf{N}}$	network Cauchy stress tensor
∇_X	gradient with respect to the material point $\mathbf{X}$ in Ω_o	$\boldsymbol{\sigma}_{\mathbf{I}}$	intermolecular Cauchy stress tensor
∇_x	gradient with respect to the point $\mathbf{x}$ in Ω	$\mathbf{P}$	first Piola-Kirchhoff stress tensor
$\mathfrak{L}$	Langevin function	$\bar{\mathbf{S}}_{\mathbf{N}}$	network second Piola-Kirchhoff stress tensor
$\mathbf{I}$	Identity matrix	$\{\bar{\mathbf{S}}_{\mathbf{I}}, \bar{\bar{\mathbf{S}}}_{\mathbf{I}}\}$	intermolecular second Piola-Kirchhoff stress tensor in $\bar{\Omega}$ and $\bar{\bar{\Omega}}$
J	determinant of the deformation gradient	$\bar{\mathbf{M}}_{\mathbf{N}}$	network Mandel stress tensor
J^θ	determinant of the thermal deformation gradient	$\{\bar{\mathbf{M}}_{\mathbf{I}}, \bar{\bar{\mathbf{M}}}_{\mathbf{I}}\}$	intermolecular Mandel stress tensor in $\bar{\Omega}$ and $\bar{\bar{\Omega}}$
J^M	determinant of the mechanical deformation gradient	$\bar{\lambda}$	average total stretch ratio
J_N	determinant of the network deformation gradient	$\{I_{1I}, J_{2I}\}$	stress invariants of the intermolecular Mandel stress tensor
J_I	determinant of the intermolecular deformation gradient	$\bar{\bar{\sigma}}_{eqI}$	Rhagava equivalent stress
J_I^e	determinant of the intermolecular elastic deformation gradient	g_I	plastic potential
$\mathbf{F}$	deformation gradient	$\bar{\bar{\mathbf{r}}}_{\mathbf{I}}$	gradient of the plastic potential
$\mathbf{F}^{\boldsymbol{\theta}}$	thermal deformation gradient	$\dot{\bar{\bar{\gamma}}}_I^p$	viscoplastic multiplier
$\{\mathbf{F}^{\mathbf{M}}, \mathbf{F}_{\mathbf{I}}^{\mathbf{M}}, \mathbf{F}_{\mathbf{N}}^{\mathbf{M}}\}$	mechanical deformation gradient contributions	α_θ	thermal expansion coefficient
$\mathbf{F}_{\mathbf{N}}^{\mathbf{e}}$	network elastic deformation gradient	$\{\lambda_0, \mu_0\}$	classical Lamé constants
$\mathbf{F}_{\mathbf{I}}^{\mathbf{e}}$	intermolecular elastic deformation gradient	E	Young's modulus
$\mathbf{F}_{\mathbf{I}}^{\mathbf{p}}$	intermolecular plastic deformation gradient	$\{E_{ref}, E_1\}$	Young's modulus at the reference temperature and a specified material parameter
$\mathbf{C}_{\mathbf{N}}^{\mathbf{e}}$	network elastic right Cauchy-Green tensor	$\{\sigma_T, \sigma_{T0}\}$	yield stress in uniaxial tension and its value at reference temperature
$\{\mathbf{C}_{\mathbf{I}}^{\mathbf{e}}, \mathbf{B}_{\mathbf{I}}^{\mathbf{e}}\}$	intermolecular elastic right and left Cauchy-Green tensors	α	pressure sensitivity parameter
$\mathbf{v}$	velocity	β	volumetric plastic strain parameter
$\mathbf{l}$	velocity gradient	$\dot{\varepsilon}_{0I}$	reference strain rate
$\mathbf{l}_{\mathbf{N}}^{\mathbf{e}}$	network elastic velocity spatial gradient	C	rate sensitivity parameter
$\mathbf{l}_{\mathbf{I}}^{\mathbf{e}}$	intermolecular elastic velocity spatial gradient	m	temperature sensitivity parameter
$\bar{\mathbf{L}}^{\boldsymbol{\theta}}$	thermal velocity spatial gradient	C_R	initial elastic modulus of the network resistance
$\bar{\bar{\mathbf{L}}}_{\mathbf{I}}^{\mathbf{p}}$	plastic velocity spatial gradient	$\bar{\lambda}_L$	locking stretch
$\mathbf{d}$	symmetric part of the velocity gradient	κ	network bulk modulus
		τ	characteristic timescale

6.1 Introduction

Due to their attractive mechanical properties, rapid processing and relatively low manufacturing cost, thermoplastic polymers are used in a large range of industrial sectors. Because of the increasing interest in, and use of, these polymers, it is fundamental to understand their behaviour under different loading conditions. There are many devices employed in automotive, aeronautical and biomedical applications which are exposed to impact loading conditions. Such devices like car safety system, leading edges in aircrafts or cranial replacements can be subjected to high strain rates which result in a complex behaviour. On the other hand, in the design and manufacturing process, the estimation of temperature evolution leading to thermal softening and thermal expansion is essential.

The nonlinear behaviour of thermoplastic polymers reflects its time, pressure, strain rate and temperature dependencies and the coupling of viscoelastic and viscoplastic behaviours [Krairi and Doghri, 2014]. In addition, their behaviour becomes more complex when large deformations are reached that influence structural parameters such as crosslinking, molecular weights and crystallinity degree [Ayoub et al., 2010]. Particularly relevant is the consideration of thermal and strain rate effects on the material behaviour. There is a strong relationship between thermoplastic polymers behaviour and temperature, with thermal softening as the temperature increases. In addition, the yielding and plastic flow behaviours are influenced by strain rate resulting in a loss in ductility and a continuous hardening as strain rate increases [Rae et al., 2007; Serban et al., 2013; El-Qoubaa et al., 2016]. This relationship becomes more complex at high strain rates of deformation where material hardening, induced by strain rate effects, is in competition with the significant thermal softening induced by adiabatic heating [Mohagheghian et al., 2015]. This coupling between the thermal and mechanical behaviour of thermoplastic polymers also affects the relaxation or transition temperatures at which the material suddenly changes its behaviour [Gaymans et al., 2000; Jordan et al., 2007; Srivastava et al., 2010; Nasraoui et al., 2012]. The transition temperatures delimit the different behaviour regions, highlighting the glass transition and the beta transition, which are related to a ductile-to-brittle change in the material behaviour (see Chapter 5.3).

The complicated behaviour of thermoplastic polymers makes it challenging to predict their mechanical response and performance when designing products made from this kind of materials. Therefore, reliable models able to describe the different aspects of thermoplastic polymers behaviour, including the variables which govern their mechanical response, are of both theoretical and practical interest. In these terms, the constitutive modelling of thermoplastic polymers has been widely investigated and constitutive models have been developed generally relying on two main approaches: phenomenological and physical.

Popelar et al. (2004) developed a phenomenological approach to describe the behaviour of semi-crystalline polymers, proposing a nonlinear viscoelastic model based on the Schapery (1984) viscoelasticity theory. Subsequent researchers developed constitutive models including viscoplasticity [Colak and Dusunceli, 2006; Zaïri et al., 2008]. Halabi et al. (2011) applied a homogenized phenomenological model to study thermoplastic cranial implants and more recently, phenomenological approaches, based on models developed for metal, have been used to consider the viscoplastic behaviour of thermoplastic polymers [Louche et al., 2009; El-Qoubaa and Othman, 2016].

The physical approaches introduce features of the microstructure in the mathematical development of the constitutive model. The physical assumptions take into account two key factors: firstly the crystalline regions in the microstructure which govern the material response in the early stages of deformation; and secondly the amorphous phase during which plastic deformation is related to relative movements between the molecule chains that control the later stages of deformation. In this regard, models developed for amorphous polymers can be employed to define the amorphous regions in semi-crystalline polymers. Haward and Thackray (1968) proposed a one-dimensional description incorporating both yielding and strain hardening; and numerous researchers proposed three-dimensional models inspired by the latter [Boyce et al., 1988; Arruda and Boyce, 1993; Wu and van der Giessen, 1995; Ayoub et al., 2010]. Mulliken and Boyce (2006) proposed a model which captures the transition in the yield behavior and also predict the post-yield large strain behaviour. Based on this approach, Sarva et al. (2007) studied the impact behaviour of polycarbonate considering large strain rate-dependent elastic-viscoplasticity. More recently, Polanco-Loria et al. (2010) developed a hyperelastic-viscoplastic material model for semi-crystalline polymers which includes pressure dependence, volumetric plastic strain and strain-rate sensitivity. Following the thermomechanical constitutive models of amorphous polymers [Boyce et al., 2000; Srivastava et al., 2010; Billon, 2012] and the non-gaussian statistic approach of entangled polymer network [Edwards and Vilgis,1986], Maurel-Pantel et al. (2015) developed a thermo-mechanical large deformation constitutive approach for semi-crystalline polymers.

In relation to semi-crystalline polymers, despite the abundant literature on their mechanical behaviour under isothermal conditions, only a few studies focus on thermomechanical modeling and these are limited to loading tests where low strain rate values are reached [Bergström et al., 2003; Maurel-Pantel et al., 2015]. Moreover, there is a critical strain rate at which the system is expected to behave adiabatically depending on thermal properties and loading conditions [Kendall et al., 2013; Kendall et al., 2014]. This effect introduces a change in the material behaviour related to the temperature

increment due to plastic dissipation and the associated thermal softening. The thermomechanical coupling must be taken into account by the constitutive model to obtain successful results in dynamic conditions. This consideration is especially relevant at high strain rates where plastic mechanical deformation leads to important local temperature increases.

The objective of this chapter is to provide a constitutive model which takes into account thermal softening, strain rate and pressure sensitivities and temperature evolution. The model follows the formulation proposed by Polanco-Loria et al. (2010), who developed their model assuming isothermal conditions. Moreover, the formulation has been developed under the assumptions of large deformation within a thermomechanical framework. The constitutive model developed herein allows for predicting the mechanical behaviour of semi-crystalline polymers not only under isothermal assumptions but also providing the evolution of temperature due to plastic dissipation, being this one of the key contributions of the present work. This point is quite relevant since at high strain rates the change in temperature due to adiabatic heating can lead to important changes in the polymer behaviour. These changes in the deformation mechanisms are controlled by transition temperatures and, therefore, the temperature prediction provided by the model is essential for evaluating if the material is working between the ductile-to-brittle and the glass transition temperatures. This is an important point since these polymers show a considerable loss in ductility and increase in stiffness and yield stress below their ductile-to-brittle temperature. In the case of exceeding the glass transition temperature, they show a marked reduction in stiffness and yield stress and also an increase in ductility. The constitutive model presented herein provides reliable predictions from the ductile-to-brittle transition until the glass transition, the temperature range within the assumptions of the model are valid.

The model has been applied to describe the behaviour of the semi-crystalline polymer polyether-ether-ketone (PEEK) in a wide range of strain rates and testing temperatures. Its parameters have been identified from experimental data of uniaxial compression and tensile tests published by Rae et al. (2007). In order to analyze the predictive capacity under dynamic conditions, the model has been implemented in a FE code to study two different problems: low velocity impact test on PEEK thin plates and dynamic necking on PEEK slender bar. In addition, both dynamic applications determine the interplay between strain rate and thermal effects and demonstrate the capacity of the model to analyze the thermomechanical behaviour of semi-crystalline polymers.

6.2 Description of the constitutive model

According to different authors [Haward and Thackray, 1968; Boyce et al., 2000], the stress-strain behaviour for thermoplastic polymers can be interpreted as a response to overcoming two basic forms of resistances to deformation:

- Intermolecular resistance (I): an intermolecular barrier to deformation which is increased by the development of strain-induced crystallization.
- Network resistance (N): an entropic resistance caused by molecular orientation.

The intermolecular resistance is taken to increase due to the strain-induced crystallization and results in the initially stiff behaviour as well as the rate and temperature dependence of initial flow. The network resistance resulting from molecular alignment provokes the strain hardening/stiffening behaviour. Based on the additive definition of stress state understood as the combination of both resistance contributions, Polanco-Loria et al. (2010) developed a constitutive model restricted to isothermal conditions. The Polanco-Loria model can exhibit a limitation when, upon the deformation process, a temperature variation is expected. However, the present model takes into account not only the material hardening due to strain rate effects but also its coupling with thermal effects which results in a competition between hardening due to strain rate sensitivity and softening due to temperature sensitivity. This effect is especially relevant for semi-crystalline polymers which exhibit a strong dependence of their mechanical behaviour on temperature. Specifically under dynamic conditions, plastic dissipation can cause a considerable temperature increase.

The work presented herein proposes a hyperelastic-thermoviscoplastic material model which takes into account thermomechanical coupling. The additive definition of stress state as the combination of resistance contributions under isothermal or adiabatic conditions, (Fig. 6.1a), allows us to configure the rheological scheme of the constitutive model, (Fig. 6.1b). The rate and temperature-dependent part (*Intermolecular resistance*, denoted by I) is taken to originate from an intermolecular barrier to deformation. A Neo-Hookean hyperelastic model was selected for describing the elastic spring characterizing the initial elastic contribution due to internal energy change, denoted by I_1. The thermoviscoplastic behaviour is taken into account by a nonlinear viscoplastic dashpot capturing the rate and temperature dependent behaviour of the material. This component has been defined in parallel to a friction element which activates the nonlinear viscoplastic dashpot when a yield function is satisfied. In this regard, the constitutive elements must be understood as a physically motivated choice but not as a faithful representation of the polymer microstructural response. The set of elements composed by the nonlinear viscoplastic dashpot and the friction element is denoted by I_2 and defines

the shape of the thermoviscoplastic contribution to the intermolecular resistance stress-strain curve. The equilibrium part of the stress-strain behaviour (*Network resistance*, denoted by N) acts as the backbone of the overall material stress-strain behaviour and originates from an evolving entropic resistance due to molecular orientation. This part is composed of a unique spring which implies a purely elastic contribution to the stress-strain behaviour. Moreover, *thermal expansion* is taken into account by the addition of an element denoted by T. Details of constitutive relations defining each element will be given next.

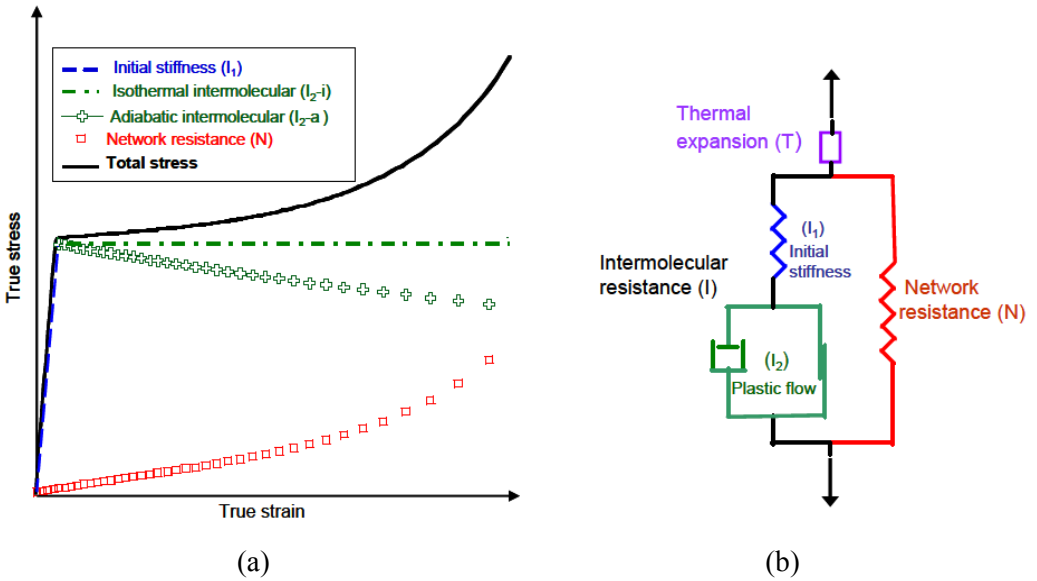

Figure 6.1: (a) Stress contributions from intermolecular and network resistances and their decompositions; (b) rheological scheme of the present constitutive model.

6.2.1 Kinematics

As shown in Fig. 6.2, four configurations have been established in order to define the kinematics of the model, going from an initial reference configuration Ω_o to a final loaded or current configuration Ω. Two intermediate configurations have been added allowing us to define the constitutive equations of both branches of the model. The first one is referred to as a dilated configuration $\overline{\Omega}$ in which only thermal deformation is accounted for, and the second one is referred to as a dilated relaxed configuration $\overline{\overline{\Omega}}$ in which both thermal and plastic deformations are considered.

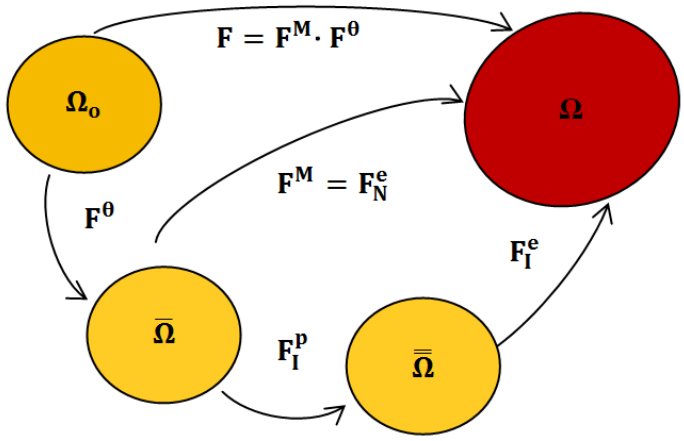

Figure 6.2: Kinematics of the model showing the reference or initial configuration $\boldsymbol{\Omega_o}$, the dilated configuration $\bar{\boldsymbol{\Omega}}$, the dilated relaxed configuration $\bar{\bar{\boldsymbol{\Omega}}}$, and the current or loaded configuration Ω.

Taking **X** as an arbitrary material point in the undeformed or reference configuration Ω_o, it is possible to reach the current configuration Ω, through the mapping $\mathbf{x} = \boldsymbol{\chi}(\mathbf{X},t)$, from which the deformation gradient (**F**), velocity (**v**) and velocity gradient (**l**) can be derived as

$$\mathbf{F} = \nabla_X \boldsymbol{\chi};\ \mathbf{v} = \dot{\boldsymbol{\chi}};\ \mathbf{l} = \nabla_x \mathbf{v} = \dot{\mathbf{F}}\mathbf{F}^{-1} \tag{6.1}$$

respectively, where ∇_X denotes the material gradient and ∇_x denotes the spatial gradient.

A multiplicative split is used to break down the deformation gradient into thermal, $\mathbf{F^\theta}$, and mechanical, $\mathbf{F^M}$, parts [Yu et al., 1997; Kamlah and Tsakmakis, 1999; Lion, 2000; Li and Xu, 2011; Chen et al., 2014; Ge et al., 2014]

$$\mathbf{F} = \mathbf{F^M F^\theta} \tag{6.2}$$

The mechanical part of the deformation gradient, $\mathbf{F^M}$, is equivalent to the intermolecular resistance, $\mathbf{F_I^M}$, and to the network resistance, $\mathbf{F_N^M}$, according to the rheological model

$$\mathbf{F^M} = \mathbf{F_I^M} = \mathbf{F_N^M} \tag{6.3}$$

Thus, the same volume change represented by the Jacobian, J^M, has been associated with both mechanical parts of the model given as the determinant of each part of the deformation gradient

$$J^M = J_I = J_N = \det(\mathbf{F^M}) \tag{6.4}$$

where J_I is the Jacobian associated with intermolecular resistance and J_N is the Jacobian associated with network resistance. The total volume change can be represented by the total Jacobian composed of both mechanical and thermal contributions

$$J=J^M J^\theta = \det(\mathbf{F}) \tag{6.5}$$

The mechanical deformation gradient of network resistance is defined as purely elastic, $\mathbf{F_N^M = F_N^e}$. The intermolecular resistance describes the thermoviscoplastic response of the material. The deformation gradient $\mathbf{F_I^M}$ can be decomposed into the component $\mathbf{F_{I_1}^M}$ associated with the Neo-Hookean hyperelastic spring and the component $\mathbf{F_{I_2}^M}$ associated with the nonlinear viscoplastic dashpot [Kroner, 1960; Lee, 1969].

$$\mathbf{F_I^M = F_{I_1}^M F_{I_2}^M} \tag{6.6}$$

The kinematics of the model can be defined in terms of the deformation gradient decomposition for the intermolecular resistance as

$$\mathbf{F_{I_1}^M = F_I^e} \tag{6.7}$$

$$\mathbf{F_{I_2}^M = F_I^p} \tag{6.8}$$

where $\mathbf{F_I^e}$ represents the elastic part due to reversible elastic mechanisms of the intermolecular resistance, and $\mathbf{F_I^p}$ represents the inelastic part due to irreversible mechanisms.

Combining Eqs. (6.2), (6.3) and (6.6) makes it possible to obtain the following expression for the total deformation gradient

$$\mathbf{F = F_I^e F_I^p F^\theta = F_N^e F^\theta} \tag{6.9}$$

where $\mathbf{F_N^e}$ represents the elastic part due to reversible elastic mechanisms of the network resistance. The intermediate dilated configuration $\bar{\Omega}$, can be obtained from Ω by mapping through $\mathbf{F^{-M}}$. In case of the dilated relaxed configuration $\bar{\bar{\Omega}}$, it can be obtained from Ω by mapping through $\mathbf{F_I^{-e}}$.

The velocity gradient **l,** in terms of the kinematics associated with the intermolecular resistance elements, can be written using Eq. (6.9) as

$$\mathbf{l} = \dot{\mathbf{F}}\mathbf{F}^{-1} = \mathbf{l_I^e} + \mathbf{F_I^e}\bar{\bar{\mathbf{L}}}_\mathbf{I}^\mathbf{p}\mathbf{F_I^{-e}} + \mathbf{F_I^e}\mathbf{F_I^p}\bar{\mathbf{L}}^\boldsymbol{\Theta}\mathbf{F_I^{-p}}\mathbf{F_I^{-e}} \tag{6.10}$$

where $\mathbf{l_I^e} = \dot{\mathbf{F}}_\mathbf{I}^\mathbf{e}\mathbf{F_I^{-e}}$ is the elastic component of the velocity gradient in the current configuration, $\bar{\mathbf{L}}^\boldsymbol{\Theta} = \dot{\mathbf{F}}^\boldsymbol{\Theta}\mathbf{F}^{-\boldsymbol{\Theta}}$ is the thermal component of the velocity gradient in the dilated configuration and the plastic component $\bar{\bar{\mathbf{L}}}_\mathbf{I}^\mathbf{p}$ can be defined in the dilated relaxed configuration $\bar{\bar{\Omega}}$ as

$$\bar{\bar{\mathbf{L}}}_\mathbf{I}^\mathbf{p} = \dot{\mathbf{F}}_\mathbf{I}^\mathbf{p}\mathbf{F_I^{-p}} \tag{6.11}$$

This velocity gradient can be decomposed into its symmetric and skew parts by $\bar{\bar{\mathbf{L}}}_\mathbf{I}^\mathbf{p} = \bar{\bar{\mathbf{D}}}_\mathbf{I}^\mathbf{p} + \bar{\bar{\mathbf{W}}}_\mathbf{I}^\mathbf{p}$. In this work, $\bar{\bar{\Omega}}$ is assumed to be invariant to the rigid body rotations of the current configuration, that is $\bar{\bar{\mathbf{W}}}_\mathbf{I}^\mathbf{p}$=0, and therefore $\bar{\bar{\mathbf{D}}}_\mathbf{I}^\mathbf{p}$=$\bar{\bar{\mathbf{L}}}_\mathbf{I}^\mathbf{p}$ [Boyce et al., 1988; Gurtin and Anand, 2005]. Regarding the thermal component of the velocity gradient, it can be also decomposed into its symmetric and asymmetric parts by $\bar{\mathbf{L}}^\boldsymbol{\Theta} = \bar{\mathbf{D}}^\boldsymbol{\Theta} + \bar{\mathbf{W}}^\boldsymbol{\Theta}$. According to Bouvard et al. (2013), the thermal contribution to the deformation gradient is assumed to be isotropic. Therefore, $\mathbf{F}^\boldsymbol{\Theta}$ is spheric and it is possible to assume $\bar{\mathbf{W}}^\boldsymbol{\Theta} = \mathbf{0}$.

The total velocity gradient can be likewise defined through the kinematics of the network resistance using Eq. (6.9) as

$$\mathbf{l} = \dot{\mathbf{F}}\mathbf{F}^{-1} = \mathbf{l_N^e} + \mathbf{F_N^e}\bar{\mathbf{L}}^\boldsymbol{\Theta}\mathbf{F_N^{-e}} \tag{6.12}$$

where $\mathbf{l_N^e} = \dot{\mathbf{F}}_\mathbf{N}^\mathbf{e}\mathbf{F_N^{-e}}$.

6.2.2 Decomposition of stress

According to the stress decomposition shown in Fig. 6.1 (left) and the arrangement of the rheological model elements depicted in Fig. 6.1 (right), the total stress is determined by the contribution of the intermolecular and the network resistances. The total Cauchy

stress $\boldsymbol{\sigma}$ in the polymer is given by the sum of the Cauchy stresses of the intermolecular resistance $\boldsymbol{\sigma_I}$ and the network resistance $\boldsymbol{\sigma_N}$

$$\boldsymbol{\sigma} = \boldsymbol{\sigma_I} + \boldsymbol{\sigma_N} \tag{6.13}$$

where the contribution of the intermolecular resistance $\boldsymbol{\sigma_I}$ is equal to both the Cauchy stress $\boldsymbol{\sigma_{I_1}}$ associated with the Neo-Hookean hyperelastic spring and the Cauchy stress $\boldsymbol{\sigma_{I_2}}$ associated with the nonlinear viscoplastic dashpot in parallel with the friction element

$$\boldsymbol{\sigma_I} = \boldsymbol{\sigma_{I_1}} = \boldsymbol{\sigma_{I_2}} \tag{6.14}$$

The spring of the intermolecular resistance provides the initial stiffness and therefore the initial slope of the stress-strain curve depending on temperature. Once the yield stress is reached, the contribution of the dashpot starts which introduces a temperature softening if temperature increases. At the same time, the model takes into account the contribution of the spring presented in the network resistance which describes a hyperelastic entropic resistance originally proposed as the eight chain model by Arruda and Boyce (1993). This model determines the network response considering eight orientations of principal stretch space, allowing it to simulate a true network response of cooperative chain stretching.

6.2.3 Thermodynamics

In this section, the thermodynamic consistency of the model is imposed by the constitutive relations and an expression establishing the temperature evolution is obtained from the first and the second thermodynamics principles. Although most authors carry out this development in the dilated relaxed configuration [Bouvard et al., 2013; Maurel-Pantel et al., 2015], here the process has been developed in the dilated configuration $\overline{\Omega}$ as it is the common intermediate configuration of the two constitutive branches. According to Holzapfel (2000), the reduced global form of energy balance expressed in spatial description is taken as the starting point

$$\frac{\mathrm{D}}{\mathrm{Dt}}\int_{\Omega} \mathrm{e}\mathrm{dv} = \int_{\Omega} (\boldsymbol{\sigma}\colon \mathbf{d} - \nabla_{\mathrm{x}}\mathbf{q} + \mathrm{r})\mathrm{dv} \tag{6.15}$$

e being the specific internal energy per unit volume, $\mathbf{q}$ the heat flux per unit area and r the heat source per unit volume in Ω. The left hand side term of this equation can be rewritten by taking into account the relation between elemental volumes in $\Omega(\mathrm{dv})$, $\overline{\Omega}(\mathrm{d}\overline{\mathrm{V}})$ and $\Omega_0(\mathrm{dV})$, namely $\mathrm{dv} = \mathrm{J}^{\mathrm{M}}\mathrm{d}\overline{\mathrm{V}} = \mathrm{JdV}$, then

$$\frac{D}{Dt}\int_{\Omega} \text{edv} = \frac{D}{Dt}\int_{\Omega_0} e_o dV = \int_{\bar{\Omega}} \left(\dot{\bar{e}} + \bar{e}tr\left(\bar{\mathbf{D}}^{\boldsymbol{\theta}}\right)\right) d\bar{V} \tag{6.16}$$

where e_0 is the specific internal energy per unit volume in Ω_0, and the relation $\frac{\partial J^{\boldsymbol{\theta}}}{\partial t} = J^{\theta}tr\left(\bar{\mathbf{D}}^{\boldsymbol{\theta}}\right)$ has been used. Notice that since the reference volume V is independent of time, the previous expression can be written $\frac{D}{Dt}\int_{\Omega_0} e_0 dV = \int_{\Omega_0} \dot{e}_0 dV$.

The right hand term in Eq. (6.15), can be written in the different configurations as

$$\int_{\Omega} (\boldsymbol{\sigma}: \mathbf{d} - \nabla_x \mathbf{q} + r)dv = \int_{\Omega_0}\left(\mathbf{P}: \dot{\mathbf{F}} - \nabla_X \mathbf{Q} + R\right)dV = \int_{\bar{\Omega}} (\boldsymbol{\sigma}: \mathbf{d} - \nabla_x \mathbf{q} + r)J^M d\bar{V} \tag{6.17}$$

where **P**, **Q** and R respectively are the first Piola-Kirchhoff stress, the heat flux per unit area and the heat source per unit volume in Ω_0.

The stress power per unit volume in Ω can be expressed using Eqs. (6.10) and (6.13) and considering the definition of the velocity gradient $\mathbf{l} = \mathbf{d} + \mathbf{w}$, as

$$\boldsymbol{\sigma}: \mathbf{d} = \boldsymbol{\sigma}: (\mathbf{l} - \mathbf{w}) = \boldsymbol{\sigma}: \mathbf{l} - \boldsymbol{\sigma}: \mathbf{w} = \boldsymbol{\sigma}: \mathbf{l} = \boldsymbol{\sigma}_\mathbf{I}: \mathbf{l} + \boldsymbol{\sigma}_\mathbf{N}: \mathbf{l} \tag{6.18}$$

where **d** is the total rate of deformation tensor and **w** is the total spin tensor.

Using the velocity gradient decomposition, Eq. (6.10), it is possible to develop the term associated with the intermolecular contribution to the stress per unit volume as

$$\boldsymbol{\sigma}_\mathbf{I}: \mathbf{l} = \boldsymbol{\sigma}_\mathbf{I}: \mathbf{l}_\mathbf{I}^\mathbf{e} + \boldsymbol{\sigma}_\mathbf{I}: \mathbf{F}_\mathbf{I}^\mathbf{e}\bar{\mathbf{L}}_\mathbf{I}^\mathbf{p}\mathbf{F}_\mathbf{I}^{-\mathbf{e}} + \boldsymbol{\sigma}_\mathbf{I}: \mathbf{F}_\mathbf{I}^\mathbf{e}\mathbf{F}_\mathbf{I}^\mathbf{p}\bar{\mathbf{L}}^{\boldsymbol{\theta}}\mathbf{F}_\mathbf{I}^{-\mathbf{p}}\mathbf{F}_\mathbf{I}^{-\mathbf{e}} = \boldsymbol{\sigma}_\mathbf{I}: \mathbf{d}_\mathbf{I}^\mathbf{e} + \boldsymbol{\sigma}_\mathbf{I}: \mathbf{F}_\mathbf{I}^\mathbf{e}\bar{\bar{\mathbf{D}}}_\mathbf{I}^\mathbf{p}\mathbf{F}_\mathbf{I}^{-\mathbf{e}} + \boldsymbol{\sigma}_\mathbf{I}: \mathbf{F}^\mathbf{M}\bar{\mathbf{D}}^{\boldsymbol{\theta}}\mathbf{F}^{-\mathbf{M}} \tag{6.19}$$

Rearranging this equation and expressing it in the dilated configuration $\bar{\Omega}$

$$\boldsymbol{\sigma}_\mathbf{I}: \mathbf{l} = J^{-M}\left(\bar{\mathbf{M}}_\mathbf{I}: \bar{\mathbf{D}}^\mathbf{p} + \bar{\mathbf{M}}_\mathbf{I}: \bar{\mathbf{D}}^{\boldsymbol{\theta}} + \bar{\mathbf{S}}_\mathbf{I}: \mathbf{F}^{\mathbf{MT}}\mathbf{d}_\mathbf{I}^\mathbf{e}\mathbf{F}^\mathbf{M}\right) \tag{6.20}$$

Using the velocity gradient decomposition, Eq. (6.12), it is possible to develop the term associated with the network contribution to the stress per unit volume as

$$\boldsymbol{\sigma}_\mathbf{N}: \mathbf{l} = \boldsymbol{\sigma}_\mathbf{N}: \mathbf{l}_\mathbf{N}^\mathbf{e} + \boldsymbol{\sigma}_\mathbf{N}: \mathbf{F}_\mathbf{N}^\mathbf{e}\overline{\mathbf{L}^{\boldsymbol{\theta}}}\mathbf{F}_\mathbf{N}^{-\mathbf{e}} = \boldsymbol{\sigma}_\mathbf{N}: \mathbf{d}_\mathbf{N}^\mathbf{e} + \boldsymbol{\sigma}_\mathbf{N}: \mathbf{F}_\mathbf{N}^\mathbf{e}\bar{\mathbf{D}}^{\boldsymbol{\theta}}\mathbf{F}_\mathbf{N}^{-\mathbf{e}} \tag{6.21}$$

Rearranging this equation and expressing it in the dilated configuration $\bar{\Omega}$

$$\boldsymbol{\sigma}_{\mathbf{N}}:\mathbf{l} = \mathrm{J}^{-\mathrm{M}}\left(\bar{\mathbf{M}}_{\mathbf{N}}:\bar{\mathbf{D}}^{\boldsymbol{\theta}} + \bar{\mathbf{S}}_{\mathbf{N}}:\mathbf{F}^{\mathbf{MT}}\mathbf{d}_{\mathbf{N}}^{\mathbf{e}}\mathbf{F}^{\mathbf{M}}\right) \tag{6.22}$$

Using the expressions developed in Eqs. (6.16), (6.17), (6.20) and (6.21) into Eq. (6.15), the local form of the balance energy can be expressed in the dilated configuration $\bar{\Omega}$ as

$$\dot{\bar{e}} + \bar{e}\mathrm{tr}\left(\bar{\mathbf{D}}^{\boldsymbol{\theta}}\right) = \bar{\mathbf{M}}_{\mathbf{I}}:\bar{\mathbf{D}}^{\mathbf{p}} + \bar{\mathbf{M}}_{\mathbf{I}}:\bar{\mathbf{D}}^{\boldsymbol{\theta}} + \bar{\mathbf{S}}_{\mathbf{I}}:\mathbf{F}^{\mathbf{MT}}\mathbf{d}_{\mathbf{I}}^{\mathbf{e}}\mathbf{F}^{\mathbf{M}} + \bar{\mathbf{M}}_{\mathbf{N}}:\bar{\mathbf{D}}^{\boldsymbol{\theta}} + \bar{\mathbf{S}}_{\mathbf{N}}:\mathbf{F}^{\mathbf{MT}}\mathbf{d}_{\mathbf{N}}^{\mathbf{e}}\mathbf{F}^{\mathbf{M}} - \bar{\nabla}_{\mathrm{x}}\bar{\mathbf{Q}} + \bar{\mathrm{R}} \tag{6.23}$$

where $\bar{e}$ is the specific internal energy, $\bar{\mathbf{Q}}$ is the heat flux per unit area and $\bar{\mathrm{R}}$ is the heat source per unit volume in $\bar{\Omega}$. $\bar{\mathbf{S}}_{\mathbf{I}}$ is the second Piola-Kirchhoff stress of the intermolecular resistance expressed in $\bar{\Omega}$ as $\bar{\mathbf{S}}_{\mathbf{I}} = \mathrm{J}^{\mathrm{M}}\mathbf{F}_{\mathbf{I}}^{-\mathbf{M}}\boldsymbol{\sigma}_{\mathbf{I}}\mathbf{F}_{\mathbf{I}}^{-\mathbf{MT}}$ and $\bar{\mathbf{M}}_{\mathbf{I}} = \mathbf{F}_{\mathbf{I}}^{\mathbf{MT}}\mathbf{F}_{\mathbf{I}}^{\mathbf{M}}\bar{\mathbf{S}}_{\mathbf{I}}$ is the Mandel stress in $\bar{\Omega}$. $\bar{\mathbf{S}}_{\mathbf{N}}$ and $\bar{\mathbf{M}}_{\mathbf{N}}$ are the corresponding stress tensors of the network resistance.

The global form of the Clausius-Duhem inequality, in spatial description [Holzapfel, 2000] is given by

$$\frac{\mathrm{D}}{\mathrm{Dt}}\int_{\Omega}\eta\mathrm{dv} + \int_{\Omega}\left(\nabla_{\mathrm{x}}\left(\frac{\mathbf{q}}{\theta}\right) - \frac{\mathrm{r}}{\theta}\right)\mathrm{dv} \geq 0 \tag{6.24}$$

This equation can be also written in local form expressed as

$$\dot{\bar{\eta}} + \bar{\eta}\mathrm{tr}\left(\bar{\mathbf{D}}^{\boldsymbol{\theta}}\right) - \frac{\bar{\mathrm{R}}}{\theta} + \frac{1}{\theta}\bar{\nabla}_{\mathrm{x}}\bar{\mathbf{Q}} - \frac{1}{\theta^{2}}\bar{\mathbf{Q}}\bar{\nabla}_{\mathrm{x}}\theta \geq 0 \tag{6.25}$$

where $\bar{\eta}$ is the specific internal entropy per unit volume and θ is the current temperature.

The Helmholtz free energy per unit volume in $\bar{\Omega}$, $\bar{\Psi}$, is defined as a function of the internal energy and entropy by

$$\bar{\Psi} = \bar{e} - \theta\bar{\eta} \tag{6.26}$$

and expressed in rate form

$$\dot{\bar{\Psi}} = \dot{\bar{e}} - \dot{\theta}\bar{\eta} - \theta\dot{\bar{\eta}} \tag{6.27}$$

The Clausius-Duhem inequality can be alternatively expressed by using Eq. (6.26) and substituting the expression for $\bar{R}$ from Eq. (6.23) into Eq. (6.25)

$$-\dot{\bar{\Psi}} - \dot{\theta}\bar{\eta} - \bar{\Psi}\mathrm{tr}(\bar{\mathbf{D}}^{\boldsymbol{\theta}}) + \bar{\mathbf{M}}_{\mathbf{I}}:\bar{\mathbf{D}}^{\mathbf{p}} + \bar{\mathbf{M}}_{\mathbf{I}}:\bar{\mathbf{D}}^{\boldsymbol{\theta}} + \bar{\mathbf{M}}_{\mathbf{N}}:\bar{\mathbf{D}}^{\boldsymbol{\theta}} + \bar{\mathbf{S}}_{\mathbf{I}}:\mathbf{F}^{\mathbf{MT}}\mathbf{d}_{\mathbf{I}}^{\mathbf{e}}\mathbf{F}^{\mathbf{M}} + \bar{\mathbf{S}}_{\mathbf{N}}:\mathbf{F}^{\mathbf{MT}}\mathbf{d}_{\mathbf{N}}^{\mathbf{e}}\mathbf{F}^{\mathbf{M}} - \frac{1}{\theta}\bar{\mathbf{Q}}\bar{\nabla}_{x}\theta \geq 0 \tag{6.28}$$

The Helmholtz free energy function was assumed to be the combination of both deformation resistance contributions as $\bar{\Psi} = \bar{\Psi}^{\mathrm{I}}(\mathbf{C}_{\mathbf{I}}^{\mathbf{e}}, \theta) + \bar{\Psi}^{\mathrm{N}}(\mathbf{C}_{\mathbf{N}}^{\mathbf{e}})$ [Reese, 1998; Vladimirov et al., 2010; Brepols et al., 2014]. These components of the Helmholtz free energy function are directly related to the stress contribution of the Neo-Hookean spring in the case of the intermolecular resistance, $\bar{\Psi}^{\mathrm{I}}(\mathbf{C}_{\mathbf{I}}^{\mathbf{e}}, \theta)$, and to the stress contribution of the modification of the 8-chain model in case of the network resistance, $\bar{\Psi}^{\mathrm{N}}(\mathbf{C}_{\mathbf{N}}^{\mathbf{e}})$. Both functions can be found elsewhere [Bergström, 2015; Anand, 1996]. Therefore, the Helmholtz free energy function was assumed to depend on the tensors $\mathbf{C}_{\mathbf{I}}^{\mathbf{e}} = \mathbf{F}_{\mathbf{I}}^{\mathbf{eT}}\mathbf{F}_{\mathbf{I}}^{\mathbf{e}}$ and $\mathbf{C}_{\mathbf{N}}^{\mathbf{e}} = \mathbf{F}_{\mathbf{N}}^{\mathbf{eT}}\mathbf{F}_{\mathbf{N}}^{\mathbf{e}}$ and temperature as $\bar{\Psi} = \bar{\Psi}(\mathbf{C}_{\mathbf{I}}^{\mathbf{e}}, \mathbf{C}_{\mathbf{N}}^{\mathbf{e}}, \theta)$ (see *Appendix A* for more details). Thus, the rate of $\bar{\Psi}$ can be calculated as

$$\dot{\bar{\Psi}} = \frac{\partial\bar{\Psi}}{\partial\mathbf{C}_{\mathbf{I}}^{\mathbf{e}}}:\dot{\mathbf{C}}_{\mathbf{I}}^{\mathbf{e}} + \frac{\partial\bar{\Psi}}{\partial\mathbf{C}_{\mathbf{N}}^{\mathbf{e}}}:\dot{\mathbf{C}}_{\mathbf{N}}^{\mathbf{e}} + \frac{\partial\bar{\Psi}}{\partial\theta}\dot{\theta} \tag{6.29}$$

The first terms of the right hand side of Eq. (6.29) can be written as

$$\begin{aligned}
&\text{(a)}\ \frac{\partial\bar{\Psi}}{\partial\mathbf{C}_{\mathbf{I}}^{\mathbf{e}}}:\dot{\mathbf{C}}_{\mathbf{I}}^{\mathbf{e}} = \frac{\partial\bar{\Psi}}{\partial\mathbf{C}_{\mathbf{I}}^{\mathbf{e}}}:\left(\dot{\mathbf{F}}_{\mathbf{I}}^{\mathbf{eT}}\mathbf{F}_{\mathbf{I}}^{\mathbf{e}} + \mathbf{F}_{\mathbf{I}}^{\mathbf{eT}}\dot{\mathbf{F}}_{\mathbf{I}}^{\mathbf{e}}\right) = 2\mathbf{F}_{\mathbf{I}}^{\mathbf{e}}\frac{\partial\bar{\Psi}}{\partial\mathbf{C}_{\mathbf{I}}^{\mathbf{e}}}\mathbf{F}_{\mathbf{I}}^{\mathbf{eT}}:\dot{\mathbf{F}}_{\mathbf{I}}^{\mathbf{e}}\mathbf{F}_{\mathbf{I}}^{-\mathbf{e}} = 2\frac{\partial\bar{\Psi}}{\partial\mathbf{C}_{\mathbf{I}}^{\mathbf{e}}}:\mathbf{F}_{\mathbf{I}}^{\mathbf{eT}}\mathbf{d}_{\mathbf{I}}^{\mathbf{e}}\mathbf{F}_{\mathbf{I}}^{\mathbf{e}} \\
&\text{(b)}\ \frac{\partial\bar{\Psi}}{\partial\mathbf{C}_{\mathbf{N}}^{\mathbf{e}}}:\dot{\mathbf{C}}_{\mathbf{N}}^{\mathbf{e}} = \frac{\partial\bar{\Psi}}{\partial\mathbf{C}_{\mathbf{N}}^{\mathbf{e}}}:\left(\dot{\mathbf{F}}_{\mathbf{N}}^{\mathbf{eT}}\mathbf{F}_{\mathbf{N}}^{\mathbf{e}} + \mathbf{F}_{\mathbf{N}}^{\mathbf{eT}}\dot{\mathbf{F}}_{\mathbf{N}}^{\mathbf{e}}\right) = 2\mathbf{F}_{\mathbf{N}}^{\mathbf{e}}\frac{\partial\bar{\Psi}}{\partial\mathbf{C}_{\mathbf{N}}^{\mathbf{e}}}\mathbf{F}_{\mathbf{N}}^{\mathbf{eT}}:\dot{\mathbf{F}}_{\mathbf{N}}^{\mathbf{e}}\mathbf{F}_{\mathbf{N}}^{-\mathbf{e}} = 2\frac{\partial\bar{\Psi}}{\partial\mathbf{C}_{\mathbf{N}}^{\mathbf{e}}}:\mathbf{F}_{\mathbf{N}}^{\mathbf{eT}}\mathbf{d}_{\mathbf{N}}^{\mathbf{e}}\mathbf{F}_{\mathbf{N}}^{\mathbf{e}}
\end{aligned} \tag{6.30}$$

Assuming $\mathbf{F}^{\boldsymbol{\theta}}$ isotropic, $\bar{\mathbf{D}}^{\boldsymbol{\theta}} = f_{\theta}\dot{\theta}\mathbf{I}$ can be expressed in terms of a temperature-dependent function f_{θ}, as Bouvard et al. proposed (2013), and then $\mathrm{tr}\left(\bar{\mathbf{D}}^{\boldsymbol{\theta}}\right) = 3f_{\theta}\dot{\theta}$. Substituting these terms and using Eqs. (6.29) and (6.30) in Eq. (6.28), the Clausius-Duhem inequality can be rewritten as

$$\begin{aligned}
&\left(\mathbf{F}_{\mathbf{I}}^{\mathbf{p}}\bar{\mathbf{S}}_{\mathbf{I}}\mathbf{F}_{\mathbf{I}}^{\mathbf{pT}} - 2\frac{\partial\bar{\Psi}}{\partial\mathbf{C}_{\mathbf{I}}^{\mathbf{e}}}\right):\mathbf{F}_{\mathbf{I}}^{\mathbf{eT}}\mathbf{d}_{\mathbf{I}}^{\mathbf{e}}\mathbf{F}_{\mathbf{I}}^{\mathbf{e}} + \left(\bar{\mathbf{S}}_{\mathbf{N}} - 2\frac{\partial\bar{\Psi}}{\partial\mathbf{C}_{\mathbf{N}}^{\mathbf{e}}}\right):\mathbf{F}_{\mathbf{N}}^{\mathbf{eT}}\mathbf{d}_{\mathbf{N}}^{\mathbf{e}}\mathbf{F}_{\mathbf{N}}^{\mathbf{e}} + \bar{\mathbf{M}}_{\mathbf{I}}:\bar{\mathbf{D}}^{\mathbf{p}} + \\
&\left(-\frac{\partial\bar{\Psi}}{\partial\theta} - 3f_{\theta}\bar{\Psi} - \bar{\eta} + f_{\theta}(\bar{\mathbf{M}}_{\mathbf{I}} + \bar{\mathbf{M}}_{\mathbf{N}}):\mathbf{I}\right)\dot{\theta} - \frac{1}{\theta}\bar{\mathbf{Q}}\bar{\nabla}_{x}\theta \geq 0
\end{aligned} \tag{6.31}$$

Following the standard arguments used in the Coleman and Noll method [Coleman and Noll, 1963; Coleman and Gurtin, 1967], Eq. (6.31) must hold for any arbitrary variation of deformation and temperature. Then, the first, second and fourth terms of this equation must vanish. In this way, the second Piola-Kirchhoff stress associated with each constitutive branch, and the specific internal entropy per unit volume can be written as

$$\begin{aligned}
&(a)\bar{\mathbf{S}}_{\mathbf{I}} = \mathbf{F}_{\mathbf{I}}^{-\mathbf{p}} 2\frac{\partial \bar{\Psi}}{\partial \mathbf{C}_{\mathbf{I}}^{\mathbf{e}}} \mathbf{F}_{\mathbf{I}}^{-\mathbf{pT}} \\
&(b)\ \bar{\mathbf{S}}_{\mathbf{N}} = 2\frac{\partial \bar{\Psi}}{\partial \mathbf{C}_{\mathbf{N}}^{\mathbf{e}}} \\
&(c)\ \bar{\eta} = -\frac{\partial \bar{\Psi}}{\partial \theta} - 3f_\theta \bar{\Psi} + f_\theta(\bar{\mathbf{M}}_{\mathbf{I}} + \bar{\mathbf{M}}_{\mathbf{N}}) : \mathbf{I}
\end{aligned} \tag{6.32}$$

Now, it is possible to reduce the dissipation inequality to

$$\bar{\mathbf{M}}_{\mathbf{I}} : \bar{\mathbf{D}}^{\mathbf{p}} - \frac{1}{\theta}\bar{\mathbf{Q}}\bar{\nabla}_x\theta \geq 0 \tag{6.33}$$

The above equations can be combined to derive the heat equation. The rate of the free energy, Eq. (6.29), is rewritten now as

$$\dot{\bar{\Psi}} = \frac{1}{2}\mathbf{F}_{\mathbf{I}}^{\mathbf{p}}\bar{\mathbf{S}}_{\mathbf{I}}\mathbf{F}_{\mathbf{I}}^{\mathbf{pT}} : \dot{\mathbf{C}}_{\mathbf{I}}^{\mathbf{e}} + \frac{1}{2}\bar{\mathbf{S}}_{\mathbf{N}} : \dot{\mathbf{C}}_{\mathbf{N}}^{\mathbf{e}} + (-\bar{\eta} - 3f_\theta\bar{\Psi} + f_\theta(\bar{\mathbf{M}}_{\mathbf{I}} + \bar{\mathbf{M}}_{\mathbf{N}}) : \mathbf{I})\dot{\theta} \tag{6.34}$$

Using this expression in Eq. (6.26) with Eq. (6.23)

$$-\bar{\mathbf{M}}_{\mathbf{I}} : \bar{\mathbf{D}}^{\mathbf{p}} + \theta\dot{\bar{\eta}} + 3\bar{\eta}f_\theta\theta\dot{\theta} + \bar{\nabla}_x\bar{\mathbf{Q}} - \bar{R} = 0 \tag{6.35}$$

From Eq. (6.32) and the expressions for both Mandel stress components, $\bar{\mathbf{M}}_{\mathbf{I}} = \mathbf{F}_{\mathbf{I}}^{\mathbf{pT}}\mathbf{C}_{\mathbf{I}}^{\mathbf{e}}\mathbf{F}_{\mathbf{I}}^{\mathbf{p}}\bar{\mathbf{S}}_{\mathbf{I}}$ and $\bar{\mathbf{M}}_{\mathbf{N}} = \mathbf{C}_{\mathbf{N}}^{\mathbf{e}}\bar{\mathbf{S}}_{\mathbf{N}}$, the rate of the entropy $\bar{\eta}$ can be obtained by

$$\dot{\bar{\eta}} = -\left[3f_\theta\frac{\partial\bar{\Psi}}{\partial\mathbf{C}_{\mathbf{I}}^{\mathbf{e}}} + \frac{\partial^2\bar{\Psi}}{\partial\theta\,\partial\mathbf{C}_{\mathbf{I}}^{\mathbf{e}}} - f_\theta\frac{\partial\left(\mathbf{F}_{\mathbf{I}}^{\mathbf{pT}}\mathbf{C}_{\mathbf{I}}^{\mathbf{e}}\mathbf{F}_{\mathbf{I}}^{\mathbf{p}} : \bar{\mathbf{S}}_{\mathbf{I}}\right)}{\partial\mathbf{C}_{\mathbf{I}}^{\mathbf{e}}}\right] : \dot{\mathbf{C}}_{\mathbf{I}}^{\mathbf{e}} - \left[3f_\theta\frac{\partial\bar{\Psi}}{\partial\mathbf{C}_{\mathbf{N}}^{\mathbf{e}}} + \frac{\partial^2\bar{\Psi}}{\partial\theta\,\partial\mathbf{C}_{\mathbf{N}}^{\mathbf{e}}} - f_\theta\frac{\partial(\mathbf{C}_{\mathbf{N}}^{\mathbf{e}} : \bar{\mathbf{S}}_{\mathbf{N}})}{\partial\mathbf{C}_{\mathbf{N}}^{\mathbf{e}}}\right] : \dot{\mathbf{C}}_{\mathbf{N}}^{\mathbf{e}} + \frac{\partial\bar{\eta}}{\partial\theta}\dot{\theta} \tag{6.36}$$

The heat capacity per unit volume at constant volume $\bar{C} = \frac{\partial\bar{e}}{\partial\theta} = \frac{\partial}{\partial\theta}(\bar{\Psi} + \theta\bar{\eta})$ can be related with the last term of Eq. (6.36), using the expression obtained in Eq. (23.3) as $\bar{C} = \theta\frac{\partial\bar{\eta}}{\partial\theta} - 3f_\theta\bar{\Psi} + f_\theta\left(\mathbf{F}_{\mathbf{I}}^{\mathbf{pT}}\mathbf{C}_{\mathbf{I}}^{\mathbf{e}}\mathbf{F}_{\mathbf{I}}^{\mathbf{p}} : \bar{\mathbf{S}}_{\mathbf{I}} + \mathbf{C}_{\mathbf{N}}^{\mathbf{e}} : \bar{\mathbf{S}}_{\mathbf{N}}\right)$. Then, the heat equation is found combining Eqs. (6.35) and (6.36) as

$$\left(\bar{C} + 3f_\theta \bar{e} - f_\theta\left(\mathbf{F_I^{pT}C_I^eF_I^p}:\bar{\mathbf{S}}_\mathbf{I} + \mathbf{C_N^e}:\bar{\mathbf{S}}_\mathbf{N}\right)\right)\dot{\theta} = \bar{\mathbf{M}}_\mathbf{I}:\bar{\mathbf{D}}^\mathbf{p} + \theta\left[\frac{3}{2}f_\theta \mathbf{F_I^p}\bar{\mathbf{S}}_\mathbf{I}\mathbf{F_I^{pT}} - f_\theta\frac{\partial\left(\mathbf{F_I^{pT}C_I^eF_I^p}:\bar{\mathbf{S}}_\mathbf{I}\right)}{\partial \mathbf{C_I^e}} + \frac{1}{2}\frac{\partial\left(\mathbf{F_I^p}\bar{\mathbf{S}}_\mathbf{I}\mathbf{F_I^{pT}}\right)}{\partial\theta}\right]:\dot{\mathbf{C}}_\mathbf{I}^\mathbf{e} + \theta\left[\frac{3}{2}f_\theta\bar{\mathbf{S}}_\mathbf{N} - f_\theta\frac{\partial(\mathbf{C_N^e}:\bar{\mathbf{S}}_\mathbf{N})}{\partial \mathbf{C_N^e}} + \frac{1}{2}\frac{\partial(\bar{\mathbf{S}}_\mathbf{N})}{\partial\theta}\right]:\dot{\mathbf{C}}_\mathbf{N}^\mathbf{e} - \bar{\nabla}_X\bar{\mathbf{Q}} + \bar{R} \tag{6.37}$$

The first term of the right side in Eq. (6.37) represents plastic dissipation and the second, third and fourth terms represent the temperature evolution due to thermoelastic coupling. Notice that, in the formulation presented, the total plastic work is assumed to be converted into heat.

6.2.4 Thermal expansion

The thermal expansion is assumed to be isotropic, being the contribution of the thermal part to the deformation gradient defined in the form

$$\dot{\mathbf{F}}^\boldsymbol{\theta} = f_\theta \mathbf{F}^\boldsymbol{\theta}\dot{\theta} \tag{6.38}$$

where $\dot{\theta}$ is the time derivative of current temperature and $f_\theta = \alpha_\theta$ is the thermal expansion coefficient.

6.2.5 Intermolecular resistance: thermoviscoplasticity relations

This part of the model describes a hyperelastic-thermoviscoplastic response due to intermolecular resistance. The second Piola-Kirchhoff stress tensor in $\bar{\bar{\Omega}}$ can be obtained from Eq. (6.32a) and the relationship $\bar{\bar{\mathbf{S}}}_\mathbf{I} = J_I^{-p}\mathbf{F_I^p}\bar{\mathbf{S}}_\mathbf{I}\mathbf{F_I^{pT}}$. This tensor is related to the Cauchy stress tensor by $\boldsymbol{\sigma}_\mathbf{I} = J_I^{-e}\mathbf{F_I^e}\bar{\bar{\mathbf{S}}}_\mathbf{I}\mathbf{F_I^{eT}}$. Therefore, the contribution of the intermolecular resistance to the Cauchy stress tensor finally reads as

$$\boldsymbol{\sigma}_\mathbf{I} = \frac{\lambda_0 \ln(J_I^e)}{J_I}\mathbf{I} + \frac{\mu_0}{J_I}(\mathbf{B_I^e} - \mathbf{I}) \tag{6.39}$$

λ_0 and μ_0 being the classical Lamé constants of the linearized theory depending on the Young's modulus E and the Poisson coefficient ν associated with the linear spring. Young's modulus E usually varies with temperature in semi-crystalline thermoplastic polymers [Rae et al., 2007; Brown et al., 2007]. In line with Bouvard et al. (2013), we chose an expression for $E(\theta)$ with a linear dependence on temperature, which was observed to fit well with the experimental data

$$E(\theta) = E_{ref} + E_1(\theta - \theta_{ref}) \tag{6.40}$$

where E_{ref} is the Young's modulus at the reference temperature θ_{ref} and E_1 is a material parameter. The elastic left Cauchy-Green deformation tensor, $\mathbf{B_I^e}$, can be written as

$$\mathbf{B_I^e} = \mathbf{F_I^e F_I^{eT}} \tag{6.41}$$

The yield criterion is written as

$$f_I = \bar{\bar{\sigma}}_{eqI} - \sigma_T = 0 \tag{6.42}$$

The Rhagava equivalent stress $\bar{\bar{\sigma}}_{eqI}$ has been employed to include the pressure dependency in the yield function [Raghava et al., 1973; Raghava and Caddell, 1973]

$$\bar{\bar{\sigma}}_{eqI} = \frac{(\alpha-1)I_{1I} + \sqrt{(\alpha-1)^2 {I_{1I}}^2 + 12\alpha J_{2I}}}{2\alpha} \tag{6.43}$$

where α is a material parameter describing the pressure sensitivity and $I_{1I} = \mathrm{tr}\,\bar{\bar{\mathbf{M}}}_\mathbf{I}$ and $J_{2I} = \frac{1}{2}\bar{\bar{\mathbf{M}}}_\mathbf{I}^\mathbf{dev} : \bar{\bar{\mathbf{M}}}_\mathbf{I}^\mathbf{dev}$ are stress invariants of the Mandel stress tensor $\bar{\bar{\mathbf{M}}}_\mathbf{I} = \mathbf{C_I^e}\bar{\bar{\mathbf{S}}}_\mathbf{I}$ expressed in the configuration $\bar{\bar{\Omega}}$. Polanco-Loria et al. (2010) assume σ_T constant. In this work, a functional dependence on temperature has been defined for σ_T to include the softening in flow stress due to thermal effects as

$$\sigma_T = \sigma_{T0}\left(1 - \left(\frac{\theta-\theta_{ref}}{\theta_{melt}-\theta_{ref}}\right)^m\right) \tag{6.44}$$

where σ_{T0} is the value of σ_T at reference temperature in uniaxial tension, m is a temperature sensitivity parameter and θ_{melt} is the melting temperature of the material considered. By varying the parameter m, it is possible to control the temperature sensitivity of the material. The expression used in Eq. (6.44) has been employed in order to define thermal softening in polymers [Louche et al., 2009] and presents a potential dependence on θ according to the Stefan-Boltzmann theory.

The plastic component of the deformation gradient is defined from the expression which relates the plastic part of the velocity gradient, $\bar{\bar{\mathbf{L}}}_\mathbf{I}^\mathbf{p}$, with the temporal variation of the plastic deformation gradient, $\dot{\mathbf{F}}_\mathbf{I}^\mathbf{p}$, Eq. (6.11). In order to define the plastic velocity

gradient on the dilated relaxed configuration $\bar{\bar{\Omega}}$, a non-associated viscoplastic flow rule is assumed following the formulation proposed by Polanco-Loria et al. (2010) as

$$\bar{\bar{\mathbf{L}}}_{\mathbf{I}}^{\mathbf{p}} = \dot{\bar{\gamma}}_{\mathrm{I}}^{\mathrm{p}} \bar{\bar{\mathbf{r}}}_{\mathbf{I}}; \qquad \bar{\bar{\mathbf{r}}}_{\mathbf{I}} = \frac{\partial g_{\mathrm{I}}}{\partial \bar{\bar{\mathbf{M}}}_{\mathbf{I}}} \tag{6.45}$$

$\dot{\bar{\gamma}}_{\mathrm{I}}^{\mathrm{p}}$ being the viscoplastic multiplier and $\bar{\bar{\mathbf{r}}}_{\mathbf{I}}$ the gradient of the plastic potential g_{I} on $\bar{\bar{\Omega}}$ defined by

$$g_{\mathrm{I}} = \frac{(\beta-1)I_{1\mathrm{I}} + \sqrt{(\beta-1)^2 {I_{1\mathrm{I}}}^2 + 12\beta J_{2\mathrm{I}}}}{2\beta} \tag{6.46}$$

where β is a parameter which controls the volumetric plastic strain.

The plastic flow direction $\bar{\bar{\mathbf{r}}}_{\mathbf{I}}$ on $\bar{\bar{\Omega}}$ is obtained as

$$\bar{\bar{\mathbf{r}}}_{\mathbf{I}} = \frac{\partial g_{\mathrm{I}}}{\partial \bar{\bar{\mathbf{M}}}_{\mathbf{I}}} = f_1 \mathbf{I} + f_2 \bar{\bar{\mathbf{M}}}_{\mathbf{I}}^{\mathbf{dev}} \tag{6.47}$$

where the functions f_1 and f_2 read

$$f_1 = \frac{\partial g_{\mathrm{I}}}{\partial I_{1\mathrm{I}}} = \frac{\beta-1}{2\beta} + \frac{(\beta-1)^2 I_{1\mathrm{I}}}{2\cdot\beta\sqrt{(\beta-1)^2 {I_{1\mathrm{I}}}^2 + 12\beta J_{2\mathrm{I}}}} \tag{6.48}$$

$$f_2 = \frac{\partial g_{\mathrm{I}}}{\partial J_{2\mathrm{I}}} = \frac{3}{\sqrt{(\beta-1)^2 {I_{1\mathrm{I}}}^2 + 12\beta J_{2\mathrm{I}}}} \tag{6.49}$$

The viscoplastic multiplier $\dot{\bar{\gamma}}_{\mathrm{I}}^{\mathrm{p}}$, depends on the rate-sensitivity parameters $\dot{\varepsilon}_{0\mathrm{I}}$ and C, and indirectly on the temperature through σ_{T}

$$\dot{\bar{\gamma}}_{\mathrm{I}}^{\mathrm{p}} = \begin{cases} 0 & \text{if } f_{\mathrm{I}} \le 0 \\ \dot{\varepsilon}_{0\mathrm{I}} \left\{ \exp\left[\frac{1}{C} \left(\frac{\bar{\bar{\sigma}}_{\mathrm{eqI}}}{\sigma_{\mathrm{T}}} - 1 \right) \right] - 1 \right\} & \text{if } f_{\mathrm{I}} > 0 \end{cases} \tag{6.50}$$

6.2.6 Network resistance

As mentioned earlier, this part of the model describes a hyperelastic entropic resistance originally proposed by Arruda and Boyce (1993). The second Piola-Kirchhoff stress tensor in $\overline{\Omega}$ can be obtained from the strain energy potential defined according to Anand et al. (1996), Eq. (6.32b), and it is related by $\boldsymbol{\sigma_N} = J_N^{-1}\mathbf{F_N}\bar{\mathbf{S}}_\mathbf{N}\mathbf{F_N^T}$ with the Cauchy stress tensor. Thus, the contribution of this part to the Cauchy stress is defined as

$$\boldsymbol{\sigma_N} = \frac{C_R}{3J_N}\frac{\bar{\lambda}_L}{\bar{\lambda}}\mathfrak{L}^{-1}\left(\frac{\bar{\lambda}}{\bar{\lambda}_L}\right)(\mathbf{B_N^*} - \bar{\lambda}^2\mathbf{I}) + \frac{\kappa \ln(J_N)\mathbf{I}}{J_N} \tag{6.51}$$

where $\mathfrak{L}^{-1}$ is the inverse of the Langevin function, C_R is the initial elastic modulus of the network resistance, $\bar{\lambda}_L$ is the locking stretch and κ is a bulk modulus. The average total stretch ratio $\bar{\lambda}$ is calculated following Eq. (6.52)

$$\bar{\lambda} = \sqrt{\frac{1}{3}\mathrm{tr}(\mathbf{B_N^*})} \tag{6.52}$$

The distortional left Cauchy-Green deformation tensor, $\mathbf{B_N^*}$, represents the distortional part of $\mathbf{F_N^e}$ defined by

$$\mathbf{B_N^*} = \mathbf{F_N^*}(\mathbf{F_N^*})^T \tag{6.53}$$

Where

$$\mathbf{F_N^*} = J_N^{-1/3}\mathbf{F_N} \tag{6.54}$$

The contribution of the network resistance to the deformation gradient can be obtained from Eq. (6.9).

The developed constitutive model has been implemented in the FE code ABAQUS/Explicit to describe the thermomechanical behavior of semi-crystalline thermoplastic polymers. Once the constitutive model is defined, it is necessary to identify the parameters for the material being considered.

6.3 Identification of model parameters for PEEK polymer

In this section, the proposed constitutive model is used to deal with the thermomechanical behaviour of polyether-ether-ketone (PEEK) of grade 450 G.

Identification process

The identification process to obtain the model parameters for semi-crystalline thermoplastic polymers is based on the correspondence of the parameters with the mechanical response of the material in terms of the following blocks:

(i) *Linear response*: the model parameters E_{ref}, E_l and ν are related to the elastic contribution to the intermolecular resistance and determine the initial elastic response of the material depending on temperature. E_{ref} and E_l define the initial slopes of the stress-strain curves depending on temperature and ν is the Poisson ratio.

(ii) *Yield stress*: the parameters σ_{T0}, C, $\dot{\varepsilon}_{0A}$ and m define the yield stress of the material. C and $\dot{\varepsilon}_{0A}$ are associated with the nonlinear viscoplastic dashpot of the intermolecular resistance and σ_{T0} and m with the friction element of the intermolecular resistance which defines the yield function. C and $\dot{\varepsilon}_{0A}$ determine the strain rate sensitivity of yield stress and m the temperature sensitivity.

(iii) *Network response*: the network contribution to the stress state is established by the parameters C_R, $\bar{\lambda}_L$ and κ. Both parameters C_R and $\bar{\lambda}_L$ are associated with the spring element of network resistance. C_R is related to the initial elastic modulus of network resistance. The parameter $\bar{\lambda}_L$ is related to the maximum (fully extended) stretch that a molecule can be exposed to and κ is a bulk modulus used in applications where the mechanical behavior of the material is only defined by the network contribution (e.g. rubber modelling).

(iv) *Volumetric plastic strain sensitivity*: the parameter β, which defines the plastic potential, must be identified in order to control inelastic volume change.

(v) *Stress state sensitivity*: the parameter α must be identified to define the pressure sensitivity of the yield stress.

The parameter calibration of the semi-crystalline thermoplastic polymer considered in this study, PEEK, is based on reported mechanical characterization covering a wide range of temperatures and strain rates [Rae et al., 2007]. Therefore, knowing the influence of the parameters on the mechanical response of the material in terms of linear response,

yielding, network response, volumetric plastic strain and stress state, the identification procedure carried out is presented next.

The parameters E_{ref}, E_1, ν, C, $\dot{\varepsilon}_{0A}$, m, β and α can be directly obtained from the analysis of experimental data, values depicted in Table 6.2

From uniaxial stress-strain curves at the reference strain rate and for the range of temperatures selected, the model parameters E_{ref} and E_1 are identified in order to define the initial slope of the curves depending on temperature. The Poisson ratio (ν) is determined from the initial relation between transverse and longitudinal strains.

Using the nominal stress-strain curves at different strain rates and temperatures in compression, the parameters C and m are obtained. The strain rate sensitivity parameter C can be found by its relationship with the slope of the yield stress-strain rate curve. The temperature sensitivity parameter m is determined by its relationship with the slope of the yield stress-temperature curve. The reference strain rate $\dot{\varepsilon}_{0A}$ is taken as the lowest strain rate used in compression tests for which experimental data varying the initial temperature are available.

Based on the observations reported by El-Qoubaa and Othman (2014) in regard to the volume change of PEEK over a wide range of strain rates and temperatures, parameter β controlling the volumetric plastic strain has been defined as β=1 assuming volume preserving since they showed that PEEK's (visco)-plastic deformation is isochoric, independently of temperature and strain rate. Finally, the parameter α was obtained from the relation observed between the yield stresses reached in uniaxial compression and tensile tests.

A numerical model with the dimensions of the specimens employed in uniaxial compression tests by Rae et al. (2007), defined with C3D8R elements, was developed in ABAQUS/Explicit. This numerical model was used to identify the parameters σ_{T0}, C_R and $\bar{\lambda}_L$ from the true stress-strain curves shown in Fig. 6.3a as the main targets in comparing the experimental and predicted curves.

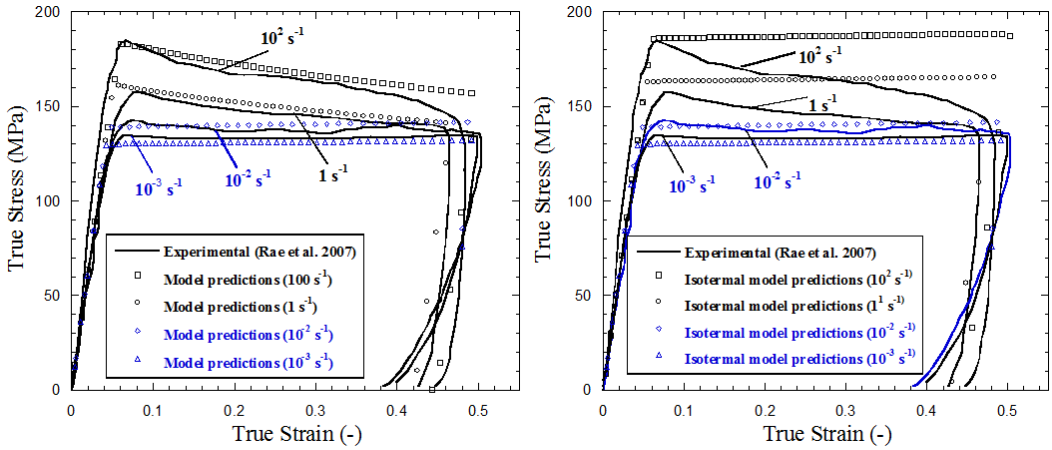

(a) (b)

Figure 6.3: Stress-strain experimental curves of PEEK at room temperature for different strain rate [Rae et al., 2007] versus: (a) model predictions; (b) predictions with isothermal hypothesis.

In these numerical simulations, temperature evolution has been included considering uniquely specific energy due to inelastic dissipation and heat conduction. Thermoelastic coupling is neglected in line with published studies for thermoplastic polymers [Bouvard et al., 2013]. Therefore, the temperature evolution can be obtained from Eq. (6.37) as

$$\dot{\theta} = \frac{\bar{\mathbf{M}}_{\mathbf{I}}:\bar{\mathbf{D}}^{\mathbf{p}}}{\bar{C}} - \frac{\bar{\nabla}_x \bar{\mathbf{Q}}}{\bar{C}} \tag{6.55}$$

Regarding the numerical implementation of the heat equation, the term associated to plastic dissipation was defined by updating the inelastic energy dissipated in each time increment. Moreover, the heat conduction is solved by the standard equation implemented in Abaqus considering the temperature as an extra degree of freedom.

Following the procedure proposed by Kendall et al. (2013; 2014) using Eq. (6.56), the rate at which the system is expected to behave adiabatically has been approximated from the size of the specimen, μ_t, and the thermal diffusivity of the specimen material, δ.

$$\begin{aligned} &(a)\delta = k/\rho\bar{C} \\ &(b)\ \mu_t = 2\sqrt{\delta\tau} \\ &(c)\ \dot{\varepsilon} = 1/\tau \end{aligned} \tag{6.56}$$

k being the thermal conductivity and τ a characteristic timescale for thermal diffusion. For PEEK compression specimens, the values of ρ and $\bar{C}$ are shown in Table 6.2, k=0.32 W/mK and μ_t=6.375 mm. Solving Eq. (6.56), a characteristic strain rate was found at $\dot{\varepsilon} \approx 10^{-2}$ s^{-1}. This characteristic strain rate is assumed as a reference value at which adiabatic heating is expected [Kendall et al., 2013; Kendall et al., 2014], and in such conditions thermal flow is neglected. Additionally, at strain rates lower than the characteristic one, isothermal conditions were assumed which permit to neglect the term associated to the inelastic dissipation. The parameters which finally define the PEEK material behaviour are depicted in Table 6.2.

Table 6.2: Material parameters for PEEK.

Initial elastic properties			**General properties**		
$\mathbf{E_{ref}}$ **(GPa)**	$\mathbf{E_1}$ **(MPa)**	**ν**	**ρ (kg/m^3)**	$\bar{\mathbf{C}}$ **(kJ/ m^{3}K)**	$\boldsymbol{\alpha_\theta}$ **(K^{-1})**
3.2	-3.0	0.4	1300	2834	$4.6 \cdot 10^{-6}$

Intermolecular resistance							
$\dot{\boldsymbol{\varepsilon}}_{\mathbf{0A}}$ **(s^{-1})**	**C**	$\boldsymbol{\sigma_{T0}}$ **(MPa)**	**m**	$\boldsymbol{\theta_{ref}}$ **(K)**	$\boldsymbol{\theta_{melt}}$ **(K)**	**α**	**β**
0.001	0.038	108	0.69	296	616	1.2	1.0

Network resistance		
$\mathbf{C_R}$ **(MPa)**	$\bar{\boldsymbol{\lambda}}_{\mathbf{L}}$	**κ**
0.4	5.5	0.0

Good agreement between the model predictions and experimental data [Rae et al., 2007] was found in terms of Young's Modulus, stress-strain curves, Fig. 6.3a, and in terms of yield stress depending on pressure, strain rate and temperature sensitivities, Figs. 6.4 and 6.5. It can be observed in Fig. 6.3b that, if isothermal conditions are assumed, the model predictions are considerably worse than the ones obtained for adiabatic conditions for strain rates higher than $\dot{\varepsilon} \approx 10^{-2} s^{-1}$, Fig. 6.3a. Moreover, as it can be seen in Figs. 4(b) and 5(b), the predictive capacity of the model is limited by the glass transition temperature. Around this value and thereafter, the degree of crystallinity and also the specific heat are no more constants for semi-crystalline polymer [Santos et al., 2013].

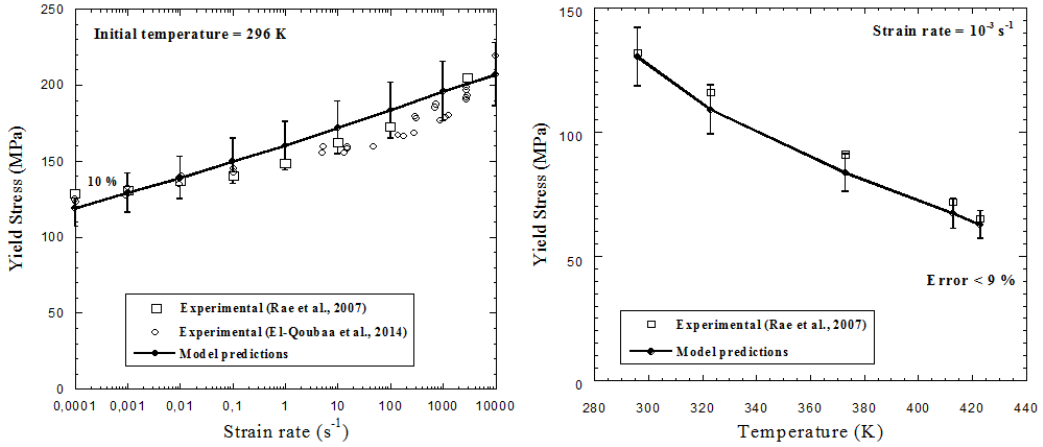

(a) (b)

Figure 6.4: Experimental data [Rae et al., 2007; El-Qoubaa,2014] versus model predictions in terms of: (a) strain rate sensitity; and (b) temperature sensitivity of PEEK for uniaxial compression tests.

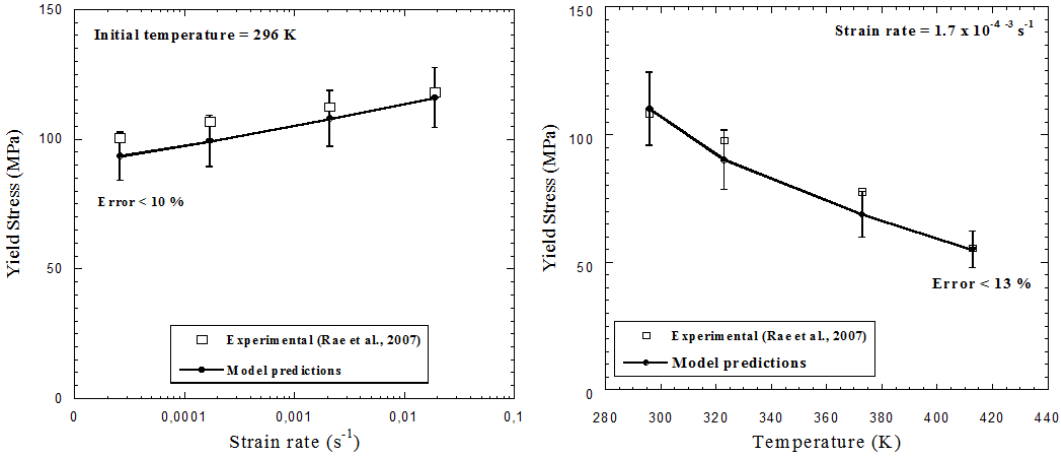

(a) (b)

Figure 6.5: Experimental data [Rae et al., 2007] versus model predictions of: (a) strain rate sensitity; and (b) temperature sensitivity of PEEK for uniaxial tensile tests.

Thermomechanical coupling

According to previous observations, the consideration of temperature evolution due to plastic dissipation and its associated material softening has been found to play an essential role. Aiming to highlight this effect, a finite element model has been developed in order to observe the importance of considering temperature evolution due to plastic dissipation, its associated material softening and its coupling with strain rate. These considerations are essential to achieve a good definition of the material response. The model is defined by a single element on which tension-compression cycles reaching considerable plastic strains are applied under adiabatic conditions imposing a displacement varying with time, Fig. 6.6a. This configuration allows us to isolate the contribution of the inelastic dissipation term in the heat equation, permitting the study of the coupling between strain rate and inelastic dissipation and the subsequent thermal softening induced. The model predictions for the evolution of yield stresses reached as the temperature increases due to plastic dissipation during the tension-compression cycles are showed in Fig. 6.6b. This loading history allows us to achieve significant temperature increments and continuous thermal softening without reaching failure strain, Fig. 6.6b.

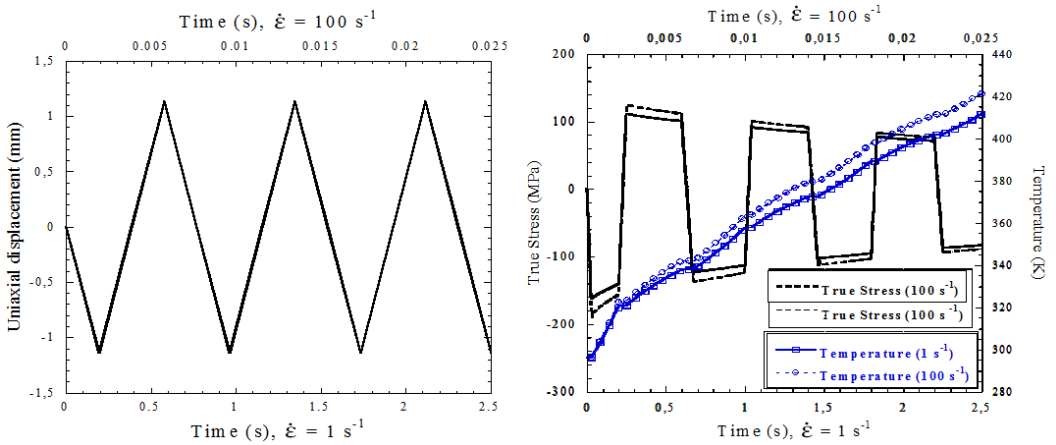

(a) (b)

Figure 6.6: (a) Applied displacement history in the tension-compression cycles; (b) Stress-time and temperature-time curve for tension-compression cycles.

During the first cycle the compressive behaviour follows the same path observed in a single test, Fig. 6.3a. Moreover, the evolution of stress and temperature for the following cycles brings forth relevant observations:

- The compressive pre-strain modifies the subsequent tensile stress-strain behaviour, and introduces a strain-induced anisotropy via network resistance, as can be noticed from the different values of tension and compression yield stresses, Fig 6b. The stress induced by the spring of the network response then acts as a backstress with respect to the intermolecular response as Polanco-Loria et al. (2010) observed.
- A continuous increase in temperature, Fig. 6.6b, activated just as the material undergoes plastic dissipation. For the tension-compression cycles imposed, the temperature evolves considerably, implying a continuous softening in the material behaviour. A strong coupling between strain rate and temperature evolution due to plastic dissipation is observed, leading to higher temperature increments with higher strain rates. Material hardening associated with strain rate increases the stress level reached at higher strain rates, resulting in higher values of plastic dissipation and increases in temperature.

6.4 Influence of thermal effects in dynamic deformation processes of semi-crystalline polymers

In this section, the importance of taking into account thermal effects on the semi-crystalline polymers behaviour is underlined. This consideration becomes more significant under dynamic loading conditions where there is a strong coupling between strain rate and thermal effects. Therefore, two different dynamic problems are presented: (i) Low velocity impact test on thin plates and (ii) dynamic necking on slender bar.

6.4.1 Low velocity impact test on PEEK thin plates

This section details the study and results of impact testing on PEEK plates. This problem was selected because impact loadings involve large and irreversible deformations, high strain rates and temperature increment due to plastic dissipation. The analysis considers impact energy (controling both impact velocity and striker mass), evolution of the impact force versus striker displacement and testing temperature.

6.4.1.1 Experimental set-up

A drop weight tower was used to conduct the impact tests, providing a perpendicular impact on the unfilled PEEK plates. This configuration allows control of both the impact velocity and the mass of the impactor in order to achieve the required impact energy. Two testing configurations of 11.25 J and 125 J were selected for the experiments. The first configuration involves a mass and an impact velocity equal to 3.6 kg and 2.5 m/s

respectively, and the second configuration involves a mass and an impact velocity equal to 10 kg and 5 m/s respectively. The lower energy was found to induce appreciable inelastic deformation and the higher energy was found to be close to the perforation limit. In addition, a climatic chamber was employed, allowing variations in the initial testing temperature (θ_o) from 293 K to 373 K.

Square specimens with an area equal to A_t=130x130 mm^2 and a thickness of 3 mm were used. They were clamped by using screws around a circular active area 100 mm in diameter (Fig. 6.7(a)). In order to avoid any perturbation during the test, the screws were symmetrically fixed. The mass of the steel striker is M_p = 0.70 kg with a hemispherical nose of 20 mm diameter. The effective mass (M_{total}) was varied from 3.6 kg until 10 kg by adding aditional mass to the setup.

A local cell placed on the striker provides its time dependent displacement $\delta_s(t)$ during the impact process, by integration of the impact force versus time curve F(t)

$$\delta_s(t) = \int_0^t \left[V_o \int_0^\tau \frac{F(\xi) - M_{total} g}{M_{total}} d\xi \right] d\tau \tag{6.57}$$

where g is the gravity acceleration.

After the impact and if no perforation of the plate occurred, the striker is hold by an anti-rebound system in order to avoid multi-hits on the specimen.

6.4.1.2 Definition of the numerical model

The experimental tests were simulated with a Lagrangian 3D finite element model developed in ABAQUS/Explicit [Abaqus v6.12 analysis user's manual, 2012].The geometry of the plate was selected to be representative of the active area of the experimental test specimens (100 mm in diameter) with a thickness of 3 mm. Fig. 6.7(b) shows the target mesh, where eight elements were distributed across the thickness of the plate. This is in consonance with the reccomendations reported elsewhere [Abaqus v6.12 analysis user's manual, 2012], where it is suggested that, when modeling any structure carrying bending loads, at least four elements should be employed through the thickness. The type of elements used to define the mesh was tri-linear elements with reduced integration (C3D8R in ABAQUS notation). The impact zone presents a mesh refinement composed of 90000 elements. In order to reduce the computational time, the peripherical zone was meshed with 64800 elements increasing progressively the element size until reaching the perimeter of the target. A convergence study was carried out using different mesh densities until an optimum configuration was obtained. Moreover, the numerical

analysis carried out satisfies the energy balance accounting for kinetic energy, external forces and internal forces (considering both elastic and inelastic components). Regarding the modelization of the striker, it has been defined as a rigid body since the experimental observations revealed absence of plastic deformation or erosion on its surface after the impact. The contact striker/plate was defined by a constant friction coefficient μ=0.2 [Borruto, 2010]. The constant value employed for this coefficient is based on the assumption of a approximately constant pressure along the striker-plate contact zone confirmed by FE analysis of different projectile-target configurations [Wang and Shi, 2013]. For the maximum energy simulation at which perforation is reached, a failure criterion based on a constant deformation equal to $\bar{\varepsilon}^{f}_{total} = 1.2$ was assumed consistently with failure values reported by Sobieraj and Rimnac (2012) and with the results previously obtained in Chapter 5.1.

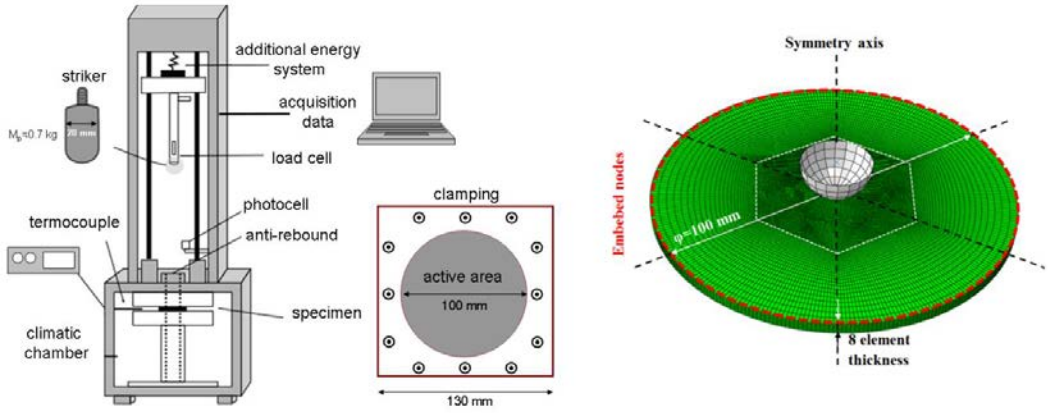

(a) (b)

Figure 6.7: (a) Experimental set-up for impact test; and (b) mesh of the numerical model for impact test.

6.4.1.3 Results and analysis

The numerical results provided by the constitutive model presented have been compared with experimental data. The force-displacement curves from the experimental tests and numerical simulations are shown in Fig. 6.8 depending on impact energy, Fig. 6.8a, and testing temperature, Fig. 6.8b. A good correlation was found between experimental and numerical results, with a maximum error lower than 10% in terms of maximum force reached and the corresponding displacement to maximum load, which demonstrates that

the model used in this study faithfully reproduces the behavior of the PEEK polymer under low velocity impact test. The shape of the force-displacement curve is fairly well captured in both loading and unloading branches. The numerical model predicts the decrease observed in the slope of experimental force-displacement curves due to thermal softening as the initial testing temperature is increased. The model also reproduces the increase in the maximum peak of force reached depending on the impact energy and the strain rate imposed in each test. Moreover, the thermal softening is not only due to the initial testing temperature but also due to the temperature evolution induced by plastic dissipation. This effect can be observed in Fig. 6.9, which shows isothermal and adiabatic estimations, resulting in a much better prediction for situations in which adiabatic heating effects and thermal softening are considered. This fact could explain the overestimation of the maximum peak of force reached by other authors [Polanco-Loria et al., 2010] who do not consider temperature increment due to plastic dissipation and the consequent softening.

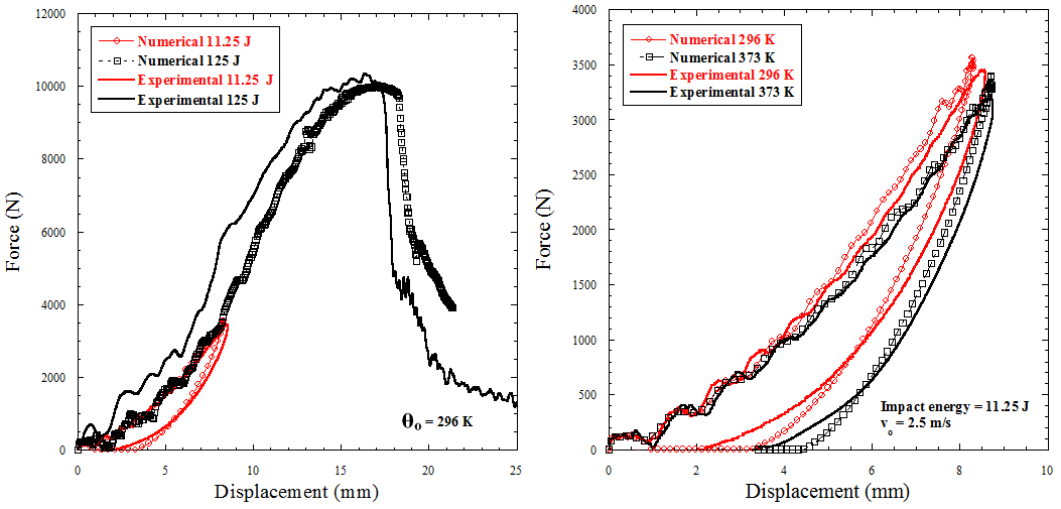

(a) (b)

Figure 6.8: Numerical and experimental force-displacement curves for low velocity impact tests: (a) different impact energy; (b) different initial testing temperatures.

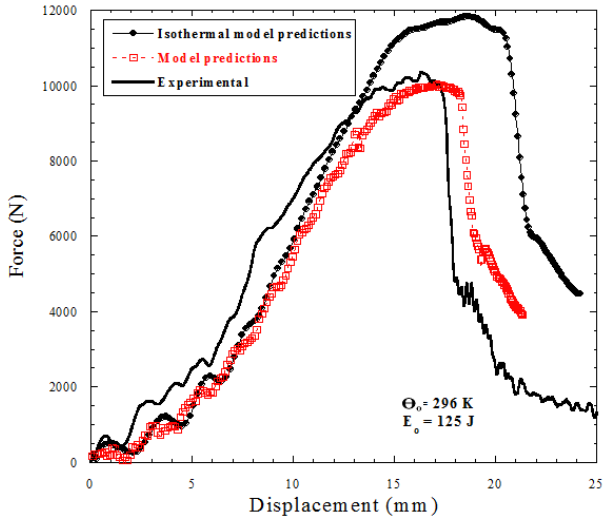

Figure 6.9: Model predictions and experimental force-displacement curves for impact tests: influence of considering plastic dissipation effects in model versus isothermal conditions.

The consideration of thermal effects is essential to know if the glass transition temperature is reached. It also provides a good prediction of the softening induced in the specimen which determines the slope of the force-displacement curve and the maximum peak of force reached. For all the experimental tests conducted, the final temperature reached after the impact was numerically predicted. These results show that the glass transition is not exceeded, so it can be concluded that the numerical predictions are valid and no sudden change in the material behaviour occurs. Moreover, Fig. 6.10 compares, in terms of force-displacement curves, the model predictions for the previous test of Fig. 6.9, and when a higher initial temperature (373 K) is imposed. The difference in terms of thermal softening between both initial temperature conditions is remarkable. It can be observed that even if the initial temperature is lower than the glass transition temperature, this last one is reached upon the deformation process due to plastic dissipation. Therefore, the temperature prediction allows for evaluating if the material is working between the ductile-to-brittle and the glass transition temperatures.

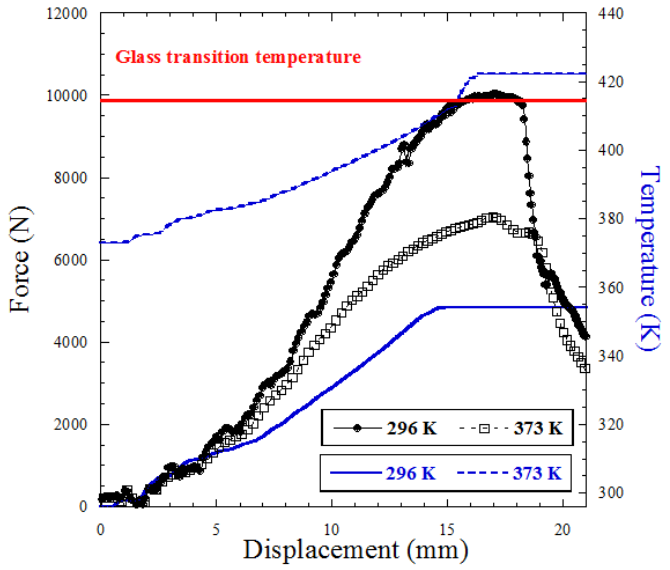

Figure 6.10: Numerical force-displacement curves and temperature evolution for impact test at kinetic impact energy equal to 125 J and initial testing temperatures equal to 296 K and 373 K.

6.4.2 Dynamic necking in a PEEK slender bar

Necking is an early indication of failure and, therefore, it is commonly utilized as a reference for evaluating the energy absorption capacity [Rodríguez-Martínez et al., 2013a]. The term necking strain denotes the stage at which full concentration of plastic flow in the neck region occurs and there is a surrounding zone where plastic flow can be neglected.

Once the predictions of the constitutive model shown a good correlation with experimental data under dynamic conditions, a parametric study has been developed in order to analyze the inertial and thermal effects on the necking and energy absorption capacity of thermoplastic semi-crystalline polymers (PEEK) by simulating cylindrical slender bars subjected to dynamic stretching. While this problem has been widely studied in metal materials, it has not been thoroughly investigated in semi-crystalline polymers. The numerical model presented below provides the localized necking strain $\bar{\varepsilon}_{neck}$ and specific energy absorbed until neck inception, E_{neck}. These variables are good indicators of the material ductility and energy absorption capacity, respectively. The localized necking strain, hereafter referred to as necking strain, has been determined in the

numerical computations following the procedure reported elsewhere [Triantafyllidis and Waldenmyer, 2004; Xue et al., 2008; Zaera et al., 2014]. The necking event is assumed to be determined by the condition $d\bar{\varepsilon}^p/dt=0$, where $\bar{\varepsilon}^p$ is the equivalent plastic strain, evaluated within the zone which surrounds the neck,

$$\bar{\varepsilon}^p = \int_0^t \dot{\bar{\varepsilon}}^p d\tau \tag{6.58}$$

where $\dot{\bar{\varepsilon}}^p$ is the plastic strain rate defined as

$$\dot{\bar{\varepsilon}}^p = \sqrt{\frac{2}{3}\bar{\bar{\mathbf{D}}}_\mathbf{I}^\mathbf{p} : \bar{\bar{\mathbf{D}}}_\mathbf{I}^\mathbf{p}} \tag{6.59}$$

Under these conditions, the necking strain is defined as the total longitudinal strain,

$$\bar{\varepsilon}_{neck} = \ln\left(\frac{L}{L_o}\right) \tag{6.60}$$

where L is the current bar length and L_o the initial one.

It must be noticed that no damage criterion is defined for these simulations. The specific energy absorbed per unit volume until neck inception, is defined by the relationship

$$E_{neck} = \frac{\int_o^{u_{neck}} F du}{V_o} \tag{6.61}$$

where V_o is the initial volume of the cylindrical bar, F is the current force applied on the specimen, u is the longitudinal displacement of the end $z=L_o$ and u_{neck} is the displacement at localized necking.

6.4.2.1 Definition of the numerical model

A cylindrical slender bar with an initial length $L_o = 2\cdot10^{-2}$ m and a circular cross section radius $r_o = 5\cdot10^{-4}$ m has been studied. A constant stretching velocity is applied on one side of the bar. The movement of the opposite side is restricted in the axial direction. The imposed loading conditions can be formulated as $V_z(r,L_o,t)=\dot{\varepsilon}_o L_o$ and $V_z(r,0,t)=0$, where t is the time and $\dot{\varepsilon}_o$ the initial strain rate. Following the methodology proposed by Zaera et al. (2014), specific initial conditions consistent with the boundary conditions have been imposed in order to avoid the propagation of waves along the bar caused by the

application of these boundary conditions in a solid at rest. Then, the initial axial velocity field is defined following the expression $V_z(r,z,0)=\dot{\varepsilon}_o z$, where z is the coordinate along the axis. The initialization of V_z was found sufficient to avoid wave propagation, without including the initialization of stress state and radial velocity. In addition, an initial temperature is imposed on the whole specimen which evolves or not depending on the thermal assumptions taken into account in the test.

The presented problem was modeled with the Lagrangian 3D FE code ABAQUS/Explicit [Abaqus v6.12 analysis user's manual, 2012]. The mesh of the model has been defined involving 3200 tri-linear elements with reduced integration (C3D8R in ABAQUS notation). The numerical round-off was sufficient to perturb the stress and the strain fields. Therefore, both geometrical and material imperfections were not introduced into the model [Rusinek and Zaera, 2007; Vadillo et al., 2012]. Moreover, the energy balance has been verified for the numerical simulations.

6.4.2.2 Results and analysis

The results and analysis of this section are focused on the following aspects: inertia, thermal softening and thermomechanical coupling. The term inertia plays a stabilizing role contributing to delay necking formation and can be defined as

$$I = \frac{r_o^2 \dot{\bar{\varepsilon}}^2 \rho}{\sigma_o} \tag{6.62}$$

r_o being a characteristic dimension and σ_o the yield stress. In a dimensionless form of the equation of movement for the problem formulation of dynamically stretching 1D solids, I is the inertial factor multiplying the acceleration. Strain rate and material hardening influence necking inception and energy absorption capacity of the material. Actually, inertia plays the main role in the material stabilization at high deformation rates, being it dominant over the hardening effects [Rodríguez-Martínez et al., 2013b]. To focus exclusively on the effect of inertia, temperature evolution due to plastic dissipation and thermal flow were not taken into account assuming isothermal conditions, Fig. 6.11. This figure shows necking strain depending on initial strain rate at a reference temperature equal to 296 K. A monotonic and non-linear increase in the necking strain with loading rate is observed in accordance with Eq. (6.62) since inertia contributes to delay necking formation. The specific energy absorbed, as it occurs with necking strain, increases continuously and non-linearly whith the loading rate. This behavior finds agreement with evidences reported for metallic materials [Altinova et al., 1996; Rodríguez-Martinez et al., 2013].

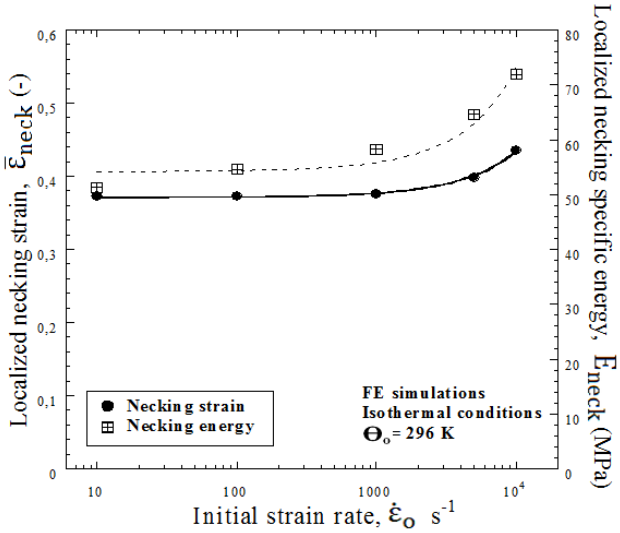

Figure 6.11: Localized necking strain and necking specific energy versus loading strain rate for PEEK polymer assuming isothermal conditions.

Initial temperature influences necking inception and energy absorption capacity of the material. Now focusing on the influence of initial temperature, isothermal conditions were considered allowing us to develop a parametric study depending on this variable, Fig. 6.12. This figure presents necking strain and specific energy depending on initial temperature at a reference strain rate equal to 10^4 s^{-1} under isothermal conditions. An increase in necking strain and a decrease in specific energy absorbed with temperature is observed. The first tendency is due to the decrease of yield stress with temperature which, according to Eq. (6.62), produces a stabilizing effect through inertia. However, this decrease in ductility does not translate into a decrease in specific energy absorption. This fact can be explained by the reduction in flow stress, Fig. 6.3, which is found to be dominant over the gain in ductility.

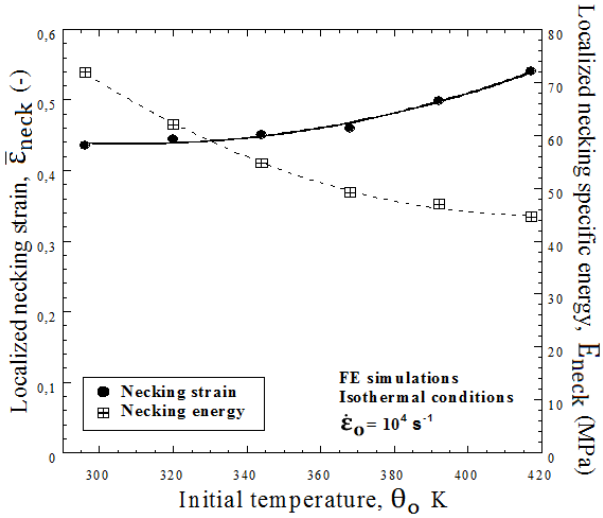

Figure 6.12: Localized necking strain and necking specific energy versus initial temperature for PEEK assuming isothermal conditions.

In order to consider coupled thermomechanical effects, Fig. 6.13 presents the comparison between the results for isothermal and adiabatic conditions. This figure shows the effect of temperature evolution upon the deformation process leading to material softening in combination with material hardening due to strain rate effects. The importance of taking into account the plastic dissipation is shown in terms of necking strain and specific energy absorbed. In this regard, Fig. 6.14 shows the strain, temperature and plastic strain rate contours of the deformed specimen for adiabatic conditions. This figure allows for visualizing the localization of the plastic strain rate in the necking zone and the consequent increase of temperature due to inelastic effects.

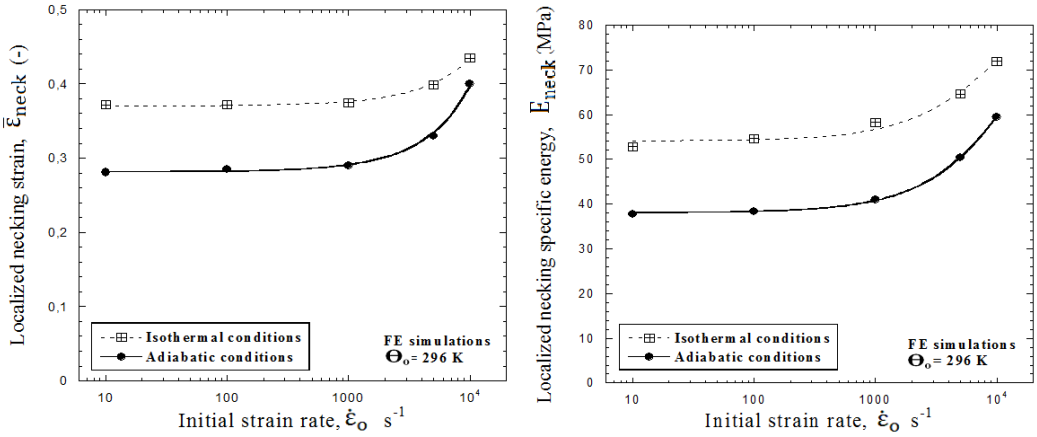

(a) (b)

Figure 6.13: (a) Localized necking strain versus loading strain rate for PEEK; (b) Specific energy per unit volume versus loading strain rate for PEEK assuming temperature evolution due to plastic dissipation.

Under isothermal conditions, numerical results showed a similar tendency of both necking strain and specific energy absorbed with strain rate, as well as under adiabatic conditions, Fig13a-b. Regarding thermal effects, the predictions obtained under isothermal conditions may mistakenly suggest that necking strain must be greater under adiabatic conditions due to the temperature evolution since necking strain increases with initial testing temperature. However, under adiabatic conditions, there is a competition between the stabilizing role played by the decrease in yield stress due to temperature increase and the destabilizing role played by thermal softening from that point. Some studies have shown that larger necking strains are reached as the material hardening is more significant [Chalal et al., 2015; Rodriguez-Martinez et al., 2015]. In this regard, as can be observed in Fig. 6.3 for strain rates higher than $\dot{\varepsilon} \approx 10^{-2}$, while PEEK behaves in a perfectly plastic way under isothermal conditions, it presents a negative hardening due to thermal softening induced by plastic dissipation. This fact leads to higher necking strains when plastic dissipation is not considered. In the higher rate regime, the results show that inertia governs the onset of the localization being dominant over material softening. Regarding absorbed specific energy, it is much lower when plastic dissipation is taken into account because of the lower values of force reached due to thermal softening. Therefore, despite the dominant role of inertia, temperature evolution must be

considered in order to achieve more realistic results in terms of ductility and energy absorption capacity.

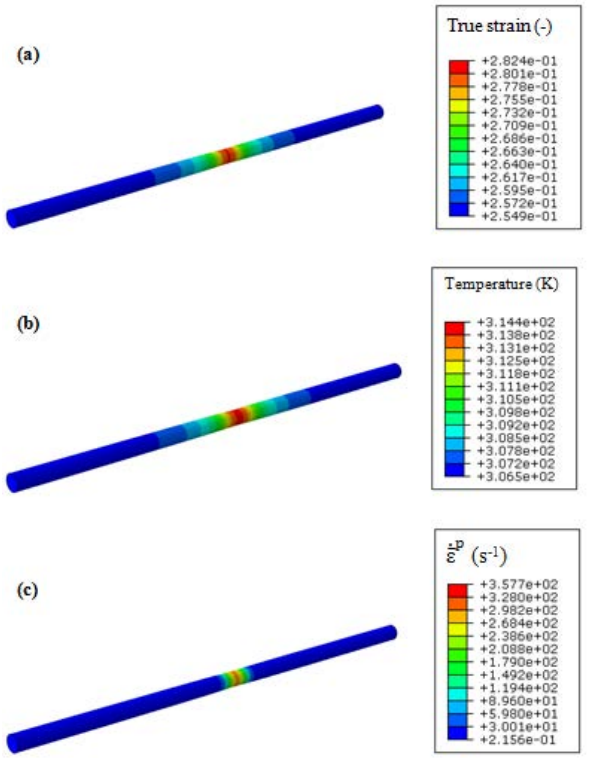

Figure 6.14: (a) True strain, (b) temperature and (c) plastic strain rate contours of the deformed specimen at necking event under adiabatic conditions at 10 s^{-1}.

6.5 Conclusions

The main contributions of this chapter are the following:

- A thermomechanical constitutive model for semi-crystalline polymers has been developed accounting for strain rate and temperature. Moreover, a consistent thermodynamic framework has been established for the model.

- The constitutive model has been implemented in a FE code and its parameters have been identified for PEEK polymer from experimental data from available literature covering a wide range of strain rates and temperatures for both tension and compression states. Good agreement between numerical predictions and

experimental data was found in terms of stress-strain curves depending on strain rate and temperature. For high strain rates, the consideration of temperature evolution and thermal softening plays an essential role to obtain accurate predictions. Aiming to highlight these thermal effects, additional numerical simulations of tension-compression cycles have been carried out. A strong coupling between strain rate and temperature evolution due to plastic dissipation was found, leading to higher temperature increments and material softening with higher strain rates.

- The predictive capacity of the model has been evaluated in two different dynamic problems: **i)** low velocity impact tests on PEEK thin plates and **ii)** dynamic necking on PEEK slender bar.

  i) Good agreement between numerical predictions and experimental data was found in terms of force-displacement curves depending on impact energy and initial testing temperature. Better predictions were found when softening associated to plastic dissipation is taken into account, which determines the slope of the force-displacement curve and the peak force reached. In addition, the numerical prediction of temperature evolution is essential to determine if the glass transition temperature is reached.

  ii) A numerical parametric study of the inertial and thermal effects on the ductility and energy absorption capacity of PEEK was carried out for isothermal and adiabatic conditions. Under isothermal conditions, a clear dependence of both necking strain and specific energy absorbed on strain rate was found. Increasing initial temperature and strain rate leads to increasing necking strain and decreasing energy absorption. For adiabatic conditions, despite the dominant role of inertia, plastic dissipation must be taken into account in order to achieve more realistic results in terms of ductility and energy absorption capacity and not overestimate them. In this regard, both necking strain and specific energy absorbed were found to decrease when plastic dissipation is considered in comparison with isothermal conditions.

The results presented in this chapter demonstrate the capacity of the model proposed to predict the thermomechanical behaviour of semi-crystalline polymers and the importance of taking into account the coupling between strain rate and temperature effects.

Chapter 7.

Continuum mechanics framework for transversely isotropic hyperelasticity

This chapter deals with the generalization of the constitutive equations of the model proposed for semi-crystalline polymers in the previous chapter, with the aim of formulating a general continuum framework for transversely isotropic hyperelastic materials. The constitutive formulation is based on a Helmholtz free energy function decoupled into the contribution of a hyperelastic-viscoelastic/viscoplastic matrix and the contribution of fibres introducing orientation and distribution dependent transverse isotropy with finite deformation kinematics. Following the postulates assumed for the Helmholtz free energy function and the methodology developed in the previous chapter, a consistent constitutive framework which allows for the specialization of the energy potentials and flow equations of each constitutive branch is proposed. In this regard, the work developed herein represents the basis on which specific constitutive models can be potentially formulated for a wide range of materials such as short fibre reinforced thermoplastic composites and many kinds of soft tissues. To this end, the model is specialized here for a specific thermoplastic composite family, PEEK, and for a specific anisotropic soft tissue, the white matter of brain tissue.

7.1 Introduction

Many materials of increasing interest behave as hyperelastic with transverse isotropy. The nature of such materials can be found in composites employed in many applications within the automotive, aeronautical and biomedical industries [Lee, 1996; Scholz et al., 2011] as well as in soft tissues in the human, animal or plant anatomy [Zulligera et al., 2004; Gasser et al., 2006; Wang et al., 2014]. To illustrate the proposed approach, this work focuses here on short fibre reinforced (SFR) thermoplastic polymers and soft tissues.

The use of thermoplastic polymers has been promoted due to their attractive mechanical properties, their low manufacturing cost and their great flexibility in terms of manufacturing technologies for structural applications [Andriyana et al., 2010]. However, sometimes a higher strength is desirable and the use of unfilled thermoplastics is not good enough. To this end, these polymers are reinforced by short fibres while retaining their economic and design advantages. The directional dependence of short fibres leads to an anisotropic mechanical behaviour which is determined by a manufacturing process dependent preferred but distributed fibre orientation [Fu et al., 2009]. Accurate and reliable constitutive models are thus of significant importance for a better understanding of the mechanical behaviour of SFR thermoplastics. In the case of amorphous polymers,

the constitutive model must account for the network response of the material as a function of the reorientation of the molecular chains [Boyce et al., 1988; Boyce and Arruda, 2000; Mulliken and Boyce, 2006]. In the case of semi-crystalline polymers, the constitutive model must also account for an intermolecular resistance associated to strain-induced crystallization [Bergström et al., 2003; Ayoub et al., 2010; Maurel-Pantel et al., 2015]. In order to faithfully describe the mechanical behaviour of these polymers, the constitutive models must take into account the strain rate, temperature and pressure dependencies. Finally, when short fibres are incorporated to the thermoplastic matrix, the fibre contribution to the mechanical response of the composite and the anisotropy induced by the fibre orientation needs to be accounted for. Homogenized models for SFR thermoplastic composites which provide a macroscopic description on the composite behaviour without taking into account the individual response of each constituent have been proposed [Dean et al., 2016]. Other models are based on the formulation of a free energy function decoupled into the matrix and the fibres contributions [Guo et al., 2007]. In particular, Qiu and Pence (1997) defined a new model based on an incompressible anisotropic finite elastic material model in which the strain energy function takes into account the penalty that the reinforced material suffers due to the extension in the reinforcing directions. Andriyana et al. (2010) developed a three-dimensional model based on a continuum approach accounting for both matrix and fibres mechanical contributions. More recently, Chebbi et al. (2016) have proposed an anisotropic hyperelastic constitutive model for short fibre reinforced polyamide where the contributions of the matrix and fibres are weighted by the fibre volume fraction.

Soft tissues are known to exhibits a hyperelastic material behaviour [Fung, 1981]. Moreover, when these soft tissues are embedded with fibres, an anisotropic behaviour is also observed [Fung, 1981; Cowin and Humphrey, 2001; Guo et al., 2007]. Several authors have proposed constitutive models for biological soft materials accounting for the matrix and fibres contributions. Gasser et al. (2006) developed a structural continuum framework to study human arteries. This framework was able to represent the dispersion of the collagen fibre orientation, and allowed them to develop a new hyperelastic free-energy function that also encompassed the anisotropic elastic properties. Another soft tissue that can be defined as hyperelastic with transverse isotropy is the skin. It consists of a ground substance and embedded collagen fibres presenting an anisotropic non-linear behaviour [Valero et al., 2015]. Another obvious example whose interest has been fuelled by the recent research programme on brain is the white matter, which presents a transverse isotropic behaviour induced by the alignment of bundles of axons [Prange and Margulies, 2002; Labus and Puttlitz, 2016]. In this regard, Velardi et al. (2006) used a transversely isotropic hyperelastic model proposed by Meaney (2003) to study the mechanical modelling of brain soft tissue under uniaxial tensile tests. Chatelin et al.

(2012) proposed a visco-hyperelastic model which takes into account rate dependency and anisotropy due to axon orientation. More recently, Labus and Puttlitz (2016) developed an anisotropic hyperelastic constitutive model for white matter based on a hyperelastic strain energy density function which also incorporates the anisotropic contribution of axons.

In this chapter, a thermodynamically consistent continuum framework for hyperelastic materials with transverse isotropy is developed. The constitutive formulation is based on a Helmholtz free energy function additively decoupled into a hyperelastic-viscoelastic/viscoplatic associated with the response of the matrix material, which is assumed isotropic; and a part associated with anisotropic deformations that represent the resistance to stretch due to fibres, as Holzapfel et al. (2000) suggested. In this context, the finite deformation kinematics, the continuum representation of distributed fibre orientation, the Helmholtz free energy function and the stress response are presented. Therefore, this constitutive framework can be used as the basis for the development of future constitutive models for this kind of materials through the specialization of the free energy functions and flow equations of each constitutive branch depending on the specific material to be modelled. As an illustration, the model is applied to short carbon fibre reinforced polyether-ether-ketone (SCFR-PEEK) and white matter. For both cases, a good correlation between experimental data from literature and model predictions has been found, showing the possibilities that the model potentially offers in terms of capturing material dependencies and deformation mechanisms.

7.2 Continuum mechanics framework

The proposed continuum mechanics framework is presented here according to the assumptions listed above. The description of the rheological framework, the finite deformation kinematics, the continuum representation of distributed fibre orientation, the Helmholtz free energy function and the stress response are introduced in this section.

7.2.1 Description of the rheological framework

Previous experimental works on SFR thermoplastic polymers and soft tissues have already established complex mechanical behaviour combining the mechanical response due to the matrix and fibres natures and due to the interphase between them [Peng et al., 2006; Guo et al., 2006]. Taking the deformation mechanisms of anisotropic hyperelastic materials as a motivation, a general rheological model is presented in Fig. 7.1. It is composed of three constitutive branches: the intermolecular (I) and network (N) branches associated to the matrix behaviour; and the fibres + interphase behaviour branch.

(i) From the observations of the mechanical response of thermoplastic polymers reinforced with different fibre contents, it can be assumed that the composite response is the result of the matrix and fibres contributions weighted by the volume fraction of each component [Andriyana et al., 2010]. The general three-dimensional continuum framework presented herein addresses these mechanical observations by considering two phases: the first one related to a thermoplastic matrix generally exhibiting hyperelastic-thermoviscoelastic/thermoviscoplastic behaviour; and the second one related to the fibres and interphase as a whole exhibiting an anisotropic reversible behaviour. In addition, if the model pretends to predict the mechanical behaviour not only of SFR thermoplastic polymers but also of the unfilled thermoplastic matrix, it must be developed under a finite deformation framework since when no fibres are included, these materials can undergo large deformations.
When an amorphous thermoplastic is used for the matrix, its mechanical behaviour can be defined by solely considering the network resistance [Arruda and Boyce, 1993]. When a semi-crystalline thermoplastic is used for the matrix, the intermolecular resistance must be included to introduce a barrier to deformation, increased by the development of strain-induced crystallization [Polanco-Loria et al., 2010; Maurel-Pantel et al., 2015]. The intermolecular branch includes a friction element shown as a discontinuous line in Fig. 7.1. This element represents a yield function and determines the nature of the polymer: viscoelastic if it is not included; or viscoplastic if it is included. The total stress due to the matrix response is obtained as the sum of both intermolecular and network resistances. Finally, the fibres and interphase phase is modelled with a direction-dependent spring which introduces the anisotropy due to fibre orientation.

(ii) From the observations of the mechanical response of many transversely isotropic soft tissues, the total stress response of the material has been observed to be the sum of the stress contribution due to fibres embedded in an isotropic matrix and the contribution of the matrix itself [Gasser et al., 2006]. Most of the models developed which follow this assumption describe the matrix response under quasi-static conditions as purely hyperelastic [Chatelin et al., 2012; Labus et al., 2016]. In this regard, if no strain rate dependency is needed, the matrix behaviour can be described by only defining the hyperelastic spring of the network branch. Moreover, if the constitutive model pretends to be potentially applied to dynamic conditions, the matrix behaviour would be captured by defining the intermolecular branch or as a combination of intermolecular and network responses in order to introduce strain rate sensitivity through the viscoelastic dashpot. Similarly to the SFR composites, the fibres can be modelled with a direction-dependent spring which introduces the anisotropy due to fibre orientation.

Therefore, according to the rheological model, see Fig. 7.1, the total stress of the composite is postulated as a combination of the stress contribution of each phase:

$$\boldsymbol{\sigma} = \boldsymbol{\sigma}_{\mathbf{M}} + \boldsymbol{\sigma}_{\mathbf{F}} \tag{7.1}$$

where $\boldsymbol{\sigma}_{\mathbf{M}}$ and $\boldsymbol{\sigma}_{\mathbf{F}}$ are the Cauchy stress contributions of the matrix and the fibres and interphase respectively. The total stress due to the matrix response is obtained as the sum of both intermolecular and network resistances, $\boldsymbol{\sigma}_{\mathbf{M}} = \boldsymbol{\sigma}_{\mathbf{I}} + \boldsymbol{\sigma}_{\mathbf{N}}$.

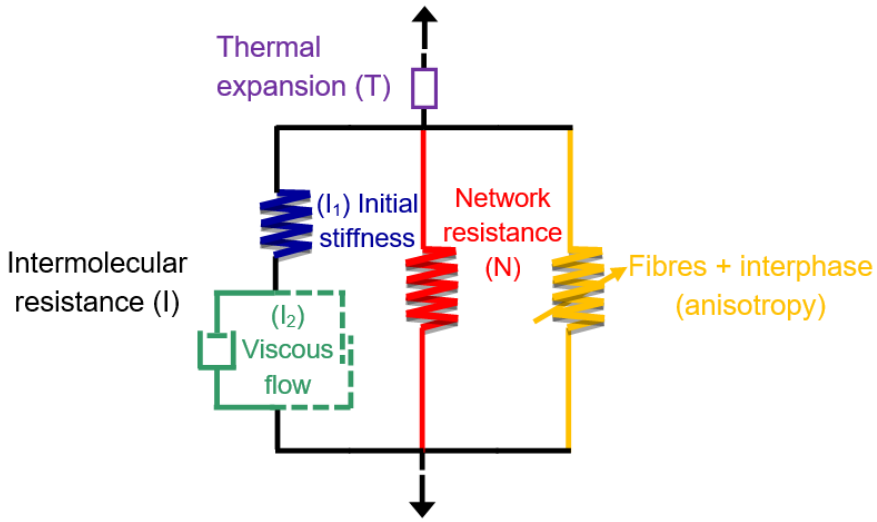

Figure 7.1: General rheological scheme: viscoplastic if the friction element shown in dash lines is present; viscoelastic otherwise.

7.2.2 Kinematics

The finite deformation kinematics are defined by four configurations, see Fig. 7.2. Starting from the reference configuration Ω_o, the current configuration Ω can be reached by mapping through the total deformation gradient $\mathbf{F}$. Two additional intermediate configurations are introduced in order to define the constitutive equations of both the matrix and fibres mechanical contributions. For this purpose, the deformation gradient is split multiplicatively into a thermal $\mathbf{F}^{\boldsymbol{\theta}}$, and mechanical $\mathbf{F}^{\mathbf{m}}$ parts [Yu et al., 1997; Ge et al., 2014]:

$$\mathbf{F} = \mathbf{F}^{\mathbf{m}}\mathbf{F}^{\boldsymbol{\theta}} \tag{7.2}$$

The first intermediate configuration is designated as the dilated configuration $\bar{\Omega}$ and accounts only for the thermal deformation, especially relevant in the polymeric matrix. Once the thermal deformation is accounted for, $\mathbf{F^m}$ goes from $\bar{\Omega}$ to Ω. Note that the mechanical part of the deformation gradient is the same for all the constitutive branches. Thus, $\mathbf{F^m} = \mathbf{F_I^m} = \mathbf{F_N^m} = \mathbf{F_F^m}$ where $\mathbf{F_I^m}$ refers to the intermolecular resistance, $\mathbf{F_N^m}$, to the network resistance, and $\mathbf{F_F^m}$, to the fibres resistance. While both network and fibres mechanical parts are defined as purely elastic, $\mathbf{F_N^e}$ and $\mathbf{F_F^e}$, respectively, the intermolecular contribution is decomposed into an elastic $\mathbf{F_I^e}$, and a viscous part $\mathbf{F_I^v}$. Following a multiplicative decomposition of the intermolecular resistance, an intermediate configuration designated as the dilated relaxed configuration $\bar{\bar{\Omega}}$ is defined to account for the thermal and plastic deformations. The following expression for the total deformation gradient is thus obtained:

$$\mathbf{F} = \mathbf{F_I^e F_I^v F^\theta} = \mathbf{F_N^e F^\theta} = \mathbf{F_F^e F^\theta} \tag{7.3}$$

The velocity gradient $\mathbf{l}$, can be written in terms of the fibres kinematics as

$$\mathbf{l} = \dot{\mathbf{F}}\mathbf{F}^{-1} = \mathbf{l_F^e} + \mathbf{F_F^e}\bar{\mathbf{L}}^{\boldsymbol{\theta}}\mathbf{F_F^{-e}} \tag{7.4}$$

where $\mathbf{l_F^e} = \dot{\mathbf{F}}_\mathbf{F}^\mathbf{e}\mathbf{F_F^{-e}}$ and $\bar{\mathbf{L}}^{\boldsymbol{\theta}}$ is the thermal component of the velocity gradient expressed in $\bar{\Omega}$. For more details about the kinematics of the thermoplastic matrix contribution consult Chapter 6.

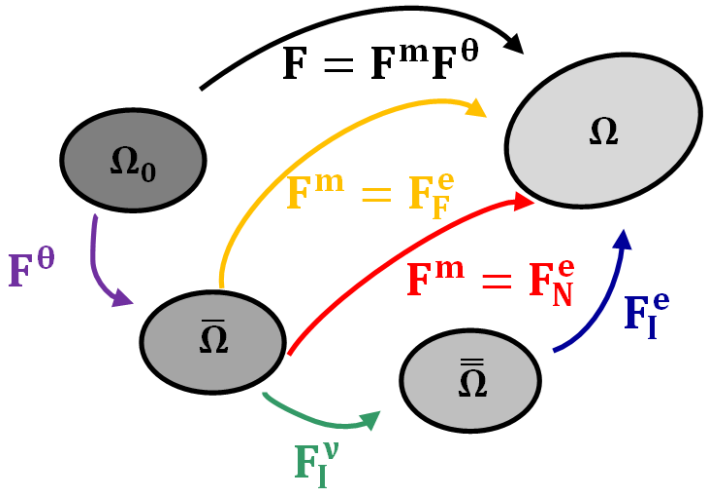

Figure 7.2: Model kinematics of the model.

7.2.3 Continuum representation of distributed fibre orientation

The fibre orientation is essential in the present model since this is the cause of mechanical anisotropy. The modelling framework considered herein assumes that the material to be modelled presents a preferred fibre orientation. While it is commonly observed in most of the anisotropic soft tissues, it cannot be generalized for SFR composites. However, in the specific case of injection moulding of the fibres, the manufacturing process is known to lead to a preferred orientation along the mould filling direction [Kammoun et al., 2011]. Note that a moderate dispersion of the fibres orientation at the final solid state is still expected [Fu et al., 2009]. For both injection moulded SFR composites and soft tissues, the orientation of the fibres and their distribution is introduced in a continuum sense through a symmetric generalized structural tensor depending on an orientation density function $\rho(\mathbf{a_o})$ characterizing the fibres distribution [Advani and Tucker, 1987; Gasser et al., 2006; Andriyana et al., 2010]:

$$\mathbf{A_o} = \frac{1}{4\pi}\int_w \rho(\mathbf{a_o})\mathbf{a_o}\otimes\mathbf{a_o}\mathrm{dw} \tag{7.5}$$

with w being the unit sphere and $\mathbf{a_o}$ being the referential fibre orientation vector defined in Ω_o. According to Andriyana et al. (2010), $\mathbf{a_o}$ is an arbitrary unit vector which can be expressed by using two Eulerian angles $\alpha\in[0,\pi]$ and $\gamma\in[0,2\pi]$, see Fig. 7.3:

$$\mathbf{a_o}(\alpha,\gamma) = \sin\alpha\cos\gamma\,\mathbf{e_1} + \sin\alpha\sin\gamma\,\mathbf{e_2} + \cos\alpha\,\mathbf{e_3} \tag{7.6}$$

defined within a rectangular Cartesian coordinate system where $(\mathbf{e})_{i=1,2,3}$ denote the axes.

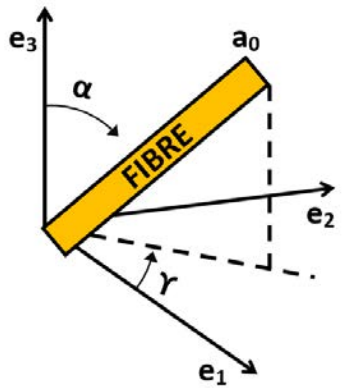

Figure 7.3: Characterization of the unit fibre orientation vector a_o by means of Eulerian angles.

The compact form of the generalized tensor of orientation can be written as

$$\mathbf{A_o} = A_{oij}\mathbf{e_i}\otimes\mathbf{e_j} \tag{7.7}$$

where the coefficients $A_{oij} = A_{oji}$ (symmetric tensor) are defined as Gasser et al. (2006) proposed:

$$\left.\begin{aligned} A_{o11} &= \frac{1}{4\pi}\int_0^{2\pi}\int_0^{\pi}\rho(\alpha,\gamma)\sin^3\alpha\cos^2\gamma\,d\alpha d\gamma \\ A_{o22} &= \frac{1}{4\pi}\int_0^{2\pi}\int_0^{\pi}\rho(\alpha,\gamma)\sin^3\alpha\sin^2\gamma\,d\alpha d\gamma \\ A_{o33} &= \frac{1}{4\pi}\int_0^{2\pi}\int_0^{\pi}\rho(\alpha,\gamma)\cos^2\alpha\sin\alpha\,d\alpha d\gamma \\ A_{o12} &= \frac{1}{4\pi}\int_0^{2\pi}\int_0^{\pi}\rho(\alpha,\gamma)\sin^3\alpha\sin\gamma\cos\gamma\,d\alpha d\gamma \\ A_{o23} &= \frac{1}{4\pi}\int_0^{2\pi}\int_0^{\pi}\rho(\alpha,\gamma)\sin^2\alpha\cos\alpha\sin\gamma\,d\alpha d\gamma \\ A_{o13} &= \frac{1}{4\pi}\int_0^{2\pi}\int_0^{\pi}\rho(\alpha,\gamma)\sin^2\alpha\cos\alpha\cos\gamma\,d\alpha d\gamma \end{aligned}\right\} \tag{7.8}$$

The compact form of this tensor of orientation and its reduction to the planar case, as observed in SFR composites [Vincent et al., 2005; Dray, 2006], is developed by Andriyana et al. (2010). With these hypotheses, the final tensor of orientation reads as

$$\mathbf{A_o} = \begin{bmatrix} A_{o11} & A_{o12} & 0 \\ A_{o12} & A_{o22} & 0 \\ 0 & 0 & 0 \end{bmatrix} \tag{7.9}$$

7.2.4 Helmholtz free energy function and stress response

The Helmholtz free energy function $\bar{\Psi}$, defined per unit volume in $\bar{\Omega}$, is decoupled here into its matrix ($\bar{\Psi}_M$) and the fibres and interphase ($\bar{\Psi}_F$) contributions. Furthermore, the matrix part is assumed to be the combination of the intermolecular ($\bar{\Psi}_M^I$) and the network ($\bar{\Psi}_M^N$) resistances. The Helmholtz free energy can also be defined depending on the elastic right Cauchy-Green deformation tensors $\mathbf{C_I^e} = \mathbf{F_I^{eT}F_I^e}$, $\mathbf{C_N^e} = \mathbf{F_N^{eT}F_N^e}$ and $\mathbf{C_F^e} = \mathbf{F_F^{eT}F_F^e}$, temperature ($\theta$) and the tensor of orientation as $\bar{\Psi} = \bar{\Psi}(\mathbf{C_I^e}, \mathbf{C_N^e}, \mathbf{C_F^e}, \theta, \mathbf{A_o})$.

$$\bar{\Psi} = \bar{\Psi}_M(\mathbf{C_I^e}, \mathbf{C_N^e}, \theta) + \bar{\Psi}_F(\mathbf{C_F^e}, \mathbf{A_o}) \tag{7.10}$$

and the matrix part of the Helmholtz free energy is assumed to be an additive combination of its intermolecular and network parts:

$$\bar{\Psi}_M = \bar{\Psi}_M^I(\mathbf{C_I^e}, \theta) + \bar{\Psi}_M^N(\mathbf{C_N^e}) \tag{7.11}$$

Following the procedure used in Chapter 6, the definition of the Helmholtz free energy assumed herein is combined with the first and second thermodynamics principles in order to obtain the following expression for the Clausius-Duhem inequality:

$$-\dot{\bar{\Psi}} - \dot{\theta}\bar{\eta} - \bar{\Psi}\mathrm{tr}\left(\bar{\mathbf{D}}^{\boldsymbol{\theta}}\right) + \bar{\mathbf{M}}_{\mathbf{I}}:\bar{\mathbf{D}}^{\boldsymbol{\nu}} + \bar{\mathbf{M}}_{\mathbf{I}}:\bar{\mathbf{D}}^{\boldsymbol{\theta}} + \bar{\mathbf{M}}_{\mathbf{N}}:\bar{\mathbf{D}}^{\boldsymbol{\theta}} + \bar{\mathbf{M}}_{\mathbf{F}}:\bar{\mathbf{D}}^{\boldsymbol{\theta}} + \bar{\mathbf{S}}_{\mathbf{I}}:\mathbf{F}^{\mathbf{mT}}\mathbf{d}_{\mathbf{I}}^{\mathbf{e}}\mathbf{F}^{\mathbf{m}} + \bar{\mathbf{S}}_{\mathbf{N}}:\mathbf{F}^{\mathbf{mT}}\mathbf{d}_{\mathbf{N}}^{\mathbf{e}}\mathbf{F}^{\mathbf{m}} + \bar{\mathbf{S}}_{\mathbf{F}}:\mathbf{F}^{\mathbf{mT}}\mathbf{d}_{\mathbf{F}}^{\mathbf{e}}\mathbf{F}^{\mathbf{m}} - \frac{1}{\theta}\bar{\mathbf{Q}}\bar{\nabla}_{\mathrm{x}}\theta \geq 0 \tag{7.12}$$

where $\bar{\mathbf{S}}_{\mathbf{I}}$, $\bar{\mathbf{S}}_{\mathbf{N}}$ and $\bar{\mathbf{S}}_{\mathbf{F}}$ are the second Piola-Kirchhoff stresses in $\bar{\Omega}$ of the intermolecular, the network and the fibre and interphase resistances; $\bar{\mathbf{M}}_{\mathbf{I}}$, $\bar{\mathbf{M}}_{\mathbf{N}}$ and $\bar{\mathbf{M}}_{\mathbf{F}}$ are the Mandel stresses in $\bar{\Omega}$ of the intermolecular, the network and the fibre and interphase resistances (related to the second Piola-Kirchhoff stress as $\bar{\mathbf{M}} = \mathbf{F}^{\mathbf{mT}}\mathbf{F}^{\mathbf{m}}\bar{\mathbf{S}}$); $\mathbf{d}_{\mathbf{I}}^{\mathbf{e}}$, $\mathbf{d}_{\mathbf{N}}^{\mathbf{e}}$ and $\mathbf{d}_{\mathbf{F}}^{\mathbf{e}}$ are the symmetric part of the velocity gradient tensors in Ω of the intermolecular, the network and the fibre and interphase resistances; $\bar{\mathbf{D}}^{\boldsymbol{\nu}}$ is the symmetric part of the intermolecular viscous velocity gradient tensor in $\bar{\Omega}$; $\bar{\eta}$ is the specific entropy per unit volume in $\bar{\Omega}$; f_θ is a temperature-dependent function; and $\bar{\mathbf{Q}}$ is the heat flux per unit volume in $\bar{\Omega}$. $\dot{\bar{\Psi}}$ can then be derived as

$$\dot{\bar{\Psi}} = \frac{\partial\bar{\Psi}}{\partial\mathbf{C}_{\mathbf{I}}^{\mathbf{e}}}:\dot{\mathbf{C}}_{\mathbf{I}}^{\mathbf{e}} + \frac{\partial\bar{\Psi}}{\partial\mathbf{C}_{\mathbf{N}}^{\mathbf{e}}}:\dot{\mathbf{C}}_{\mathbf{N}}^{\mathbf{e}} + \frac{\partial\bar{\Psi}}{\partial\mathbf{C}_{\mathbf{F}}^{\mathbf{e}}}:\dot{\mathbf{C}}_{\mathbf{F}}^{\mathbf{e}} + \frac{\partial\bar{\Psi}}{\partial\theta}\dot{\theta} \tag{7.13}$$

Therefore, by substituting Eq. (7.13) into Eq. (7.12), the Clausius-Duhem inequality can be rewritten as

$$\left(\mathbf{F}_{\mathbf{I}}^{\boldsymbol{\nu}}\bar{\mathbf{S}}_{\mathbf{I}}\mathbf{F}_{\mathbf{I}}^{\boldsymbol{\nu}\mathbf{T}} - 2\frac{\partial\bar{\Psi}}{\partial\mathbf{C}_{\mathbf{I}}^{\mathbf{e}}}\right):\mathbf{F}_{\mathbf{I}}^{\mathbf{eT}}\mathbf{d}_{\mathbf{I}}^{\mathbf{e}}\mathbf{F}_{\mathbf{I}}^{\mathbf{e}} + \left(\bar{\mathbf{S}}_{\mathbf{N}} - 2\frac{\partial\bar{\Psi}}{\partial\mathbf{C}_{\mathbf{N}}^{\mathbf{e}}}\right):\mathbf{F}_{\mathbf{N}}^{\mathbf{eT}}\mathbf{d}_{\mathbf{N}}^{\mathbf{e}}\mathbf{F}_{\mathbf{N}}^{\mathbf{e}} + \left(\bar{\mathbf{S}}_{\mathbf{F}} - 2\frac{\partial\bar{\Psi}}{\partial\mathbf{C}_{\mathbf{F}}^{\mathbf{e}}}\right):\mathbf{F}_{\mathbf{F}}^{\mathbf{eT}}\mathbf{d}_{\mathbf{F}}^{\mathbf{e}}\mathbf{F}_{\mathbf{F}}^{\mathbf{e}} + \bar{\mathbf{M}}_{\mathbf{I}}:\bar{\mathbf{D}}^{\boldsymbol{\nu}} + \left(-\frac{\partial\bar{\Psi}}{\partial\theta} - 3f_\theta\bar{\Psi} - \bar{\eta} + f_\theta(\bar{\mathbf{M}}_{\mathbf{I}} + \bar{\mathbf{M}}_{\mathbf{N}} + \bar{\mathbf{M}}_{\mathbf{F}}):\mathbf{I}\right)\dot{\theta} - \frac{1}{\theta}\bar{\mathbf{Q}}\bar{\nabla}_{\mathrm{x}}\theta \geq 0 \tag{7.14}$$

where The second Piola-Kirchhoff stress associated to each constitutive branch can be obtained using the Coleman and Noll method [Coleman and Noll, 1963; Coleman and Gurtin, 1967]:

$$\bar{\mathbf{S}}_{\mathbf{I}} = \mathbf{F}_{\mathbf{I}}^{-\boldsymbol{\nu}} 2 \frac{\partial \bar{\Psi}}{\partial \mathbf{C}_{\mathbf{I}}^{\mathbf{e}}} \mathbf{F}_{\mathbf{I}}^{-\boldsymbol{\nu}\mathbf{T}} \tag{7.15.1}$$

$$\bar{\mathbf{S}}_{\mathbf{N}} = 2 \frac{\partial \bar{\Psi}}{\partial \mathbf{C}_{\mathbf{N}}^{\mathbf{e}}} \tag{7.15.2}$$

$$\bar{\mathbf{S}}_{\mathbf{F}} = 2 \frac{\partial \bar{\Psi}}{\partial \mathbf{C}_{\mathbf{F}}^{\mathbf{e}}} \tag{7.15.3}$$

7.2.5 Thermal contribution to the deformation gradient and temperature evolution

The thermal expansion, especially relevant in the matrix mechanical behaviour of polymeric composites, is assumed to be isotropic. The thermal contribution to the deformation gradient is defined as

$$\dot{\mathbf{F}}^{\boldsymbol{\theta}} = f_\theta \mathbf{F}^{\boldsymbol{\theta}} \dot{\theta} \tag{7.16}$$

where $\dot{\theta}$ is the time derivative of current temperature that can be computed along the deformation process as (for more details see Chapter 6)

$$\begin{aligned} &\left(\bar{C} + 3 f_\theta \bar{e} - f_\theta \left(\mathbf{F}_{\mathbf{I}}^{\boldsymbol{\nu}\mathbf{T}} \mathbf{C}_{\mathbf{I}}^{\mathbf{e}} \mathbf{F}_{\mathbf{I}}^{\boldsymbol{\nu}} : \bar{\mathbf{S}}_{\mathbf{I}} + \mathbf{C}_{\mathbf{N}}^{\mathbf{e}} : \bar{\mathbf{S}}_{\mathbf{N}} + \mathbf{C}_{\mathbf{F}}^{\mathbf{e}} : \bar{\mathbf{S}}_{\mathbf{F}}\right)\right) \dot{\theta} = \bar{\mathbf{M}}_{\mathbf{I}} : \bar{\mathbf{D}}^{\boldsymbol{\nu}} + \\ &\theta \left[\frac{3}{2} f_\theta \mathbf{F}_{\mathbf{I}}^{\boldsymbol{\nu}} \bar{\mathbf{S}}_{\mathbf{I}} \mathbf{F}_{\mathbf{I}}^{\boldsymbol{\nu}\mathbf{T}} - f_\theta \frac{\partial \left(\mathbf{F}_{\mathbf{I}}^{\boldsymbol{\nu}\mathbf{T}} \mathbf{C}_{\mathbf{I}}^{\mathbf{e}} \mathbf{F}_{\mathbf{I}}^{\boldsymbol{\nu}} : \bar{\mathbf{S}}_{\mathbf{I}}\right)}{\partial \mathbf{C}_{\mathbf{I}}^{\mathbf{e}}} + \frac{1}{2} \frac{\partial \left(\mathbf{F}_{\mathbf{I}}^{\boldsymbol{\nu}} \bar{\mathbf{S}}_{\mathbf{I}} \mathbf{F}_{\mathbf{I}}^{\boldsymbol{\nu}\mathbf{T}}\right)}{\partial \theta}\right] : \dot{\mathbf{C}}_{\mathbf{I}}^{\mathbf{e}} + \theta \left[\frac{3}{2} f_\theta \bar{\mathbf{S}}_{\mathbf{N}} - f_\theta \frac{\partial \left(\mathbf{C}_{\mathbf{N}}^{\mathbf{e}} : \bar{\mathbf{S}}_{\mathbf{N}}\right)}{\partial \mathbf{C}_{\mathbf{N}}^{\mathbf{e}}} + \frac{1}{2} \frac{\partial \left(\bar{\mathbf{S}}_{\mathbf{N}}\right)}{\partial \theta}\right] : \dot{\mathbf{C}}_{\mathbf{N}}^{\mathbf{e}} + \\ &\theta \left[\frac{3}{2} f_\theta \bar{\mathbf{S}}_{\mathbf{F}} - f_\theta \frac{\partial \left(\mathbf{C}_{\mathbf{F}}^{\mathbf{e}} : \bar{\mathbf{S}}_{\mathbf{F}}\right)}{\partial \mathbf{C}_{\mathbf{F}}^{\mathbf{e}}} + \frac{1}{2} \frac{\partial \left(\bar{\mathbf{S}}_{\mathbf{F}}\right)}{\partial \theta}\right] : \dot{\mathbf{C}}_{\mathbf{F}}^{\mathbf{e}} - \bar{\nabla}_{\mathrm{x}} \bar{\mathbf{Q}} + \bar{R} \end{aligned} \tag{7.17}$$

where $\bar{C}$ is the heat capacity per unit volume, $\bar{e}$ is the specific internal energy per unit volume in $\bar{\Omega}$ and $\bar{R}$ is the heat source per unit volume in $\bar{\Omega}$.

Note that in most cases when dealing with soft tissues, the thermal formulation is neglected. In this sense, it can be assumed that $f_\theta \approx 0$ and $\bar{C} \approx \infty$ and, therefore, both thermal expansion and temperature evolution are not taken into account anymore.

The continuum mechanics framework presented herein pretends to be a general constitutive framework which assures consistency, and allows for the specialization of the free energy functions depending on the specific matrix and fibres to be modelled. In this regard, note that the constitutive model developed in Chapter 6 is a specialization of this constitutive framework for semi-crystalline thermoplastic polymers.

7.3 Specialization of the constitutive framework for SFR thermoplastic composites: application to PEEK composites

In this section, the Helmholtz free energy functions, the evolution equations and the complete definition of the rheological elements are specified for each constitutive branch to determine the mechanical behaviour of SCFR-PEEK composites.

7.3.1 Specialization of the matrix response

The contributions of the intermolecular and network resistances are here defined exactly as in Chapter 6 describing the mechanical behaviour of PEEK matrix.

7.3.2 Specialization of the fibres and interphase response

The free energy associated to the fibres and interphase contribution and accounting for the anisotropy due to fibre orientation is defined by making use of the fourth invariant

$$I_{4F} = \mathrm{tr}(\mathbf{A_o C_F^e}) \tag{7.18}$$

which characterizes the state of the fibres and can be used to obtain the stretch of the material in the fibre direction $\bar{\lambda}_F$:

$$\bar{\lambda}_F = \sqrt{I_{4F}} \tag{7.19}$$

The form adopted for the Helmholtz free energy function of the fibre and interphase can be decoupled into two terms [Qiu and Pence, 1997]:

$$\bar{\Psi}_F(\mathbf{C_F^e}, \mathbf{A_o}) = \phi_F[\underbrace{C_{F1}(I_{1F}-3) + C_{F2}(I_{1F}-3)^2 + C_{F3}(I_{1F}-3)^3}_{\text{Back stress}} + \underbrace{C_{F4}(I_{4F}-1)^2}_{\substack{\text{Anisotropy due to} \\ \text{fibre orientation}}}] \tag{7.20}$$

where $I_{1F} = \mathrm{tr}\mathbf{C_F^e}$, and C_{F1}, C_{F2}, C_{F3} and C_{F4} are material parameters.

The first term in Eq. (7.20) introduces a back stress independent of the fibre orientation. This contribution is added in order to avoid unrealistic stress states and rigidities when the loading is applied transversely to the fibres direction. In such situations, because of the use of the *law of mixtures*, the axial total stress of the composite would be equal to the matrix contribution times the matrix volume fraction. Therefore, this back stress is needed to avoid a less stiff composite response than the one of the matrix alone.

Regarding the second term in Eq. (7.20), it is generally called *the standard reinforcing model* and introduces the anisotropy in the mechanical behaviour of the composite due to fibre orientation.

The C_{F4} material parameter adopts different values depending on the stress state of the fibres. These values are controlled by the stretch of the material in the fibre direction as

$$C_{F4} = \begin{cases} C_{FC4} & \text{if } \bar{\lambda}_F \leq 1 \\ C_{FT4} & \text{if } \bar{\lambda}_F > 1 \end{cases} \tag{7.21}$$

where C_{FC4} is the value adopted when the fibre is subjected to compression stress states and C_{FT4} the value adopted when the fibre is subjected to tension stress states.

The constitutive equation for the fibres and interphase can be derived by using Eq. (7.15.3) and the stress tensors relation $\boldsymbol{\sigma_F} = J_F^{-1}\mathbf{F_F^m}\bar{\mathbf{S}}_\mathbf{F}\mathbf{F_F^{mT}}$:

$$\boldsymbol{\sigma_F} = \phi_F\left[\frac{2}{J_F}(C_{F1} + 2C_{F2}(I_{1F} - 3) + 3C_{F3}(I_{1F} - 3)^2)\mathbf{B_F^{edev}} + \frac{4}{J_F}C_{F4}[I_{4F} - 1]\mathbf{F_F^e A_o F_F^{eT}}\right] \tag{7.22}$$

where $J_F = \det(\mathbf{F_F^m})$ is the Jacobian of the fibres and interphase resistance.

7.4 Specialization of the constitutive model for transversely isotropic soft tissues: application to white matter

As it was done in the previous section for SFR thermoplastics, the continuum framework is specialized here by defining the Helmholtz free energy functions. The aim of this section is not the exclusive development of a new and sophisticated constitutive model for white matter but rather to demonstrate that under the assumptions made in the general framework of this work, it is possible to capture the mechanical deformation mechanisms which govern its material behaviour. This specialization is limited to the mechanical response of white matter under quasi-static loading. In this sense, the thermal sensitivity and the rate-dependency associated to the intermolecular branch were neglected.

7.4.1 Specialization of the continuum representation of distributed axon orientation

The last few years have seen an increase of interest in the mechanical structure of the brain tissue. To this end, many research initiatives have focussed on the development and

use of novel experimental techniques able to identify the underlying axonal structure of the white matter. Diffusion tensor imaging (DTI), in particular, has leveraged the use of magnetic resonance imaging (MRI) to measure directional water diffusion in soft tissues. The application of DTI to the brain tissue, and more concretely to the white matter, provides information on axonal orientation and axonal dispersion along the tissue. Significant efforts have recently been made to incorporate the information obtained from DTI into finite element models [Chatelin et al., 2011]. This is generally done by defining for each finite element a unit vector with the preferred axon orientation, as well as a fractional anisotropy (FA) coefficient that represents the *degree of anisotropy*. The coefficient FA is defined from the eigenvalues λ_i of the diffusion tensor as proposed by Pierpaoli and Basser (1996):

$$\mathrm{FA} = \frac{\sqrt{3[(\lambda_1-\langle\lambda\rangle)^2+(\lambda_2-\langle\lambda\rangle)^2+(\lambda_3-\langle\lambda\rangle)^2]}}{\sqrt{2(\lambda_1^2+\lambda_2^2+\lambda_3^2)}} \tag{7.23}$$

where

$$\langle\lambda\rangle = (\lambda_1+\lambda_2+\lambda_3)/3 \tag{7.24}$$

The anisotropic unit vector $\mathbf{a_o}$ is defined as the mean orientation of the axons in each voxel volume. The direction of the unit vector $\mathbf{a_o}$ is given by the eigenvector associated with the maximal eigenvalue of the diffusion tensor [Chatelin et al., 2011].

Assuming that the axons are axisymmetrically distributed about the preferred direction $\mathbf{a_o}$, a transverse isotropic response is expected. In order to define a modified structure tensor $\mathbf{H_o}$ depending on a single dispersion parameter ξ, Gasser et al. (2006) proposed the following compact form:

$$\mathbf{H_o} = \xi\mathbf{I} + (1-3\xi)\mathbf{a_o}\otimes\mathbf{a_o} \tag{7.25}$$

In this work, a functional dependence on FA is introduced for the dispersion parameter ξ as

$$\xi = -\frac{1}{3}\mathrm{FA} + \frac{1}{3} \tag{7.26}$$

According to the definition of FA, this coefficient ranges from 0 to 1 and represents the degree of anisotropy in the axon orientation for each voxel volume. Therefore, when FA

adopts a value of 0, it describes an isotropic distribution of the axons and, in this case, the structure tensor is spherical. In the case of an ideal coalignment of the axons, the FA coefficient adopts a value of 1 and the structure tensor reduces then to $\mathbf{H_o} = \mathbf{a_o} \otimes \mathbf{a_o}$.

7.4.2 Specialization of the isotropic matrix response

The brain tissue can be structurally divided into gray and white matters. While the mechanical response of gray matter can be faithfully described as isotropic, this is not the case of the white matter because of the presence of bundles of axons inducing transversely isotropic mechanical behaviour. Regarding the white matter, its mechanical behaviour has been modelled as the combination of an isotropic response associated to the glial matrix and an anisotropic response associated to the axonal contribution [Feng et al., 2013; Ning et al., 2006; Velardi et al., 2006].

The isotropic glial matrix contribution is defined in the network branch by using a Gent strain-energy function [Gent, 1996]:

$$\bar{\Psi}_M^N(\mathbf{C_N^e}) = -\frac{\mu(\theta)}{2} j_m \ln\left(1 - \frac{I_{1N}^* - 3}{j_m}\right) + \frac{1}{2}\kappa(J_N - 1)^2 \tag{7.27}$$

where j_m is a dimensionless parameter controlling the limited chain extensibility, $I_{1N}^* = \mathrm{tr}\mathbf{C_N^*}$ is the deviatoric first strain invariant and κ is the bulk modulus. The distortional right Cauchy-Green deformation tensor is defined by $\mathbf{C_N^*} = (\mathbf{F_N^*})^T \mathbf{F_N^*}$. The shear modulus of the matrix depends on temperature through $\mu(\theta) = c(\theta - \theta_{ref}) + \mu_o$, where c is a material parameter, θ_{ref} is the reference temperature and μ_o the shear modulus at reference temperature.

The constitutive equation for the network resistance can be derived by using Eq. (7.15.2) and the stress tensors relation $\boldsymbol{\sigma_N} = J_N^{-1} \mathbf{F_N^m} \bar{\mathbf{S}}_N \mathbf{F_N^{mT}}$ as

$$\boldsymbol{\sigma_N} = \frac{\mu(\theta)}{J_N} \frac{1}{1 - \frac{I_{1N}^* - 3}{j_m}} \mathbf{B_N^{*dev}} + \kappa(J_N - 1)\mathbf{I} \tag{7.28}$$

where $\mathbf{B_N^{*dev}}$ is the deviatoric part of the distortional left Cauchy-Green deformation tensor.

If the incompressibility assumption is made for white matter ($J_N = 1$), the previous equation can be rewritten as

$$\boldsymbol{\sigma_N} = \frac{\mu(\theta)}{1-\frac{I_{1N}^{*}-3}{J_m}}\mathbf{B_N^{*dev}} \tag{7.29}$$

7.4.3 Specialization of the anisotropy induced by axon orientation

The free energy associated to the fibres and interphase contribution and accounting for the anisotropy induced by the axon orientation is defined by the free energy function proposed by Velardi et al. (2006):

$$\bar{\Psi}_F(\mathbf{C_F^e}, \mathbf{A_o}) = \frac{2k(FA)\mu(\theta)}{\alpha^2}\left(\left(\hat{I}_{4F}\right)^{\alpha/2} + 2\left(\hat{I}_{4F}\right)^{-\alpha/4} - 3\right) \tag{7.30}$$

where α is a material parameter and k(FA) is a material parameter quantifying the increase of stiffness in the fibre direction and depends on FA, which in turn varies within the white matter. Budday et al. (2016) have demonstrated that the white matter stiffness is region-dependent and there is an inverse relation between stiffness and FA, increasing the first when FA is lower. Thus, taking into account the variation of the parameter k within the white matter, the constitutive model can be fully calibrated to predict the white matter mechanical behaviour as a function of the anisotropy induced by the axons while accounting for the stiffness variations arising from the varying region-dependent stiffness. $\hat{I}_{4F}$ denotes an invariant of the modified structure tensor $\mathbf{H_o}$ that is defined as

$$\hat{I}_{4F} = \mathrm{tr}(\mathbf{H_o C_F^e}) \tag{7.31}$$

The Cauchy stress expression for this axonal contribution can be derived by using Eq. (7.15.3) and the stress tensors relation $\boldsymbol{\sigma_F} = J_F^{-1}\mathbf{F_F^m}\bar{\mathbf{S}}_F\mathbf{F_F^{mT}}$:

$$\boldsymbol{\sigma_F} = \frac{4k(FA)\mu(\theta)}{\alpha^2}\left[\frac{\alpha}{2}\left(\left(\hat{I}_{4F}\right)^{\frac{\alpha}{2}-1} - \left(\hat{I}_{4F}\right)^{\frac{\alpha}{4}-1}\right)\right]\mathbf{F_F^e H_o F_F^{eT}} \tag{7.32}$$

7.5 Results and discussion

In this section, the predictions of the model specializations for PEEK composites and white matter are presented.

7.5.1 Results and discussion for PEEK composites

The material parameters for PEEK composites are provided in Table 7.1. This model takes into account strain rate and temperature dependencies, pressure sensitivity, fibre volume fraction influence and transverse isotropy due to fibre orientation. In Fig. 7.4, the influence of fibre volume fraction is shown by varying the model parameter ϕ_F from 0 % to 30 %, confirming the stiffening effect of an increased amount of short fibres in the thermoplastic matrix. In addition, Fig. 7.5(a) shows the experimental [Rae et al., 2007] and predictive stress-strain response of unfilled PEEK under compression loading for different strain rates. The strain rate dependency is well captured in terms of yield stress hardening. For high strain rates, inelastic dissipation leads to temperature increase inducing thermal softening (for more details see Chapter 6). Reinforcing PEEK with short fibres leads to a clear stiffening of the material. This effect of fibre stiffening is shown in Fig. 7.5(b) where experimental results of stress-strain SCFR-PEEK 30 % material behaviour in different loading conditions are compared to the model predictions. It can be observed that, on the one hand, the composite shows a stiffer response under compression than tension and, on the other hand, the composite shows a stiffer response when the loading is applied along the preferred fibre orientation. In general terms, the model predictions capture the dependencies and deformation mechanisms of the material. For SCFR-PEEK 30 %, the shape prediction of the stress-strain curve is well captured. Note that the model defines the back stress of the fibre response independently on the stress state and, therefore, the model predictions for both compression and tension states are practically the same when the loading conditions are applied in the transverse direction to the preferred fibre orientation.

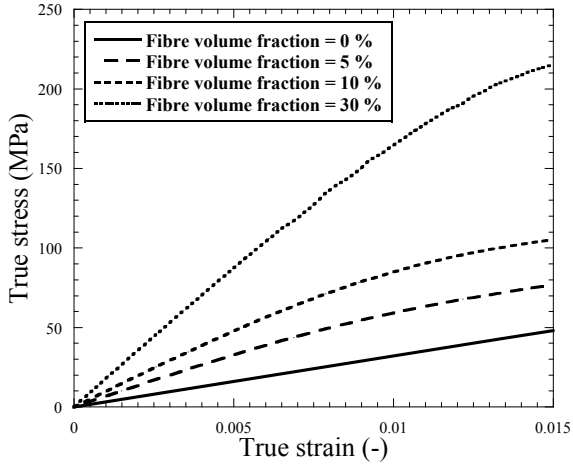

Figure 7.4: Model predictions of tension stress-strain curves for PEEK composites for different fibre volume fractions.

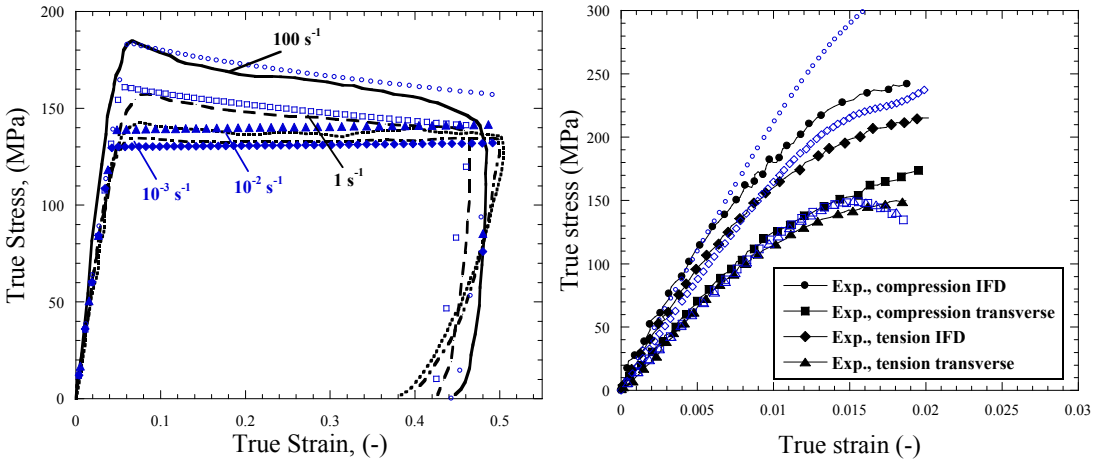

(a) (b)

Figure 7.5: Stress-strain experimental curves of: (a) unfilled PEEK; and (b) SCFR-PEEK 30 % [Rae et al., 2007] versus model predictions.

Table 7.1: Material parameters for SCFR PEEK.

Initial elastic properties			**General properties**		
E_{ref} (GPa)	E_1 (MPa)	ν	ρ (kg/m^3)	$\bar{C}$ (kJ/ m^{3}K)	α_θ (K^{-1})
3.2	-3.0	0.4	1300	2834	$4.6 \cdot 10^{-6}$

Intermolecular resistance							
$\dot{\varepsilon}_{0A}$ (s^{-1})	C	σ_{T0} (MPa)	m	θ_{ref} (K)	θ_{melt} (K)	α	β
0.001	0.038	108	0.69	296	616	1.2	1.0

Fibre resistance				
C_{F1} (GPa)	C_{F2} (GPa)	C_{F3} (GPa)	C_{FC4} (GPa)	C_{FT4} (GPa)
22	$-19 \cdot 10^3$	$70 \cdot 10^5$	6	3

Network resistance		
C_R (MPa)	$\bar{\lambda}_L$	κ
0.4	5.5	0.0

7.5.2 Results and discussion for white matter

The material parameters for white matter are provided in Table 7.2. Fig. 7.6 shows published experimental data of tensile tests for white matter when the loading is applied in both axon and transverse directions [Labus and Puttlitz, 2016]. These curves are in good agreement with the model predictions. From the results shown in Fig. 7.6, it seems that the free energy chosen for the matrix response is accurate enough. However, although the function selected for the fibre contribution reproduces the transverse isotropy due to axon orientation, it could be improved by introducing exponential terms in this function as Chatelin et al. (2012) proposed. It must be emphasized that the recent study carried out by Liu et al. (2016) demonstrates a temperature-dependence of the brain mechanical properties. According to that, the shear modulus of glial matrix response of white matter has been defined depending on temperature (Eq. (7.33)). In this regard, the model predicts accurately the shear modulus of this tissue for a temperature range from 293 K to 313 K, see Fig. 7.7. In addition, the intermolecular branch could be incorporated to this model in order to take into account the rate dependency of the mechanical behaviour of the material through a flow rule defined for the viscoelastic dashpot. Note that, if viscoelastic effects are considered, temperature increment due to inelastic dissipation should be taken into account thus leading to softer shear modulus along the deformation process.

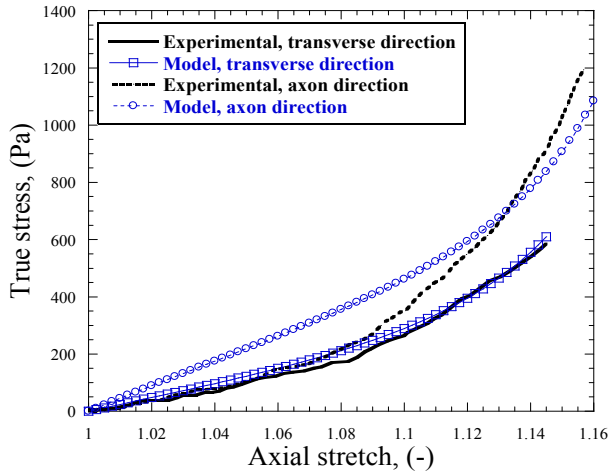

Figure 7.6: Stress-stretch experimental curves of white matter [Labus and Puttlitz, 2016] versus model predictions.

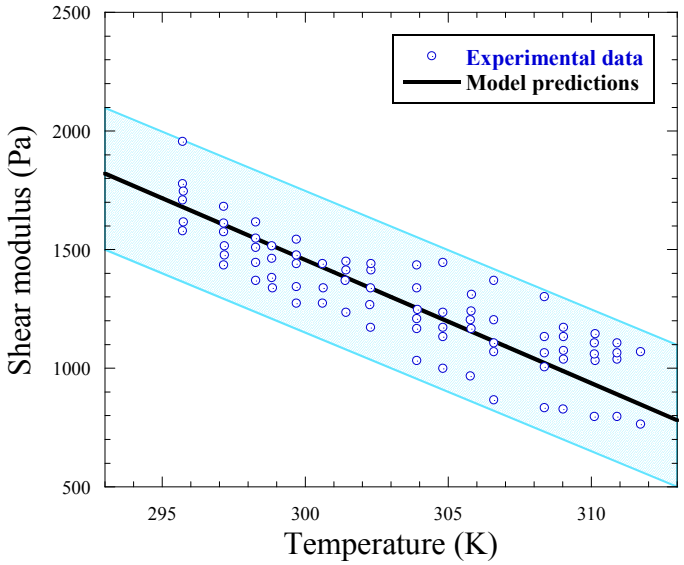

Figure 7.7: Experimental data of shear modulus [Liu et al., 2016] versus model predictions in terms of temperature sensitivity for brain tissue.

Table 7.2: Material parameters for white matter.

General properties	**Glial matrix resistance**			
ρ (kg/m^3)	**μ_0 (Pa)**	**j_m**	**θ_{ref} (K)**	**c (Pa/K)**
1040	1820	0.05	293	-0.052
Axon resistance				
α			**k**	
-5.0			1.77	

7.6 Conclusions

The main contributions of this chapter are the following:

- A consistent continuum framework has been established for transversely isotropic hyperelastic materials. The formulation is based on a Helmholtz free energy function decoupled into the contribution of a hyperelastic-viscoelastic/viscoplastic matrix and the contribution of fibres introducing transverse isotropy. This formulation can be potentially applied for a wide range

of materials such as short fibre reinforced thermoplastic composites and many kinds of soft tissues. The model was specialized for PEEK composites and white matter.

- The resulting constitutive models were implemented in a FE code and their material parameters were identified for PEEK composites and white matter. A good agreement between numerical predictions and experimental data was found in terms of stress-strain curves.

The results presented in this chapter demonstrate the versatility and capacity of the proposed continuum mechanics framework to the development of constitutive models which potentially predict the mechanical behaviour of different materials: from short fibre reinforced composites to soft tissues.

Chapter 8.

Application of constitutive modelling to the study of PEEK cranial implants under impact loading

In the previous chapters, the need and the usefulness of constitutive models which feed numerical tools have been highlighted. One of the most interesting sectors where these numerical models can provide more benefits is in the biomedical sector. The models and methodology proposed in this work can help clinicians to optimize biomedical devices and to evaluate health conditions caused by mechanical factors, such as in the study of impact loading on the head. For example, the human head can be subjected to numerous impact loadings such as those produced by a fall or during sport activities. These accidents can result in skull fracture and in some complex cases, part of the skull may need to be replaced by a biomedical implant. Even when the skull is not damaged, such accidents can result in brain swelling treated by decompressive craniectomy. Usually, after recovery, the part of the skull that has been removed is replaced by a prosthesis. In such situations, a numerical tool able to analyse the choice of prosthetic material depending on the patient's specific activity has the potential to be extremely useful to clinicians. This chapter focuses on the development and use of a numerical model for the analysis of cranial implants under impact conditions. In particular, the thermoplastic polymer studied in previous chapters, PEEK, is one of the main biomaterials employed for this kind of prosthesis, the other being a bioceramic material, macroporous hydroxyapatite (HA). This chapter analyzes the suitability of PEEK implants and compares it with HA implants. In order to study the suitability of these implants, a finite element head model comprising scalp, skull, cerebral falx, cerebrospinal fluid and brain tissues, with a cranial implant replacing part of the skull, has been developed from magnetic resonance imaging data. A numerical model of the human head under impact loading is then implemented and validated, and a numerical comparison of the mechanical impact response of PEEK and HA implants is presented. This comparison was carried out in terms of the effectiveness of both implants in ensuring structural integrity and preventing traumatic brain injury. The results obtained in this chapter highlight the need to take into account environmental mechanical considerations to select the optimal implant for the specific patient. Finally, a novel methodology is proposed to assess the need for further clinical evaluation in case of impact for both implants over a large range of impact conditions.

8.1 Introduction

The human head is often subjected to impact loading during automobile accidents, falls or sport-related events. These impact conditions can lead to mechanically-induced head injury, which constitutes one of the major causes of accidental death [Sahoo et al., 2016].

Head injuries are generally grouped into three categories: scalp damage, skull fracture, brain injury, or a combination of these [Khalil and Hubbard, 1977]. Skull fracture occurs when the tolerance limit of the skull is exceeded due to mechanical loading. These fractures result in permanent damage and account for 32% of all head injuries, sustained by pedestrians, motorcyclists, vehicle occupants and sportsmen [Fredriksson et al., 2001]. In some cases, where there is contamination from a laceration, the fractured zone of the skull can be removed and later replaced by a biomedical implant whose main functions are cosmetic and to act as a structural component protecting the brain against external loads. However, the replacement of part of the skull does not necessarily result from skull fracture. In this regard, cranial implants are also widely used after decompressive craniectomy. This has become a relatively common intervention when managing traumatic brain injury (TBI), subarachnoid hemorrhage, severe intracranial infection and stroke [Honeybul and Ho, 2016]. In these terms, the main aim of neurosurgeons dealing with the reconstruction of large and complex-formed bone defects is a predictable and stable functional and aesthetic result [Eolchiyan, 2014]. Often, when decompressive surgery is needed, the use of an autologous bone for large cranial reconstructions is not possible due to size, unacceptable appearance, or infection, fragmentation and bone resorption after grafting has occurred [Rosenthal et al., 2014]. Neurosurgeons have to choose a material to be used; polyether-ether-ketone (PEEK) and macroporous hydroxyapatite (HA) are the most common biomaterials selected due to their biocompatibility and mechanical properties.

Large cranial defects are often dealt with through cranioplasties involving PEEK implants designed from preoperative high-resolution computed tomography (CT) scans. The direct contact between the implant and bone tissue is ensured by the customisation of the implant from the CT images thus achieving a precise definition of its contour and curvature [Halabi et al., 2011]. The suitability of using PEEK for implants is known and its biocompatibility has been studied and demonstrated [Horak et al., 2010; Jockisch et al., 1992; Rivard et al., 2002].

Macroporous HA is a bioceramic material which constitutes 60 % of bone, and has similar mechanical characteristics. This material exhibits a number of properties which make it suitable to be used in skull defect reconstructions: biocompatible, sterilisable, adequate weight, compatible with diagnostic imaging and easy to design and manufacture [Stefini et al., 2013]. The presence of calcium and phosphate ions (similarly to natural bone) participates to the formation of new bone tissues on the surface of the implant [Chistolini et al., 1999]. Furthermore, HA mimics the macroporous structure of the living bone. This structure allows new bone to grow by filling not only the voids on the surface of the cranioplasty, but also the pores within the internal structure [Frassanito et al.,

2013]. As such, once the prosthesis has been placed in the skull and bone has grown within, the implant can be treated as a composite material where HA acts as the matrix and bone as the reinforcement. Moreover, HA shows excellent biocompatibility due to the absence of host immune reactions [Boyde et al., 1999; Marcacci et al., 1999; Olmi et al., 1984]. However, despite these advantages, HA implants are rigid and offer a considerably lower resilience than human bone. This fact implies a minor mechanical resistance and minor energy absorption capability with respect to human bone [Frassanito et al., 2013].

When dealing with large cranial defects, an important aspect to take into account is the load-bearing capacity of the structural prostheses, since the patients need to go back to active life, with their heads potentially subjected to future impact loadings. While the use of biocompatible materials such as PEEK and HA in cranial implants is widely accepted, there is a lack of knowledge in terms of their mechanical response under potential future impact loads arising from the patient life style. The main aim of the research presented in the current chapter is to develop a computational tool able to simulate the mechanical behaviour of implants under impact loading which can help clinicians to determine the optimal patient-specific implant material. As a second contribution, a numerical tool is proposed to evaluate the risk of implant failure when a patient has been involved in a given accidental impact. To this end, a finite element head model (FEHM) has been developed from magnetic resonance imaging (MRI) data comprising scalp, skull, cerebral falx, cerebrospinal fluid (CSF), brain tissues and an implant replacing part of the skull. The FEHM is used to study the mechanical response under a wide range of impact conditions. Numerical simulations were conducted in order to compare the mechanical response of PEEK and HA cranial implants. This analysis was carried out by focussing on the implant effectiveness in avoiding failure and TBI, while covering an impact velocity range from 1 m/s to 7 m/s for several impact locations on the skull along three different paths: from the parietal zone to vertex; from the parietal zone to occipital; and from the parietal zone to frontal. Ultimately, selection criteria for implant materials and a roadmap for further clinical assessments of bone and/or implant failure in case of post-operative impact are proposed.

8.2 Finite Element Human Head

8.2.1 Geometry and mesh generation from MRI

In this thesis, a detailed finite element model of a human head has been developed in order to study the suitability of two different cranial implants subjected to impact loads. The head model comprises the scalp, the skull, the cerebral falx, the CSF, the ventricles, the brain and a cranial implant replacing part of the skull, see Fig. 8.1(a). The geometrical information was obtained from full-head, high resolution anatomical T1 and T2-weighted MRI images of a subject available from the Human Connectome Project (HCP Subject ID: 100307) [Van Essen et al., 2013]. The anatomical images were used as input to "BET2" [Smith, 2002; Jenkinson et al., 2005] in the FSL software library [Smith et al., 2002], to extract inner skull, outer skull and outer scalp surfaces. The skull-stripped brain was further segmented into white matter, gray matter and ventricles using the Amira software [Amira]. In order to guarantee the anonymity of the patient from which the images were obtained, the MRI images are released "de-faced" by the HCP [Milchenko and Marcus, 2013], i.e. blurred at the eyes, nose and ears. These parts in the scalp and skull components were manually reconstructed in our model without affecting the brain. The implant geometry was designed in accordance with the average dimensions used when dealing with unilateral decompressive craniectomy.

The resulting multi-component (see Fig. 8.1) optimised FE model weighs 3.91 kg and is composed of 792,773 tetrahedral elements, for which spatial convergence was verified.

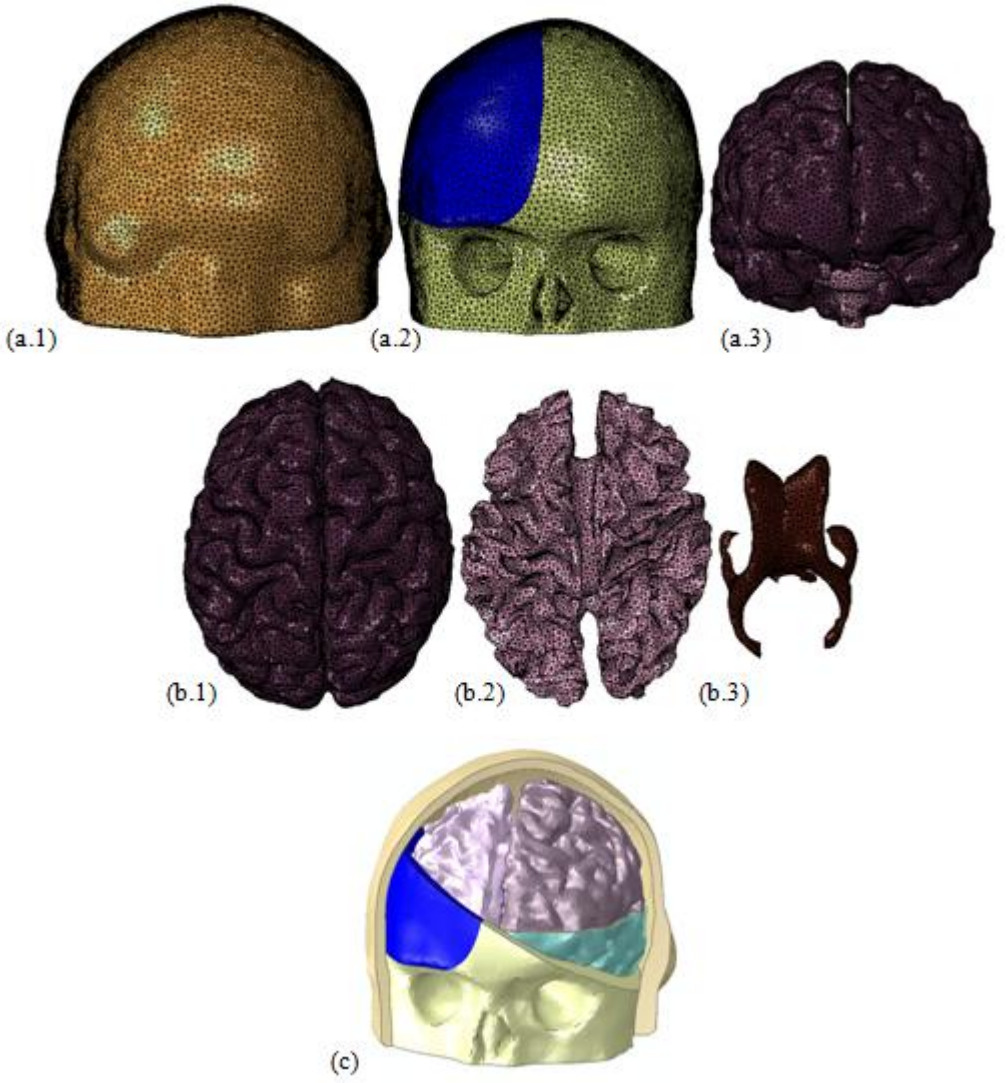

Figure 8.1: Full head finite element model showing various components: (a.1) scalp; (a.2) skull + implant; (a.3) brain tissues; (b.1) gray matter; (b.2) white matter; (b.3) ventricles; (c) whole head model.

8.2.2 Loading conditions

In order to study the load-bearing capacity of the structural prostheses and their effectiveness in protecting brain tissues, simulations have been conducted for impact conditions representative of falls. Many scenarios involving the fall of a person result in serious head injuries. A common scenario is the fall from bed, where the head is usually

the most frequent body part injured [Sadigh et al., 2004]. Schulz et al. (2008) reproduced falls from a bed and obtained, for an impact of 4.2 m s-1, a resultant head velocity normal component to ground between 3.44 m s-1 and 3.86 m s-1. Another example of fall which involves serious head injuries is observable in bicycle accidents. A fall from a bike can occur in many different ways and the variation of kinematics, head orientation and velocity can be large [Fahlstedt et al., 2012]. Fahlstedt et al. (2012) simulated a real bike accident and obtained a resultant linear velocity of the head just before impact of 5.3 m s-1 with a normal component to ground of 4 m s-1. The FEHM presented here was validated in terms of kinematics against three scenarios and the impact velocity range was thus defined from 1 m s-1 to 7 m s-1 covering the range observed in these different falls. The simulations herein were carried out by using the FE solver Abaqus [Abaqus, 2012].

The mechanical response of the head was observed to vary depending on the impact location. This fact is basically due to the non uniformity of the skull thickness and the structural influence of its shape. In addition, in the peripheral zone of the implant where some screws are located to fix it to the bone, the stresses around the screws can localise with higher values, thus leading to lower impact velocities at which implant fails. Therefore, the head orientation was varied in the simulations with the aim of studying the critical impact velocity which results in implant failure depending on the impact location. As a consequence, the impact locations were chosen along three skull paths: from parietal bone to vertex; from parietal bone to occipital bone; and from parietal bone to frontal bone. The assumption in all simulations is that the body impacts before the head does using the neck as a pivot, thus reducing the inertial effects to the weight of the head.

For the analysis of the implant effectiveness in protecting brain tissue, a specific impact scenario was selected as worst-case reference for comparison. For this purpose, an orientation angle of 30º between head and ground was selected because a) it was found to be the critical value which introduces a perpendicular impact directly on the implant and, b), it is in the parietal zone where the skull thickness is thinner, see Fig. 8.2.

The ground was defined as a rigid body since it is much stiffer than the head tissues. Following Fahlstedt et al. (2012), this contact was modelled which a penalty contact algorithm with a constant friction coefficient value set to 0.4.

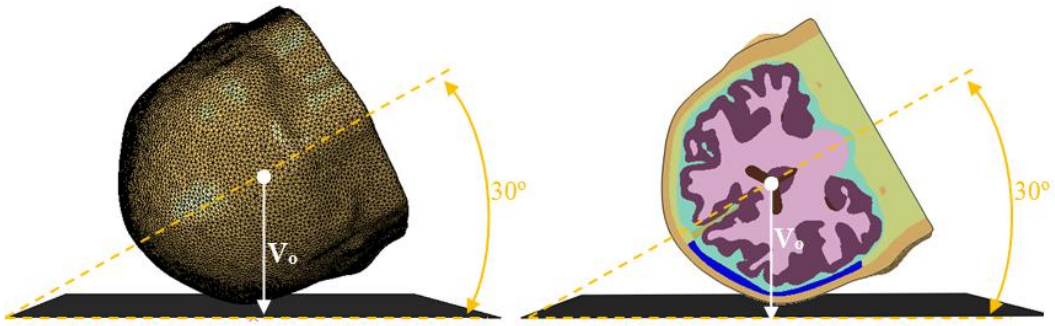

Figure 8.2: Critical impact on parietal zone.

8.2.3 Injury criteria and evaluation procedure

In this work, the effectiveness of each implant is determined following two methodologies: the structural integrity of the implant and the potential TBI.

Material fracture and plastic deformation have been established as reliable indicators of structural integrity [Goh and Lee, 2002]. When dealing within a general case where the influence of screws in the stress distribution along the implant is neglected, fracture and plastic deformation are estimated at the macroscale by the ultimate strength and yield stress of the material used. The ultimate strength for bone has been estimated to be 92.72 MPa [Wood, 1971; Zhou et al., 2016]. For HA+Bone this value is evaluated to be 20.50 MPa from the analysis carried out earlier. In PEEK, the deformation experienced along the impact process is more localised than in the case of HA or bone because its ductile behaviour. It results in different strain rates along the PEEK implant structure and, consequently, different stress thresholds to reach yielding because of its rate-dependent properties. Since a constitutive model has been defined taking into account rate dependencies, it can be determined when the PEEK implant reaches yielding depending on the strain rate in each zone. Moreover, when the impact takes place close to the peripheral zone of the implant, the effect introduced by the screws in concentrating the stress must be considered. As the FEHM does not include the screws, a complementary analysis is done in order to capture the stress concentration effect which should be applied in the surroundings of the screws location.

To this end, a numerical model of a representative volume of the bone-implant interface has was developed and the stress distribution was analyzed when screws are considered and when they are not. Different stress states were applied to a 120×60×6 mm3 plate. The thickness of the plate was selected to be representative of the skull and the other two

dimensions were optimized to avoid introducing a geometrical influence on the stress distribution. These results were compared with simulations under the same conditions but including two screws of 1.5 mm rigidly together with a distance of 12 mm between them. Thus, the concentration ratio to be applied in the peripheral zone of the implant was selected as the maximum one found from uniaxial compression; uniaxial tension; shearing; and out-of-plane stress states. The concentration ratio for the bone zone affected by the screws was found equal to 1.29; the average one for the PEEK zone affected by the screws was found equal to 1.28; and the one for the HA zone affected by the screws was found equal to 1.32.

Table 8.1: Thresholds of brain injury criteria [Tse et al., 2014].

Parameter	Thresholds	Reference
Pressure	***Criterion 1*** >235 kPa → injury <173 kPa → minor or no injury	[Ward et al., 1980]
Shear stress	***Criterion 2*** 11-16.5 kPa → severe injury	[Kang et al., 1997]
Von Mises stress	***Criterion 3*** >18 kPa → 50% probability of moderate neurological lesions >38 kPa → 50% probability of severe neurological lesions	[Baumgartner and Willinger, 1997]
	Criterion 4 ≥26 kPa → axonal damage	[Deck and Willinger, 2008]
Strain	***Criterion 5*** >0.25 → structural damage >0.20 → functional damage >0.10 → reversible damage	[Galbraith et al., 1993]

In order to define a common framework to analyse the efficiency of both implants in protecting the brain against impact loads, some indicators have been used for TBI assessment in terms of mechanical variables such as pressure, shear stress, von Mises stress and strain. These post-traumatic biomechanical parameters are compared with brain tissue tolerance thresholds in the literature as collected by Tse et al. (2014), see Table 8.1. Following the methodology presented by these authors, the critical anatomical locations are reported and a dimensionless parameter is used as a mechanical equivalent of brain injuries. This dimensionless parameter is defined in a similar way as the cumulative strain damage measure proposed by Takhounts and Eppinger (2003), is thus chosen as the ratio

between the number of elements reaching the critical value associated to damage and the total number of elements which compose the brain tissue.

The constitutive modelling of the mechanical behaviour of each human tissue and HA is explained in detail in *Appendix C*. For the PEEK implant, it was employed the constitutive model developed and validated for this material in Chapter 6.

8.3 Results and discussion

Numerical simulations of impacts on the FEHM were conducted for an impact velocity range of 1 m s-1 to 7 m s-1 for three possible scenarios: when the subject has a PEEK implant; when the subject has a HA implant; and when the subject's skull presents no previous damage. The results and discussion of these simulations are introduced in three sections: acceleration-time predictions; critical impact velocity predictions; and TBI predictions.

8.3.1 Acceleration-time validation

In this section, the model predictions for acceleration-time curves are compared with available data from the literature in order to ensure that the impact conditions imposed are representative of real accidents and falls. In addition, a comparison between the mechanical response of the head when PEEK implant, HA implant and no implant are incorporated, is done in terms of acceleration-time curves. Three cases are considered here for comparison. Schulz et al. (2008) reported experimental data of the fall of a person from a bed and Fahlstedt et al. (2012) reported numerical data of a bike accident reconstruction. The resultant velocity component in the perpendicular direction to ground was estimated between 3.44 m s-1 and 3.86 m s-1 for the fall from bed and 4 m s-1 for the bike accident. The third set of data corresponds to measurements performed during experiments in which human heads cut from cadavers were impacted against a rigid plate [Loyd et al., 2014].

In Fig. 8.3(a), the model predictions for acceleration-time curves of perpendicular head drops when no implant is included in the FEHM are compared with literature data. The numerical acceleration-time data presented herein were obtained from the force-time curves by dividing the force values by the mass of the whole head. It can be observed that both fall from bed and bike accident cases are within the impact velocity and acceleration ranges simulated. The effective impact velocity estimated by Loyd et al. (2014) was 2.42 m s-1 and the head drop was conducted on the vertex location. The model prediction shows a slightly overestimation of the maximum acceleration reached compared with the

experiment. This can be explained by the lower mass of the head tested post-mortem (≈ 3.2 kg) thus implying a lower inertial contribution to the impact process. From the results shown in Fig. 8.3(a), it can be concluded that the model predictions conducted cover the impact velocity and acceleration ranges found in common accidents which involve head impacts.

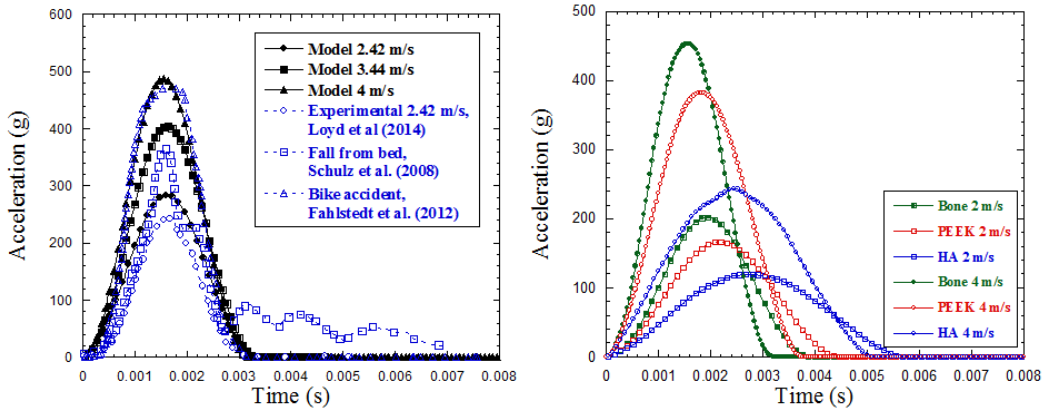

(a) (b)

Figure 8.3: Acceleration-time numerical predictions of the model: (a) comparison with published data; and (b) comparison between PEEK implant, HA implant and no implant predictions.

Moreover, the acceleration-time response of the human head during impact was analysed for both PEEK and HA. The results, presented in Fig. 8.3(b), show the higher peaks of acceleration for PEEK for 2 m s-1 and 4 m s-1 impacts. In contrast, the deformation experienced by the implant is more significant for HA. This is consistent with the lower HA Young's modulus, which also results in a prolongation of the contact duration. While the use of a softer material for the implant results in a major deformation and thus trauma, it also implies a higher damping effect in reducing brain motion.

8.3.2 Critical impact velocity predictions inducing implant failure

When considering the conditions for implant failure during impacts, two factors have to be taken into account: the impact velocity and the impact location. An increase in the impact velocity implies a higher impact energy leading to higher stresses in the implant. This results in a higher risk of implant failure as the impact velocity increases. The impact location plays an important role not only because of the variation of the thickness and the variation of the structural stiffness along the skull, but also because of the

presence of screws and their role in concentrating the stress. As a consequence, a parametric study varying both impact velocity and impact location was carried out along three different paths covering the most common impact scenarios in fall accidents. This study allows us to estimate the impact velocity which is expected to result in implant failure for all the scenarios considered.

The three skull paths are: from parietal bone to vertex (Fig. 8.4(a.1)); from parietal bone to occipital bone (Fig. 8.4(a.2)); and from parietal bone to frontal bone (Fig. 8.4(a.3)). The critical impact velocity resulting in implant failure for each point is presented in Figure 6(b) for PEEK implant and in Fig. 8.4(c) for HA+Bone implant. In both cases the parietal-vertex path is the weakest. In addition, there is an inverse relationship between critical impact velocity and distance to implant interface, where the implant-bone interface where the screws are located is the weakest and most critical zone. For the parietal-vertex and parietal-occipital paths, the critical impact velocity presents a minimum at the implant-bone interface (0 mm) due to the presence of the screws. As the distance between impact location and the implant-bone interface increases, the critical impact velocity continuously increases until reaching the critical impact velocity of the impacted material. However, while the parietal-frontal path also shows a minimum in the implant-bone interface, the impact velocity does not present a continuous increase by augmenting the distance to the main interface (0 mm). This is due to the closeness of the lower interface of the implant, which is also affected by the possible presence of screws. Accordingly, it can be established that lower velocities can result in implant failure if the impact takes place closer to the peripheral zone of the implant where the fixation system to bone is located. Note that the proposed approach does consider a continuous distribution of screws along the interface instead of just a few. This implies that the results presented here are “worst-case scenarios”.

The mechanical properties of the material used in the implant are found to play the predominant role in avoiding implant failure. For all the scenarios tested, the PEEK implant exhibits a better mechanical response against impact loading than the HA+Bone implant. A good indicator of the load bearing capacity of these materials is the critical impact velocity resulting in implant failure when the impact takes place far enough from the peripheral zone of the implant where the effect of the screws can be neglected. In this regard, this velocity was determined from impact simulations with an orientation angle of 30º between the head and ground where the PEEK implant, the HA+Bone implant and no implant were considered (see Fig. 8.2). The critical impact velocity for PEEK was found to be 6.5 m s-1 and, in the case of bone and HA+Bone it was found to be 54 % and 80 % less than this, respectively. The difference between PEEK and HA+Bone in terms of energy absorption capability results in different implant failure patterns. When a PEEK

implant is employed, the implant failure occurs predominantly in the bone part even in some situations in which the impact takes place in the implant zone. However, when a HA+Bone implant is employed, the implant failure occurs predominantly in the implant zone instead of the bone. It must be noticed that the critical impact velocities resulting in implant failure have been obtained for a case where the ground is considered purely rigid. This assumption corresponds to the most critical situation.

Overall, these results suggest that the biomaterial to be used in the cranial implant should be selected depending on the specific patient and his exposure to impact loadings. In this regard, the macroporous HA+Bone implant is observed to behave in a very brittle way when it is subjected to impacts of different natures. This brittle behaviour and associated catastrophic failure of the HA implant has already been reported by Adetchessi et al. (2012), who presented a clinical case of a 25-year-old man. After a cranioplasty using macroporous HA prosthesis, the patient had to undergo surgery again because of the implant failure due to impact during a generalized seizure. In the second intervention a PEEK solution was finally used.

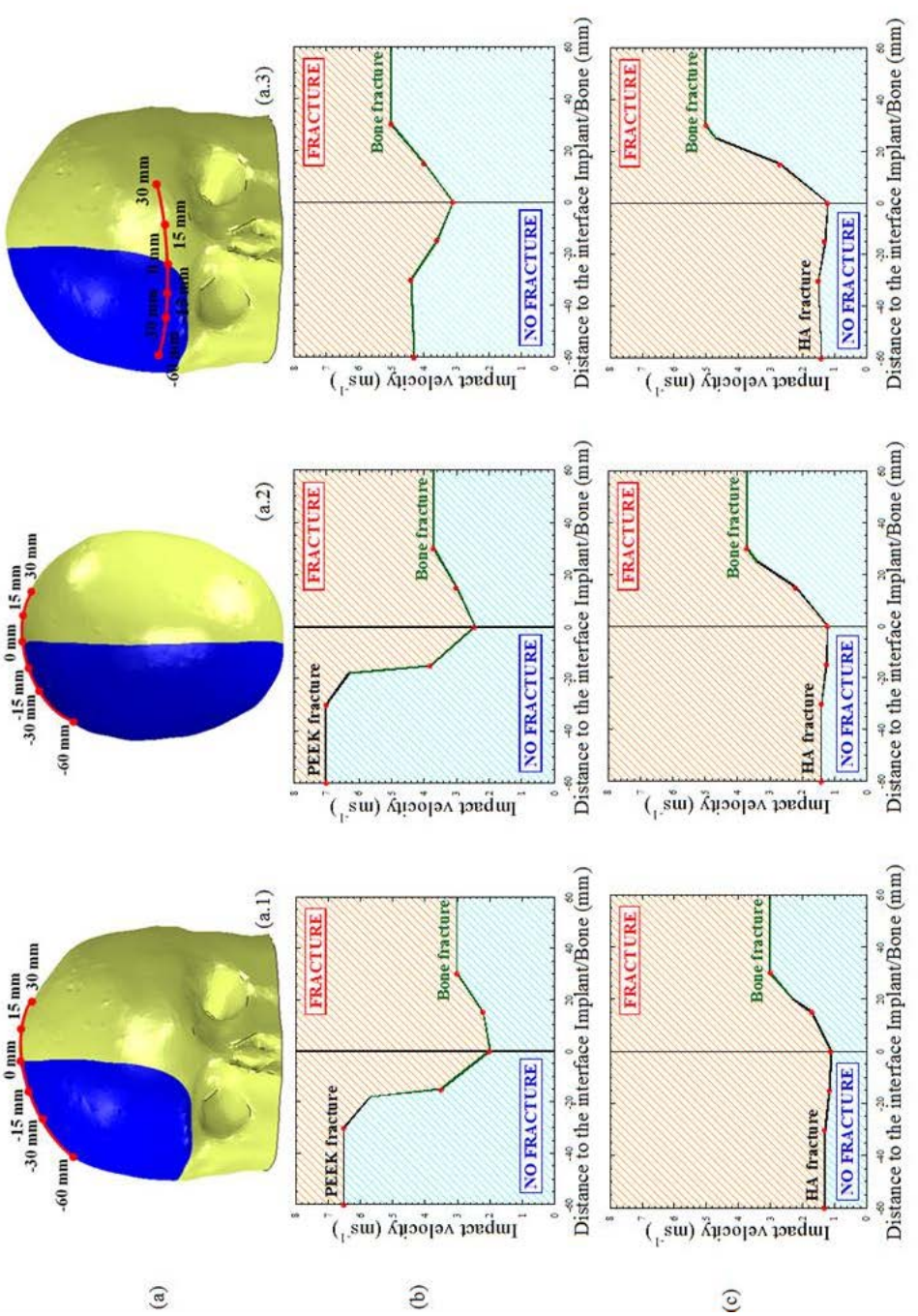

Figure 8.4: (a) Impact localisation points defined along the three skull paths studied: (a.1) parietal-vertex; (a.2) parietal-occipital; and (a.3) parietal-frontal. Risk of fracture as a function of impact velocity and distance to the implant interface along different paths for: (b) PEEK implant; and (c) HA implant.

8.3.3 TBI predictions

Since the main function of the implant is to protect the brain against external loads, the effectiveness of both implants in avoiding TBI is compared here. In the biomechanics community, the risk of TBI has been determined based on intracranial biomechanical parameters. The aim of this work is not to determine the most suitable criterion for evaluating TBI. Instead, this section focuses on comparing the effectiveness of both cranial implants by applying different criteria proposed in previous studies, see Table 8.1. Therefore, as mentioned previously, a dimensionless parameter providing the percentage of brain tissue with probability of damage is determined for each biomechanical parameter depending on the impact velocity. For this study, an orientation angle between the head and ground of 30º leading to a perpendicular impact on the implant has been adopted as a common impact scenario for comparison, see Fig. 8.2.

The results are provided in Fig. 8.5. The intracranial pressure based criterion (Criterion 1) was found not to vary significantly between the two implants studied because the threshold values are reached in almost the whole brain at relatively low impact velocities (lower than 3 m s-1), and is not studied further here. For the remaining criteria, a higher TBI level for macroporous HA+Bone implant than for PEEK implant is observed. In Fig. 8.5, the percentages of damaged tissue as a function of impact velocity are presented for the remaining criteria.

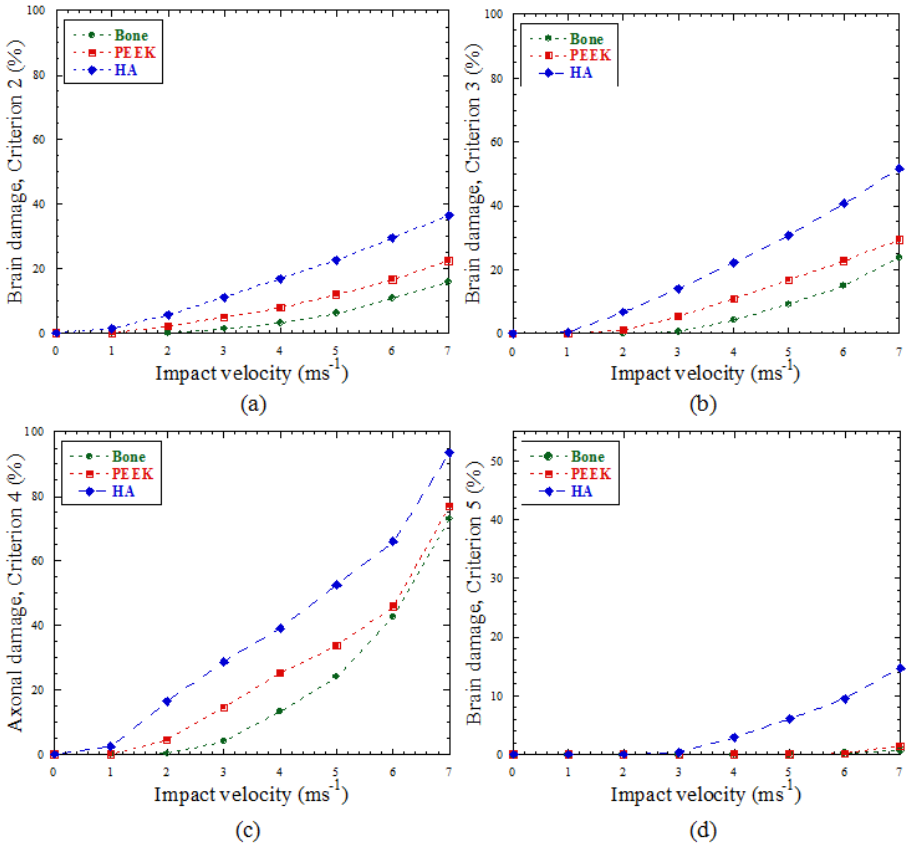

Figure 8.5: Percentage of damaged elements in brain tissue based on: (a) Criterion 2; (b) Criterion 3; (c) Criterion 4; and (d) Criterion 5

TBI can be understood as a combination of the deformation process due to brain motion and the deformation process due to the indentation process on the skull. In this regard, the stiffness of the material used in the implant, defined by its Young's modulus, plays a predominant role in the brain deformation. On the one hand, a lower stiffness has a beneficial effect due to its higher damping effect of the implant which results in a reduction of the brain motion. This damping effect is easily observed in the results shown in Fig. 8.3(b), where a lower material stiffness results in lower acceleration values and in a prolongation of the contact duration. On the other hand, a lower stiffness leads to a larger trauma by a more important deflection of the implant directly affecting the brain tissue. Fig. 8.6 shows the anatomical location and extension of severe brain damage in dark colours and moderate brain damage in light colours according to Criterion 3, see Table 8.1. It can be observed that the predominant deformation is produced by the implant bending and is localized at the contact zone where the impact takes place. A direct relationship is here established between the Young's modulus of the material used

for the implant and the effectiveness of the prosthesis in avoiding TBI under the specified loading conditions. In this case, bone is the best TBI protective material, followed by PEEK, and eventually the HA+Bone implant.

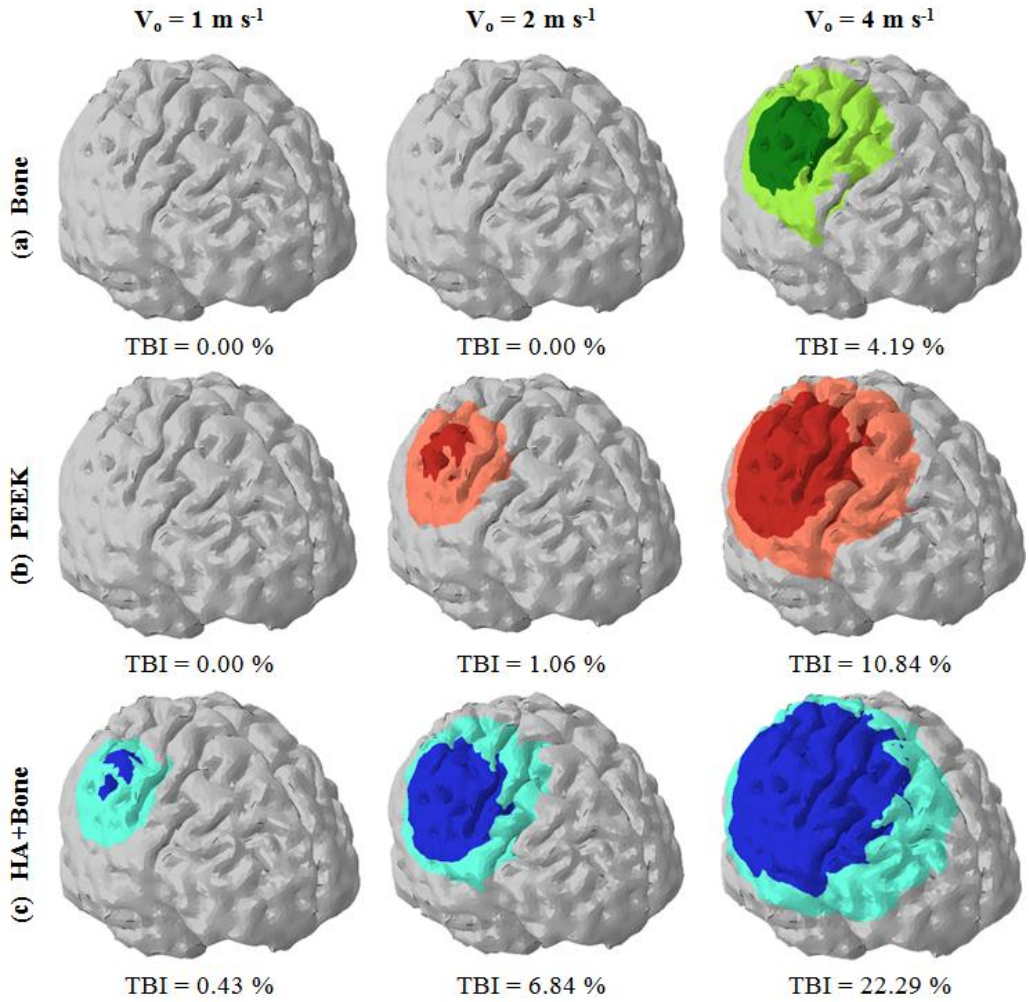

Figure 8.6: Severe brain damage (dark colours and TBI percentages) and moderate damage (light colours) at impact velocities of 1 m s-1, 2 m s-1 and 4 m s-1 when: (a) no implant is used; (b) a PEEK implant is used; and (c) a HA implant is used.

8.4 Conclusions

The constitutive model for PEEK presented in Chapter 6 has been used to the study of a biomedical application that, in combination with a the development of a numerical head model from anonymous MRI, has allowed for the comparison of the mechanical behaviour under impact loading of two cranial implants: PEEK and macroporous HA+Bone. The model was validated in terms of the kinematics of head under impact conditions and used to:

(i) Compare the mechanical response of the two cranial implants under a wide range of impact conditions. In terms of implant failure and TBI, the numerical results showed a better mechanical behaviour of PEEK implant under the loading conditions tested. However, a high risk of fracture was found when a HA implant is subjected to impact loading.

(ii) Provide a roadmap for the determination of the risk of implant failure when the subject has been exposed to any accident involving impact loading.

There are of course many clinical considerations when choosing a cranial implant. These include cost, availability and timescales, among others. Manufacturers of such implants are frequently found to claim greater biointegration, lower infection rates, easier implant techniques and other rather hard-to-demonstrate benefits. Eventually, an implant is required to provide: a) protection with b) an acceptable cosmetic result. Both HA and PEEK (among others) provide these. However, patients receiving implants are more likely to suffer from neurological deficits and epilepsy than the general population, and these both increase the risks of falls, and injury to the implant and underlying brain. Additionally, the patients that have made a good enough recovery may well wish to go back to sports and exercise, which may well increase these risks further. As a conclusion, a patient specific assessment of what the implant will need to withstand in the future is recommended to tailor the choice of implant accordingly.

Chapter 9.
Summary and conclusions

9.1 Concluding remarks

The main objective of this Doctoral Thesis is the development of a general continuum mechanics framework and associated methodology for the formulation of hyperelastic-based constitutive models; with a number of specific, related, objectives. This section highlights the principal insights associated with each objective:

Analysis of the mechanical behaviour of hyperelastic materials

- The mechanical behaviour of PEEK polymer has been studied for a wide range of loading conditions.
    - An experimental campaign has been conducted covering impact energies from 21 J to 131 J.
    - Unfilled PEEK has been observed to behave in a ductile manner without evidence of brittle failure.
    - A preliminary modelling of the mechanical behaviour of unfilled PEEK has been proposed and validated. This modelling has provided numerical insights into the mechanisms that govern the deformation process. These results highlight the need to take into account the thermomechanical coupling, especially at high strain rates.
- The mechanical behaviour of SCFR PEEK has been studied for a wide range of loading conditions.
    - An experimental investigation has been conducted covering impact energies from 21 J to 131 J.
    - The reinforcement of PEEK with short carbon fibres has been observed to: introduce anisotropy due to fibre orientation; increase the stiffness of the composite; and reduce the energy absorption capacity because of a change in the material behaviour from ductile to brittle.
    - A preliminary modelling of the mechanical behaviour of SCFR PEEK based on the homogenization of the elastic material properties and anisotropic damage has been proposed and validated.
- The influence of temperature on the mechanical behaviour of PEEK composites has been studied for a wide range of loading conditions.
    - An experimental investigation has been conducted on unfilled PEEK and SCFR PEEK specimens covering impact tests where the testing temperature was varied from 200 K to 300 K.
    - Experimental evidence has shown a ductile-to-brittle transition in the mechanical behaviour of PEEK that depends on a critical combination of temperature and strain rate.

- The existence of this ductile-to-brittle transition at low temperatures reduces drastically the energy absorption capacity of PEEK composites. This effect is more evident in unfilled PEEK than SCFR PEEK.

Development of a new constitutive model for semi-crystalline thermoplastic polymers

- A new constitutive model for semi-crystalline thermoplastic polymers has been developed taking into account the experimental and numerical insights from the analysis of the mechanical behaviour of hyperelastic materials. This model accounts for strain rate and temperature dependencies and pressure sensitivity within a thermodynamically consistent framework formulated in finite deformations.
- The model parameters have been identified for unfilled PEEK and the model has been validated for a wide range of loading conditions.
- The predictive capacity of the model has been evaluated in two dynamic problems:
  - Low velocity impact tests on PEEK plates: the model highlights the need to consider thermomechanical coupling under dynamic conditions in terms of temperature evolution due to inelastic dissipation.
  - Dynamic necking on PEEK slender bars: inertial and thermal effects have been studied on ductility and energy absorption capability of PEEK. Strain rate has been found to increase both necking strain and energy absorption capability. Temperature has been found to increase necking strain and decrease energy absorption capability. For adiabatic conditions, the consideration of inelastic dissipation has been demonstrated to be needed for reliable predictions.

Development of a general continuum mechanics framework for transversely isotropic hyperelastic materials

- A general continuum mechanics framework for transversely isotropic hyperelastic materials has been developed. This model is formulated in terms of Helmholtz free energy function and allows for the particularization of the energy potentials and flow equations for specific materials.

- The general framework has been particularized leading to a new constitutive model for SCFR PEEK composites. The model parameters have been identified and provided.
- The general framework has been particularized leading to a new constitutive model for brain white matter. The model parameters have been identified and provided. Here, two novel ideas have been proposed to taking into account different mechanical behaviour within the white matter due to anisotropy induced by axon orientation and dispersion, and region-dependent stiffness related with FA.

Application of the developed constitutive models to the study of the mechanical behaviour of cranial implants under impact loading

- A FEHM comprising scalp, skull, cerebral falx, cerebrospinal fluid and brain tissue, with a cranial implant replacing part of the skull, has been developed from magnetic resonance imaging data.
- The constitutive models developed in this thesis have been used in the FEHM to the study the mechanical behaviour of PEEK cranial implants under impact loading.
- PEEK cranial implants have been compared with other common cranial implants in terms of structural integrity and potential TBI. The numerical results have shown a better mechanical behaviour of PEEK implant under the loading conditions tested for both criteria.
- A roadmap has been provided for the determination of the risk of implant failure when the subject has been exposed to any accident involving impact loading.

9.2 Future works

The research carried out in this Doctoral Thesis provides new ideas and methodologies on the development of hyperelastic-based constitutive models and may motivate future contributions within this line of investigation. Following this research line, some new works and collaborations have been started:

Constitutive modelling of polymers

- The parameters of the constitutive model developed for semi-crystalline thermoplastic polymers can be indentified for different materials of this type. In this regard, an identification process of these parameters for many thermoplastic polymers is being carried out in order to provide an extensive library of *calibrated constitutive models* for semi-crystalline polymers.
- The constitutive model developed for semi-crystalline thermoplastic polymers provides reliable predictions from the ductile-to-brittle transition until the glass transition, the temperature range within the assumptions of the model are valid. To support the development of a constitutive model for the whole temperature range, we are working on the formulation of a specific free energy able to represent the caloric behaviour of PEEK and its influence on thermomechanical behaviour.
- The general constitutive framework allows the formulation of new constitutive models that describe the mechanical behaviour of a wide variety of polymeric materials. In this regard, extended models can be proposed by adding new constitutive branches that describe other deformation mechanisms (see *Appendix D*).
- The development of failure criteria and damage evolution laws that describe the mechanical behaviour of polymers during the processes of deformation and failure.

Constitutive modelling of soft tissues

- Development of a more sophisticated constitutive model for the brain white matter that accounts for strain rate sensitivity and anisotropy induced by axon orientation.
- Combination of experimental and computational techniques to develop a finite element brain model that allows the description of the real mechanical behaviour of brain tissue and the analysis of brain injuries due to mechanical loading.
- Collaboration with medical institutions to implement the computational tools and methodologies developed for supporting clinical decisions.

9.3 Acknowledgment

The author of the Doctoral Thesis is indebted to the Ministerio de Ciencia e Innovación de España (ProjectDPI/2011-24068) and to the Ministerio de Economía y Competitividad de España (ProjectDPI/2014-57989-P) for financial support towards part of this work.

9.3.1 Acknowledgment to University of Oxford

I would like to highlight the scientific collaboration with the University of Oxford and the John Radcliffe Hospital of Oxford during research for this Doctoral Thesis that has permitted me to apply the results of investigation to real problems. This collaboration has also opened a wide range of potentials avenues for research that will be explored immediately following the PhD defence.

I want to especially thank Antoine Jérusalem, Professor of the Department of Engineering Sciences of University of Oxford and Principal Investigator of Computational Mechanics of Materials Group, for his support and considerable contribution to this project, and the many insights I have gained from him.

9.3.2 Acknowledgement to Université de Lorraine

I would like to highlight the scientific collaboration with Alexis Rusinek, Professor in Laboratory of Mechanics, Biomechanics, Polymers and Structures of the Université de Lorraine. His collaboration has been essential for the analysis of hyperelastic materials under extreme loading conditions.

9.4 List of publications

Below are listed the publications related to this doctoral Thesis.

Publications indexed in Journal Citation Report (JCR)

Authors (by order of signature): **D. García-González,** A. Rusinek, T. Jankowiak, **A. Arias**
Title: Mechanical impact behavior of polyether-ether-ketone (PEEK)
Journal: COMPOSITE STRUCTURES
Type: Indexed in Journal Citation Reports (Science Citation Index).
Impact factor:3,32; Position =3/24, **cuartil Q1**. Category: Materials Science, Composites
Volume: 124 Pages, initial: 88; final: 99 Date: 2015
Citations: 12

Authors (by order of signature): **D. García-González**, M. Rodríguez-Millán, A. Vaz-Romero, **A. Arias**
Title: High impact velocity on multi-layered composite of polyether ether ketone and aluminium
Journal: COMPOSITE INTERFACES
Type: Indexed in Journal Citation Reports (Science Citation Index)
Impact factor:0,73; Position =16/24 cuartil Q3. Category: Materials Science, Composites
Volume: 124 Pages, initial: 705 final: 715 Date: 2015
Citations: 3

Authors (by order of signature): **D. García-González**, M. Rodríguez-Millán, A. Rusinek, **A. Arias**
Title: Investigation of mechanical impact behavior of short carbon-fiber-reinforced PEEK composites
Journal: COMPOSITE STRUCTURES
Type: Indexed in Journal Citation Reports (Science Citation Index)
Impact factor:3,32; Position=3/24, **cuartil Q1**. Category: Materials Science, Composites
Volume: 133 Pages, initial: 1116 final: 1126 Date: 2015
Citations: 3

Authors (by order of signature): **D. García-González**, M. Rodríguez-Millán, A. Rusinek, **A. Arias**
Title: Low temperature effect on impact energy absorption capability of PEEK composites
Journal: COMPOSITE STRUCTURES
Type: Indexed in Journal Citation Reports (Science Citation Index)
Impact factor:3,32; Position=3/24, **cuartil Q1**. Category: Materials Science, Composites
Volume: 134 Pages, initial: 440 final: 449 Date: 2015
Citations: 5

Authors (by order of signature): **D. García-González**, R. Zaera, **A. Arias**
Title: A hyperelastic-thermoviscoplastic constitutive model for semi-crystalline polymers: Application to PEEK under dynamic loading conditions
Journal: INTERNATIONAL JOURNAL OF PLASTICITY
Type: Recogida en Journal Citation Reports (Science Citation Index)
Impact factor:5.623; Position=2/135, **cuartil Q1**. Category: Mechanics
DOI: http://dx.doi.org/10.1016/j.ijplas.2016.09.011
Citations: 0

Authors (by order of signature): **D. García-González**, J. Jayamohan, S.N. Sotiropoulos, S.-H. Yoon, J. Cook, C.R. Siviour, **A. Arias**, A. Jérusalem.
Title: On the mechanical behaviour of PEEK and HA cranial implants under impact loading
State: UNDER REVIEW in JOURNAL OF MECHANICAL BEHAVIOR OF BIOMEDICAL MATERIALS

Authors (by order of signature): **D. García-González**, S. Garzon-Hernandez, **A. Arias**
Title: Combining viscoelasticity and thermo-viscoplasticity for modelling semi-crystalline polymers: Application to UHMWPE
State: SUBMITTED

Authors (by order of signature): **D. García-González**, A. Jérusalem, S. Garzon-Hernandez, R. Zaera, **A. Arias**
Title: A continuum mechanics model for anisotropic hyperelastic materials: From short fibre reinforced thermoplastic composites to soft tissues
State: SUBMITTED

International conferences (in all of them the author of the thesis has been the Oral Speaker)

D. García-González, J. Jayamohan, S.N. Sotiropoulos, S.-h. Yoon, J. Cook, C. Siviour, A. Arias and A. Jérusalem. *A 3D numerical model for the prediction of the mechanical response of cranial implants*. **International Conference: Soft Tissue Mechanics Workshop, Manchester, UK (2016).**

D. García-González, S. Garzon-Hernandez, A. Arias. *A constitutive model for thermoplastic composites under dynamic loading*. **International Conference: 19th International Conference on Composite Structures, Porto (2016).**

D. García-González, S. Garzón, M. Rodriguez-Millán, A. Arias. *Single and multiple impact behavior of thermoplastic composites*. **International Conference: 2nd International Conference on Mechanics of Composites, Porto (2016).**

D. García-González, I. Funes-Vecino, M. Rodríguez-Millán, A. Rusinek, A. Arias. *Experimental punching technique for ductile fracture testing*. **International Conference: Annual International Workshop on Dynamic Behaviour of Structures and Materials, Interaction and Friction Across the Strain Rates, London (2015).**

D. García-González, R. Zaera, I. Funes-Vecino, A. Arias. *Dynamic punch behavior of polyether-ether-ketone (PEEK)*. **International Conference: 9th European Solid Mechanics Conference, Madrid (2015).**

D. García-González, A. Rusinek, T. Jankowiak, A. Arias. *Impact Mechanical Behaviour of Carbon Fiber Reinforced Peek*. **International Conference: International Conference on Composite Structures, Lisbon (2015).**

D. García-González, A. Rusinek, T. Jankowiak, A. Arias. *Numerical and experimental behavior of PEEK composite materials under low impact energy*. **International Conference: International Conference on Advances in Composite Materials and Structures, Istanbul (2015).**

D. García-González, A. Aynat, A. Arias. *Análisis experimental y numérico del comportamiento dinámico de estructuras híbridas de aplicación biomédica*. **International Conference: 3º Encontro Português de Materiais e Estruturas Compósitas, Lisbon (2014).**

D. García-González, A. Aynat, A. Vaz, M.Rodríguez, A. Arias. *High impact velocity on multi-layered composite of polycarbonate and aluminium*. **International European Conference Composite ECCM 16, Seville (2014).**

D. García-González, A. Aynat, M.Rodríguez, A. Vaz-Romero, A. Arias. *Thermomechanical behaviour of composite sandwich panels of polymer/metal under low-velocity impact loading.* **International Conference: European Conference on Composite ECCM 16, Seville (2014).**

D. García-Gónzalez, Aynat, A. Arias. *Numerical modelling of hybrid metal composite for prosthetic intervertebral discs*. **International Conference: European Conference on Composite ECCM 16, Seville (2014).**

Chapter 10.
Conclusiones

10.1 Conclusiones

En cumplimiento de la normativa, este capítulo incluye en castellano la información correspondiente a conclusiones y trabajos futuros.

El objetivo principal de esta Tesis Doctoral ha sido el desarrollo de un marco general de la mecánica del continuo y de la metodología asociada para la formulación de modelos constitutivos de base hiperelástica. Con esta finalidad se han planteado una serie de objetivos específicos. Esta sección destaca las principales conclusiones asociadas con cada objetivo:

Análisis del comportamiento mecánico de materiales hiperelásticos

- Se ha estudiado el comportamiento mecánico del polímero PEEK para un amplio intervalo de condiciones de carga.
    - Se ha llevado a cabo una investigación experimental que comprende energías de impacto desde 21 J hasta 131 J.
    - Se ha observado que el PEEK sin reforzar se comporta de manera dúctil sin evidencia de fallo frágil.
    - Se ha propuesto y validado un modelo preliminar del comportamiento mecánico del PEEK sin refuerzo. Este modelo ha proporcionado información numérica sobre los mecanismos que rigen el proceso de deformación. Estos resultados ponen de relieve la necesidad de tener en cuenta el acoplamiento termo-mecánico, especialmente a altas velocidades de deformación.
- Se ha estudiado el comportamiento mecánico del polímero PEEK reforzado con fibra corta (SCFR PEEK) para un amplio intervalo de condiciones de carga.
    - Se ha llevado a cabo una investigación experimental que comprende las energías de impacto desde 21 J hasta 131 J.
    - Se ha observado que el SCFR PEEK: introduce anisotropía debido a la orientación de las fibras; aumenta la rigidez del material compuesto; y reduce la capacidad de absorción de energía debido a un cambio en el comportamiento global de dúctil a frágil.
    - Se ha propuesto y validado un modelo preliminar del comportamiento mecánico del SCFR PEEK basado en la homogeneización de las propiedades del material elástico y considerando un daño isótropo.
- Se ha estudiado la influencia de la temperatura en el comportamiento mecánico de los materiales compuestos de PEEK para un amplio intervalo de condiciones de carga.

- Se ha llevado a cabo una investigación experimental sobre probetas de PEEK sin reforzar y de SCFR PEEK bajo condiciones de impacto donde la temperatura de ensayo se ha variado desde 200 K hasta 300 K.
- Los resultados experimentales has mostrado una transición de dúctil a frágil en el comportamiento mecánico del PEEK que depende de una combinación de temperatura y velocidad de deformación.
- La existencia de esta transición dúctil-frágil a bajas temperaturas reduce drásticamente la capacidad de absorción de energía de los materiales compuestos PEEK. Este efecto es más evidente en el PEEK sin reforzar que en el SCFR PEEK.

Desarrollo de un nuevo modelo constitutivo para polímeros termoplásticos semi-cristalinos

- Se ha desarrollado un nuevo modelo constitutivo para polímeros termoplásticos semi-cristalinos, cuyas hipótesis de comportamiento se basan en las observaciones experimentales y numéricas del análisis del comportamiento mecánico de materiales hiperelásticos. Este modelo tiene en cuenta las dependencias del comportamiento mecánico con la velocidad de deformación y con la temperatura y la influencia del estado tensional dentro de un marco termodinámicamente consistente formulado en grandes deformaciones.
- Se han identificado los parámetros del modelo para el PEEK y el modelo ha sido validado para un amplio rango de condiciones de carga.
- La capacidad predictiva del modelo ha sido evaluada en dos problemas dinámicos:
    - Ensayos de impacto a baja velocidad en placas de PEEK: el modelo destaca la necesidad de considerar el acoplamiento termo-mecánico en condiciones dinámicas en términos de evolución de la temperatura debido a la disipación inelástica.
    - Tracción dinámica en barras esbeltas de PEEK: se han estudiado los efectos inerciales y térmicos sobre la ductilidad y la capacidad de absorción de energía del PEEK. Se ha observado que la velocidad de deformación aumenta la deformación de inestabilidad plástica y la capacidad de absorción de energía. Se ha observado que la temperatura aumenta la deformación de inestabilidad plástica y disminuye la capacidad de absorción de energía. Para condiciones adiabáticas, se ha demostrado que la consideración de la disipación inelástica es necesaria para una predicción fiable del comportamiento mecánico de estos materiales.

Desarrollo de un marco general de la mecánica del continuo para materiales de base hiperelástica transversalmente isótropos

- Se ha desarrollado un marco general de la mecánica del continuo para materiales de base hiperelástica transversalmente isótropos. Este modelo está formulado en base a la función de energía libre de Helmholtz y permite la particularización de los potenciales de energía y ecuaciones de flujo para materiales específicos.
- El marco general se ha particularizado dando lugar a un nuevo modelo constitutivo para los materiales compuestos SCFR PEEK. Se han identificado y proporcionado los parámetros del modelo para estos materiales.
- El marco general ha sido particularizado dando lugar a un nuevo modelo constitutivo para la materia blanca del cerebro. Se han identificado y proporcionado los parámetros del modelo para este material. En este modelo se han propuesto dos ideas originales para tener en cuenta diferentes comportamientos mecánicos dentro de la materia blanca debidos a la anisotropía inducida por la orientación y dispersión de axones y a la distinta rigidez en función de la región de la materia blanca, relacionada con el parámetro FA.

Aplicación de los modelos constitutivos desarrollados al estudio del comportamiento mecánico de implantes craneales bajo cargas de impacto

- A partir de datos de resonancia magnética, se ha desarrollado un modelo de cabeza en elementos finitos (FEHM) compuesto por tejido dérmico, cráneo, líquido cefalorraquídeo y el tejido cerebral, incluyendo un implante craneal termoplástico que sustituye parte del cráneo.
- Los modelos constitutivos desarrollados en esta tesis se han utilizado en el FEHM para estudiar el comportamiento mecánico de los implantes craneales de PEEK bajo cargas de impacto.
- Los implantes craneales de PEEK se han comparado con otros implantes craneales empleados en la actualidad en términos de integridad estructural y lesión cerebral traumática (TBI) potencial. Los resultados numéricos han mostrado un mejor comportamiento mecánico del implante de PEEK para ambos criterios bajo las condiciones de carga ensayadas.
- Se ha proporcionado una herramienta para la determinación del riesgo de fallo del implante cuando el sujeto ha estado expuesto a cualquier accidente que implique carga de impacto.

10.2 Trabajos futuros

La investigación llevada a cabo en esta Tesis Doctoral aporta nuevas ideas y metodologías sobre el desarrollo de modelos constitutivos con base hiperelástica y sirve de base para contribuciones futuras dentro de esta línea de investigación. Siguiendo esta línea de investigación, se han iniciado nuevos proyectos y colaboraciones:

Modelización constitutiva de polímeros

- Los parámetros del modelo constitutivo desarrollado para polímeros semi-cristalinos pueden ser identificados para diferentes materiales de este tipo. En este sentido, se está llevando a cabo un proceso de identificación de estos parámetros para distintos polímeros termoplásticos a fin de proporcionar una extensa base de modelos constitutivos calibrados para polímeros semi-cristalinos.
- El modelo constitutivo desarrollado para polímeros semi-cristalinos proporciona predicciones fiables desde la transición dúctil-frágil hasta la transición vítrea, el rango de temperatura donde las hipótesis del modelo son válidas. Para desarrollar un modelo constitutivo para todo el rango de temperaturas, se está trabajando en la formulación de una función de energía libre específica capaz de representar el comportamiento calórico del PEEK y su influencia en el comportamiento termo-mecánico.
- El marco constitutivo general permite la formulación de nuevos modelos constitutivos que describen el comportamiento mecánico de una amplia variedad de materiales poliméricos. En este sentido, se pueden proponer modelos extendidos añadiendo nuevas ramas constitutivas que describen otros mecanismos de deformación (ver Apéndice D).
- El desarrollo de criterios de fallo y leyes de evolución del daño que describan el comportamiento mecánico de los polímeros durante los procesos de deformación y fallo.

Modelado constitutivo de tejidos blandos

- Desarrollo de un modelo constitutivo más sofisticado para la materia blanca del cerebro que tenga en cuenta la sensibilidad a la velocidad de deformación y la anisotropía inducida por la orientación de los axones.
- Combinación de técnicas experimentales y computacionales para desarrollar un modelo cerebral de elementos finitos que permita describir el comportamiento mecánico real del tejido cerebral y el análisis de lesiones cerebrales debidas a cargas mecánicas.

- Colaboración con instituciones médicas para implementar las herramientas computacionales y metodologías desarrolladas al apoyo de decisiones clínicas.

Appendix

Appendix A. Helmholtz free energy

The explicit expression for the Helmholtz free energy $\bar{\Psi} = \bar{\Psi}^{I}(\mathbf{C_I^e}, \theta) + \bar{\Psi}^{N}(\mathbf{C_N^e})$ is presented and the constitutive expressions of the model are derived from it.

The contribution of the intermolecular resistance to the free energy can be defined through the following Neo-Hookean potential energy function [Bergström, 2015]

$$\bar{\Psi}^{I}(\mathbf{C_I^e}, \theta) = \frac{1}{2}\lambda_0(\theta)\ln(J_I^e) - \mu_0(\theta)\ln(J_I^e) + \frac{1}{2}\mu_0(\theta)[\mathrm{tr}(\mathbf{C_I^e}) - 3] \tag{A.1}$$

Regarding the contribution of the network resistance to the free energy, it can be defined by potential energy function proposed by Anand (1996)

$$\bar{\Psi}^{N}(\mathbf{C_N^e}) = C_R\bar{\lambda}_L^{\,2}\left\{\left(\frac{\bar{\lambda}}{\bar{\lambda}_L}\right)\mathfrak{L}^{-1}\left(\frac{\bar{\lambda}}{\bar{\lambda}_L}\right) + \ln\left[\frac{\mathfrak{L}^{-1}\left(\frac{\bar{\lambda}}{\bar{\lambda}_L}\right)}{\sinh\left[\mathfrak{L}^{-1}\left(\frac{\bar{\lambda}}{\bar{\lambda}_L}\right)\right]}\right]\right\} + \frac{1}{2}\kappa(\ln(J_N))^2 \tag{A.2}$$

The terms $\frac{\partial\bar{\Psi}}{\partial\mathbf{C_I^e}}$, $\frac{\partial\bar{\Psi}}{\partial\mathbf{C_N^e}}$ and $\frac{\partial\bar{\Psi}}{\partial\theta}$ read as

$$\frac{\partial\bar{\Psi}}{\partial\mathbf{C_I^e}} = \frac{1}{2}\lambda_0(\theta)\ln(J_I^e)\,\mathbf{C_I^{-e}} - \frac{1}{2}\mu_0(\theta)\mathbf{C_I^{-e}} + \frac{1}{2}\mu_0(\theta)\mathbf{I} \tag{A.3}$$

$$\frac{\partial\bar{\Psi}}{\partial\mathbf{C_N^e}} = \frac{1}{2}\frac{C_R}{3}\frac{\bar{\lambda}_L}{\bar{\lambda}}\mathfrak{L}^{-1}\left(\frac{\bar{\lambda}}{\bar{\lambda}_L}\right)\left(\mathbf{I} - \bar{\lambda}^2\mathbf{C_N^{-*}}\right) + \frac{1}{2}\kappa\ln(J_N)\mathbf{C_N^{-*}} \tag{A.4}$$

$$\frac{\partial\bar{\Psi}}{\partial\theta} = \frac{1}{2}\frac{E_1\nu}{(1+\nu)(1-2\nu)}\ln(J_I^e) - \frac{E_1}{2(1+\nu)}\ln(J_I^e) + \frac{1}{2}\frac{E_1}{2(1+\nu)}[\mathrm{tr}(\mathbf{C_I^e}) - 3] \tag{A.5}$$

Therefore, the constitutive equations for both resistances can be derived by using the stress tensors relations $\boldsymbol{\sigma}_\mathbf{I} = J_I^{-1}\mathbf{F_I^M}\bar{\mathbf{S}}_\mathbf{I}\mathbf{F_I^{MT}}$ $\boldsymbol{\sigma}_\mathbf{N} = J_N^{-1}\mathbf{F_N^M}\bar{\mathbf{S}}_\mathbf{N}\mathbf{F_N^{MT}}$ and the equations $\bar{\mathbf{S}}_\mathbf{I} = \mathbf{F_I^{-p}}2\frac{\partial\bar{\Psi}}{\partial\mathbf{C_I^e}}\mathbf{F_I^{-pT}}$ and $\bar{\mathbf{S}}_\mathbf{N} = 2\frac{\partial\bar{\Psi}}{\partial\mathbf{C_N^e}}$. Regarding the specific internal entropy per unit volume, it can be derived by using Eq. (A.5) into the following expression

$$\bar{\eta} = -\frac{\partial\bar{\Psi}}{\partial\theta} - 3f_\theta\bar{\Psi} + f_\theta(\bar{\mathbf{M}}_\mathbf{I} + \bar{\mathbf{M}}_\mathbf{N}):\mathbf{I} \tag{A.6}$$

Appendix B. Time-integration of plastic and thermal flows

The plastic deformation gradient of the intermolecular constitutive branch is obtained by integrating the plastic flow rule, Eq. (6.11), following the procedure proposed by van Dommelen et al. (2003). The plastic component of the velocity gradient $\bar{\bar{\mathbf{L}}}^{\mathbf{p}}_{\mathbf{I}}$ is assumed to be constant during each time increment. Thus, the plastic deformation gradient at time level $t_{n+1} = t + \Delta t$ reads as

$$\mathbf{F}^{\mathbf{p}}_{\mathbf{I}\,\mathbf{n+1}} = \mathbf{F}^{\mathbf{p}}_{\mathbf{I}\,\mathbf{n}} \exp\left(\Delta t\, \bar{\bar{\mathbf{L}}}^{\mathbf{p}}_{\mathbf{I}\,\mathbf{n}}\right) \tag{B.1}$$

The tensor exponential can be numerically evaluated by the diagonalization of $\bar{\bar{\mathbf{L}}}^{\mathbf{p}}_{\mathbf{I}\,\mathbf{n}}$ or by the Padé approximation. If Padé approximation is chosen, the incremental plastic deformation gradient reads as

$$\mathbf{F}^{\mathbf{p}}_{\mathbf{I}\,\mathbf{inc}} = \exp\left(\Delta t\, \bar{\bar{\mathbf{L}}}^{\mathbf{p}}_{\mathbf{I}\,\mathbf{n}}\right) \approx \left(\mathbf{I} - \frac{\Delta t}{2}\bar{\bar{\mathbf{L}}}^{\mathbf{p}}_{\mathbf{I}\,\mathbf{n}}\right)^{-1}\left(\mathbf{I} + \frac{\Delta t}{2}\bar{\bar{\mathbf{L}}}^{\mathbf{p}}_{\mathbf{I}\,\mathbf{n}}\right) \tag{B.2}$$

The determinant of the exponential approximation term must be corrected by a straightforward normalization for finite increments because it may deviate from unity

$$\mathbf{F}^{\mathbf{p}}_{\mathbf{I}\,\mathbf{n+1}} = \left(J^{p}_{I\,inc}\right)^{\mathbf{-1/3}}\mathbf{F}^{\mathbf{p}}_{\mathbf{I}\,\mathbf{inc}}\mathbf{F}^{\mathbf{p}}_{\mathbf{I}\,\mathbf{n}} \tag{B.3}$$

being $J^{p}_{I\,inc} = \det\left(\mathbf{F}^{\mathbf{p}}_{\mathbf{I}\,\mathbf{inc}}\right)$.

Regarding the thermal deformation gradient, it can be obtained by integrating the Eq. (6.38)

$$\mathbf{F}^{\boldsymbol{\theta}}_{\mathbf{n+1}} = \mathbf{F}^{\boldsymbol{\theta}}_{\mathbf{n}} \exp\left[f_{\theta}(\theta_{n+1} - \theta_{n})\right] \tag{B.4}$$

In this equation, the current temperature at the end of the increment, θ_{n+1}, can be obtained from Eq. (6.38) as

$$\theta_{n+1} = \theta_{n} + \frac{\Delta t}{\left(\bar{C} + 3 f_{\theta}\bar{e}_{n} - f_{\theta}\left(\mathbf{F}^{\mathbf{pT}}_{\mathbf{I}\,\mathbf{n}}\mathbf{C}^{\mathbf{e}}_{\mathbf{I}\,\mathbf{n}}\mathbf{F}^{\mathbf{p}}_{\mathbf{I}\,\mathbf{n}} : \bar{\mathbf{S}}_{\mathbf{I}\,\mathbf{n}} + \mathbf{C}^{\mathbf{e}}_{\mathbf{N}\,\mathbf{n}} : \bar{\mathbf{S}}_{\mathbf{N}\,\mathbf{n}}\right)\right)}\Gamma_{n} \tag{B.5}$$

where F_n is the sum of the terms associated to inelastic dissipation, thermoelastic coupling, heat conduction and heat sources, Eq. (B.6), evaluated at the beginning of the increment.

$$\mathrm{F} = \bar{\mathbf{M}}_\mathbf{I} : \bar{\mathbf{D}}^\mathbf{p} + \theta \left[\frac{3}{2} f_\theta \mathbf{F}_\mathbf{I}^\mathbf{p} \bar{\mathbf{S}}_\mathbf{I} \mathbf{F}_\mathbf{I}^{\mathbf{pT}} - f_\theta \frac{\partial \left(\mathbf{F}_\mathbf{I}^{\mathbf{pT}} \mathbf{C}_\mathbf{I}^\mathbf{e} \mathbf{F}_\mathbf{I}^\mathbf{p} : \bar{\mathbf{S}}_\mathbf{I} \right)}{\partial \mathbf{C}_\mathbf{I}^\mathbf{e}} + \frac{1}{2} \frac{\partial \left(\mathbf{F}_\mathbf{I}^\mathbf{p} \bar{\mathbf{S}}_\mathbf{I} \mathbf{F}_\mathbf{I}^{\mathbf{pT}} \right)}{\partial \theta} \right] : \dot{\mathbf{C}}_\mathbf{I}^\mathbf{e} + \theta \left[\frac{3}{2} f_\theta \bar{\mathbf{S}}_\mathbf{N} - f_\theta \frac{\partial (\mathbf{C}_\mathbf{N}^\mathbf{e} : \bar{\mathbf{S}}_\mathbf{N})}{\partial \mathbf{C}_\mathbf{N}^\mathbf{e}} + \frac{1}{2} \frac{\partial (\bar{\mathbf{S}}_\mathbf{N})}{\partial \theta} \right] : \dot{\mathbf{C}}_\mathbf{N}^\mathbf{e} - \bar{\nabla}_\mathrm{x} \bar{\mathbf{Q}} + \bar{\mathrm{R}} \tag{B.6}$$

Appendix C. Constitutive modelling of the mechanical behaviour of human head tissues and biomaterials

In this appendix, the constitutive modelling of each tissue and biomaterial is discussed in detail. The constitutive modelling of the human tissues included in the FEHM is individually chosen from the literature. For PEEK, the constitutive model previously developed and validated for this specific material in Chapter 6 is used here. An experimental programme aimed at characterising experimentally macroporous HA has been carried out with specimens manufactured from a real cranial implant. As a second step, its mechanical properties after bone regrowth have been numerically estimated.

C.1. Scalp

Ottenio et al. (2015) tested skin specimens from a human back and identified an anisotropic rate-dependent behaviour of the skin. These properties are known to vary with its localization in the human body as has been observed in experimental studies [Annaidha et al., 2012; Dunn and Silver, 1983; Khatam et al., 2014; Jacquemoud et al., 2007; Vogel, 1972; Zahouani et al., 2009].

More particularly, Gambarotta et al. (2005) carried out an experimental and numerical study of the mechanical behaviour of human scalp. The authors finally proposed a rate-independent, isotropic and hyperelastic constitutive model based on the phenomenological scheme developed by Tong and Fung (1976). However, because of the computational cost of numerical simulations which involve a full head model, most previous FEHM traditionally define scalp as an isotropic and homogeneous material by linear elastic constitutive laws [Horgan and Gilchrist, 2003; Liu et al., 2007; Sahoo et al., 2014; Willinger et al., 2000; Zhang et al., 2001]. In this work, it has been thus assumed the scalp mechanical behaviour to be rate-independent, isotropic, homogeneous and linear elastic, see Table C.1.

Table C.1: Material properties for scalp.

Scalp			
Density (kg/m^3)	**Poisson's ratio**	**Young's Modulus (MPa)**	**Reference**
1100	0.42	16.7	[Horgan and Gilchrist, 2003; Liu et al., 2007; Sahoo et al., 2014 Zhang et al., 2001]

C.2. Skull and falx

The bone microstructure is a complex, heterogeneous, multiphasic and anisotropic composite [Doblaré et al., 2004; Tse et al., 2015]. However, most of the FEHM published before have constitutively defined the skull bone behaviour as isotropic, homogeneous and linear elastic as first approximation [Halabi et al., 2011; Sahoo et al., 2014; Takhounts et al., 2008; Tse et al., 2015; Willinger et al., 1995; Zhang et al., 2001]. In this work, following the material description assumed by these authors, the skull bone structure is treated as an isotropic, homogeneous and linear elastic material. However, since skull bone is composed by two external layers of cortical bone and a core of cancellous bone, a homogenized Young's modulus has been defined based on the modulus of each layer and their thicknesses, see Table 2. The mechanical properties for cortical bone are based on the experimental data reported by Wood (1971), where the data defining the Young's modulus (GPa) of the cranial human bone for different strain rates was fitted as:

$$E = 16 + 1.93\log(\dot{\varepsilon}) \tag{C.1}$$

The mechanical properties of cancellous bone core, also known as diploe, can be obtained from the experimental work published by Melvin et al. (1969). Both cortical and cancellous bones' Young's moduli were selected for a strain rate of 1 s^{-1}, the average strain rate observed on the skull structure in the numerical simulations of this work.

The falx cerebri is a layer of the dura mater located between the cerebral hemispheres which plays an important role in restricting brain motion. Here, it is geometrically defined as isolated from the dura mater and in direct contact with bone. The constitutive behaviour of the falx is defined as linear elastic [Chafi et al., 2010; Kleiven et al., 2002; Takhounts et al., 2008; Zhou et al., 1995], see Table C.2.

Table C.2: Material properties for skull bone and falx.

Tissue	Density (kg/m^3)	Poisson's ratio	Young's Modulus (MPa)	Reference
Skull bone	1728	0.22	8000	[Wood, 1971]
Falx	1133	0.45	31.5	[Chafi et al., 2010; Takhounts et al., 2008]

C.3. Mechanical behaviourof CSF and ventricles

CSF is a biological fluid with Newtonian characteristics that fills the space between the skull and the brain tissues, as well as the ventricles [Ommaya, 1968]. Under impact conditions, the CSF plays a protective role by damping brain movement and, thus, reducing shear stresses. In previous works where a FEHM has been used, some authors described the CSF mechanical behaviour as linear elastic [Gao, 2007; Giovanni et al., 2005; Horgan and Gilchrist, 2003; Horgan and Gilchrist, 2004; Sahoo et al., 2014; Zhang et al., 2001]. However, due to the Newtonian behaviour of the CSF and its similarity with water in terms of viscosity [Horgan and Gilchrist, 2004; Ommaya, 1968], a more accurate description of the CSF viscous constitutive behaviour is adopted here with the water mechanical properties:

$$\boldsymbol{\sigma} = -\mathrm{P}\mathbf{I} + 2\eta\dot{\boldsymbol{\varepsilon}} \tag{C.2}$$

where P is the pressure, $\mathbf{I}$ is the identity tensor, η is the dynamic viscosity and $\dot{\boldsymbol{\varepsilon}}$ is the deviatoric strain rate. The viscosity of the material drives the shear stress contribution while pressure P corresponds to the volumetric stress contribution. Under shock conditions P depends on the current density ρ through the Mie-Grüneisen equation of state:

$$\mathrm{P} = \frac{\rho_o c_o^2 \varsigma}{(1-s\varsigma)^2}\left(1 - \frac{_o\varsigma}{2}\right) + \ {}_o\rho_o E_m \tag{C.3}$$

where $\varsigma = 1 - \rho_o/\rho$ is the nominal volumetric compressive strain with ρ_o as the initial density. c_o is the speed of sound in water, s is the slope of the u_s-u_p curve in the Hugoniot formulation, where u_s and u_p are the shock and particle velocities. $_o$ is the

Grüneisen coefficient and E_m is the internal energy per unit mass. The values of the material parameters for CSF are given in Table C.3.

The ventricles being filled with CSF are assumed here to have CSF mechanical properties [Zhang et al., 2001].

Table C.3: Material properties for CSF.

CSF and ventricles					
Density (kg/m^3)	**c_0 (m/s)**	**s**	**Γ_0**	**η (Pas)**	**Reference**
1000	1450	1.99	0.11	0.00089	[Jérusalem and Dao, 2012]

C.4. Brain tissue

Human brain tissue as a whole has been defined as a nonlinear solid with very small volumetric drained compressibility and viscous contributions to its solid phase deformation [Goriely et al., 2015]. In this work, the human brain was separated into gray and white matters. This division allows more accurate determination of the brain injuries induced by the impact loading. Some authors, who have considered the brain tissue as a whole, describe the brain mechanical behaviour as linear elastic [Khalil and Hubbard, 1977; Liu et al., 2007; Ruan et al., 1991; Shuck and Advani, 1972; Ueno et al., 1989; Willinger et al., 1999; Willinger et al., 2000]. Other authors include a linear viscoelastic law with a relaxation shear modulus [Jirousek et al., 2005; Rashid et al., 2014; Sahoo et al., 2014; Tse et al., 2015; Willinger et al., 2000; Zhang et al., 2001]. However, the distinction between gray and white matters is mechanically necessary, since white matter has been found to be stiffer than gray matter in compression and shear [Budday et al., 2015]. The authors following this approach usually follow a linear viscoelastic law for the relaxation shear moduli [Al-Bsharat et al., 1999; Horgan and Gilchrist, 2004; Zhang et al., 2001]. In addition, some authors [Saez et al., 2016; Sahoo et al., 2014] introduced the anisotropy induced by the fibre orientation through white matter in an anisotropic visco-hyperelastic material law.

Because of the type of impacts considered here are assumed to mostly affect the gray matter, one unique set of parameters is used for both gray and white matters mechanical behaviours. The value for the bulk modulus was determined experimentally by Stalnaker (1969). The effects of the brain viscoelasticity in shear behaviour are taken into account through the following expression*: *(*Note that for simplicity, the expression is presented*

under a constant strain condition; its full formulation and implementation involved the usual convolution used in viscoelastic constitutive modelling.)

$$G(t) = G_\infty + (G_o - G_\infty)e^{-\beta t} \quad \text{(C.4)}$$

where G_o, G_∞ and β represent the short-time modulus, the long-time modulus and the decay constant. These parameters for brain tissue were determined by Shuck and Advani (1972), and have been used in subsequent FEHMs [Tse et al., 2015; Willinger et al., 1999]. The parameters for both bulk and shear brain responses are given in Table C.4.

Table C.4: Material properties for brain tissue.

Gray and White matters					
Density (kg/m^3)	**Bulk modulus (GPa)**	**G_o (kPa)**	**G_∞ (kPa)**	**β (s^{-1})**	**Reference**
1040	2.19	528	168	35	[Tse et al., 2014; Shuck and Advani, 1972; Willinger et al., 1999; Stalnaker, 1969]

C.5. Macroporous HA implant

The mechanical properties of macroporous HA vary considerably with the porosity of the material, the size and the distribution of the pores [Hing et al., 1999]. The lack of knowledge and literature about the mechanical properties of the exact macroporous HA material employed in cranial implants made it necessary to conduct characterization tests on specimens manufactured from a real prosthesis.

Mechanical characterization of macroporous HA

Specimens were manufactured from a cranial implant (Custombone, Finceramica, Italy). As these implants are curved, regions of low curvature were first selected in order to produce specimens. Square sections were cut from these regions, which were then ground into cylinders of 10 mm diameter and 6 mm height; exact heights varied but were measured for each specimen prior to testing. These specimens were then tested in compression. Preliminary experiments were performed using a commercial screw-driven testing machine (Instron 5982). In view of the small strains-to-failure, displacements were measured using a contacting extensometer attached to the loading platens close to the

specimen, and then confirmed using image correlation software (DaVis version 8, LA Vision) to track the deformation of the specimen from a series of photographs taken during the loading. The results for three tests are shown in Fig. C.1. They exhibit a high repeatability with the onset of failure at about 2.2 MPa and an apparent Young's modulus of approximately 0.265 GPa. In order to provide further data for the constitutive model, the material was compressed *in situ* in an X-ray tomography system (Zeiss 510 Versa), using a 5 kN compressive stage (Deben). 360º full scanning with 1,601 projections and 85/319 mm of source/detector distances were performed applying x0.4 magnification, 14.26 µm pixel size, a source operated at 140 kV and 71 µA and 2 s exposure time. The reconstructed geometries provided the porosity of the specimen, 30%, that, in combination with the measurement of the apparent density of the specimens, 1700±110 kg m^{-3}, allowed us to determine the density of HA, 2500 kg m^{-3}. In addition, the reconstructed geometries were then used in finite element (FE) simulations described in the next section.

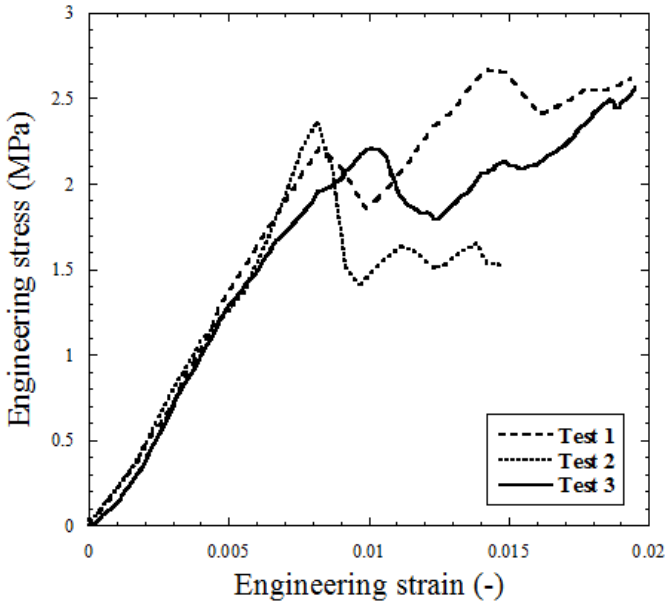

Figure C.1: Engineering stress-engineering strain experimental results of the compression tests carried out on macroporous HA specimens.

Constitutive modelling of macroporous HA cranial implant

In order to assess the relevant mechanical properties of the implant, its homogenized behaviour after bone growth needs to be considered. In the first stage, the non-porous HA

properties were obtained by reproducing numerically the experimental tests carried out on the specimens manufactured from a real cranial implant. The tomography images taken from a specific specimen allow for generation of a FE model accounting for a realistic pore distribution, see Fig. C.2(a)-(b). The boundary conditions for this model are defined accordingly to the experimental conditions. Under the assumption of linear elastic mechanical response until fracture, the numerical model provides force-displacement curves in a good agreement with the experimental data, see Fig. C.2(c). The calibrated values for the Young's modulus and ultimate strength obtained for pure HA are, respectively, 0.75 GPa and 58 MPa.

The experimental results showed a very brittle behaviour of the macroporous HA bioceramic material. This is in agreement with previous studies on ceramic materials [Hing et al., 1999]. However, it has been observed that when reinforcement is added into a ceramic matrix, not only is the fracture toughness significantly increased but also the propensity for catastrophic failure is reduced [Deng et al., 2016]. In this regard, the composite HA+Bone can be considered as a particulate reinforced material composite where HA acts as the matrix and bone as the reinforcement. In such materials, a common assumption is to consider that the composite yielding or breaking starts when, in any material point inside the matrix phase, the yield stress or ultimate strength are reached [Zahr Viñuela and Pérez-Castellanos, 2015]. In this work, the ultimate strength of the homogenised HA+Bone was obtained following this assumption since it is the most conservative one.

Under the assumption that the macroporous HA material filled with bone is going to fail trough the matrix, a numerical model of the HA+Bone specimen was developed by substituting the pores of the previous HA model for bone, see Fig. C.2(d). The boundary conditions applied were the same used as in the model without bone. The properties of cancellous bone were used for bone tissue grown inside the HA pores: a density of ρ=1500 kg m^{-3}, a Young's modulus of E=4.6 GPa and a Poisson's ratio of ν=0.05 [Sahoo et al., 2014]. This numerical model was finally used for the evaluation of the macroscopic mechanical properties of the HA+Bone specimen as a whole, see Fig. C.2(e). The homogenised density, Young's modulus and ultimate strength were found to be 2224.65 kg m^{-3}, 1.25 GPa and 20.50 MPa, respectively.

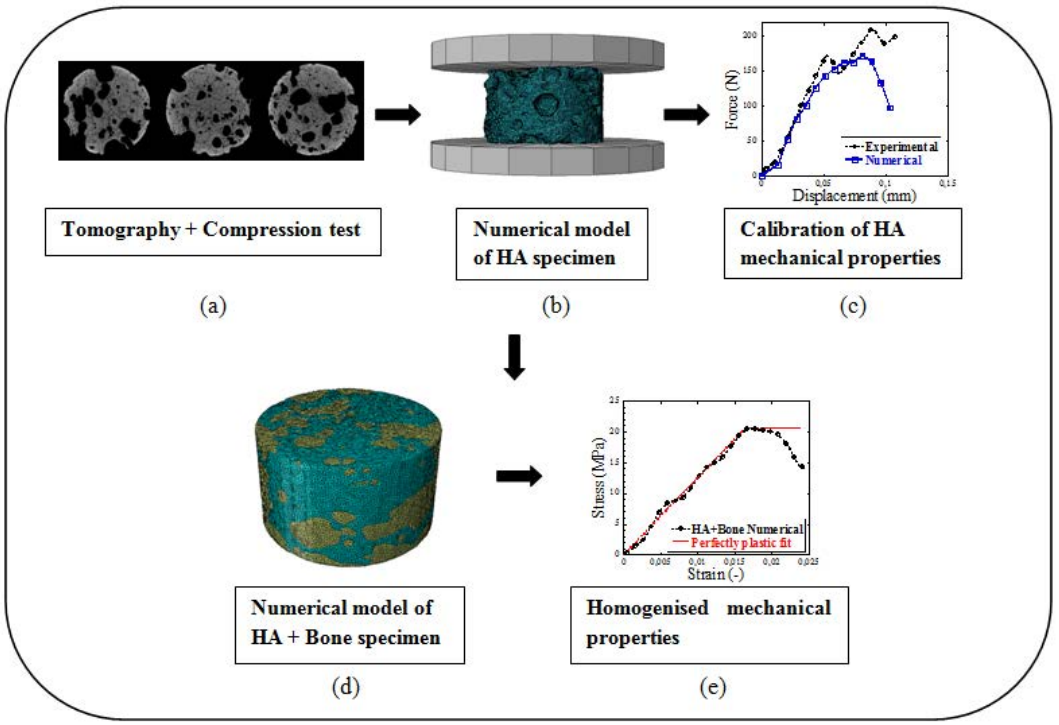

Figure C.2: Scheme of the procedure followed in this work for the constitutive definition of macroporous HA+Bone.

Appendix D. Extension of the Garcia-Gonzalez model for semi-crystalline polymers: combining viscoelasticity and viscoplasticity. Application to UHMWPE

This appendix proposes an extension of the constitutive model developed in *Chapter 6* for semi-crystalline polymers (hereafter referred to as Garcia-Gonzalez model). The Garcia-Gonzalez model takes into account material hardening due to strain rate sensitivity, temperature evolution during the deformation process due to heat generation induced by plastic dissipation, thermal softening and thermal expansion of the material. Here, a new constitutive branch has been added in order to incorporate viscoelasticity and combine viscoelastic and viscoplastic behaviours. The parameters of the constitutive model have been identified for ultra-high-molecular-weight-polyethylene (UHMWPE) from experimental data published by Brown et al. (2007). The constitutive model has shown a good predictive capacity of the mechanical behaviour of UHMWPE for a wide range of strain rate and temperature conditions.

D.1. Extension of the Garcia-Gonzalez model

Semi-crystalline polymers often exhibit complex viscous effects where both viscoelastic and viscoplastic behaviours are combined. In addition, their stress-strain response can be physically interpreted as the combination of overcoming an intermolecular resistance which is increased by the development of strain-induced crystallization; and a network resistance caused by molecular orientation. The intermolecular resistance may exhibit rate-dependency that can be described by viscoplasticity. The network resistance is commonly defined as purely elastic but it may also exhibit rate-dependency that can be potentially described by viscoelasticity. In addition, as shown in *Chapter 6*, these viscous contributions to the mechanical behaviour of thermoplastic polymers lead to temperature increments due to inelastic dissipation and, as a consequence, induce thermal softening in the material behaviour.

Motivated on the evidence introduced above, this section proposes an extension of the Garcia-Gonzalez model to incorporate viscoelasticity in the mechanical response of semi-crystalline thermoplastic materials. The main contribution of this section is the incorporation of a third viscous constitutive branch within the consistent framework formulated in finite deformations. This introduces viscoelasticity through a non-linear hyperelastic response which depends on strain rate. Therefore, a modified eight-chain model has been included in this viscous branch in series with a viscoelastic dashpot, see Fig. D.1. In addition, the network resistance (N) has been modified to incorporate a non-

linear temperature-dependent hyperelastic part that is defined by a modified eight-chain spring.

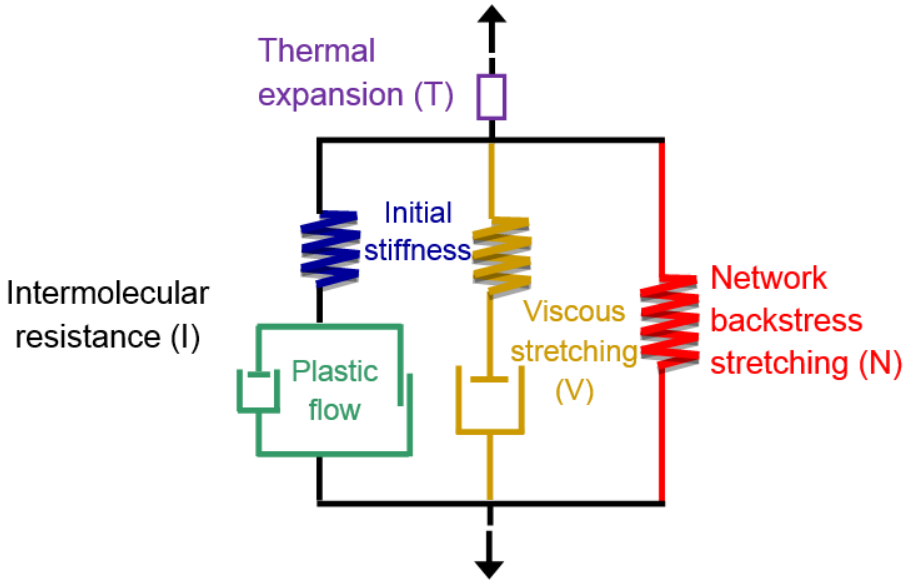

Figure D.1: Rheological scheme of the constitutive model.

According to the arrangement of the rheological model elements depicted in Fig. D.1, the total Cauchy stress $\boldsymbol{\sigma}$ is determined by the contribution of the intermolecular $\boldsymbol{\sigma_I}$, the network backstress $\boldsymbol{\sigma_N}$ and the viscous $\boldsymbol{\sigma_V}$ resistances:

$$\boldsymbol{\sigma} = \boldsymbol{\sigma_I} + \boldsymbol{\sigma_N} + \boldsymbol{\sigma_V} \tag{D.1}$$

D.1.1. Kinematics

The kinematics of the model proposed herein are based on the establishment of five spatial configurations, see Fig. D.2. This kinematics goes from an initial reference configuration Ω_o to a final deformed or current configuration Ω. Three more spatial configurations have been defined to allow the determination of the constitutive equations associated to each constitutive element. The first one is referred to as a dilated configuration $\overline{\Omega}$ in which only thermal deformation is accounted for; the second one is referred to as a plastic dilated relaxed configuration $\overline{\overline{\Omega}}$ in which both thermal and plastic deformations are accounted for; and the third one is referred to as a viscous dilated

relaxed configuration $\widetilde{\Omega}$ in which both thermal and viscous deformations are accounted for.

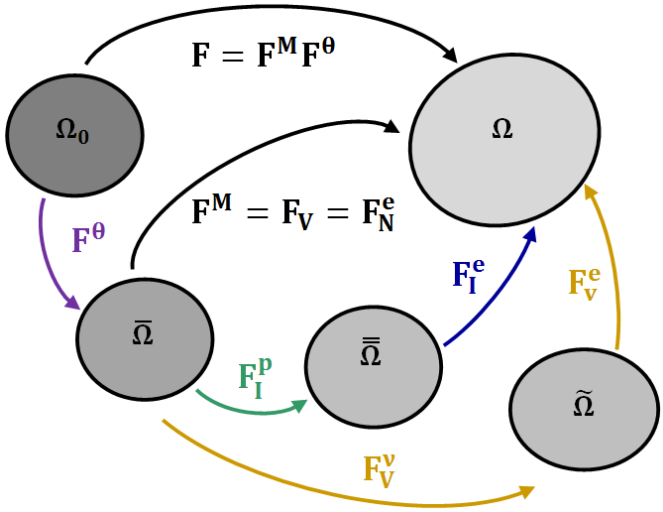

Figure D.2: Kinematics of the model showing the reference or initial configuration Ω_o, the dilated configuration $\bar{\Omega}$, the plastic dilated relaxed configuration $\bar{\bar{\Omega}}$, the viscous dilated relaxed configuration $\tilde{\Omega}$, and the current or loaded configuration Ω.

According to the kinematics, the deformation gradient $\mathbf{F}$ is broken down into thermal, $\mathbf{F^\theta}$, and mechanical, $\mathbf{F^M}$, parts. Thus, the total deformation gradient read as:

$$\mathbf{F} = \mathbf{F^M F^\theta} \tag{D.2}$$

The mechanical part of the deformation gradient, $\mathbf{F^M}$, is equivalent for the three constitutive branches according to the rheological model. The mechanical part associated to the network resistance is defined as purely elastic; the part associated to the intermolecular resistance is divided into elastic, $\mathbf{F_I^e}$, and plastic, $\mathbf{F_I^p}$, components; and the part associated to the viscoelastic resistance is divided into elastic, $\mathbf{F_V^e}$, and viscous, $\mathbf{F_V^v}$, components. Therefore, the total deformation gradient can be decomposed depending on the constitutive branch as:

$$\mathbf{F} = \mathbf{F_I^e F_I^p F^\theta} = \mathbf{F_N^e F^\theta} = \mathbf{F_V^e F_V^v F^\theta} \tag{D.3}$$

The velocity gradient **l,** in terms of the kinematics associated with the viscous resistance elements, can be written using Eq. (D.3) as:

$$\mathbf{l} = \dot{\mathbf{F}}\mathbf{F}^{-1} = \mathbf{l}_{\mathbf{V}}^{\mathbf{e}} + \mathbf{F}_{\mathbf{V}}^{\mathbf{e}}\tilde{\mathbf{L}}_{\mathbf{V}}^{\boldsymbol{\nu}}\mathbf{F}_{\mathbf{V}}^{-\mathbf{e}} + \mathbf{F}_{\mathbf{V}}^{\mathbf{e}}\mathbf{F}_{\mathbf{V}}^{\boldsymbol{\nu}}\bar{\mathbf{L}}^{\boldsymbol{\theta}}\mathbf{F}_{\mathbf{V}}^{-\boldsymbol{\nu}}\mathbf{F}_{\mathbf{V}}^{-\mathbf{e}} \tag{D.4}$$

where $\mathbf{l}_{\mathbf{V}}^{\mathbf{e}} = \dot{\mathbf{F}}_{\mathbf{V}}^{\mathbf{e}}\mathbf{F}_{\mathbf{V}}^{-\mathbf{e}}$ is the elastic component of the velocity gradient in the current configuration and the viscous component $\tilde{\mathbf{L}}_{\mathbf{V}}^{\boldsymbol{\nu}}$ can be defined in the viscous dilated relaxed configuration $\widetilde{\Omega}$ as:

$$\tilde{\mathbf{L}}_{\mathbf{V}}^{\boldsymbol{\nu}} = \dot{\mathbf{F}}_{\mathbf{V}}^{\boldsymbol{\nu}}\mathbf{F}_{\mathbf{V}}^{-\boldsymbol{\nu}} \tag{D.5}$$

This velocity gradient, as well as the plastic velocity gradient of the intermolecular resistance $\bar{\tilde{\mathbf{L}}}_{\mathbf{I}}^{\mathbf{p}} = \bar{\tilde{\mathbf{D}}}_{\mathbf{I}}^{\mathbf{p}} + \bar{\tilde{\mathbf{W}}}_{\mathbf{I}}^{\mathbf{p}}$, can be decomposed into its symmetric and skew parts by $\tilde{\mathbf{L}}_{\mathbf{V}}^{\boldsymbol{\nu}} = \tilde{\mathbf{D}}_{\mathbf{V}}^{\boldsymbol{\nu}} + \tilde{\mathbf{W}}_{\mathbf{V}}^{\boldsymbol{\nu}}$. In this model, $\widetilde{\Omega}$ and $\bar{\tilde{\Omega}}$ are assumed to be invariant to the rigid body rotations of the current configuration, that is $\tilde{\mathbf{W}}_{\mathbf{V}}^{\boldsymbol{\nu}}=\bar{\tilde{\mathbf{W}}}_{\mathbf{I}}^{\mathbf{p}}=0$, and therefore $\tilde{\mathbf{D}}_{\mathbf{V}}^{\boldsymbol{\nu}}=\tilde{\mathbf{L}}_{\mathbf{V}}^{\boldsymbol{\nu}}$ and $\bar{\tilde{\mathbf{D}}}_{\mathbf{I}}^{\mathbf{p}}=\bar{\tilde{\mathbf{L}}}_{\mathbf{I}}^{\mathbf{p}}$. The thermal contribution is assumed isotropic, so that $\mathbf{F}^{\boldsymbol{\theta}}$ is spherical and it is possible to assume $\bar{\mathbf{W}}^{\boldsymbol{\theta}} = \mathbf{0}$.

More details about the kinematics of the intermolecular and network resistances are provided in *Chapter 6*.

D.1.2. Thermodynamics

This section provides the modelling assumptions made for the formulation of the Helmholtz free energy function from which the constitutive equations derive following the methodology proposed in *Chapter 6*. In addition, the thermodynamic consistency is verified from the development of the Clausius-Duhem inequality expressed in the dilated configuration (this is the common configuration for the three constitutive branches).

The Helmholtz free energy function per unit volume in the dilated configuration $\bar{\Psi}$, is defined as the additive combination of the deformation resistances as:

$$\bar{\Psi}(\mathbf{C}_{\mathbf{I}}^{\mathbf{e}}, \mathbf{C}_{\mathbf{V}}^{\mathbf{e}}, \mathbf{C}_{\mathbf{N}}^{\mathbf{e}}, \theta) = \bar{\Psi}^{\mathrm{I}}(\mathbf{C}_{\mathbf{I}}^{\mathbf{e}}, \theta) + \bar{\Psi}^{\mathrm{V}}(\mathbf{C}_{\mathbf{V}}^{\mathbf{e}}) + \bar{\Psi}^{\mathrm{N}}(\mathbf{C}_{\mathbf{N}}^{\mathbf{e}}, \theta) \tag{D.6}$$

where the Helmholtz free energy depends on the elastic right Cauchy-Green deformation tensors $\mathbf{C_I^e} = \mathbf{F_I^{eT}F_I^e}$, $\mathbf{C_V^e} = \mathbf{F_V^{eT}F_V^e}$ and $\mathbf{C_N^e} = \mathbf{F_N^{eT}F_N^e}$, and temperature θ.

From the definition of the Helmholtz free energy $\bar{\Psi} = \bar{e} - \theta\bar{\eta}$, the time derivative of $\bar{\Psi}$ can be calculated as:

$$\dot{\bar{\Psi}} = \frac{\partial\bar{\Psi}}{\partial\mathbf{C_I^e}}:\dot{\mathbf{C}}_\mathbf{I}^\mathbf{e} + \frac{\partial\bar{\Psi}}{\partial\mathbf{C_V^e}}:\dot{\mathbf{C}}_\mathbf{V}^\mathbf{e} + \frac{\partial\bar{\Psi}}{\partial\mathbf{C_N^e}}:\dot{\mathbf{C}}_\mathbf{N}^\mathbf{e} + \frac{\partial\bar{\Psi}}{\partial\theta}\dot{\theta} \tag{D.7}$$

Using these modelling assumptions for the definition of $\bar{\Psi}$, the Clausius-Duhem inequality can be obtained from the combination of the first and second thermodynamics principles as:

$$\left(\mathbf{F_I^p}\bar{\mathbf{S}}_\mathbf{I}\mathbf{F_I^{pT}} - 2\frac{\partial\bar{\Psi}}{\partial\mathbf{C_I^e}}\right):\mathbf{F_I^{eT}d_I^eF_I^e} + \left(\mathbf{F_V^v}\bar{\mathbf{S}}_\mathbf{V}\mathbf{F_V^{vT}} - 2\frac{\partial\bar{\Psi}}{\partial\mathbf{C_V^e}}\right):\mathbf{F_V^{eT}d_V^eF_V^e} + \left(\bar{\mathbf{S}}_\mathbf{N} - 2\frac{\partial\bar{\Psi}}{\partial\mathbf{C_N^e}}\right):\mathbf{F_N^{eT}d_N^eF_N^e} + \bar{\mathbf{M}}_\mathbf{I}:\bar{\mathbf{D}}^\mathbf{p} + \bar{\mathbf{M}}_\mathbf{V}:\bar{\mathbf{D}}^\mathbf{v} + \left(-\frac{\partial\bar{\Psi}}{\partial\theta} - 3f_\theta\bar{\Psi} - \bar{\eta} + f_\theta(\bar{\mathbf{M}}_\mathbf{I} + \bar{\mathbf{M}}_\mathbf{V} + \bar{\mathbf{M}}_\mathbf{N}):\mathbf{I}\right)\dot{\theta} - \frac{1}{\theta}\bar{\mathbf{Q}}\bar{\nabla}_x\theta \geq 0 \tag{D.8}$$

where $\bar{\mathbf{S}}_\mathbf{V}$ is the corresponding second Piola-Kirchhoff stress tensor of the viscous resistance expressed in the configuration $\bar{\Omega}$ as $\bar{\mathbf{S}}_\mathbf{V} = \mathrm{J}^\mathrm{M}\mathbf{F_V^{-M}}\boldsymbol{\sigma}_\mathbf{V}\mathbf{F_V^{-MT}}$ and $\bar{\mathbf{M}}_\mathbf{V} = \mathbf{F_V^{MT}F_V^M}\bar{\mathbf{S}}_\mathbf{V}$ is the Mandel stress tensor in $\bar{\Omega}$. $\mathbf{d_I^e}$, $\mathbf{d_N^e}$ and $\mathbf{d_V^e}$ are the symmetric part of the velocity gradient tensors in Ω of the intermolecular, the network and the viscous resistances; f_θ is a temperature-dependent function; $\bar{\eta}$ is the specific entropy per unit volume in $\bar{\Omega}$; and $\bar{\mathbf{Q}}$ is the heat flux per unit volume in $\bar{\Omega}$.

Using standard arguments of the Coleman and Noll method, the second Piola-Kirchhoff stress tensor associated with each constitutive branch and the specific internal entropy per unit volume that satisfy the second law of thermodynamics along arbitrary thermodynamic processes must read as:

$$\bar{\mathbf{S}}_\mathbf{I} = \mathbf{F_I^{-p}}2\frac{\partial\bar{\Psi}}{\partial\mathbf{C_I^e}}\mathbf{F_I^{-pT}} \tag{D.9.1}$$

$$\bar{\mathbf{S}}_\mathbf{N} = 2\frac{\partial\bar{\Psi}}{\partial\mathbf{C_N^e}} \tag{D.9.2}$$

$$\bar{\mathbf{S}}_\mathbf{V} = \mathbf{F_V^{-v}}2\frac{\partial\bar{\Psi}}{\partial\mathbf{C_V^e}}\mathbf{F_V^{-vT}}\dot{\theta} \tag{D.9.3}$$

$$\bar{\eta} = -\frac{\partial\bar{\Psi}}{\partial\theta} - 3f_\theta\bar{\Psi} + f_\theta(\bar{\mathbf{M}}_\mathbf{I} + \bar{\mathbf{M}}_\mathbf{V} + \bar{\mathbf{M}}_\mathbf{N}):\mathbf{I} \tag{D.9.4}$$

D.1.3. Thermal expansion

The thermal expansion is assumed to be isotropic, being the contribution of the thermal part to the deformation gradient defined in the form:

$$\dot{\mathbf{F}}^{\boldsymbol{\theta}} = f_\theta \mathbf{F}^{\boldsymbol{\theta}} \dot{\theta} \tag{D.10}$$

where $\dot{\theta}$ is the time derivative of current temperature and $f_\theta = \alpha_\theta$ is the thermal expansion coefficient. The temperature evolution equation can be deduced following the methodology used in *Chapter 6*, consult this chapter for more details, as:

$$\begin{aligned}&\left(\bar{C} + 3f_\theta \bar{e} - f_\theta\left(\mathbf{F}_\mathbf{I}^{\mathbf{pT}}\mathbf{C}_\mathbf{I}^{\mathbf{e}}\mathbf{F}_\mathbf{I}^{\mathbf{p}} : \bar{\mathbf{S}}_\mathbf{I} + \mathbf{C}_\mathbf{N}^{\mathbf{e}} : \bar{\mathbf{S}}_\mathbf{N} + \mathbf{F}_\mathbf{V}^{\mathbf{vT}}\mathbf{C}_\mathbf{V}^{\mathbf{e}}\mathbf{F}_\mathbf{V}^{\mathbf{v}} : \bar{\mathbf{S}}_\mathbf{V}\right)\right)\dot{\theta} = \bar{\mathbf{M}}_\mathbf{I} : \bar{\mathbf{D}}^{\mathbf{p}} + \bar{\mathbf{M}}_\mathbf{V} : \bar{\mathbf{D}}^{\mathbf{v}} \\ &\theta\left[\frac{3}{2}f_\theta \mathbf{F}_\mathbf{I}^{\mathbf{p}}\bar{\mathbf{S}}_\mathbf{I}\mathbf{F}_\mathbf{I}^{\mathbf{pT}} - f_\theta \frac{\partial\left(\mathbf{F}_\mathbf{I}^{\mathbf{pT}}\mathbf{C}_\mathbf{I}^{\mathbf{e}}\mathbf{F}_\mathbf{I}^{\mathbf{p}} : \bar{\mathbf{S}}_\mathbf{I}\right)}{\partial \mathbf{C}_\mathbf{I}^{\mathbf{e}}} + \frac{1}{2}\frac{\partial\left(\mathbf{F}_\mathbf{I}^{\mathbf{p}}\bar{\mathbf{S}}_\mathbf{I}\mathbf{F}_\mathbf{I}^{\mathbf{pT}}\right)}{\partial\theta}\right] : \dot{\mathbf{C}}_\mathbf{I}^{\mathbf{e}} + \theta\left[\frac{3}{2}f_\theta \bar{\mathbf{S}}_\mathbf{N} - f_\theta \frac{\partial(\mathbf{C}_\mathbf{N}^{\mathbf{e}} : \bar{\mathbf{S}}_\mathbf{N})}{\partial \mathbf{C}_\mathbf{N}^{\mathbf{e}}} + \frac{1}{2}\frac{\partial(\bar{\mathbf{S}}_\mathbf{N})}{\partial\theta}\right] : \dot{\mathbf{C}}_\mathbf{N}^{\mathbf{e}} \\ &+\theta\left[\frac{3}{2}f_\theta \mathbf{F}_\mathbf{V}^{\mathbf{v}}\bar{\mathbf{S}}_\mathbf{V}\mathbf{F}_\mathbf{V}^{\mathbf{vT}} - f_\theta \frac{\partial\left(\mathbf{F}_\mathbf{V}^{\mathbf{vT}}\mathbf{C}_\mathbf{V}^{\mathbf{e}}\mathbf{F}_\mathbf{V}^{\mathbf{v}} : \bar{\mathbf{S}}_\mathbf{v}\right)}{\partial \mathbf{C}_\mathbf{V}^{\mathbf{e}}} + \frac{1}{2}\frac{\partial\left(\mathbf{F}_\mathbf{V}^{\mathbf{v}}\bar{\mathbf{S}}_\mathbf{V}\mathbf{F}_\mathbf{V}^{\mathbf{vT}}\right)}{\partial\theta}\right] : \dot{\mathbf{C}}_\mathbf{V}^{\mathbf{e}} - \bar{\nabla}_\mathrm{x}\bar{\mathbf{Q}} + \bar{\mathrm{R}}\end{aligned} \tag{D.11}$$

where $\bar{C}$ is the heat capacity per unit volume.

D.1.4. Intermolecular and network resistances: thermo-viscoplasticty

Intermolecular resistance

The details of the constitutive formulation of the intermolecular resistance are provided in *Chapter 6*.

Network backstress resistance

This part of the model describes a hyperelastic entropic resistance defined by a modification of the originally eight-chain model proposed by Arruda and Boyce (1993). This modification follows the formulation introduced by Anand (1996) but including temperature sensitivity. The Cauchy stress associated to this resistance is defined as:

$$\boldsymbol{\sigma}_\mathbf{N} = \frac{(C_R + C_\theta(\theta - \theta_{ref}))}{3J_N}\frac{\bar{\lambda}_L}{\bar{\lambda}}\mathfrak{L}^{-1}\left(\frac{\bar{\lambda}}{\bar{\lambda}_L}\right)(\mathbf{B}_\mathbf{N}^{*} - \bar{\lambda}^2\mathbf{I}) \tag{D.12}$$

where $\mathfrak{L}^{-1}$ is the inverse of the Langevin function, C_R is the initial elastic modulus of the network backstress resistance, C_θ is a material parameter controling the elastic modulus dependence on temperature and $\bar{\lambda}_L$ is the locking stretch. $\bar{\lambda} = \sqrt{\frac{1}{3}\mathrm{tr}(\mathbf{F}_\mathbf{N}^{\mathbf{e}*}(\mathbf{F}_\mathbf{N}^{\mathbf{e}*})^{\mathrm{T}})}$ is the

average total stretch ratio, with $\mathbf{F_N^{e*}} = J_N^{-1/3}\mathbf{F_N^e}$ being the distortional part of $\mathbf{F_N^e}$ and $J_N = \det(\mathbf{F_N^e})$.

D.1.5. Viscous resistance: viscoelasticity

The viscous part is the most relevant contribution to the Garcia-Gonzalez model. This part of the model describes a viscous material response related with the hardening induced by the rate-dependent effects on network stretching. To define this constitutive branch, an eight-chain model is defined for the non-linear spring that depends on the elastic part of the deformation gradient associated with the viscous resistance. In addition, a viscous flow rule is introduced to define the contribution of the linear dashpot. This idea was originally proposed by Bergstrom and Boyce (2001) for elastomers modelling. The Cauchy stress associated with the viscous resistance is defined as:

$$\boldsymbol{\sigma_V} = \frac{C_\nu}{3J_V}\frac{\bar{\lambda}_{VL}}{\bar{\lambda}_V}\mathfrak{L}^{-1}\left(\frac{\bar{\lambda}_V}{\bar{\lambda}_{VL}}\right)(\mathbf{B_V^{e*}} - \bar{\lambda}_V^2\mathbf{I}) \tag{D.13}$$

where C_ν and $\bar{\lambda}_{VL}$ are material parameters and the average viscous stretch ratio $\bar{\lambda}_V$ is calculated as:

$$\bar{\lambda}_V = \sqrt{\frac{1}{3}\mathrm{tr}(\mathbf{B_V^{e*}})} \tag{D.14}$$

The distortional left Cauchy-Green viscous deformation tensor, $\mathbf{B_V^{e*}}$, is determined by the distortional part of $\mathbf{F_V^e}$ defined by Eq. (D.16).

$$\mathbf{B_V^{e*}} = \mathbf{F_V^{e*}}(\mathbf{F_V^{e*}})^T \tag{D.15}$$

$$\mathbf{F_V^{e*}} = J_V^{-1/3}\mathbf{F_V^e} \tag{D.16}$$

In order to define the viscous velocity gradient in the viscous dilated relaxed configuration $\widetilde{\Omega}$, a viscoelastic flow rule is assumed following the formulation proposed by Bergstrom (2015) as:

$$\tilde{\mathbf{L}}_\mathbf{V}^\nu = \dot{\tilde{\gamma}}_V^\nu \widetilde{\mathbf{N}}_\mathbf{V}; \quad \widetilde{\mathbf{N}}_\mathbf{V} = \frac{\boldsymbol{\sigma}_\mathbf{V}^{\mathbf{dev}}}{\tau_V} \tag{D.17}$$

where $\dot{\tilde{\gamma}}_V^{\nu}$ is the viscoelastic multiplier, $\widetilde{\mathbf{N}}_{\mathbf{V}}$ provides the direction of the viscoelastic flow, $\boldsymbol{\sigma}_{\mathbf{V}}^{\mathbf{dev}}$ is the deviatoric part of $\boldsymbol{\sigma}_{\mathbf{V}}$ and $\tau_V = \sqrt{\mathrm{tr}\left(\boldsymbol{\sigma}_{\mathbf{V}}^{\mathbf{dev}}\boldsymbol{\sigma}_{\mathbf{V}}^{\mathbf{dev}}\right)}$ is the effective stress driving the viscous flow.

The rate equation for viscous flow is given by:

$$\dot{\tilde{\gamma}}_V^{\nu} = \frac{\tau_V}{\sigma_{VT}} \tag{D.18}$$

where σ_{VT} is a material constant.

D.2. Identification of model parameters and model predictions

This section summarizes the correspondence of the model parameters with the mechanical response of semi-crystalline polymers, then, the identification of the parameters for UHMWPE is presented. The model predictions are compared with experimental data for a wide range of strain rate and temperature conditions.

D.2.1. Correspondence of the model parameters with mechanical response of the material

The parameters of the extended Garcia-Gonzalez model present certain correspondence with the mechanical response of the material. This makes it easier to identify the proper values for a specific polymer. Such correspondence is introduced in terms of the following blocks:

(i) *Linear response*: the model parameters E_{ref}, E_1 and ν determine the initial elastic response of the material depending on temperature.

(ii) *Yield stress*: the parameters σ_{T0}, C, $\dot{\varepsilon}_{0A}$ and m define the yield stress of the material. C and $\dot{\varepsilon}_{0A}$ determine the yield stress' strain rate sensitivity and m the temperature sensitivity.

(iii) Viscous response: the model parameters C_ν and $\bar{\lambda}_{VL}$ determine the stress contribution of the spring of the viscous constitutive branch. C_ν is related to the initial elastic modulus of viscous resistance and $\bar{\lambda}_{VL}$ is related to the maximum (fully extended) stretch that a molecule can be exposed to. The material parameter σ_{VT} determines the viscoelastic multiplier that governs the flow rule associated with the linear dashpot.

(iv) *Network response*: the network contribution to the stress state is established by the parameters C_R, C_θ, $\bar{\lambda}_L$ and κ. C_R and C_θ determine the initial elastic modulus of network resistance depending on temperature. The parameter $\bar{\lambda}_L$ is related to the maximum stretch that a molecule can be exposed to and κ is a bulk modulus used in applications where only the network contribution is active (e.g. rubber modelling).

(v) *Volumetric plastic strain sensitivity*: the parameter β introduces the sensitivity of the material with inelastic volume change. This parameter can be defined as $\beta = 1$ assuming volume preserving.

(vi) *Stress state sensitivity*: the parameter α represents the relationship between yield stress in compression and tension and determines the pressure sensitivity.

Taking into account the correspondence of the model parameters with the mechanical response of the material, the parameters of the proposed model have been identified for UHMWPE. For this identification process, experimental data that covers a wide range of strain rate and temperature loading conditions have been used. This experimental data and details about the experiments performance are reported by Brown et al. (2007). The model parameters identified from these experiments are provided in Table D.1.

Table D.1: Material parameters for UHMWPE.

Initial elastic properties			**General properties**		
$\mathbf{E_{ref}}$ **(GPa)**	$\mathbf{E_1}$ **(MPa/K)**	**ν**	**ρ (kg/m^3)**	$\bar{\mathbf{C}}$ **(kJ/ m^{3}K)**	$\boldsymbol{\alpha_\theta}$ **(K^{-1})**
0.541	-6.5	0.46	940	1900	$124.5 \cdot 10^{-6}$

Intermolecular resistance								
$\dot{\boldsymbol{\varepsilon}}_{\mathbf{0A}}$ **(s^{-1})**	**C**	$\boldsymbol{\sigma_{T0}}$ **(MPa)**	**m**	$\boldsymbol{\theta_{ref}}$ **(K)**	$\boldsymbol{\theta_{melt}}$ **(K)**	$\boldsymbol{\theta_{min}}$ **(K)**	**α**	**β**
0.1	0.048	37.5	0.7	293	406	198	1.2	1.0

Viscous resistance			**Network resistance**		
$\mathbf{C_V}$ **(MPa)**	$\bar{\boldsymbol{\lambda}}_{\mathbf{VL}}$	$\boldsymbol{\sigma_{VT}}$ **(MPa)**	$\mathbf{C_R}$ **(MPa)**	$\mathbf{C_\theta}$ **(MPa/K)**	$\bar{\boldsymbol{\lambda}}_{\mathbf{L}}$
12.5	5	0.05	23	-0.15	5.5

D.2.2. Model predictions

The constitutive model proposed herein has been implemented in a VUMAT subroutine and applied to a numerical model with the dimensions of the specimens used in compression tests by Brown et al. (2007). This numerical model was defined with C3D8R elements and developed in ABAQUS/Explicit.

The expression developed for the determination of temperature evolution, Eq. (D.11) has been reduced taking into account uniquely specific energy due to plastic dissipation of the intermolecular resistance; viscous dissipation of the viscoelastic resistance; and heat conduction. Thermoelastic coupling is neglected in line with published studies for thermoplastic polymers [Bouvard et al., 2013]. The temperature evolution is thus reduced to:

$$\dot{\theta} = \frac{\overline{\mathbf{M}}_{\mathbf{I}}:\overline{\mathbf{D}}^{\mathbf{p}}}{\overline{C}} + \frac{\overline{\mathbf{M}}_{\mathbf{V}}:\overline{\mathbf{D}}^{\mathbf{v}}}{\overline{C}} - \frac{\overline{\nabla}_x \overline{\mathbf{Q}}}{\overline{C}} \tag{D.19}$$

The model predictions show a good agreement with experimental [Brown et al., 2007] in terms of strain rate and temperature sensitivities. In this regard, Fig. D.3 shows the yield stress model predictions depending on strain rate and temperature, and their comparison with the experimental values. This predictive capacity is determined by the intermolecular constitutive branch that accounts for strain rate sensitivity through the viscoplastic flow rule, and for temperature sensitivity through the term σ_T that introduces thermal softening in the viscoplastic flow rule.

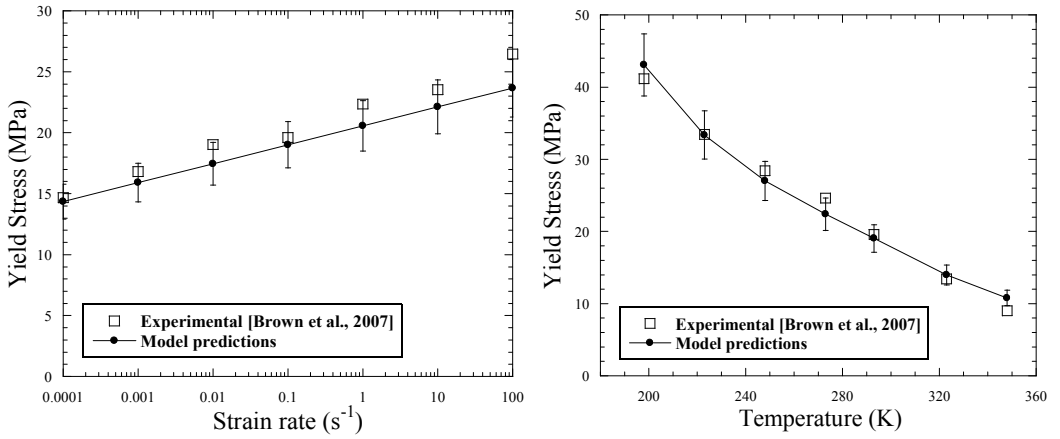

(a) (b)

Figure D.3: Experimental data [Brown et al., 2007] versus model predictions in terms of: (a) strain rate sensitivity; and (b) temperature sensitivity of UHMWPE for uniaxial compression tests.

Furthermore, the model not only predicts the strain rate and temperature dependences on yield stress, but also on the stress response along the whole deformation process. With the aim of highlighting the predictive capacity of the extended Garcia-Gonzalez model, a comparison between model predictions and experimental data [Brown et al., 2007] is provided in Fig. D.4. This figure shows stress-strain curves for UHMWPE covering a wide range of strain rate and temperature conditions. A good agreement between model predictions and experiments is observed in these terms. In this regard, the model faithfully predicts the initial slope of the stress-strain curve depending on temperature. This is determined by the definition of $E(\theta)$ in the intermolecular resistance. In addition, once the yield point is reached, the stress-shape is mainly governed by the viscous and network resistances, especially at large deformations where their contribution is more relevant. The rate-dependent non-linear behaviour at large deformations is determined by the viscous resistance through the viscoelastic dashpot, Fig. D.4a. Moreover, the network resistance introduces temperature dependence in the non-linear behaviour at large deformations, Fig. D.4b.

Therefore, it can be concluded that the modifications introduced in the Garcia-Gonzalez model for semi-crystalline polymers allow new possibilities in the constitutive modelling of this type of materials. Concretely, these modifications allow us to introduce temperature-dependent behaviour associated to the network resistance and couple viscoelastic and viscoplastic deformation mechanisms.

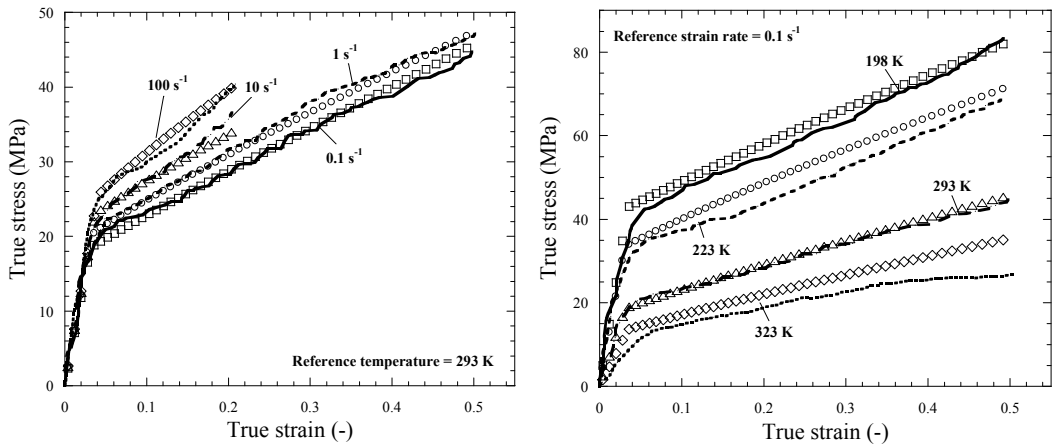

Figure D.4: Stress-strain experimental curves of UHMWPE [Brown et al., 2007] versus model predictions for: (a) different strain rates; and (b) different temperatures.

Bibliography

References

1 Adams, R.D., Gaitonde, J.M., 1993. Low-temperature flexural dynamic measurements on PEEK, HTA and some of their carbon fibre composites. Compos. Sci. Technol. 47, 271-287.

2 Adetchessi, A.T., Pech-Gourg, G., Metellus, P., Fuentes, S., 2012. Fracture précoce d'une cranioplastie en céramique macroporeuse d'hydroxyapatite. Neurochirurgie 58, 382-385.

3 Advani, S.G., Tucker III, C.L., 1987. The Use of Tensors to Describe and Predict Fiber Orientation in Short Fiber Composites. J. Rheol. 31(8), 751–784.

4 Khan, A.S., Suh, Y.S., Kazmi, R., 2004. Quasi-static and dynamic loading responses and constitutive modeling of titanium alloys. Int. J. Plasticity 20(12), 2233-2248.

5 Al-Bsharat, A.S., Hardy, W.N., Yang, K.H., Khalil, T.B., Tashman, S., King, A.I., 1999. Brain/skull relative displacement magnitude due to blunt head impact: New experimental data and model, In: Proceedings of the 1999 43rd Stapp Car Crash Conference; San Diego, CA, USA P-350, 321-332.

6 Altynova, M., Hu, X., Daehn, G.S., 1996. Increased ductility in high velocity electromagnetic ring expansion. Metall. Mater. Trans. A. 27, 1837–1844.

7 Anand L., 1996. A constitutive model for compressible elastomeric solids. Comput. Mech. 18, 339-355.

8 Andriyana, A., Billon, N., Silva, L., 2010. Mechanical response of a short fiber-reinforced thermoplastic: Experimental investigation and continuum mechanical modeling. Eur. J. Mech. A-Solid 29, 1065–1077.

9 Annaidha, A.N., Bruyèred, K., Destradea, M., Gilchrist, M.D., Otténiod, M., 2012. Characterization of the anisotropic mechanical properties of excised human skin. J. Mech. Behav. Biomed. 5, 139-148.

10 Arias, A., Rodríguez-Martínez, J.A., Rusinek, A., 2008. Numerical simulations of impact behaviour of thin steel plates subjected to cylindrical, conical and hemispherical non-deformable projectiles. Eng. Fract. Mech. 5, 1635-1656.

11 Arias, A., Zaera, R., Lopez-Puente, J.L., Navarro, C., 2003. Numerical modeling of the impact behavior of new particulate-loaded composite materials. Compos. Struct. 61, 151–159.

12 Arruda, E., Boyce, M., Jayachandran, R., 1995. Effects of strain rate, temperature and thermomechanical coupling on the finite strain deformation of glassy polymers. Mech. Mater. 19 (2–3), 193–212.

13 Arruda, E.M., Boyce, M.C., 1993. A three-dimensional constitutive model for the large stretch behavior of rubber elastic materials. J. Mech. Phys. Solids 41 (2), 389-412.

14 Asgharpur, Z., Baumgartner, D., Willinger, R., Graw, M., Peldschus, S., 2013. The validation and application of a finite element human head model for frontal skull fracture analysis. J. Mech. Behav. Biomed. 33, 16-23.

15 Ashby, M., Jones, D.R.H., 2001. An introduction to micro-structures, processing and design. In: Engineering Materials, Ed. Pergamon Press.

16 Ayoub, G., Zaïri, F., Naït-Abdelaziz, M., Gloaguen, J.M., 2010. Modelling large deformation behaviour under loading–unloading of semicrystalline polymers: Application to a high density polyethylene. Int. J. Plast. 26, 329-347.

17 Baumgartner, D., Willinger, R., 2005. Human head tolerance limits to specific injury mechanisms inferred from real world accident numerical reconstruction. Revue Européenne des Éléments 14, 421–443.

18 Bergström, J., 2015. Mechanics of solid polymers: theory and computational modeling, first ed. William Andrew, San Diego, USA.

19 Bergström, J.S., Rimnac, C.M., Kurtz, S.M., 2003. Prediction of multiaxial mechanical behavior for conventional and highly crosslinked UHMWPE using a hybrid constitutive model. Biomaterials 24, 1365–1380.

20 Billon, N., 2012. New constitutive modelling for time-dependent mechanical behaviour of polymers close to glass transition: fundamental and experimental validation. J. Appl. Polym. Sci. 125 (6), 4390–4401.

21 Bjerke, T., Li, Z., Lambros, J., 2002. Role of plasticity in heat generation during high rate deformation and fracture of polycarbonate. Int. J. Plasticity 18, 549–567

22 Bless, S., Jurick, D., 1998. Design for multi-hit capability. Int. J. Impact Eng. 10, 905-908

23 Budday, S., Sommer, G., Birkl, C., Langkammer, C., Haybaeck. J., Kohnert, J., Bauer, M., Paulsen, F., Steinmann, P., Kuhl, E, Holzapfel, G.A., 2016. Mechanical characterization of human brain tissue, Acta Biomater., doi: http://dx.doi.org/10.1016/j.actbio.2016.10.036.

24 Borruto, A., 2010. A new material for hip prosthesis without considerable debris release. Med. Eng. Phys. 32, 908–913.

25 Bourmaud, A., Ausias, G., Lebrun, G., Tachon, M., Baley, C., 2013. Observation of the structure of a composite polypropylene/flax and damage mechanisms under stress. Ind. Crop. Prod. 43, 225–236

26 Bouvard, J.L., Francis, D.K., Tschopp, M.A., Marin, E.B., Bammann, D.J., Horstemeyer, M.F., 2013. An internal state variable material model for predicting the time, thermomechanical, and stress state dependence of amorphous glassy polymers under large deformation. Int. J. Plast. 42, 168–193.

27 Boyce, M.C., Arruda, E.M., 1990. An experimental and analytical investigation of the large strain compressive and tensile response of glassy polymers. Polym. Eng. Sci. 30 (20), 1288–1298.

28 Boyce, M.C., Arruda, E.M., 2000. Constitutive models of rubber elasticity: a review. Rubber Chem. Technol. 73, 504-523.

29 Boyce, M.C., Parks, D.M., Argon, A.S., 1988. Large inelastic deformation of glassy polymers. Part I: rate dependent constitutive model. Mech. Mater. 7, 15-33.

30 Boyce, M.C., Socrate, S., Llana, P.G., 2000. Constitutive model for the finite deformation stress–strain behavior of poly(ethylene terephthalate) above the glass transition. Polymer 41, 2183-2201.

31 Boyde, A., Corsi, A., Quarto, R., Cancedda, R., Bianco, P., 1999. Osteoconduction in large macroporous hydroxyapatite ceramic implants: Evidence for a complementary integration and disintegration mechanism. Bone 24, 579–89.

32 Brepols, T., Vladimirov, I.N., Reese, S., 2014. Numerical comparison of isotropic hypo- and hyperelastic-based plasticity models with application to industrial forming processes. Int. J. Plast.63, 18–48.

33 Brown, E.N., Willms, R.B., Gray, G.T., Rae, P.J., Cady, C.M., Vecchio, K.S., Flowers, J., Martinez, M.Y., 2007. Influence of molecular conformation on the constitutive response of polyethylene: A comparison of HDPE, EHMWPE, and PEX. Exp. Mech. 47, 381-393.

34 Brydon, H.L., Hayward, R., Harkness, W., Bayston, R., 1995. Physical properties of cerebrospinal fluid of relevance to shunt function. 2: The effect of protein upon CSF surface tension and contact angle. Brit. J. Neurosurg. 9, 645-651.

35 Budday, S., Nay, R., de Rooij, R., Steinmann, P., Wyrobek, T., Ovaert, T.C., Kuhl, E., 2015. Mechanical properties of gray and white matter brain tissue by indentation. J. Mech. Behav. Biomed. 46, 318-330.

36 Caccese, V., Ferguson, J., Edgecomb, M., 2013. Optimal design of honeycomb material used to mitigate head impact. Compos. Struct. 100, 404-412.

37 Chafi, M.S., Karami, G., Ziejewski, M., 2010. Biomechanical assessment of brain dynamic responses due to blast pressure waves. Ann. Biomed. Eng. 38, 490-504.

38 Chalal, H., Abed-Meraim, F., 2015. Hardening effects on strain localization predictions in porous ductile materials using the bifurcation approach. Mech. Mater. 91, 152–166.

39 Chatelin, S., Deck, C., Willinger, R., 2012. An anisotropic viscous hyperelastic constitutive law for brain material finite-element modeling. Biorheology; doi:10.1007/s12573-012-0055-6.

40 Chebbi, E., Wali, M., Dammak, F., 2016. An anisotropic hyperelastic constitutive model for short glass fiber-reinforced polyamide. Int. J. Eng. Sci. 106, 262–272.

41 Chen, F., Ou, H., Lu, B., Long, H., 2016.A constitutive model of polyether-ether-ketone (PEEK). J. Mech. Behav. Biomed. 53, 427–433.

42 Chen, J., Liu, L., Liu, Y., Leng, J., 2014. Thermoviscoelastic shape memory behavior for epoxy-shape memory polymer. Smart Mater. Struct. 23, 055025.

43 Cheng, J., Nemat-Nasser, S., 2000. A model for experimentally-observed high-strain-rate dynamic strain aging in titanium. Acta Mater. 48, 3131-3144.

44 Chistolini, P., Ruspantini, I., Bianco, P., Corsi, A., Cancedda, R., Quarto, R., 1999. Biomechanical evaluation of cell-loaded and cell-free hydroxyapatite implants for the reconstruction of segmental bone defects. J. Mater. Sci. Mater. M. 10, 739–42.

45 Chukov, D., Stepashkin, A., Maksimkin, A., Tcherdyntsev, V., Kaloshkinm, S., Kuskov, K., Bugakov, V., 2015. Investigation of structure, mechanical and tribological properties of short carbon fiber reinforced UHMWPE-matrix composites. Compos. Part B-Eng. 76, 79-88.

46 Colak, O.U., Dusunceli, N., 2006. Modeling viscoelastic and viscoplastic behavior of high density polyethylene (HDPE). J. Eng. Mater. T. 128 (4), 572-578.

47 Coleman, B.D., Gurtin, M.E., 1967. Thermodynamics with internal state variables. The J. Chem. Phys. 47, 597.

48 Coleman, B.D., Noll, W., 1963. The thermodynamics of elastic materials with heat conduction and viscosity. Arch. Rational Mech. Analysis 13, 167-178.

49 Colón-Emeric, C., Pieper, C., Grubber, J., 2015. Correlation of hip fracture with other fracture types: Toward a rational composite hip fracture. Bone 81, 67-71.

50 Cowin, S.C., Humphrey, J.D., 2001. Cardiovascular Soft Tissue Mechanics, Springer.

51 Dano, M.L., Gendron, G., Maillette, F., Bissonnette, B., 2006. Experimental Characterization of Damage of Random Short Glass Fiber Reinforced Composites. J. Thermoplast. Compos. 19(1), 79-96.

52 Dano, M.L., Gendron, G., MIR, H., 2002. Mechanics of Damage and Degradation in Random Short Glass Fiber Reinforced Composites. J. Thermoplast. Compos. 15(1), 169-177

53 Dassault Systèmes Abaqus v6.12 Documentation-ABAQUS analysis user's manual. Abaqus Inc; 2012.

54 Davim, J., Reis, P., Lapa, V., António, C., 2003. Machinability study on polyetheretherketone (PEEK) unreinforced and reinforced (GF30) for applications in structural components. Compos. Struct. 62(1), 67-73.

55 Dean, A., Reinoso, J., Sahraee, S., Rolfes, R., 2016. An invariant-based anisotropic material model for short fiber-reinforced thermoplastics: Coupled thermo-plastic formulation. Composites 90, 186–199.

56 Deck, C., Willinger, R., 2008. Improved head injury criteria based on head FE model. Int. J. Crashworthiness 13(6), 667-678.

57 Deng, Y., Li, W., Wang, R., Shao, J., Geng, P., Ma, J., 2016. The temperature-dependent fracture models for fiber-reinforced ceramic matrix composites. Compos. Struct. 140, 534–539.

58 Díez-Pascual, A.M., Guan, J., Simard, B., Gómez-Fatou, M.A., 2012. Poly(phenylene sulphide) and poly(ether ether ketone) composites reinforced with single-walled carbon nanotube buckypaper: II – Mechanical properties, electrical and thermal conductivity. Compos. Part A-Appl. S.43, 1007–1015.

59 Doblaré, M., García, J.M., Gómez, M.J., 2004. Modelling bone tissue fracture and healing: a review. Eng. Fract. Mech. 71, 1809-1840.

60 Dray, D., 2006. Prédiction des propriétés thermo-élastiques d'un composite injecté et chargé de fibres courtes. PhD thesis, Ecole Nationale Supérieure d'Arts et Métiers de Paris.

61 Duan, Y., Saigal, A., Greif, R., 2001. A uniform phenomenological constitutive model for glassy and semicrystalline polymers. Polym. Eng. Sci. 41, 1322-1328.

62 Dunn, M.G., Silver, F.H., 1983. Viscoelastic behavior of human connective tissues: relative contribution of viscous and elastic components. Connect. Tissue Res. 12, 59–70.

63 Edwards, S.F., Vilgis, Th., 1986. The effect of entanglements in rubber elasticity. Polymer 27, 483-492.

64 El Halabi, F., Rodriguez, J.F., Rebolledo, L., Hurtós, E., Doblaré, M., 2011. Mechanical characterization and numerical simulation of polyether-ther-ketone (PEEK) cranial implants. J. Mech. Behav. Biomed. 4, 1819-1832.

65 El-Qoubaa, Z., Othman, R., 2015. Characterization and modeling of the strain rate sensitivity of polyetheretherketone's compressive yield stress. Mater. Design 66, 336–345.

66 El-Qoubaa, Z., Othman, R., 2014. Volume change in PEEK under compression loads over wide ranges of strain rate and temperature. J. Strain Anal. Eng. Des. 49, 315–24.

67 El-Qoubaa, Z., Othman, R., 2016. Strain rate sensitivity of polyetheretherketone's compressive yield stress at low and high temperatures. Mech. Mater. 95, 15–27.

68 Eolchiyan, S.A., 2014. Complex skull defects reconstruction with CAD/CAM titanium and polyetheretherketone (PEEK) implants. Zhurnal Voprosy Neirokhirurgii Imeni N.N. Burdenko 75, 3-13.

69 Epee, A., Lauro, F., Bennani, B., Bourel, B., 2011. Constitutive model for a semi-crystalline polymer under dynamic loading. Int. J. Solids Struct. 48, 1590-1599.

70 Evans, W.J., Isaac, D.H., Saib, K.S., 1996. The effect of short carbon fibre reinforcement on fatigue crack growth in PEEK. Compos. Part A-Appl. S. 27A, 547-554.

71 Fahlstedt, M., Baeck, K., Halldin, P., Sloten, J.V., Goffin, J., Depreitere, B., Kleiven, S., 2012. Influence of impact velocity and angle in a detailed reconstruction of a bicycle accident. ICORBI Conference 84, 787-799.

72 FEI Amira 6.0.1

73 Feng, Y., Okamoto, R.J., Namani, R., Genin, G.M., Bayly, P., 2013. Measurements of mechanical anisotropy in brain tissue and implications for transversely isotropic material models of white matter. J. Mech. Behav. Biomed. Mater. 23, 117–132.

74 Frassanito, P., De Bonis, P., Mattogno, P.P., Mangiola, A., Novello, M., Brinchi, D., Pompucci, A., Anile, C., 2013. The fate of a macroporous hydroxyapatite cranioplasty four years after implantation: Macroscopical and microscopical findings in a case of recurrent atypical meningioma. Clin. Neurol. Neurosur. 115, 1496-1498.

75 Fredriksson, R., Håland, Y., Yang, J., 2001. Evaluation of a New Pedestrian Head Injury Protection System with a Sensor in the Bumper and Lifting of the Bonnet's Rear Part. 17th ESV Conference, Amsterdam, Netherlands.

76 Fu, S-Y., Lauke, B., Mai, Y-W., 2009. Science and Engineering of Short Fibre Reinforced Polymer Composites, Woodhead Publishing.

77 Fung, Y.C., 1981. Biomechanics: Mechanical Properties of Living Tissues, Springer.

78 G'Sell, C., Jonas, J., 1979. Determination of the plastic behaviour of solid polymers at constant true strain rate. J. Mater. Sci. 14, 583–591.

79 Galbraith, J.A., Thibault, L.E., Matteson, D.R., 1993. Mechanical and electrical responses of the squid giant axon to simple elongation. J. Biomech. Eng. 115, 13–22.

80 Gambarotta, L., Massabo, R., Morbiducci, R., Raposio, E., Santi, P., 2005. In vivo experimental testing and model identification of human scalp skin. J. Biomech. 38, 2237–2247.

81 Gambirasio, L., Rizzi, E., 2014. On the calibration strategies of the Johnson-Cook strength model: Discussion and applications to experimental data. Mat. Sci. Eng. A-Struct. 610, 370-413.

82 Gao, C., 2007. Finite element modelling of the human brain and application in neurosurgical, PHD Dissertation, Singapore.

83 Gasser, T.C., Ogden, R.W., Holzapfel, G.A., 2006. Hyperelastic modelling of arterial layers with distributed collagen fibre orientations. J. Roy. Soc. Interface 3, 15–35.

84 Gaymans, R., Hamber, M., Inberg, J., 2000. The brittle–ductile transition temperature of polycarbonate as function of test speed. Polym. Eng. Sci. 40, 256–262.

85 Ge, Q., Luo, X., Iversen, C.B., Nejad, H.B., Mather, P.T., Dunn, M.L., Qi, H.J., 2014. A finite deformation thermomechanical constitutive model for triple shape polymeric composites based on dual thermal transitions. Int. J. Solids Struct. 51, 2777-2790.

86 Gent, A.N., 1996. A New Constitutive Relation for Rubber. Rubber Chem. Technol. 69(1), 59–61.

87 Ghorbel, E., 2008. A viscoplastic constitutive model for polymeric materials. Int. J. Plasticity 24, 2032-2058.

88 Giovanni, B., Chiandussi, G., Gaviglio, I., 2005. Development and validation of a new finite element model of human head, In: Proceedings 19th International Technical Conference on the Enhanced Safety of Vehicles (ESV), Washington, D.C., Paper No. 05-0441.

89 Goh, J.C.H., Lee, P.V.S., Ng, P., 2002. Structural integrity of polypropylene prosthetic sockets manufactured using the polymer deposition technique. P. I. Mech. Eng. H 216, 359-68.

90 Gómez-del Río, T., Zaera, R., Barbero, E., Navarro, C., 2005. Damage in CFRPs due to low velocity impact at low temperature. Compos. Part B-Eng. 36, 41-50.

91 Goriely, A., Geers, M.G.D., Holzapfel, G.A., Jayamohan, J., Jérusalem, A., Sivaloganathan, S., Squier, W., van Dommelen, J.A.W., Waters, S., Kuhl, E., 2015. Mechanics of the brain: perspectives, challenges, and opportunities. Biomech. Model. Mechanobiol 14, 931-965

92 Green, S., 2012. Chapter 3 - Compounds and Composite Materials, In: PEEK biomaterials handbook. William Andrew Elsevier; p. 23-48.

93 Guo, Z., Peng, X., Moran, B., 2006. A composites-based hyperelastic constitutive model for soft tissue with application to the human annulus fibrosus. J. Mech. Phys. Solids 54, 1952–1972.

94 Guo, Z., Peng, X., Moran, B., 2007a. Large deformation response of a hyperelastic fibre reinforced composite: Theoretical model and numerical validation. Composites 38, 1842–1851.

95 Guo, Z., Peng, X., Moran, B., 2007b. Mechanical response of neo-Hookean fiber reinforced incompressible nonlinearly elastic solids. Int. J. Solids Struct. 44, 1949–1969.

96 Gurtin, M.E., Anand, L., 2005. The decomposition F = FeFp, material symmetry, and plastic irrotationality for solids that are isotropic-viscoplastic or amorphous. Int. J. Plast. 21, 1686-1719.

97 Halabi, F., Rodríguez, J., Rebolledo, L., Hurtos, E., Doblaré, M., 2011. Mechanical characterization and numerical simulation of polyether–ether–ketone (PEEK) cranial implants. J. Mech. Behav. Biomed. 4, 1819–1832.

98 Hamdan, S., Swallowe, G., 1996. Crystallinity in PEEK and PEK after mechanical testing and its dependence on strain rate and temperature. J. Polym. Sci. Pol. Phys. 34, 699–705.

99 Hashin, Z., 1962. The elastic moduli of heterogeneous materials. J. Appl. Mech. 29, 143-150.

100 Haward, R.N., Thackray, G., 1968. The use of a mathematical model to describe isothermal stress-strain curves in glassy thermoplastics. Proceedings of the Royal Society of London. Series A, Math. Phys. Sci. 302, 453–472.

101 Hibbitt H, Karlsson B, Sorensen P. Abaqus v6.12 documentation—ABAQUS analysis user's manual. Providence (RI): Dassault Systèmes Simulia 2012.

102 Hill, R., 1964. Theory of mechanical properties of fiber-strengthened materials: I. Elastic behavior. J. Mech. Phys. Solids 12, 199-212.

103 Hing, K.A., Best, S.M., Bonfield, W., 1999. Characterization of porous hydroxyapatite. J. Mater. Sci. Mater. Med. 10, 135-145.

104 Holzapfel, G.A., 2000. Nonlinear solid mechanics: A continuum approach for engineering. Chichester: Wiley.

105 Holzapfel, G.A., Gasser, T.C., Ogden, R.W., 2000. A new constitutive framework for

arterial wall mechanics and a comparative study of material models. J. Elasticity 61, 1–48.

106 Honeybul, S., Ho, K.M., 2016. Predicting long-term neurological outcomes after severe traumatic brain injury requiring decompressive craniectomy: A comparison of the CRASH and IMPACT prognostic models, Injury, http://dx.doi.org/10.1016/j.injury.2016.04.017

107 Horak, Z., Pokorny, D., Fulin, P., Slouf, M., Jahoda, D., Sosna, A., 2010. Polyetheretherketone (PEEK). Part I: prospects for use in orthopaedics and traumatology. Acta Chir. Orthop. Tr. 77, 463–469.

108 Horgan, T.J., Gilchrist, M., 2003. The creation of three-dimensional finite element models for simulating head impact biomechanics. Int. J. Crashworthiness 8, 353-366.

109 Horgan, T.J., Gilchrist, M.D., 2004. Influence of FE model variability in predicting brain motion and intracranial pressure changes in head impact simulations. Int. J. Crashworthiness 9, 401–418.

110 Jacquemoud, C., Bruyère-Garnier, K., Coret, M., 2007. Methodology to determine failure characteristics of planar soft tissues using a dynamic tensile test. J. Biomech. 40, 468–475.

111 Jaekel, D., MacDonald, D., Kurtz, S., 2011. Characterization of PEEK biomaterials using the small punch test. J. Mech. Behav. Biomed. 4, 1275-1282.

112 Jeng, C., Chen, M., 2000. Flexural failure mechanisms in injection-moulded carbon fibre/PEEK composites. Compos. Sci. Technol. 60, 1863-1872.

113 Jenkinson M., Pechaud M., Smith S., BET2: MR-based estimation of brain, skull and scalp surfaces, in Eleventh Annual Meeting of the Organization for Human Brain Mapping (2005).

114 Jérusalem, A., Dao, M., 2012. Continuum modeling of a neuronal cell under blast loading. Acta Biomater. 8, 3360–3371.

115 Jirousek, O., Jíra, J., Jírová, J., Micka, M., 2005. Finite Element Model of Human Skull Used for Head Injury Criteria Assessment, In: M.D. Gilchrist (Ed.) IUTAM Symposium on Impact Biomechanics: From Fundamental Insights to Applications 459-467: Springer Netherlands.

116 Jockisch, K.A., Brown, S.A., Bauer, T.W., Merritt, K., 1992. Biological response to chopped–carbon–fiber-reinforced peek. J. Biomed. Mater. Res. 26, 133–146.

117 Johnson GR, Cook WH. A constitutive model and data for metals subjected to large strains high strain rates and high temperatures. In: Proceedings of Seventh International Symposium Ballistics; 1983.

118 Johnson, G.R., Cook, W.H., 1985. Fracture characteristics of three metals subjected to various strains, strain rates, temperatures and pressures. Eng. Fract. Mech. 21(1), 31–48.

119 Jonas, A., Legras, R., Issi, J., 1991. Differential scanning calorimetry and infra-red crystallinity determinations of polyaryl ether ether ketone. Polymer 32 (18), 3364-3370.

120 Jordan, J.L., Siviour, C.R., Foley, J.R., Brown, E.N., 2007. Compressive properties of extruded polytetrafluoroethylene. Polymer 48, 4184–4195.

121 Kamlah, M., Tsakmakis, C., 1999. Use of isotropic thermoelasticity laws in ®nite viscoplasticity models. Continuum Mech. Therm. 11, 73-88.

122 Kammoun, S., 2011a. Micromechanical modeling of the progressive failure in short glass-fiber reinforced thermoplastics. In: PhD Thesis. Université catholique de Louvain.

123 Kammoun, S., Doghri, I., Adam, L., Robert, G., Delannay, L., 2011b. First pseudo-grain failure model for inelastic composites with misaligned short fibers. Compos. Part A-Appl. S. 42, 1892–1902.

124 Kammoun, S., Doghri, I., Brassart, L., Delannay, L., 2015. Micromechanical modeling of the progressive failure in short glass–fiber reinforced thermoplastics – First Pseudo-Grain Damage model. Compos. Part A-Appl. S. 73, 166-175.

125 Kang, H.S., Willinger, R., Diaw, B., Chinn, B., 1997. Validation of a 3D anatomic human head model and replication of head impact in motorcycle accident by finite element modeling. 41st Stapp Car Crash Conference, Lake Buena Vista, USA, 329–338.

126 Karger, J., Friedrich, K., 1989. Temperature and strain-rate effects on the fracture toughness of poly (ether ether ketone) and its short glass-fiber reinforced composite. Polymer 27, 1753–1760.

127 Kendall, M.J., Siviour, C.R., 2013. Experimentally simulating adiabatic conditions: Approximating high rate polymer behavior using low rate experiments with temperature profiles. Polymer 54, 5058-5063.

128 Kendall, M.J., Siviour, C.R., 2014. Novel temperature measurement method & thermodynamic investigations of amorphous polymers during high rate deformation. Polymer 55, 2514-2522.

129 Khalil, T.B, Hubbard, R.P., 1977. Parametric study of head response by finite element modeling. J. Biomech. 10, 119-132.

130 Khan, A., Zhang, H., 2001. Finite deformation of a polymer: experiments and modeling. Int. J. Plast. 17, 1167-1188.

131 Khatam, H., Liu, Q., Ravi-Chandar, K., 2014. Dynamic tensile characterization of pig skin. Acta Mech. Sinica 30, 125–132.

132 Kleiven S., Hardy W.N., 2002. Correlation of the FE model of the human head with local brain motion-consequences for injury prediction, In: Proceedings of 46th Stapp Car Crash Conference, Ponte Vedra, USA, 123-144. Society of Automotive Egineers (SAE), SAE Paper No. 2002-22-0007.

133 Krairi, A., Doghri, I., 2014. A thermodynamically-based constitutive model for thermoplastic polymers coupling viscoelasticity, viscoplasticity and ductile damage. Int. J. Plast. 60, 163-181.

134 Krairi, A., Doghri, I., 2014. A thermodynamically-based constitutive model for thermoplastic polymers coupling viscoelasticity, viscoplasticity and ductile damage. Int. J. Plast. 60, 163-181.

135 Kroner, E., 1960. Allgemeine kontinuumstheorie der versetzungen und eigenspannungen. Arch. Ration. Mech. An. 4, 273-334.

136 Kulkarni, A., Aswini, N., Dandekar, C.R., Makhe, S., 2012. Modeling of short fiber reinforced injection moulded composite. In: IOP Conference Mater Sci Eng.

137 Kurtz, S.M., Day, J., Ong, K., 2012. Isoelastic polyaryletheretherketone implants for total joint replacement. In: Kurtz S, editor. PEEK biomaterials handbook. William Andrew Elsevier; p. 221-242.

138 Kurtz, S., Devine, J., 2007. PEEK biomaterials in trauma, orthopedic, and spinal implants. Biomaterials 28, 4845-4869.

139 Labus, K.M., Puttlitz, C.M., 2016. An anisotropic hyperelastic constitutive model of brain white matter in biaxial tension and structural–mechanical relationships. J. Mech. Behav. Biomed. 62, 195–208.

140 LATI High Performance Thermoplastic. Polyether-ether-ketone material properties, <http://www.lati.com>;2015.

141 Lee, D.J., 1996. On studies of tensile properties in injection molded short carbon fiber reinforced PEEK composite. KSME J. 10, 362-371.

142 Lee, E., 1969. Elastic-plastic deformation at finite strains. ASME T. J. Appl. Mech. 36.

143 Li, G., Xu, W., 2011. Thermomechanical behavior of thermoset shape memory polymer programmed by cold-compression: Testing and constitutive modeling. J. Mech. Phys. Solids 59, 1231–1250.

144 Lion, A., 2000. Constitutive modelling in finite thermoviscoplasticity: a physical approach based on nonlinear rheological models. Int. J. Plast. 16, 469–494.

145 Liu, Z.S., Luo, X.Y., Lee, H.P., Lu, C., 2007. Snoring source identification and snoring noise prediction. J. Biomech. 40, 861-870.

146 Liu, Y-L., Lia, G-Y., He, P., Mao, Z-Q., Cao, Y., 2016. Temperature-dependent elastic properties of brain tissues measured with the shear wave elastography method. J. Mech. Behav. Biomed.: doi: http://dx.doi.org/10.1016/j.jmbbm.2016.09.026

147 Louche, H., Piette-Coudol, F., Arrieux, R., Issartel, J., 2009. An experimental and modeling study of the thermomechanical behavior of an ABS polymer structural component during an impact test. Int. J. Impact Eng. 36, 847–861.

148 Lovald, S., Kurtz, S., 2012. Applications of polyetheretherketone in trauma, arthroscopy and cranial defect repair. In: Kurtz S, editor. PEEK biomaterials handbook. William Andrew Elsevier; p. 243–60.

149 Loyd, A.M., Nightingale, R.W., Song, Y., Luck, J.F., Cutcliffe, H., Myers, B.S., Bass, C.D., 2014. The response of the adult and ATD heads to impacts onto a rigid surface. Accident Anal. Prev. 72, 219-229.

150 Marcacci, M., Kon, E., Zaffagnini, S., Giardino, R., Rocca, M., Corsi, A., Benvenuti, A., Bianco, P., Quarto, R., Martin, I., Muraglia, A., Cancedda, R., 1999. Reconstruction of extensive long-bone defects in sheep using porous hydroxyapatite sponges. Calcified Tissue Int. 64, 83–90.

151 Maurel-Pantel, A., Baquet, E., Bikard, J., Bouvard, J.L., Billon, N., 2015. A thermo-mechanical large deformation constitutive model for polymers based on material network description: Application to a semi-crystalline polyamide 66. Int. J. Plast. 67, 102–126.

152 McCrum, N.G., Buckley, C.P., Bucknall, C.B., 2003. Viscoelasticity. In: Principles of polymer engineering. Oxford Science.

153 Meaney, D.F., 2003. Relationship between structural modeling and hyperelastic material behavior: application to CNS white matter. Biomech. Model. Mechanbiol 1, 279–293.

154 Melvin, J.W., Robbins, D.H., Roberts, V.L., 1969. The mechanical behavior of the diploë layer of the human skull in compression. Dev. Mech. 5, 811–818.

155 Milchenko, M., Marcus, D., 2013. Obscuring surface anatomy in volumetric imaging data. Neuroinformatics 11(1), 65-75.

156 Millett, J., Bourne, N., Stevens, G., 2006. Taylor impact of polyether ether ketone. Int. J. Impact Eng. 32, 1806-1094.

157 Mohagheghian, I., McShane, G.J., Stronge, W.J., 2015. Impact perforation of monolithic polyethylene plates: Projectile nose shape dependence. Int. J. Impact Eng. 80, 162-176.

158 Molazemhosseini, A., Tourani, H., Naimi-Jamal, M., Khavand, A., 2013. Nanoindentation and nanoscratching responses of PEEK based hybrid composites reinforced with short carbon fibers and nano-silica. Polym. Test. 32, 525–534.

159 Monea, A., Van Perre, G., Baeck, K., Delye, H., 2014. Verschueren P. The relation between mechanical impact parameters and most frequent bicycle related head injuries. J. Mech. Behav. Biomed. 33, 3-15.

160 Mooney, M., 1940. A theory of large elastic deformation, Journal of Applied Physics, 11(9), 582-592.

161 Mortazavian, S., Fatemi, A., 2015. Effects of fiber orientation and anisotropy on tensile strength and elastic modulus of short fiber reinforced polymer composites. Compos: Part B-Eng. 72, 116–129.

162 Motz, H., Schultz, J.M., 1989. The Solidification of PEEK. Part I: Morphology. J. Thermoplast. Compos. 2, 248-266.

163 Mouhmid, B., Imad, A., Benseddiq, S., Maazouz, A., 2006. A study of the mechanical behavior of a glass fibre reinforced polyamide 6,6: experimental investigation. Polym. Test. 25, 544-552-

164 Mourad, A., Elsayed, H., Barton, D., Kenawy, M., Abdel-Latif, L., 2003. Ultra high molecular polyethylene deformation and fracture behaviour as a function of high strain rate and triaxial state of stress. Int. J. Fracture 120, 505-515.

165 Müller, V., Kabel, M., Andrä, H., Böhlke, T., 2015. Homogenization of linear elastic properties of short-fiber reinforced composites – A comparison of mean field and voxel-based methods. Int. J. Solids Struct. 67–68, 56-70.

166 Mulliken, A.D., Boyce, M.C., 2006. Mechanics of the rate-dependent elastic-plastic deformation of glassy polymers from low to high strain rates. Int. J. Solids Struct.44, 1331-1356.

167 Nasiri-Abarbekoh, H., Ekrami, A., Ziaei-Moayyed, A., Shohani, M., 2012. Effects of rolling reduction on mechanical properties anisotropy of commercially pure titanium. Mater. Design 34, 268-274.

168 Nasraoui, M., Forquin, P., Siad, L., Rusinek, A., 2012. Influence of strain rate, temperature and adiabatic heating on the mechanical behaviour of poly-methyl-methacrylate: Experimental and modelling analyses. Mater. Des. 37, 500–509.

169 Niinomi, M., 2008. Mechanical biocompatibilities of titanium alloys for biomedical applications. J. Mech. Behav. Biomed. 1, 30-42.

170 Ning, X., Zhu, Q., Lanir, Y., Margulies SS. 2006. A transversely isotropic viscoelastic constitutive equation for brainstem undergoing finite deformation. J. Biomech. Eng. 128, 925–933.

171 Notta-Cuvier, D., Lauro, F., Bennani, B., 2014. An original approach for mechanical modelling of short-fiber reinforced composites with complex distributions of fiber orientation. Compos. Part A-Appl. S. 62, 60-66.

172 Notta-Cuvier, D., Lauro, F., Bennani, B., 2015. Modelling of progressive fiber/matrix debonding in short-fiber reinforced composites up to failure. Int. J. Solids Struct. 66, 140-150.

173 Ogden, R.W., 1997. Non-Linear Elastic Deformations. Dover, New York.

174 Olmi, R.M., Ravaglioni, A., Krajewski, A., Pizzoferrato, A., 1984. Impianti di idrossiapatite in femori di conigli. Osservazioni istologiche e microradiografiche. Chir. Organi Mov. 69, 383–90.

175 Ommaya, A.K., Fass, F., Yarnell, P., 1968. Whiplash injury and brain damage: An experimental study. J.A.M.A. 204, 285–289.

176 Ottenio, M., Tran, D., Annaidh, A.N., Gilchrist, M.D., Bruyère, K., 2015. Strain rate and anisotropy effects on the tensile failure characteristics of human skin. J. Mech. Behav. Biomed. 41, 241-250.

177 Peng, X.Q., Guo, Z.Y., Moran, B., 2006. An anisotropic hyperelastic constitutive model with fiber-matrix shear interaction for the human annulus fibrosus. J. Appl. Mech. 73(5), 815-824.

178 Pernas-Sánchez, J., Artero-Guerrero, J.A., Zahr-Viñuela, J., Varas, D., López-Puente, J., 2014. Numerical analysis of high velocity impacts on unidirectional laminates. Compos. Struct. 107, 629-634.

179 Pervin, F., Chen, W.W., 2009. Dynamic mechanical response of bovine gray matter and white matter brain tissues under compression. J. Biomech. 42, 731–735.

180 Pettarin, V., Elic, G.E., Frontini, P.M., Leskovics, K., Lenkey, G.Y.B, Czigany, T., 2006. Analysis of low temperature impact fracture data of thermoplastic polymers making use of an inverse methodology. Eng. Fract. Mech. 73, 738-749.

181 Pierpaoli, C., Basser, P.J., 1996. Toward a quantitative assessment of diffusion anisotropy. Magn. Reson. Med. 36(6), 893–906.

182 Polanco-Loria, M., Clausen, A.H., Berstad, T., Hopperstad, O.S., 2010. Constitutive model for thermoplastics with structural applications. Int. J. Impact Eng. 37, 1207-1219.

183 Popelar, C.F., Popelar, C.H., Kenner, V.H., 2004. Viscoelastic material characterization and modelling of polyethylene. Polym. Eng. Sci. 30, 577–586.

184 Pouriayevali, H., Arabnejad, S., Guo, Y., Shim, V., 2013. A constitutive description of the rate-sensitive response of semi-crystalline polymers. Int. J. Impact Eng. 62, 35-47.

185 Prange, M.T., Margulies, S.S., 2002. Regional, directional, and age dependent properties of the brain undergoing large deformation. J. Biomech. Eng. 124, 244–252.

186 Qiu, G.Y., Pence, T.J., 1997. Remarks on the Behavior of Simple Directionally Reinforced Incompressible Nonlinearly Elastic Solids. J. Elasticity 49:1–30.

187 Rae, P., Brown, E., Orler, E., 2007. The mechanical properties of poly(ether-ether-ketone) (PEEK) with emphasis on the large compressive strain response. Polymer 48, 598–615.

188 Raghava, R., Caddell, R.M., Yeh, G.S.Y., 1973. The macroscopic yield behaviour of polymers. J. Mater. Sci. 8, 225-232.

189 Raghava, R.S., Caddell, R.M., 1973. Macroscopic yield criterion for crystalline polymers. Int. J. Mech. Sci. 15, 967–974.

190 Ramsteiner, F., Theysohn, R., 1979. Tensile and Impact Strengths of Unidirectional, Short Fiber-reinforced Thermoplastics. Composites 10, 111-119.

191 Rashid, B., Destrade, M., Gilchrist, M.D., 2014. Mechanical characterization of brain tissue in tension at dynamic strain rates. J. Mech. Behav. Biomed. 33, 43–54.

192 Recht, R.F., Ipson, T.W., 1963. Ballistic perforation dynamics. J. Appl. Mech. 30, 384-390.

193 Reese, S., 1998. Multiplicative thermo-viscoplasticity: A thermodynamic model and its finite element implementation. Tech. Mech.18, 209-216.

194 Regrain, C., Laiarinandrasana, L., Toillon, S., Sai, K., 2009. Multi-mechanism models for semi-crystalline polymer: constitutive relations and finite element implementation. Int. J. Plasticity 25, 1253–1279.

195 Rezaei, R., Yunus, R., Ibrahim, N., 2009. Effect of fiber length on thermomechanical properties of short carbon fiber reinforced polypropylene composites. Mater. Design 30, 260-263.

196 Rittel, D., 1999. The conversion of plastic work to heat during high strain rate deformation of glassy polymers. Mech. Mater. 31, 131–139

197 Rivard, C.H., Rhalmi, S., Coillard, C., 2002. In vivo biocompatibility testing of peek polymer for a spinal implant system: a study in rabbits. J. Biomed. Mater. Res. 62, 488–498.

198 Rivlin, R.S., 1948. Large elastic deformations of isotropic materials. IV. Further developments of the general theory, Philosophical Transactions of the Royal Society of London. Series A, Mathematical and Physical Sciences, 241(835), 379-397.

199 Rodríguez-Martínez, J.A., Rittel, D., Zaera, R., Osovski, S., 2013a. Finite element analysis of AISI 304 steel sheets subjected to dynamic tension: the effects of martensitic transformation and plastic strain development on flow localization. Int. J. Impact Eng. 53, 206–216.

200 Rodríguez-Martínez, J.A., Vadillo, G., Fernández-Sáez, J., Molinari, A., 2013b. Identification of the critical wavelength responsible for the fragmentation of ductile rings expanding at very high strain rates. J. Mech. Phys. Solids 61, 1357-1376.

201 Rodríguez-Martínez, J.A., Vadillo, G., Zaera, R., Fernández-Sáez, J., Rittel, D., 2015. An analysis of microstructural and thermal softening effects in dynamic necking. Mech. Mater. 80, 298–310.

202 Rosenthal, G., Ng, I., Moscovici, S., Lee, K., Lay, T., Martin, C., Manley, G.T., 2014. Polyethererketone implants for the repair of large cranial defects: a 3-center experience. Neurosurgery 75, 523-529.

203 Ruan, J.S., Khalil, T., King, A.I., 1991. Human head dynamic response to side impact by finite element modeling. J. Biomech. Eng. 113, 276–283.

204 Rubio-López, A., Olmedo, A., Santiuste, C., 2015. Modelling impact behavior of all-cellulose composite plates. Compos. Struct. 122, 139-143.

205 Rusinek, A., Rodríguez-Martínez, J., Zaera, R., Klepaczko, J., Arias, A., 2009. Sauvelet C. Experimental and numerical study on the perforation process of mild steel sheets subjected to perpendicular impact by hemispherical projectiles. Int. J. Impact Eng. 36 (4), 565-587.

206 Rusinek, A., Zaera, R., 2007. Finite element simulation of steel ring fragmentation under radial expansión. Int. J. Impact Eng. 34, 799–822.

207 Sadigh, S., Reimers, A., Andersson, R., Laflamme, L., 2004. Falls and fall-related injuries among the elderly: a survey of residential-care facilities in a Swedish municipality. J. Commun. Health 29, 129-140.

208 Saez, P., Sotiropoulos, S.N., Goriely, A., Jérusalem, A. The role of anisotropic elasticity in the mechanics and damage of the brain. J. R. Soc. Interface (under review).

209 Sahoo, D., Deck, C., Willinger, R., 2014. Development and validation of an advanced

anisotropic visco-hyperelastic human brain FE model. J. Mech. Behav. Biomed. 33, 24-42.

210 Sahoo, D., Deck, C., Yoganandan, N., Willinger, R., 2016. Development of skull fracture criterion based on real-world head trauma simulations using finite element head model. J. Mech. Behav. Biomed. 57, 24-41.

211 Santos, W., Sousa, J.A., Gregorio R., 2013. Thermal conductivity behaviour of polymers around glass and crystalline melting temperatures. Polym. Test. 32, 987-994.

212 Sarausa, J., Remiro, P., 1995. The mechanical behaviour of PEEK short fiber composites. J. Mater. Sci. 30, 3501-3508.

213 Sarva, S., Mulliken, A.D., Boyce, M.C, 2007. Mechanics of Taylor impact testing of polycarbonate. Int. J. Solids Struct. 44, 2381-2400.

214 Schapery, R.A., 1984. Correspondence principles and a generalised J integral for large deformation and fracture analysis of viscoelastic media. Int. J. Fracture 25, 195–223.

215 Scholz, M.S., Blanchfield, J.P., Bloom, L.D., Coburn, B.H., Elkington, M., Fuller, J.D., Gilbert, M.E., Muflahi, S.A., Pernice, M.F., Rae, S.I., Trevarthen, J.A., White, S.C., Weaver, P.M., Bond, I.P., 2011. The use of composite materials in modern orthopaedic medicine and prosthetic devices: A review. Compos. Sci. Technol. 71(16), 1791-1803.

216 Schulz, B.W., Lee, W.E., Lloyd, J.D., 2008. Estimation, simulation, and experimentation of a fall from bed. J. Rehabil. Res. Dev. 45, 1227-1236.

217 Serban, D.A., Weber, G., Marsavina, L., Silberschmidt, V.V., Hufenbach, W., 2013. Tensile properties of semi-crystalline thermoplastic polymers: Effects of temperature and strain rates. Polym. Test. 32, 413-425.

218 Shuck, L.Z., Advani, S.H., 1972. Rheological response of human brain tissue in shear. J. Basic Eng. 94, 905–911.

219 Smith, S.M., 2002. Fast robust automated brain extraction. Hum. Brain Mapp. 17(3), 143-155.

220 Smith, S.M., Jenkinson, M., Woolrich, M.W., Beckmann, C.F., Behrens, T.E.J., Johansen-Berg, H., Bannister, P.R., De Luca, M., Drobnjak, I., Flitney, D.E., Niazy, R., Saunders, J., Vickers, J., Zhang, Y., De Stefano, N., Brady, J.M., Matthews, P.M., 2004. Advances in functional and structural MR image analysis and implementation as FSL. NeuroImage 23(S1), 208-219.

221 Sobieraj, M., Kurtz, S., Rimnac, C., 2005. Large deformation compression induced crystallinity degradation of conventional and highly crosslinke UHMWPEs. Biomaterials 26, 6430-6439.

222 Sobieraj, M., Kurtz, S., Rimnac, C., 2009. Notch sensitivity of PEEK in monotonic tension. Biomaterials 30, 6485-6494.

223 Sobieraj, M., Rimnac, C., 2012. Fracture, fatigue and noch behavior of PEEK, in: Kurtz S, editor, PEEK Biomaterials Handbook, William Andrew Elsevier, p. 61-73.

224 Sobieraj, M., Kurtz, S., Rimnac, C., 2009. Notch sensitivity of PEEK in monotonic tension. Biomaterials 30, 6485–94.

225 Solomon, S., Bakar, A., Mohd, Z., 2007. Drop weight impact properties of (CO) injection molded short glass fiber/short carbon fiber/ polyamide 6 hybrid composites. J. Reinf. Plast. Comp. 26, 405-418.

226 Srivastava, V., Chester, S.A., Ames, N.M., Anand, L., 2010. A thermo-mechanically-coupled large-deformation theory for amorphous polymers in a temperature range which spans their glass transition. Int. J. Plast. 26, 1138–1182.

227 Stalnaker, R.L., 1969. Mechanical properties of the head, Ph.D. dissertation, West Virginia University.

228 Stefini, R., Esposito, G., Zanotti, B., Iaccarino, C., Fontanella, M.M., Servadei, F., 2013. Use of "custom made" porous hydroxyapatite implants for cranioplasty: postoperative analysis of complications in 1549 patients. Surg. Neurol. Int. 4-12.

229 Steinberg, E.L., Rath, E., Shlaifer, A., Chechik, O., Maman, E., Salai, M., 2013. Carbon fiber reinforced PEEK Optima—A composite material biomechanical properties and wear/debris characteristics of CF-PEEK composites for orthopedic trauma implants. J. Mech. Behav. Biomed. 17, 221-228

230 Swallowe, G.M., Fernandez, J.O., Hamdan, S., 1997. Crystallinity increases in semi crystalline polymers during high rate testing. J. Phys. IV 7(3), 453-458.

231 Takhounts, E., Eppinger, R., 2003. On the development of the SIMon finite element head model. 47th Stapp Car Crash Conference, San Diego, USA. Society of Automotive Engineers (SAE) 107–133.

232 Takhounts, E.G., Ridella, S.A., Hasija, V., Tannous, R.E., Campbell, J.Q., Malone, D., Danelson, K., Stitzel, J., Rowson, S., Duma, S., 2008. Investigation of Traumatic Brain Injuries Using the Next Generation of Simulated Injury Monitor (SIMon) Finite Element Head Model. Stapp Car Crash Journal 52, 1-31.

233 Talbot, M., Springer, G., Berglund, L., 1987. The effects of crystallinity on the mechanical properties of PEEK polymer and graphite fiber reinforced PEEK. J. Compos. Mater. 21, 1056-1081.

234 Tong, P., Fung, Y.C., 1976. The stress–strain relationships for the skin. J. Biomech. 9, 649–657.

235 Triantafyllidis, N., Waldenmyer, J.R., 2004. Onset of necking in electro-magnetically formed rings. J. Mech. Phys. Solids 52, 2127–2148.

236 Tse, K.M., Tan, L.B., Lee, S.J., Lim, S.P., Lee, H.P., 2015. Investigation of the relationship between facial injuries and traumatic brain injuries using a realistic subject-specific finite element head model. Accident Anal. Prev. 79, 13-32.

237 Tsukamoto, H., 2010. A mean-field micromechanical formulation of a nonlinear constitutive equation of a two-phase composite. Comp. Mater. Sci. 50, 560–570.

238 Tucker, C.L., Liang, E., 1999. Stiffness predictions for unidirectional short-fiber composites: Review and evaluation. Compos. Sci. Technol. 59, 655-671.

239 Ueno, K., Melvin, J.W., Lundquist, E., Lee, M.C., 1989. Two-Dimensional finite element analysis of human brain impact responses: application of a scaling law. Crashworthiness and Occupant Protection in Transportation Systems. New York, ASME. AMD- Vol 106.

240 Vadillo, G., Rodríguez-Martínez, J.A., Fernández-Sáez, J., 2012. On the interplay between strain rate and strain rate sensitivity on flow localization in the dynamic expansion of ductile rings. Int. J. Solids Struct. 49, 481–491.

241 Valero, C., Javierre, E., García-Aznar, J.M., Gómez-Benito, M.J., Menzel, A., 2015. Modeling of anisotropic wound healing. J. Mech. Phys. Solids 79, 80–91

242 Van den Kroonenberg, A., Hayes, W., McMahon, T., 1996. Hip impact velocities and body configurations for voluntary falls from standing height. J. Biomech. 29, 807–811.

243 van Dommelen, J.A.W., Parks, D.M., Boyce, M.C., Brekelmans, W.A.M., Baaijens, F.P.T., 2003. Micromechanical modeling of the elasto-viscoplastic behavior of semi-crystalline polymers. J. Mech. Phys. Solids 51, 519-541.

244 Van Essen, D.C., Smith, S.M., Barch, D.M., Behrens, T.E., Yacoub, E., Ugurbil, K., 2013. The Wu-Minn Human Connectome Project: an overview. Neuroimage 80, 62-79.

245 Velardi, F., Fraternali, F., Angelillo, M., 2006. Anisotropic constitutive equations and experimental tensile behavior of brain tissue. Biomech. Model. Mechan. 5, 53–61.

246 Verschueren, P., Delye, H., Depreitere, B., Van Lierde, C., Haex, B., Berckmans, D., Verpoest, I., Goffin, J., Vander Sloten, J., Van Perre, G., 2007. A new test set-up for skull fracture characterisation. J. Biomech. 40, 3389-3396.

247 Vincent, M., Giroud, T., Clarke, A., Eberhardt, C., 2005. Description and modeling of fiber

orientation in injection molding of fiber reinforced thermoplastics. Polymer 46, 6719–6725.

248 Vladimirov, I.N., Pietryga, M.P., Reese, S., 2010. Anisotropic finite elastoplasticity with nonlinear kinematic and isotropic hardening and application to sheet metal forming. Int. J. Plast. 26, 659–687.

249 Vogel, H.G., 1972. Influence of age, treatment with corticosteroids and strain rate on mechanical properties of rat skin. Biochim. Biophys. Acta 286, 79–83.

250 Wang, A., Lin, R., Stark, C., Dumbleton, J., 1999. Suitability and limitations of carbon fiber reinforced PEEK composites as bearing surfaces for total joint replacements. Wear 724, 225–229.

251 Wang, N., Liu, W., Huang, J., Ma, K., 2014. The structure–mechanical relationship of palm vascular tissue. J. Mech. Behav. Biomed. 36, 1–11.

252 Wang, Z., Zhou, Y., Mallick, P., 2002. Effects of temperature and strain rate on the tensile behaviour of short fiber reinforced polyamide-6. Polym. Composite 5, 858-871.

253 Wang, X., Shi, J., 2013. Validation of Johnson–Cook plasticity and damage model using impact experiment. Int. J. Impact Eng. 60, 67–75.

254 Ward C.C., Chan M., Nahum A.M., 1980. Intracranial pressure – a brain injury criterion. 24th Stapp Car Crash Conference, Warrendale, USA. Society of Automotive Engineers (SAE), 347–360 SAE Paper No. 801304.

255 Willinger, R., Baumgartner, D., Chinn, B., Neale, M., 2000. Head tolerance limits derived from numerical replication of real world accidents, In: Proceedings of International ICORBI Conference on the Biomechanics of Impacts, Montpellier, France, 209-221.

256 Willinger, R., Kang, H.S., Diaw, B.M., 1999. 3D human head finite element model validation against two experimental impacts. Ann. Biomed. Eng. 27, 403-410.

257 Willinger, R., Taleb, L., Kopp, C.M., 1995. Modal and temporal analysis of head mathematical models. J. Neurotraum. 12, N4.

258 Wood, J.L., 1971. Dynamic response of human cranial bone. J. Biomech. 4, 1–12.

259 Wu, P.D., van der Giessen, E., 1995. On neck propagation in amorphous glassy polymers under plane strain tension. Int. J. Plast. 11, 211-235.

260 Xue, Z., Vaziri, A., Hutchinson, J., 2008. Material aspects of dynamic neck retardation. J. Mech. Phys. Solids 56, 93–113.

261 Yoganadan, N., Pintar, N., Sances, A., Wals, P., Ewing, C., Thomas, D., Snyder, R., 1995.

Biomechanics of skull fracture. J. Neurotraum. 12(4), 659-668.

262 Yu, J.S., Maniatty, A.M., Knorr, D.B., 1997. Model for predicting thermal stresses in thin crystalline films. J. Mech. Phys. Solids 45, 511-534.

263 Zaera, R., Rodríguez-Martínez, J.A., Vadillo, G., Fernández-Sáez, J., 2014. Dynamic necking in materials with strain induced martensitic transformation. J. Mech. Phys. Solids 64, 316–337.

264 Zahouani, H., Pailler-Mattei, C., Sohm, B., Vargiolu, R., Cenizo, V., Debret, R., 2009. Characterization of the mechanical properties of a dermal equivalent compared with human skin in vivo by indentation and static friction tests. Skin Res. Technol. 15, 68–76.

265 Zahr Viñuela, J., Pérez-Castellanos, J.L., 2015. The anisotropic criterion of von Mises (1928) as a yield condition for PMMCs. A calibration procedure based on numerical cell-analysis. Compos. Struct. 134, 613–632.

266 Zaïri, F., Naït-Abdelaziz, M., Gloaguen, J.M., Lefebvre, J.M., 2008. Modelling of the elasto-viscoplastic damage behaviour of glassy polymers. Int. J. Plast. 24, 945–965.

267 Zhang, G., Scharlb, A., 2009. Correlation of the tribological behaviors with the mechanical properties of poly-ehter-ether-ketones (PEEKs) with different molecular weights and their fiber filled composites. Wear 266, 337-344.

268 Zhang, L., Yang, K.H., Dwarampudi, R., Omori, K., Li, T., Chang, K., Hardy, W.N., Khalil, T.B., King, A., 2001. Recent advances in brain injury research: a new human head model development and validation, In: Proceedings of 45th Stapp Car Crash Conference, San Antonio, USA, 369-394. Society of Automotive Engineers (SAE), SAE Paper No. 2001-22-0017.

269 Zhou, C., Khalil, C.T.B., King, A.I., 1995. A new model comparing impact responses of the homogeneous and inhomogeneous human brain, In: Proceedings of 39th Stapp Car Crash Conference, San Diego, USA, 121-137. Society of Automotive Engineers (SAE). SAE Paper No. 952714.

270 Zhou, Z., Jiang, B., Cao, L., Zhu, F., Mao, H., Yang, K.H., 2016. Numerical simulations of the 10-year-old head response in drop impacts and compression tests. Comput. Meth. Prog. Bio. 131, 13-25.

271 Zhu, K., Schmauder, S., 2003. Prediction of the failure properties of short fiber reinforced composites with metal and polymer matrix. Comp. Mater. Sci. 28(3–4), 743-748.

272 Zulligera, M.A., Fridez, P., Hayashi, K., Stergiopulos, N., 2004. A strain energy function for arteries accounting for wall composition and structure. J. Biomech. 37, 989–1000.

Universidad Carlos III de Madrid
Department of Continuum Mechanics and Structural Analysis